ISBN 978-82-326-0976-5 (printed version)
ISBN 978-82-326-0977-2 (electronic version)
ISSN 1503-8181

Doctoral Thesis
Bo Zhao

Doctoral theses at NTNU, 2015:160

Bo Zhao

Particle Filter for Fault Diagnosis: Applications to Dynamic Positioning Vessels and Underwater Robotics

NTNU – Trondheim
Norwegian University of
Science and Technology

Doctoral theses at NTNU, 2015:160
NTNU

NTNU
Norwegian University of
Science and Technology
Faculty of Engineering Science and Technology
Department of Marine Technology

NTNU – Trondheim
Norwegian University of
Science and Technology

Bo Zhao

Particle Filter for Fault Diagnosis: Applications to Dynamic Positioning Vessels and Underwater Robotics

Thesis for the degree of Philosophiae Doctor

Trondheim, June 2015

Norwegian University of Science and Technology

NTNU – Trondheim
Norwegian University of
Science and Technology

NTNU
Norwegian University of Science and Technology

Thesis for the degree of Philosophiae Doctor

ISBN 978-82-326-0976-5 (printed version)
ISBN 978-82-326-0977-2 (electronic version)
ISSN 1503-8181

Doctoral theses at NTNU, 2015:160

Printed by Skipnes Kommunikasjon as

Abstract

Safety remains an important consideration in control system design. This is particularly true for the control systems that are employed by the offshore petroleum and maritime industries, in which authorities continually claim to have developed more and more rigorous methods and processes to ensure safety and reliability. In addition to the use of more traditional approaches to conducting redundancy design, backup system design, robust design, and failure mode and effect analysis, these methods often involve the use of fault tolerant design to enhance the safety and reliability of the control system.

As a common practice, segregation and redundant design are used for dynamic positioning vessels to isolate faulty components and prevent the propagation of faults. However, many incidents still occur as a result of fault escapes from the segregation on a torpid detection. In more severe cases, false detection can actually cause faults and may result in an even more dangerous situation that has more catastrophic consequences. Hence, precise and timely fault diagnosis is necessary for the operator or the automation system to take appropriate action.

This thesis presents a brief overview of the existing fault diagnose methods, with a particular focus on particle-filter-based framework for fault diagnosis. The paper commences with a brief review of the background, theory, and typical features of the particle filter before progressing to examine the relationships and differences between the particle filter and other traditional stochastic filters. Switching mode hidden Markov model were employed to model a system with potential faults and a new methodology that uses a particle filter as fault diagnosis filter was developed. This method was then applied on an underwater robotic, which worked in complex environmental disturbance and suffered from different failure modes. Experimental results from ROV sea trails verified that the new fault diagnosis design is effective and reliable.

Some sections of this thesis have been previously published as journal papers and conference papers:

- Bo Zhao, Mogens Blanke, and Roger Skjetne. Particle Filter ROV Navigation Using Hydroacoustic Position and Speed Log Measurements. In American Control Conference (ACC), 2012.
- Bo Zhao, Mogens Blanke, and Roger Skjetne. Particle Filter-Based Fault-Tolerant ROV Navigation Using Hydroacoustic Position and Doppler Velocity Measurements. In 9th IFAC Conference on Manoeuvring and Control of Marine Craft, 2012.
- Bo Zhao, Skjetne, R., Blanke, M., Dukan, F., "Particle Filter for Fault Diagnosis and Robust Navigation of Underwater Robot," IEEE Trans. Control Systems Technology, 22:6, 2399-2407, Nov. 2014.
- Bo Zhao and Roger Skjetne, "A Unified Framework for Fault Detection and Diagnosis Using Particle Filter," Modeling, Identification and Control, Vol. 35, No. 4, 2014.

Preface

This thesis is submitted to the Norwegian University of Science and Technology (NTNU) in partial fulfilment of the requirements for the degree of philosophy doctor.

This doctoral work was performed at the Centre for Ships and Ocean Structure (CeSOS), and Department of Marine Technology, NTNU, Trondheim, with Professor Roger Skjetne as main supervisor and under the guidance of co-supervisor Professor Mogens Blanke.

This work is partially supported by the RCN research project 199567, “Arctic DP.”

Acknowledgements

I would like to thank my supervisor, Professor Roger Skjetne, from the Centre for Ships and Ocean Structures (CeSOS) and Department of Marine Technology, Norwegian University of Science and Technology (NTNU), for his excellent guidance and significant contribution to this thesis. He provided valuable help with planning the research, ensuring activities were aligned, and identifying appropriate experiment opportunities. I was his first PhD student and, simultaneously, his first foreign PhD student, he gave up a significant amount of his own time to help me to secure accommodation, meet visa requirements, etc. His valuable help made it much easier for me to adjust to the Norwegian environment and society. He was a supportive supervisor and I will be forever grateful for his assistance.

I also would like to thank my co-supervisor, Professor Mogens Blanke, from CeSOS, NTNU and Technology and Department of Electrical Engineering, Technical University of Denmark (DTU). His brilliant insight into my research topic and his style of guiding students, step by step, from simple to complex, benefited me immensely during the whole project. This work would not have been possible without his instructions, suggestions, and comments. I was also deeply motivated by his work ethic.

Many thanks also to my co-supervisor, Professor Thos Inge Fossen, from Department of Engineering Cybernetics, NTNU. It was nice experience working with him. In addition, his lectures led me onto a higher level of navigation, guidance and control.

I am grateful to all the members of the Applied Underwater Robotics Laboratory. It was only through their input and cooperation that I could conduct appropriate experiments. PhD candidate Fredrik Dukan helped me with the ROV control system design, coding, and debugging; and PhD candidates Mauro Candeloro and Daniel de Almeida Fernandes shared their experience of the ROV structure and control system. I would also like to thank Prof. Asgeir J. Sørensen from CeSOS, who granted me the time and equipment required to conduct the ROV experiment.

I wish to thank Prof. Torgeir Moan, who organized and efficiently directed the CeSOS, where I completed the majority of my PhD study, and the staff of the CeSOS and the Department of Marine Technology, in particular Sigrid Bakken Wold.

Thanks to the PhD candidates and all the other members of CeSOS and the Department of Marine Technology. It was my pleasure to work with all of you. Special thanks to Dr. Biao Su, PhD candidates Qin Zhang, Ulrik Jørgensen, and Øivind Kåre Kjerstad for the useful and helpful discussions.

Moreover, I am deeply indebted to my parents in China. Their selfless love and support have motivated me to go this far, and further.

Contents

Abstract i

Preface iii

Acknowledgements v

Contents ix

List of Figures xii

List of Tables xiii

List of Algorithms xiii

Abbreviation xv

1 Introduction 1
- 1.1 Background . . . 1
  - 1.1.1 Safety Issues in the Offshore Oil Industry . . . 1
  - 1.1.2 Brief Review of Fault Diagnosis . . . 5
  - 1.1.3 Brief Review of Particle Filter . . . 7
- 1.2 Structure of this thesis and contributions . . . 8

2 Particle Filter 11
- 2.1 Introduction to the Filtering Technology . . . 11
- 2.2 Mathematical preliminaries . . . 12
  - 2.2.1 Basics . . . 12
  - 2.2.2 Bayesian Probability . . . 21
  - 2.2.3 Hidden Markov Model . . . 22
- 2.3 Recursive Bayesian filtering . . . 26
  - 2.3.1 General Form . . . 26
  - 2.3.2 The Kalman Filter . . . 28
  - 2.3.3 Extended Kalman filter . . . 32
  - 2.3.4 Gaussian Sum Filter . . . 34
  - 2.3.5 Unscented Kalman filter . . . 39
- 2.4 Particle filter . . . 42

2.4.1 Pointwise Expression of Distribution 42
2.4.2 Importance Sampling and Proposal Distribution 43
2.4.3 Sequential Importance Sampling Partial Filter 47
2.4.4 Degeneracy Problem, Resampling, and Sampling Importance Resample PF 49
2.4.5 Case Study: PF-based Navigation System 52
2.4.6 Case Study: Wave Filtering for DP Vessel Using Particle Filter 62
2.5 Conclusion 67

3 Fault Diagnosis with Particle Filter 69
3.1 Introduction 69
3.2 Switching Mode Hidden Markov Model 71
3.2.1 Modelling Examples 72
3.2.2 Discussion Regarding the HMM 77
3.3 Understanding the Behaviour of Switching Mode HMM 77
3.3.1 Internal View 77
3.3.2 External View 79
3.4 Algorithm of Using PF for FD on Switching Mode HMM 79
3.4.1 PF Algorithm 79
3.4.2 Fault Diagnosis Algorithm 83
3.5 Relevant Topics 85
3.5.1 Adaptive Resampling Algorithm 85
3.5.2 Rao-Blackwellization 88
3.5.3 Mode Ambiguity 89
3.6 Study Cases: Examples of Diagnosis for Basic Anomalies 91
3.6.1 Changing DC Level in White Noise 91
3.6.2 Signal Drifting 92
3.6.3 Missing Measurement 95
3.7 Study Case: PF for Fault Diagnosis and Robust Navigation of DP Vessels 98
3.7.1 Scenario 98
3.7.2 Analysis and Modelling of Failure Modes 98
3.7.3 Particle Filter Design 100
3.7.4 Simulation and Result 101
3.8 Conclusion 103

4 Application: Particle Filter for Robust Navigation of Underwater Robot 107
4.1 Introduction 107
4.2 ROV manoeuvring Model 108
4.2.1 The ROV Minerva 108
4.2.2 Kinematics 111
4.2.3 Kinetics 111
4.2.4 Thruster Control 112
4.2.5 Sensor Model 112
4.2.6 Resulting ROV Model 114

4.3 Anomaly Analysis 115
4.3.1 Mode $\Delta^{\mathrm{HPR},1}$ – HPR dropout 115
4.3.2 Mode $\Delta^{\mathrm{HPR},2}$ – HPR Measurement Outliers 116
4.3.3 Mode $\Delta^{\mathrm{DVL},1}$ – DVL Dropout 117
4.3.4 DVL Bias 117
4.3.5 Modes $\Delta^{\mathrm{THR},t,1}$ and $\Delta^{\mathrm{THR},t,2}$ – Insufficient Thrust and Zero Thrust 117
4.3.6 Simultaneous Faults 118
4.4 Navigation System Design 119
4.4.1 Separating the Heave and Yaw DOFs 119
4.4.2 Mode Transitions 119
4.4.3 Switching Mode HMM for the ROV 120
4.5 Full-scale Test Campaign 121
4.5.1 Setup 121
4.5.2 Discussion of the Results 123
4.6 Conclusion 132

5 Conclusion and Future Work **137**

Glossary **138**

References **138**

List of Figures

1.1 Dynamic positioning system 1. 2
1.2 Dynamic positioning system 2. 3
1.3 ROV Minerva in operation. 5

2.1 CDF and empirical CDF; PDF and normalized histogram. 16
2.2 Probability plots for different sample size. 17
2.3 Example: empirical distributions approaching the real distribution. . . 19
2.4 Example: empirical distributions approaching the real distribution - 2 20
2.5 A vessel in the NE frame. 24
2.6 Comparisons of different approximations methods. 27
2.7 EKF approximation of nonlinear system - 1 34
2.8 EKF approximation of nonlinear system - 2 35
2.9 Gaussian sum approximation of nonlinear system - 1 36
2.10 Gaussian sum approximation of nonlinear system - 2 37
2.11 Gaussian sum approximation of nonlinear system - 3. 38
2.12 Comparison of the proposal distributions. 45
2.13 Distributions of the vessel position states. 53
2.14 Distributions of the states and position measurement. 54
2.15 The prior estimation and the posterior estimation by PF. 56
2.16 Time history of the estimation. 57
2.17 Estimation error time history. 58
2.18 Time series of estimation error and variance. 60
2.19 Time series of the likelihood of the “true” states. 61
2.20 Illustration of likelihood. 61
2.21 The performance of PF based wave filtering and nonlinear passive filter 66

3.1 The Markov chain of mode transition. 74
3.2 Decayed output. 75
3.3 Principle of using PF for fault detection. 78
3.4 Mode transition in continuous and discrete systems. 79
3.5 One cycle of the PF for switching mode HMM 80
3.6 The estimation of the PF on switching mode HMM 83
3.7 Illustration of mode ambiguity. 90
3.8 Detection of one-time jump in mean model 91
3.9 Segmentation in changing mean model. 93

3.10 Detection and estimation of signal drifting 94
3.11 Simulation of handling missing measurement 1. 96
3.12 Simulation of handling missing measurement 2. 97
3.13 PF base FDD for DP vessel (GPSS bias) 103
3.14 PF base FDD for DP vessel (GPSS drifting) 104
3.15 PF base FDD for DP vessel (GPSS outliers) 105

4.1 ROV Minerva. 108
4.2 ROV Minerva and the notations of its kinematics. 109
4.3 Overview of thruster configuration. 109
4.4 HPR measurement time series. 115
4.5 HPR outliers analysis. 116
4.6 ROV control system architecture 1. 122
4.7 ROV control system architecture 2. 122
4.8 Basic ROV navigation performance. 125
4.9 2D plot of the position measurement PF estimate. 126
4.10 Effect of HPR outliers. 127
4.11 HPR outliers detection. 128
4.12 Outliers detection rate. 129
4.13 Navigation when HPR dropout. 130
4.14 Navigation when DVL dropout. 131
4.15 ROV navigation during DVL bias. 132
4.16 ROV navigation during DVL bias. 133
4.17 Diagnosis of thruster loss. 134
4.18 ROV navigation during HPR and DVL dropout. 135
4.19 ROV navigation during HPR outliers and DVL dropout. 136

List of Algorithms

1 Sequential importance sampling particle filter 48
2 Multinomial resampling. 50
3 Sampling importance resample particle filter. 51

4 SIRPF for FD on switching mode HMM. 84
5 Adaptive resampling. 87

Abbreviations

$\trianglelefteq$	elementally smaller than or equal to
$\boldsymbol{x}^{(i)}$	sample i
$\delta(\cdot)$	Dirac measure function
$\mathbb{D}[X]$	the variance of random variable X
$\mathbb{E}[\boldsymbol{X}]$	the mathematical expectation of random vector $\boldsymbol{X}$
$\mathcal{N}(\boldsymbol{\mu}, \boldsymbol{\Sigma})$	n-dimensional multivariate normal PDF with mean $\boldsymbol{\mu} \in \mathbb{R}^n$ and covariance matrix $\boldsymbol{\Sigma} \in \mathbb{R}^{n \times n}$
$\mathbb{R}^n$	n-dimensional Euclidean space
$\mathcal{X}_k$	$\{\boldsymbol{x}_0\ \boldsymbol{x}_1\ \ldots\ \boldsymbol{x}_k\}$
$\mathcal{Y}_k$	$\{\boldsymbol{y}_1\ \boldsymbol{y}_2\ \cdots\ \boldsymbol{y}_k\}$
$\mathrm{Cov}[\boldsymbol{X}]$	the covariance matrix of $\boldsymbol{X}$
$\mathrm{diag}(\boldsymbol{x})$	The diagonal matrix with vector $\boldsymbol{x}$ as its diagonal entries.
$\rho(\cdot)$	Dirac function
$\sim$	"subject to"
$\xrightarrow{a.s.}$	converges almost surely to
$\xrightarrow{p}$	converges in probability to
AUV	autonomous underwater vehicles
BOP	blow out preventer
CDF	cumulative distribution function
DOF	degree of freedom
DP	dynamic positioning
DVL	Doppler velocity log
EKF	extended Kalman filter
FD	fault diagnosis
FMEA	failure modes & effects analysis
GSF	Gaussian sum filter

HIL	hardware-in-the-loop
HMM	hidden Markov model
HPR	hydroacoustic position reference
i.i.d.	ideally identically distributed
IMCA	International Marine Contractors Association
KF	Kalman filter
NED	North-East-Down
PDF	probability density function
PF	Particle filter
PMF	probability mass function
ROV	remotely operated underwater vehicle
SM-HMM	Switching mode hidden Markov model
std	standard deviation
UKF	unscented Kalman filter
UT	unscented transformation

Chapter 1

Introduction

1.1 Background

1.1.1 Safety Issues in the Offshore Oil Industry

In recent decades, scientists have extended their explorations of hydrocarbon from onshore to offshore. At the same time, the offshore oil industry has experienced rapid technological developments in the equipment that is available to conquer the harsh oceanic environment. The level of automation involved in offshore drilling, oil production, and supportive vessels has been steadily increasing. As too have the automation systems that have been specifically designed to enhance the safety and reliability of the vessels conduct their various missions.

The majority of the time, offshore installations and marine crafts are isolated in remote areas of the sea. They are far away from rescue, both spatially and temporally. Hence, it is very important that the offshore oil industry treat safety as a primary concern. The authorities require fully redundant design of the vessels. Furthermore, each newbuild vessel undergoes rigorous verification and validation, and existing vessels are subject to regular inspections and tests. Ship owners and operators also take safety issues seriously, and it is mandatory that comprehensive risk assessments are performed prior to the operation of equipment and vessels. However, incidents in the offshore oil industry still occur, and these accidents regularly result in economic losses, environmental damage and even the loss of human life. Thus, it is important that further studies are performed to identify methods of enhancing the safety and reliability of ships, offshore installations, and offshore operations.

Dynamic positioning vessels

Dynamic positioning (DP) vessels represent just one example of control systems that have been developed to ensure the safe and efficient operation of vessels. A DP vessel is required to maintain a given position through a process that is referred to as *station*

Figure 1.1: Dynamic positioning system: Offshore Support Vessel Toisa Perseus. In the background, the fifth-generation deepwater drillship Discoverer Enterprise can be seen. (Source: [Wikipedia, 2013])

keeping or *position keeping*. It achieves this through the appropriate application of thrusters. When a DP vessel is in a station-keeping mode, it maintains a desired position and heading in the horizontal plane. A small deviation from the desired position and direction is permitted. Station keeping is widely used in many offshore operations, such as drilling, loading and offloading, pipe-laying, etc. It is designed to ensure that vessels remain in their operational range in order to avoid collision between marine crafts.

The DP system enables a vessel to perform station-keeping activities. A DP system consists of several subsystems: the dynamic positioning computer system coordinates other subsystems, takes sensor input, and calculates control commands; the power management system ensures the power supply and avoids blackouts; the thruster control system takes thrust commands from the DP computer system and performs the lower level control of the thrusters; the position reference system reports the position of the vessel; and the sensor system measures environment disturbance.

All these offshore operations are critical to the safe operation of the vessel and prevent a loss-position, which could have catastrophic consequences. In the event that the vessel does stray from a certain operation radius when performing the drilling operation ([IMCA, 1999]), emergency disconnection has to be performed ([Deegan, 1998], [Bakken and Smedvig, 2001]), or crude oil will erupt from the well, endanger human life and result in an environmental disaster. [Anonymous, 2012] reported an incident

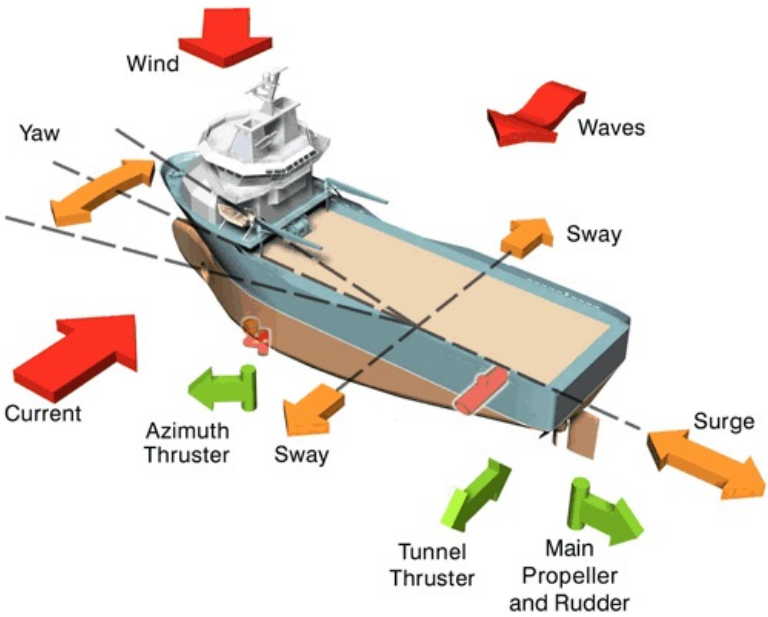

Figure 1.2: Dynamic positioning vessel with its 3 DOFs (surge, sway, yaw) motion, external disturbances, and thruster forces. Source: –.

during which an offshore diving support vessel lost position with divers below. There are other reports of DP drive-off due to a misleading position reference ([Marine, 2004]). Unfortunately, DP incidents, which potentially lead to the loss-position of DP vessels, occur on a regular basis. Data from the IMCA indicates that there were 1.08 incidents per vessel on average in 2007.

The *drive-off* case described by [Anonymous, 2012] is more severe than the so-called *drift-off*. Drift-off occurs when the DP vessel loses position due to an external force, such as wind, waves, and ocean current, while drive-off is caused by the DP system itself; for example, due to a misleading position reference or a fail-to-full thruster, which results in the DP system "pushing" itself away from the desired position.

A number of researchers have developed methodologies that aim to enhance the reliability of the DP system in its design and integration phases. In the design phase, failure modes and effects analyses (FMEA) ([IMCA, 2002]) is required. FMEA is a systematic analysis of the systems to whatever level of detail is required to demonstrate that no single failure will cause an undesired event. The aim of FMEA is to identify potential design flaws to minimize the risk of failure by either proposing design changes or, if these are not possible, making appropriate changes to operational procedures. Plenty of research has described the use of FMEA ([Cornes and Stockton, 1998], [DNV, 2004], and [Harper, 2008]).

Alternatively, hardware-in-the-loop (HIL) testing techniques can be employed to verify and validate the DP software. A DP-HIL vessel simulator is a real-time simulator that has a direct interface to a DP computer system. The simulator calculates the ves-

sel motion and other responses to simulate operation in a real environmental. Testing personnel introduce various failure modes to the simulator, and the response of the DP system is recorded and analysed. A range of on-board systems and equipment are activated in response to the calculated motion of the simulated vessel; for example, the power system, thrusters, sensors, and position reference systems. Appropriate data is collected by the corresponding sensor and transmitted back to the DP computers ([Johansen et al., 2005]). A number of researchers have examined the use of DP-HIL tests ([Phillips and Miller, 2000], [Marine, 2004], [Johansen et al., 2005], [Johansen and Sørensen, 2009], and [Sørensen, 2011]).

FMEA and HIL tests are powerful tools that can enhance the reliability of a DP system by identifying defects and detecting potential safety issues during the design and manufacture phases. These approaches can eliminate the majority of the design flaws that are present in the hardware and software. However, there is a distinct lack of methods that can detect, isolate, and estimate a fault on a real-time basis, and accidents that result from a small fault in the DP system as a result of erratic software actions are common and have significant consequences. Hence, in the case of an almost fully redundant system, i.e., the DP system, it is critical that faults are diagnosed in order to make good use of the redundant equipment. The more information that is available about the fault, the better it can be handled. A number of researchers have studied the diagnosis and fault-tolerant control for DP systems. Besides the overview paper provided by [Blanke, 2005], a detailed fault tolerant design for ship propulsion system was provided by [Blanke et al., 1998], and then followed by the work of [Wu et al., 2006], [Zhang et al., 2009], and [Garg et al., 2011]. In terms of research that has focused specifically on the thrusters and propellers, valuable studies have been conducted by [Spjtvold and Johansen, 2009], [Fu et al., 2011], and [Chin, 2012]. Several papers have focussed on a position-mooring system; for example, those conduced by [Fang and Blanke, 2011] and [Fang et al., 2013]. [Shi et al., 2012] discussed sensor faults in DP.

Underwater robotics

Underwater robotics are widely used in various sub-sea operations, typically in scientific research and survey, offshore hydrocarbon exploration and production. Underwater robotics fall into two categories: remotely operated underwater vehicles (ROVs) and autonomous underwater vehicles (AUVs). AUVs play an important role in wide-range seabed survey; however, ROVs, which are more complex, offer finer control and are highly safety-critical, are generally preferred because they can work in close proximity to offshore hydrocarbon exploration installations. Given this proximity, accurate and reliable positioning and control of the ROVs are required to realize high precision and fault-tolerant ROV navigation. [Kinsey et al., 2006] discussed some of the commonly used ROV navigation sensors. These sensors use different principles and have different features; as such, their update rate, precision, and range are generally different. ROVs are usually equipped with several types of sensors that work in combination to form an integrated navigation system that overcomes the disadvantages of each type of sensor to obtain an accurate and reliable position estimate. Some of the applications of ROV integrated navigation were reported in [Blain et al., 2003],

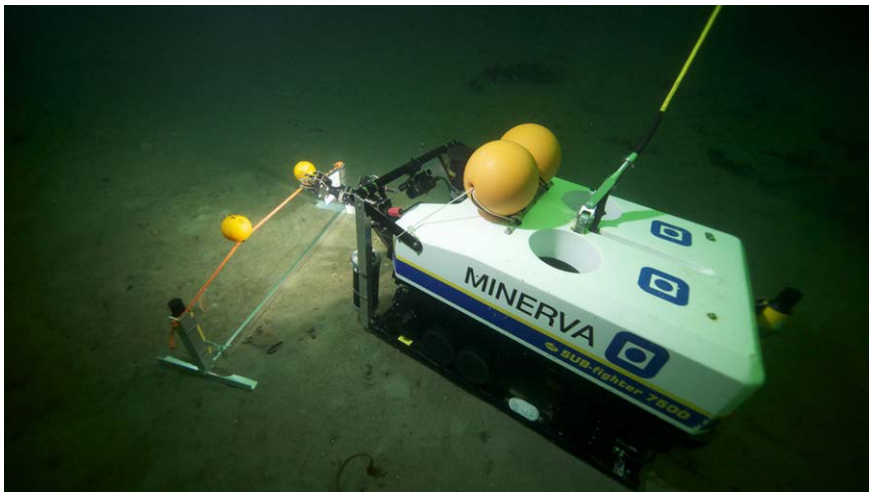

Figure 1.3: ROV Minerva in operation. Photo by AUR Lab (Source: [AUR-Lab, 2013]).

[Kinsey and Whitcomb, 2004], and [Dukan et al., 2011]. In these applications, sensors are assumed reliable; however, sensor faults are frequently encountered in practice, making it necessary to detect and accommodate the sensor faults. Such faults can be diagnosed by checking the consistency of the measurements from the redundant sensors; however, it is not always possible to install redundant sensors on ROVs because of limitations. In this case, making use of all available information from different types of sensors to achieve a model-based software redundancy is preferred ([Fauske et al., 2007], and [Filaretov et al., 2012]). Moreover, actuator faults are also important ([Antonelli, 2003], [Alessandri et al., 1999], and [Bono et al., 1999]).

1.1.2 Brief Review of Fault Diagnosis

Due to the increasing requirements of safety, reliability, and performance, fault-tolerant design for control systems has drawn significant attention. Faults in actuators, sensors, or other system components in conventional feedback control designs, may result in unsatisfactory performance, or even instability. Thus, to maintain the performance of the system, it is important to ensure the system works continues to operate in a degraded, but safe, condition when faults occur. This is particularly vital in safety-critical systems, such as those employed in aircraft, submarines, nuclear power stations, chemical plants, etc. In such systems, the consequences of a minor fault in a component or any loss of system functionality can be catastrophic, as was the case in the DP incidents reported and discussed by [Deegan, 1998] and [Jenssen and Hauge, 2002]. Therefore, the demand for reliable, safe, and fault-tolerant control designs is high.

In order to realize a fault tolerance system, it is first important to detect and diagnose faults. Two approaches can be employed to achieve this: an analytical approach and a

heuristic approach.

According to [Isermann, 2006], the analytical approach further consists of two methods: a signal-processing-based method and a model-based method. The analytical approach that is based on signal processing considers the time domain (statistical) and/or frequency domain features of output signals. The threshold, amplitude, mathematical expectation, variance, correlation, and frequency spectrum (Fourier analysis) must be inspected using a signal-processing-based method. In addition, advanced analytical methods, such as wavelet analysis, intelligent analysis (such as neural networks and fuzzy logic), cluster analysis, and some other methods from pattern recognition, can also be applied. An example of a study that involved a signal-processing-based method was that conducted by [Galeazzi et al., 2012] in which the parametric roll motion of a vessel was detected by comprehensively applying several signal-processing-based FD methods. Other examples can be found in [Henao et al., 2003], where faults in induction machine drives were studied; and [Hussain and Gabbar, 2011], who studied gear faults based on pulse shape analysis.

A model-based analytical FDD was discussed in detail by [Blanke et al., 2006]. The basic idea behind model-based fault detection can be outlined as follows: the nominal system behaviour derived from the mathematical model or the predicted behaviour by the model is compared with the actual system behaviour, as derived from the measurements. The essential objective of this method is to design residual generators, which are functions of the input and measurement of a system. A residual generator produces a residual signal, which is close to zero when the system is fault-free and differs from zero when there is fault present. A fault is detected whenever the residual exceeds a pre-designed threshold. The threshold is designed according to given design parameters, such as the *mean-time-to-detect* and the *false-alarm-rate*. The diagnosis of fault leans on examining the behaviour of the residual. In the case of multiple faults, several residual generators are usually designed. A fault is isolated when its corresponding residuals exceed the threshold, while other residuals remain close to zero. However, for the stochastic systems described by state space models, much of the development in fault detection schemes has relied on the system being linear and the noise and disturbances being Gaussian.

This method is very practical and has wide applications. For example, [Blanke et al., 1998] employed it in a fault tolerant design for a ship propulsion system. It has also been used to produce a fault tolerant design for station keeping vessels ([Blanke, 2005]), and [Bak et al., 1996] applied a model-based analytical FDD to a satellite orientation control system.

There have been a number of recent innovations in model-based FD ([Bashi et al., 2011], [Shang and Liu, 2011], and [Meskin et al., 2013]). [Shang and Liu, 2011] developed an unscented Kalman filter (UKF)-based method to detect and isolate both temperature sensor and valve actuator faults in a high-performance aircraft bleed air temperature control system. Two UKFs were designed to detect two failure modes. Since UKF was used in the FD scheme, the detection algorithm exhibited the ability to adopt the nonlinearity of the system. [Bashi et al., 2011] considered fault detection in large-scale systems in which many practically identical units operate in a shared environment. A special class of hybrid system mathematical models were introduced

to describe such multi-unit systems, and a general approach for estimation and change detection was proposed. The proposed algorithm also considered mode switching and parameter drift, so it could handle sudden, incipient, and pre-existing faults. [Meskin et al., 2013] proposed a real-time fault detection and isolation scheme based on the concept of multiple model for aircraft jet engines, and the current operating mode of the system was detected according to an evaluation of the maximum probability criteria.

1.1.3 Brief Review of Particle Filter

Particle filter (PF), which is inherited from the Bayesian estimation and the Monte Carlo method, has been studied for decades. For example, [Handschin, 1970] and [Akashi and Kumamoto, 1977] conducted some of the early studies in which the Monte Carlo technique was used to estimate states in stochastic process. However, the shortage of computational power at that time limited the further development of this promising approach. The idea of particle filter was first formally introduced by [Gordon et al., 1993] in a study in which the fundamental idea of using the Monte Carlo method to estimate state in a hidden Markov system was recovered from literature. This method was further enriched by [Kitagawa, 1996], [Liu and Chen, 1998], and many other researchers. The book produced by [Doucet et al., 2001] contained a lot of important research. A good early tutorial was produced by [Arulampalam et al., 2002], and their work represents a very practical introduction to the PF. Recent improvements in PF were summarized in [Cappe et al., 2007] and [Doucet and Johansen, 2009]

PFs may be perceived to represent a serious alternative to real-time applications as classically approached by the (extended) Kalman filter ([Gustafsson, 2010]). The more nonlinearity or the more non-Gaussian noise that the system model exhibits, the more potential PFs have, especially in applications where computational power is rather cheap and the sampling rate is moderate. The PF has drawn great attention since it was proposed. It is a powerful tool to solve the estimation problems that are associated with nonlinear non-Gaussian circumstances. Moreover, PF has been wildly applied; for example, in navigation ([Zhao et al., 2012b]), target tracking ([Karlsson and Gustafsson, 2006]), computer vision, digital communications, speech recognition, machine learning, and many other areas (see [Chen, 2003] for more detail).

Particle filter for fault diagnosis

Diagnosing faults in systems is one of the most significant branches of particle filter applications. Three early studies that involved the use of PF for fault diagnosis include those completed by [Kadirkamanathan et al., 2000], [Li and Kadirkamanathan, 2001], and [Kadirkamanathan et al., 2002], in which the authors developed a method that combined the state estimation by a particle filter in a multiple model environment and likelihood ratio approach to detect and isolate faults in stochastic nonlinear dynamic systems. When this method is employed, the fault in the system is modelled as parameters of the model. The estimation of the state from the particle filter is used to

derive the likelihood of these parameters. Once the likelihood of a parameter exceeds a pre-defined threshold, it claims the system is with fault.

Another success story involving the application of a particle filter in fault detection was described in a series of papers ([Verma et al., 2001] [Thrun et al., 2002] [Verma et al., 2003], and [Verma et al., 2004]). In these papers, a fault detection problem involving a space rover was examined and a so-called *risk sensitive particle filter* and *variable resolution particle filter* were developed. The two new particle filters aimed to improve the efficiency with which the particle filter detected faults. The risk sensitive particle filter deals with those anomalies that rarely happen but, when they do, have severe consequences. It tries to distribute more particles, i.e., computation on these type of anomalies to improve the overall effectiveness of the particle filter. The variable resolution particle filter is more result-oriented, i.e., the faults result in similar consequences are represented by so-called abstract particles. By doing so, a limited number of particles are, therefore, sufficient for representing large portions of the state space when the likelihood that this part of the state space will be occupied is low.

[Koutsoukos et al., 2002] produced a particle-filtering-based estimation, monitoring, and diagnosis algorithm that focused on the interaction between continuous and discrete dynamics in hybrid systems. The hybrid estimation methodology was demonstrated on a rocket propulsion system. [de Freitas, 2002] described a Rao-Blackwellised particle-filtering-based fault diagnosis approach ([Doucet et al., 2000b]). The approach presented in [de Freitas, 2002] combined a particle filter that was designed to compute the distribution of the discrete states with a bank of Kalman filters that were required to compute the distribution of the continuous states. In order to effectively track the behaviour of the discrete states, there needs to be a large number of Kalman filters in the filter bank. One possible method of improving the performance of the above-mentioned approach was stated in [Morales-Menendez et al., 2002] who employed a one-step look-ahead approach. [Funiak and Williams, 2003] combined this approach with probabilistic hybrid automata to allow continuous variables to affect discrete state transitions, which might be a more precise model of the reality than the hidden Markov model considered in alternative research.

A more recently reported approach to use particle filters for fault diagnosis was resented by [Caron et al., 2007] who used a hidden Markov model with variable transition probabilities that were estimated online from data. The application involved a multi-sensor fusion for land vehicle positioning. In [Caron et al., 2007], the latent parameters and hyper parameters that were introduced into the system model resulted in a high computational burden.

1.2 Structure of this thesis and contributions

Chapter 2 commences with an overview of the mathematical foundation and formulation of probability and statistics. Then, the concept of recursive Bayesian filtering is introduced. The Kalman filter, extended Kalman filter, Gaussian sum filter, and unscented Kalman filter, which all belong to the recursive Bayesian filtering technique,

are briefly reviewed. In addition, the Kalman filter is newly proved in the Bayesian recursive filtering point of view, then the particle filter and related topics are introduced and discussed. Two case studies are employed to illustrate the behaviour and performance of the particle filter. One of the case studies addresses the mechanism of the particle filter. The following issues are discussed:

- The prior and posterior distributions estimated by the particle filter.
- The estimation performance according to different types of particle filters.

A particle-filter-based wave filter for dynamic positioning vessel was designed in the second study. In addition to the assumptions made by [Fossen and Strand, 1999], the noise and update rate in position reference signals are considered. The different setups of particle filters are compared. Except for the introductory knowledge of this area, the main contribution of this chapter is the partile-filter-based wave filter for dynamic positioning vessels.

Chapter 3 extends the usage of the particle filter to the fault diagnosis problem. First, the switching mode hidden Markov model for system with possible faults is introduced. Then the algorithm of the particle filter for fault diagnosis is provided. After the discussion of a few relevant topics, a case study involving the use of this method for diagnosing faults in the position reference system of a dynamic positioning vessel is studied. This case study continues with the dynamic positioning wave filtering problem described in Chapter 2, but the common failure modes of the GNSS and hydroacoustic position reference sensors are also considered. The aim of the design is to produce a reliable and robust navigation system that can be employed for dynamic positioning even when failure occurs in the sensors. The simulation results indicate that the particle-filter-based navigation system design can effectively detect the failure of positioning sensors and result in an acceptable estimation of the vessel position when failure occurs. The main contributions in this chapter are: 1) the demostration of using particle filter on switching model hidden Markov model for fault detection and diagnosis, and 2) the faul tolerant design of the dynamic positioning vessel wave filter.

An ROV experiment for validating the proposed particle-filter-based fault diagnosis algorithm is given in detail in Chapter 4. The model of the Minerva ROV used in the experiment is first provided. Then, the failure modes of the ROV navigation sensors and thrusters are discussed. Using these preparations, a PF-based robust ROV navigation system is designed. The results from the ROV sea trail is given and discussed at the end of this chapter. The simulation and experimental result regarding this robust navigation system design is also seen in [Zhao et al., 2012a,b, 2013]. The main contribution of this chapter is the design, implementation, and experiment of the ROV robust navigation system.

Chapter 5 summarizes this thesis, and briefly looks into the future research and application of the proposed PF-based FD method.

Chapter 2

Particle Filter

> *"Now, since our condition accommodates things to itself, and transforms them according to itself, we no longer know things in their reality; for nothing comes to us that is not altered and falsified by our Senses. When the compass, the square, and the rule are untrue, all the calculations drawn from them, all the buildings erected by their measure, are of necessity also defective and out of plumb. The uncertainty of our senses renders uncertain everything that they produce."*
>
> – Michel de Montaigne, "*Apology for Raimund Sebond*".

2.1 Introduction to the Filtering Technology

In principle, filtering is a method that physically extracts interesting objects from crude material. The human being has been using filtering processes for a long time. The coffee filter is a good example of the physical use of a filter in the modern world. It separates the coffee from the mixture. However, the filter can also be extensively be used in informatics, where people want to extract essential information from raw data. Raw data can be acquired from various tools, such as rulers, scales, meters, and other sensors, with the purpose of acquiring a measure of reality. However, researchers have come to the conclusion that no matter how accurate the instrument is and how carefully the measurement is taken, the environment can always disturb the result. This means that measured raw data are only distorted reality. Hence, the filtering philosophy is applied. In statistics, it turns into least square, experimental design and other methods. In cybernetics and signal processing, it becomes "filtering" techniques.

A measure of the reality is also called observation. The observations show randomness. The probability theory studies the concepts and methods of random events and random variables. It models the random events in the real world as random variables. While statistics focuses on collecting, analysing, and interpreting a group of data, stochastic are concerned with studying the behaviour of a system with random inputs.

Filtering in cybernetics and signal processing has been narrowed down to a technique that starts by attenuating the noise in a measurement. Then, in order to achieve a better control performance, it is necessary to observe not only the output but also the overall status of the system. This technique is always referred as state observer. The Kalman filter ([Kalman, 1960]) coupled with its various extensions, has dominated both research and industry as the most mature observer since it was first introduced in 1960. The limitation of the Kalman filter is that it only applies to the linearity of the system. As its important descendent, the extended Kalman filter locally linearizes a nonlinear system, and runs a standard Kalman filter on these local linearized approximations. The performance of the extended Kalman filter works nicely in systems that exhibit weak non-linearity.

A number of filters have been specially designed for nonlinear systems. For example, [Fossen and Strand, 1999] designed nonlinear observers that were based on nonlinear-system theory in order to ensure the estimation error exponentially converged. Elsewhere, in stochastic filtering theory, there are unscented Kalman filters, particle filters, and so on. The unscented Kalman filter features the distribution of the system states with a group of characteristic points, which are referred to as sigma points. The system states are estimated by propagating these sigma points. The particle filter estimates the states of the system by simulating the behaviour of the system states with a group of particles. It is compatible with a large class of systems, linear or nonlinear, with Gaussian or without Gaussian noise, white or with coloured noise.

This chapter describes the tool that was most commonly used in this thesis, the particle filter, which is a stochastic filter. The chapter starts with a brief review of the concepts of probability, statistics, and stochastic process as the basis of stochastic filtering. It then presents examples of stochastic filters. At the end of the chapter, the theory of particle filter is introduced using two practical examples.

2.2 Mathematical preliminaries

2.2.1 Basics

Definition 2.1 *Let S be a set, and 2^S represents the power set of S. Then a subset $\mathcal{F} \subset 2^S$ is a* ***σ-algebra*** *if*

1. $\emptyset \in \mathcal{F}$;
2. $A \in \mathcal{F} \Rightarrow A \setminus X \in \mathcal{F}$, *where* $A \setminus X$ *is the complement of* A;
3. $A_1, A_2, \ldots \in \mathcal{F} \Rightarrow \bigcup_i A_i \in \mathcal{F}$, $i = 1, 2, \ldots$.

Definition 2.2 *A set function P on a σ-algebra $\mathcal{F}$ is a* ***probability measure*** *when*

1. *the codomain of P is $[0, 1]$, and P returns 0 for the empty set and 1 for the entire space;*
2. *for $A_1, A_2, \ldots \in \mathcal{F}$, $P\left(\bigcup_i A_i\right) = \sum_i P\left(A_i\right)$, $i = 1, 2, \ldots$.*

Remark 2.1 $P(A \setminus X) = 1 - P(A)$, *since* $P(A \setminus X) + P(A) = P((A \setminus X) \cup (A)) = P(X) = 1$.

Definition 2.3 *A* ***probability space*** *is a triple* $(\Omega, \mathcal{F}, P)$, *where*

1. Ω *is the sample space which is non-empty;*
2. $\mathcal{F} \subseteq \Omega$ *is a* σ*-algebra;*
3. $P : \mathcal{F} \to [0, 1]$ *is a probability measure.*

Definition 2.4 ***random variable***

The basic concept of probability theory – random variable – has no commonly accepted definition. [Cramer, 1999] described random variables as follows:[1]

> Consider a determined *random experiment* $\mathfrak{E}$, which may be repeated a large number of times under uniform conditions. We shall suppose that the result of each particular experiment is given by a certain number of real quantities $\xi_1, \xi_2, \ldots, \xi_k$, where $k \geq 1$.
>
> We then introduce a corresponding variable point or vector $\xi = (\xi_1, \ldots, \xi_k)$ in the k-dimensional space $\boldsymbol{R}_k$. We than call ξ a k–dimensional random variable. Each performance of the experiment $\mathfrak{E}$ yields as its result an *observed value* of the variable ξ, the coordinates of which are the values of $\xi_1, \ldots, \xi_k$ observed on that particular occasion.
>
> Let S denote some simple set of points in $\boldsymbol{R}_k$, say a k– dimensional interval, and let us consider the event $\xi < S$ [2], which may or may not occur at any particular performance of $\mathfrak{E}$. We shall assume that this event has a definite probability P, in the sense explained in 13.5. The number P will obviously depend on the set S, and will accordingly be denoted by any of the expressions
>
> $$P = P(S) = P(\xi < S).$$

In the above quotation, Cramer also introduced the cumulative distribution function as:

Definition 2.5 *Given a probability space* $(\Omega, \mathcal{F}, P)$ *on* $\mathbb{R}^n$, *for every real vector* $\boldsymbol{x}$, *the* ***cumulative distribution function*** *(CDF) of a real-valued random vector* $\boldsymbol{X}$ *is given by*

$$F_{\boldsymbol{X}}(\boldsymbol{x}) = P(\boldsymbol{X} \trianglelefteq \boldsymbol{x}). \tag{2.1}$$

Definition 2.6 *Let* $f_{\boldsymbol{X}}(\boldsymbol{x}) = \frac{d F_{\boldsymbol{X}}(\boldsymbol{x})}{d \mu}$ *denote Radon-Nikodym density of probability distribution* $F_{\boldsymbol{X}}(\boldsymbol{x})$ *w.r.t. a measure* μ. *When* $\boldsymbol{x}$ *is discrete and* μ *is a counting*

[1] Notations in the quotation are modified to comply with the notations of this thesis.

[2] If ξ is a vector, so is S, then this should be understood as ξ is elementarily less than S. – by author

measure, $f_{\boldsymbol{X}}(\boldsymbol{x})$ is a ***probability mass function*** *(PMF) ; when $\boldsymbol{x}$ is continuous and μ is a Lebesgue measure, $f_{\boldsymbol{X}}(\boldsymbol{x})$ is a* ***probability density function*** *(PDF).*

Definition 2.7 *Given random vector (or variable) $\boldsymbol{X}$ and $\boldsymbol{Y}$, the CDF of the* ***joint random vector*** *$(\boldsymbol{X}, \boldsymbol{Y})$ is*

$$F_{(\boldsymbol{X},\boldsymbol{Y})}(\boldsymbol{x}, \boldsymbol{y}) = P(\boldsymbol{X} \trianglelefteq \boldsymbol{x}, \boldsymbol{Y} \trianglelefteq \boldsymbol{y}). \tag{2.2}$$

Definition 2.8 *Given random vector (or variable) $\boldsymbol{X}$ and $\boldsymbol{Y}$, they are* ***independent*** *if and only if*

$$F_{(\boldsymbol{X},\boldsymbol{Y})}(\boldsymbol{x}, \boldsymbol{y}) = F_{\boldsymbol{X}}(\boldsymbol{x}) F_{\boldsymbol{Y}}(\boldsymbol{y}), \tag{2.3}$$

or equivalently,

$$f_{(\boldsymbol{X},\boldsymbol{Y})}(\boldsymbol{x}, \boldsymbol{y}) = f_{\boldsymbol{X}}(\boldsymbol{x}) f_{\boldsymbol{Y}}(\boldsymbol{y}). \tag{2.4}$$

Definition 2.9 *Given a probability space $(\Omega, \mathcal{F}, P)$ on $\mathbb{R}^n$, for random variables $X_1, \ldots, X_n$, the* ***marginal probability*** *of sub-group random variables $X_p, \ldots, X_q$ ($\{p, \ldots, q\} \in \{1, \ldots, n\}$) is*

$$F_{(X_p,\ldots,X_q)}(x_1, \ldots, x_k) = F_{(X_1,\ldots,X_n)}(x_1, \ldots, x_k, +\infty, \ldots, +\infty) \tag{2.5}$$

$$= \int_{-\infty}^{+\infty} \int_{-\infty}^{+\infty} \cdots \int_{-\infty}^{+\infty} F_{(X_1,\ldots,X_n)}(x_1, \ldots, x_n)\, dx_i \cdots dx_j. \tag{2.6}$$

$$(\{i, \ldots, j\} = \{1, \ldots, n\} \setminus \{p, \ldots, q\}) \tag{2.7}$$

The ***marginal density function*** *of $X_1, \ldots, X_k$ is*

$$f_{(X_1,\ldots,X_k)}(x_1, \ldots, x_k) = \frac{d\, F_{(X_1,\ldots,X_n)}(x_1, \ldots, x_k, +\infty, \ldots, +\infty)}{d\, \mu}. \tag{2.8}$$

Definition 2.10 *Given a probability space $(\Omega, \mathcal{F}, P)$ on $\mathbb{R}^n$, for random vectors (or variables) $\boldsymbol{X}, \boldsymbol{Y}$, the* ***conditional cumulative distribution function*** *of given $\boldsymbol{X} \trianglelefteq \boldsymbol{x}$ relative to the hypothesis $\boldsymbol{Y} \trianglelefteq \boldsymbol{y}$ is*

$$F_{(\boldsymbol{X}|\boldsymbol{Y})}(\boldsymbol{x}|\boldsymbol{y}) = P(\boldsymbol{X} \trianglelefteq \boldsymbol{x} | \boldsymbol{Y} \trianglelefteq \boldsymbol{y}) \tag{2.9}$$

$$= \frac{P(\boldsymbol{X} \trianglelefteq \boldsymbol{x}, \boldsymbol{Y} \trianglelefteq \boldsymbol{y})}{P(\boldsymbol{Y} \trianglelefteq \boldsymbol{y})} \tag{2.10}$$

$$= \frac{F_{(\boldsymbol{X},\boldsymbol{Y})}(\boldsymbol{x}, \boldsymbol{y})}{F_{\boldsymbol{Y}}(\boldsymbol{y})} \tag{2.11}$$

and the ***conditional probability density function*** *is*

$$f_{(\boldsymbol{X}|\boldsymbol{Y})}(\boldsymbol{x}|\boldsymbol{y}) = \frac{f_{(\boldsymbol{X},\boldsymbol{Y})}(\boldsymbol{x}, \boldsymbol{y})}{f_{\boldsymbol{Y}}(\boldsymbol{y})}. \tag{2.12}$$

Theorem 2.1 ***The law of total probability:*** *Given a probability space $(\Omega, \mathcal{F}, P)$, and $\{B_i\}$, $i = 1, 2, \ldots$ is a finite or countably infinite partition of Ω, then for any event E of the same probability space:*

$$P(E) = \sum_i P(E \cap B_i) \tag{2.13}$$

$$= \sum_i P(E|B_i) P(B_i). \tag{2.14}$$

he basic concepts associated with probability are outlined above. Another important concept that is of relevance to the use of a particle filter is *empirical distribution*, which describes the cumulative density function with empirical measure of samples. This concept, and the related theorems, describe the relationship between the results from random experiments and the random variable.

Definition 2.11 *Let $(\boldsymbol{X}_1, \ldots, \boldsymbol{X}_{n_s})$ be i.i.d. real random variables with the common CDF $F(\boldsymbol{x})$. Then the* ***empirical distribution function*** *is defined as*

$$\hat{F}_{n_s}(\boldsymbol{x}) = \frac{\text{number of elements in the sample} \trianglelefteq \boldsymbol{x}}{n_s} = \frac{1}{n_s} \sum_{i=1}^{n_s} \mathbf{1}\{\boldsymbol{X}_i < \boldsymbol{x}\}, \tag{2.15}$$

where $\mathbf{1}\{\mathcal{E}\}$ is the indicator of event $\mathcal{E}$.

Theorem 2.2 ***Weak law of large numbers:*** *The sample average converges in probability towards the expected value μ*

$$\bar{\boldsymbol{X}}_n \xrightarrow{p} \boldsymbol{\mu} \text{ when } n \to \infty,$$

or for any positive number ε

$$\lim_{n\to\infty} \Pr\left(\left|\bar{\boldsymbol{X}}_n - \boldsymbol{\mu}\right| \trianglerighteq \varepsilon\right) = 0.$$

Theorem 2.3 ***Strong law of large numbers:*** *The sample average converges almost surely to the expected value, as*

$$\bar{\boldsymbol{X}}_n \xrightarrow{a.s.} \boldsymbol{\mu} \text{ when } n \to \infty,$$

or

$$\Pr\left(\lim_{n\to\infty} \bar{\boldsymbol{X}}_n = \boldsymbol{\mu}\right) = 1$$

The laws of large numbers describe the relationship between the samples and the population, and can be extended to the following lemma.

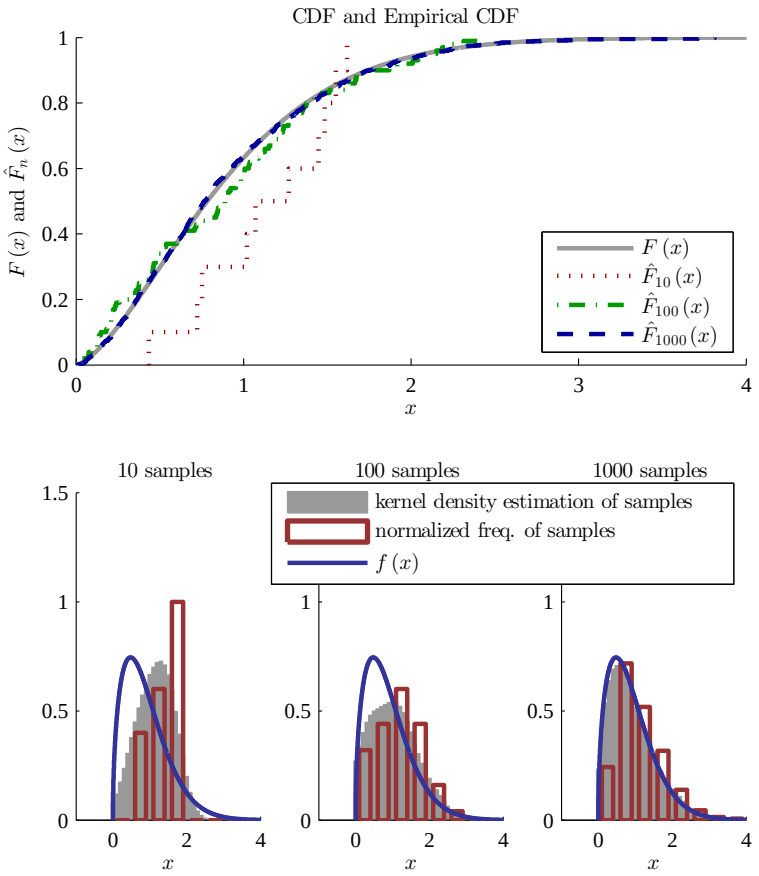

Figure 2.1: Weibull CDF and empirical CDF curves, and Weibull PDF and normalized histogram.

Lemma 2.1 *By the strong law of large numbers, the estimator $\hat{F}_n(\boldsymbol{x})$ in Definition 2.11 converges to $F(\boldsymbol{x})$ as $n \to \infty$ almost surely, for every value of $\boldsymbol{x}$*

$$\hat{F}_n(\boldsymbol{x}) \overset{a.s.}{\to} F(\boldsymbol{x}), \tag{2.16}$$

that is

$$\lim_{n\to\infty} \sup_{\boldsymbol{x}\in\mathbb{R}^m} \left|\hat{F}_n(\boldsymbol{x}) - F(\boldsymbol{x})\right| = 0, \tag{2.17}$$

thus the estimator is consistent [Van der Vaart, 2000].

Example 2.1 *Figure 2.1 depicts the CDF and PDF curves of Weibull distribution with scale parameter 1 and shape parameter 1.5, and its empirical approximates with sample size 10, 100, and 1000, respectively. The three axes at the bottom show the*

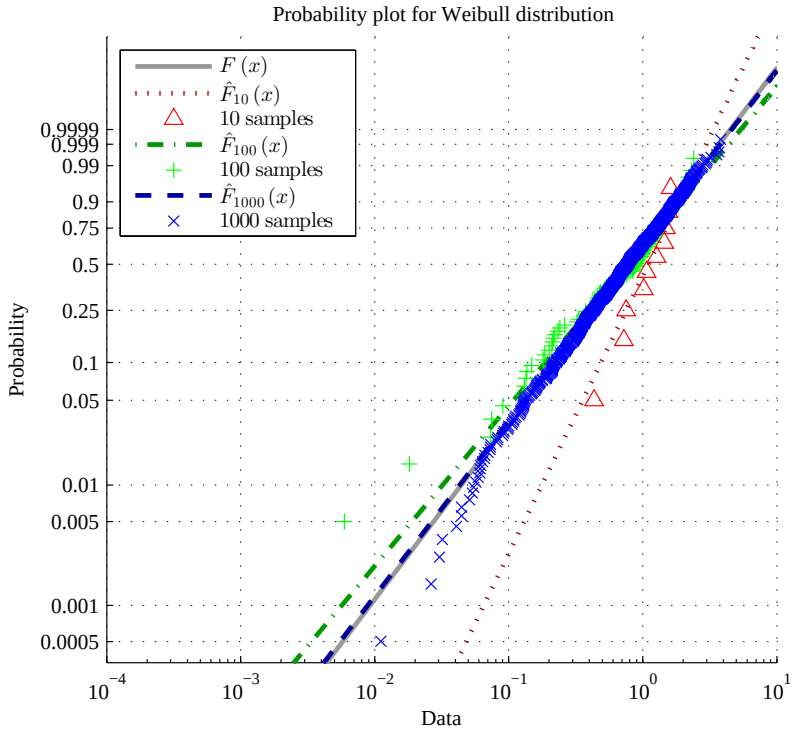

Figure 2.2: Probability plots of the samples under different sample sizes, compared with the true distribution.

kernel density estimation of samples and the normalized histogram of the samples, as compared to the analytical distribution curve. The approximate becomes more accurate as the number of samples increases. Figure 2.2 depicts the probability plot, where the accuracy of the approximations is presented.

The following central limit theorem and the lemma from it shows how the empirical CDF is close to (or converges to) the true distribution.

Theorem 2.4 ***Lindeberg-Lévy central limit theorem:*** *Suppose* $\{X_i, i = 1, 2, \ldots\}$ *is a sequence of i.i.d. random variables with* $\mathbb{E}[X_i] = \mu$ *and* $\mathbb{D}[X_i] = \sigma^2 < \infty$, *and let* $S_n = \frac{1}{n}\sum_{i=1}^{n} X_i$. *Then as* n *approaches infinity, the random variables* $\sqrt{n}(S_n - \mu)$ *converge in distribution to a normal distribution* $N(0, \sigma^2)$, *as*

$$\sqrt{n}\left(\frac{1}{n}\sum_{i=1}^{n} X_i - \mu\right) \xrightarrow{d} N(0, \sigma^2). \tag{2.18}$$

In the case, $\sigma > 0$, *convergence in distribution means that the CDF of* $\sqrt{n}(S_n - \mu)$

converge pointwise to the CDF of the $N\left(0,\sigma^2\right)$ *distribution, such as for every real number* z*,*

$$\lim_{n\to\infty}\Pr\left[\sqrt{n}\left(S_n-\mu\right)<z\right]=\Phi\left(z/\sigma\right), \tag{2.19}$$

where $\phi\left(x\right)$ *is the CDF of standard normal distribution evaluated at* x*. Note that the convergence is uniform in* z *in the sense that*

$$\lim_{n\to\infty}\sup_{z\in R}\left|\Pr\left[\sqrt{n}\left(S_n-\mu\right)<z\right]-\Phi\left(z/\sigma\right)\right|=0, \tag{2.20}$$

where sup *denotes the least upper bound of the set.*

Lemma 2.2 *Continue with Definition 2.11. Let random variable* $Y_i\left(x\right)=1\left\{X_i<x\right\}$*, such that*

$$Y_i\left(x\right)=\left\{\begin{array}{ll}1 & X_i<x\\ 0 & X_i\geq x\end{array}\right. . \tag{2.21}$$

Then $E\left[Y_i\left(x\right)\right]=\int_{-\infty}^{x}f_X\left(x\right)dx=F\left(x\right)$*, while* $D\left[Y_i\left(x\right)\right]=E\left[Y_i^2\left(x\right)\right]-E^2\left[Y_i\left(x\right)\right]=F\left(x\right)\left(1-F\left(x\right)\right)$*. This means given* $x_0\in R$*,*

$$E\left[Y_i\left(x_0\right)\right] = F\left(x_0\right) \tag{2.22}$$

$$D\left[Y_i\left(x_0\right)\right] = F\left(x_0\right)\left(1-F\left(x_0\right)\right)<\infty. \tag{2.23}$$

Use the central limit theorem, yields

$$\sqrt{n}\left(\frac{1}{n}\sum_{i=1}^{n}Y_i\left(x_0\right)-F\left(x_0\right)\right)\xrightarrow{d}N\left(0,F\left(x_0\right)\left(1-F\left(x_0\right)\right)\right), \tag{2.24}$$

this is

$$\hat{F}_n\left(x_0\right)=\frac{1}{n}\sum_{i=1}^{n}Y_i\left(x_0\right)\xrightarrow{d}N\left(F\left(x_0\right),\frac{1}{n}F\left(x_0\right)\left(1-F\left(x_0\right)\right)\right). \tag{2.25}$$

□

This lemma shows that the accuracy (variance) of pointwise estimation of the empirical CDF to the real CDF is proportional to the reciprocal of the number of samples. This can be a formal answer to what we observed in the previous Example 2.1; i.e., the accuracy of the approximation increases as the number of samples increases. Furthermore, it can also be reasoned from the lemma that the estimation variance is 0 when $F\left(x\right)=0$ or $F\left(x\right)=1$, which means the empirical distributions always converge to the true distribution when $x\to-\infty$ or $x\to+\infty$, while the estimation accuracy is low when $F\left(x\right)$ is close to 0.5. This can also be observed in the following example.

Example 2.2 *Repeating the empirical approach of the Weibull distribution in Example 2.1* 1000 *times, with sample sizes* 10, 100, *and* 1000 *, respectively. The results are provided in Figure 2.3 grouped by sample size. The left column of Figure 2.3 shows the CDF and the* 1000 *empirical CDF approximations. And the right column shows the relationship between the* $F(x)-\hat{F}_{1000}(x)$ *and* $F(x)$*.*

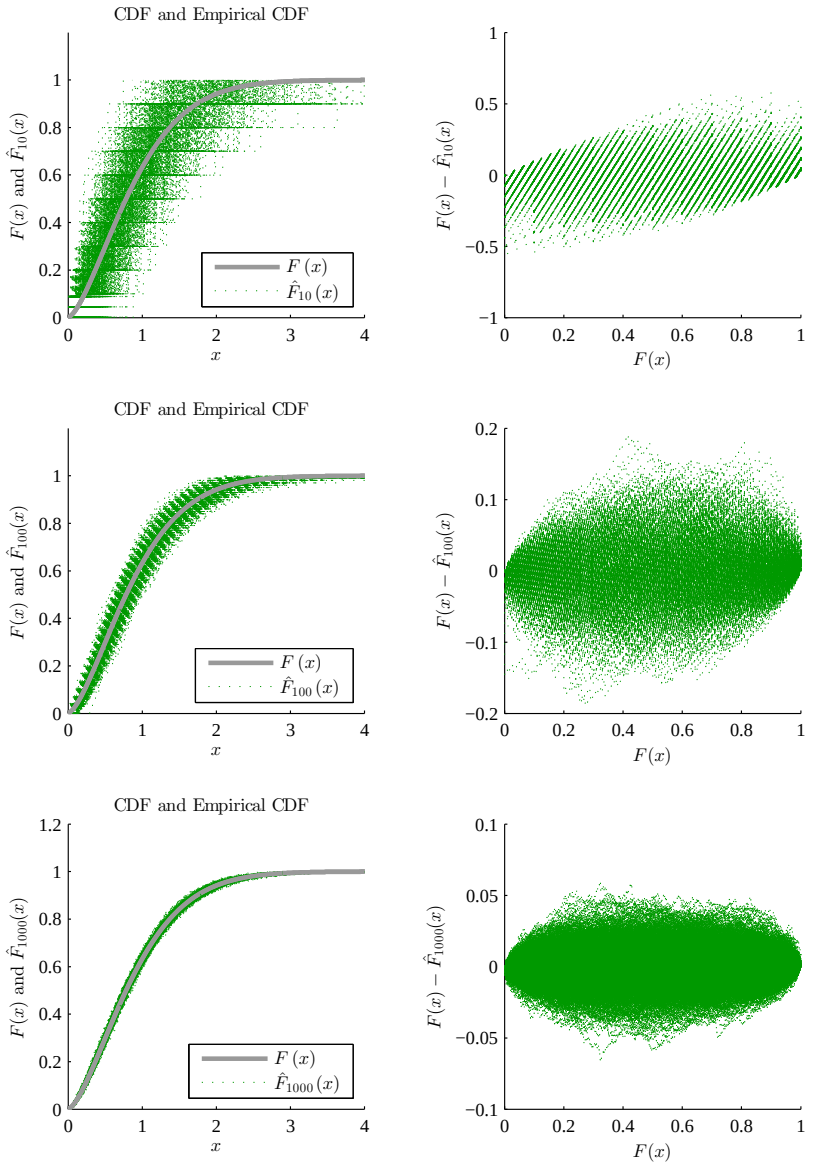

Figure 2.3: Example: empirical distribution approaching the real distribution with different sample sizes.

As the sample size increases, the approximation gets more accurate so that the curves of $F(x) - \hat{F}_{1000}(x)$ *become more centralized. Furthermore, the maximum inaccuracy occurs around the point* $F(x) = 0.5$*, which verifies Lemma 2.2.*

From these Weibull approximation results, one may develop the assumption that the

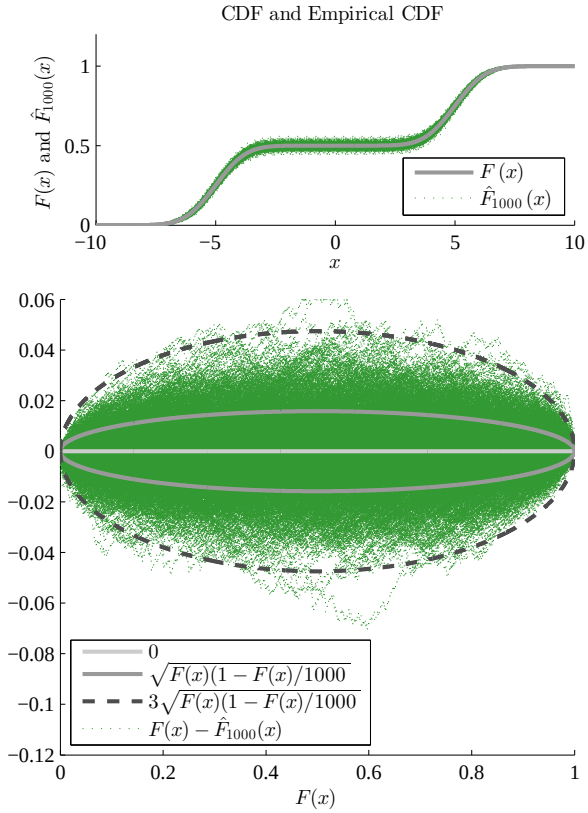

Figure 2.4: Example: empirical distribution approaching a Gaussian mixture distribution.

approximation accuracy is poor where the PDF is large in value, i.e., the CDF changes fast. Another example can be used to clarify this issue. The same empirical approximation is applied to a Gaussian mixture distribution. The distribution is structured by two Gaussian distributions with means -5 *and* 5*, variances* 1 *and* 1*. The mixing proportions are* 0.5*,* 0.5*. The result, presented in Figure 2.4, shows that the maximum approximation uncertainty occurs around* $F(x) = 0.5$*, where the CDF curve is flat, i.e. the* $f(x)$ *is close to* 0*. This shows that the approximation accuracy is not related to the shape of the CDF. The solid and dash lines are the the* X*-axis,* $\sqrt{F(x)(1-F(x)/1000}$*; i.e., the standard deviation of the approximation error in Equation* (2.25)*, and* $3\sqrt{F(x)(1-F(x)/1000}$*; i.e., the* 3σ *limit. The figure shows that the majority of the approximation errors are located in the* 3σ *limit, which verifies the result in Equations* (2.24) *and* (2.25) *in Lemma 2.2.*

2.2.2 Bayesian Probability

To interpret the mechanism of the particle filter, we also need to introduce the concept of *Bayesian probability*, which is named after English mathematician Thomas Bayes. Bayesian probability represents one method of interpreting probability through, connecting *the posterior probability*, *the prior probability*, the *likelihood*, and the *evidence* with the *Bayes' law*:

$$P(H|E) = \frac{P(E|H)\,P(H)}{P(E)}, \tag{2.26}$$

where

- Event H denotes the *hypothesis*.
- Event E denotes the *evidence*.
- $P(E|H)$ is the *likelihood* which shows the probability of E given H; i.e., the probability of evidence E being observed when the hypothesis H is true.
- $P(H)$ is *the prior* that gives the probability of H before E is observed.
- $P(E)$ is the probability that the evidence occurs.
- $P(H|E)$ is the posterior probability and is the probability of H given the observed evidence; i.e., the extent to which E supports H.

The Bayes' rule can be derived from Definition 2.10. It is simple but meaningful in probability theory giving its important position in reasoning. Because the probability that the evidence is seldom known while the conditional probability is relatively easier to obtain, the Bayes' law is usually used in combination with the law of total probability, resulting in the following form:

Assuming the space of the hypothesis H is partitioned into H_1, H_2, ..., H_n, and the probabilities $P(E|H_i)$, $i = 1, 2, \ldots, n$ are known (usually by statistical model or experience), then the posterior is obtained by

$$P(H|E) = \frac{P(E|H)\,P(H)}{\sum_{i=1}^{n} P(E|H_i)\,P(H_i)}. \tag{2.27}$$

When the partition of the space H is continuous instead of discrete, Equation (2.27) can be transformed into

$$P(H|E) = \frac{P(E|H)\,P(H)}{\int_{i=1}^{\infty} P(E|H_i)\,P(H_i)}, \tag{2.28}$$

where $H_i, i = 1, 2, \ldots$ constructs a partition of H, such as $\bigcup_{i=1}^{\infty} H_i = H$.

Bayes inference and Bayes prediction

The Bayes' rule can be generalized to *Bayes inference* and *Bayes prediction*. Given i.i.d. observations $\boldsymbol{x}_i\,(i=1,2,\ldots)$ from distribution $f\left(\boldsymbol{x}\,|\boldsymbol{\theta}\right)$, and $\boldsymbol{\theta}$ is unknown but depending on a hyper-parameter $\boldsymbol{\alpha}$, such that $\boldsymbol{\theta}\sim f\left(\boldsymbol{\theta}\,|\boldsymbol{\alpha}\right)$.

Directly applying the Bayes' law, yields

$$f\left(\boldsymbol{\theta}\,|\boldsymbol{x}_1,\ldots,\boldsymbol{x}_n,\boldsymbol{\alpha}\right)=\frac{f\left(\boldsymbol{x}_1,\ldots,\boldsymbol{x}_n\,|\boldsymbol{\theta}\right)f\left(\boldsymbol{\theta}\,|\boldsymbol{\alpha}\right)}{f\left(\boldsymbol{x}_1,\ldots,\boldsymbol{x}_n\,|\boldsymbol{\alpha}\right)},\tag{2.29}$$

or shrinks to

$$f\left(\boldsymbol{\theta}\,|\boldsymbol{x}_1,\ldots,\boldsymbol{x}_n\right)=\frac{f\left(\boldsymbol{x}_1,\ldots,\boldsymbol{x}_n\,|\boldsymbol{\theta}\right)f\left(\boldsymbol{\theta}\right)}{f\left(\boldsymbol{x}_1,\ldots,\boldsymbol{x}_n\right)},\tag{2.30}$$

when only $\boldsymbol{\theta}\sim f\left(\boldsymbol{\theta}\right)$, that is the prior distribution of $\boldsymbol{\theta}$ is known, where

- $f\left(\boldsymbol{x}_1,\ldots,\boldsymbol{x}_n\,|\boldsymbol{\theta}\right)=\prod_{i=1}^{n}f\left(\boldsymbol{x}_i\,|\boldsymbol{\theta}\right)$ is the likelihood, or sampling distribution in this special case.
- $f\left(\boldsymbol{\theta}\,|\boldsymbol{\alpha}\right)$ is the prior probability, which is the distribution of the parameter before observation.
- $f\left(\boldsymbol{x}_1,\ldots,\boldsymbol{x}_n\,|\boldsymbol{\alpha}\right)$ is the evidence, or marginal likelihood in this case. This distribution cannot be obtained directly, but can be calculated via the law of total probability

  $$f\left(\boldsymbol{x}_1,\ldots,\boldsymbol{x}_n\,|\boldsymbol{\alpha}\right)=\int_{\boldsymbol{\theta}}f\left(\boldsymbol{x}_1,\ldots,\boldsymbol{x}_n\,|\boldsymbol{\theta}\right)f\left(\boldsymbol{\theta}\,|\boldsymbol{\alpha}\right)d\boldsymbol{\theta}.\tag{2.31}$$

  It is sometimes difficult to obtain an analytical solution of this integration. However, since the denominator is a constant, we have

  $$f\left(\boldsymbol{\theta}\,|\boldsymbol{x}_1,\ldots,\boldsymbol{x}_n,\boldsymbol{\alpha}\right)\propto f\left(\boldsymbol{x}_1,\ldots,\boldsymbol{x}_n\,|\boldsymbol{\theta}\right)f\left(\boldsymbol{\theta}\,|\boldsymbol{\alpha}\right),\tag{2.32}$$

- $f\left(\boldsymbol{\theta}\,|\boldsymbol{x}_1,\ldots,\boldsymbol{x}_n,\boldsymbol{\alpha}\right)$ is the posterior distribution, which is the distribution of the parameter $\boldsymbol{\theta}$ after the observation.

The Bayesian inference inspires *Bayesian prediction*, such as

$$f\left(\boldsymbol{x}_{n+1}\,|\boldsymbol{x}_1,\ldots,\boldsymbol{x}_n,\boldsymbol{\alpha}\right)=\int_{\boldsymbol{\theta}}f\left(\boldsymbol{x}_{n+1}\,|\boldsymbol{\theta}\right)f\left(\boldsymbol{\theta}\,|\boldsymbol{x}_1,\ldots,\boldsymbol{x}_n,\boldsymbol{\alpha}\right)d\boldsymbol{\theta}.\tag{2.33}$$

2.2.3 Hidden Markov Model

The *state-space model* has been widely used in control theory to represent systems. The *state-space model of a discrete time-variant system* adopts the form

$$\boldsymbol{x}_{k+1}=\boldsymbol{g}_k\left(\boldsymbol{x}_k,\boldsymbol{u}_k\right)\tag{2.34a}$$

$$\boldsymbol{y}_k=\boldsymbol{h}_k\left(\boldsymbol{x}_k,\boldsymbol{u}_k\right),\tag{2.34b}$$

where

- k is the time index.
- $\boldsymbol{x} \in \mathbb{R}^{N_x}$ is the *state* variables of the system, and defined as the smallest possible subset of system variables that can describe the entire state of the system at any given time.
- $\boldsymbol{u} \in \mathbb{R}^{N_u}$ is the *input* to the system, which is assumed to be deterministic and known.
- $\boldsymbol{y} \in \mathbb{R}^{N_y}$ is the *output (observation)* of the system.
- $\boldsymbol{g} : \mathbb{R}^{N_x} \times \mathbb{R}^{N_u} \to \mathbb{R}^{N_x}$ is *process function* , which represents the evolution of the states of the system.
- $\boldsymbol{h} : \mathbb{R}^{N_x} \times \mathbb{R}^{N_u} \to \mathbb{R}^{N_y}$ is *observation function*, which describe how the observation is made from the system.
- $\boldsymbol{x}_0$ and $\boldsymbol{u}_k, k = 0, 1, \ldots$ are assumed to be known.

A modified model, which also considers the stochastic behaviour of the system due to noise acting or uncertainty of the system, is

$$\boldsymbol{x}_{k+1} = \boldsymbol{g}_k \left(\boldsymbol{x}_k, \boldsymbol{u}_k, \boldsymbol{w}_k \right) \tag{2.35}$$

$$\boldsymbol{y}_k = \boldsymbol{h}_k \left(\boldsymbol{x}_k, \boldsymbol{u}_k, \boldsymbol{v}_k \right), \tag{2.36}$$

where in addition to the variables in Equation (2.34)

- $\boldsymbol{w} \in \mathbb{R}^{N_w}$ is the system noise, represents the system uncertainty and unmodelled dynamic.
- $\boldsymbol{v} \in \mathbb{R}^{N_v}$ is the measurement noise, represents the phenomenon that the measurement cannot precisely reflect the measured object.

Intuitively, the behaviour of system (2.34a) under given input series can be deterministically predicted by simulating the first-order difference equation, such as

$$\boldsymbol{x}_{k+1} = \boldsymbol{x}_0 + \sum_{i=1}^{k} \boldsymbol{g}_i \left(\boldsymbol{x}_i, \boldsymbol{u}_i \right). \tag{2.37}$$

However, because of the unknown noise terms $\boldsymbol{w}$, this cannot be done for system (2.35). Therefore, the distribution of the system states may spread in the space according to a certain distribution, even though the initial states and the input series are the same. In addition, because of the nonlinearity of the process function, it is difficult to develop a description of the distribution of $\boldsymbol{x}_k$ in a close form. We refer to the following model to describe this stochastic behaviour of the process

$$\boldsymbol{X}_{k+1} | \boldsymbol{x}_k, \boldsymbol{u}_k \sim \boldsymbol{g}_k \left(\boldsymbol{x}_k, \boldsymbol{u}_k \right) \tag{2.38a}$$

$$\boldsymbol{Y}_k | \boldsymbol{x}_k, \boldsymbol{u}_k \sim \boldsymbol{h}_k \left(\boldsymbol{x}_k, \boldsymbol{u}_k \right), \tag{2.38b}$$

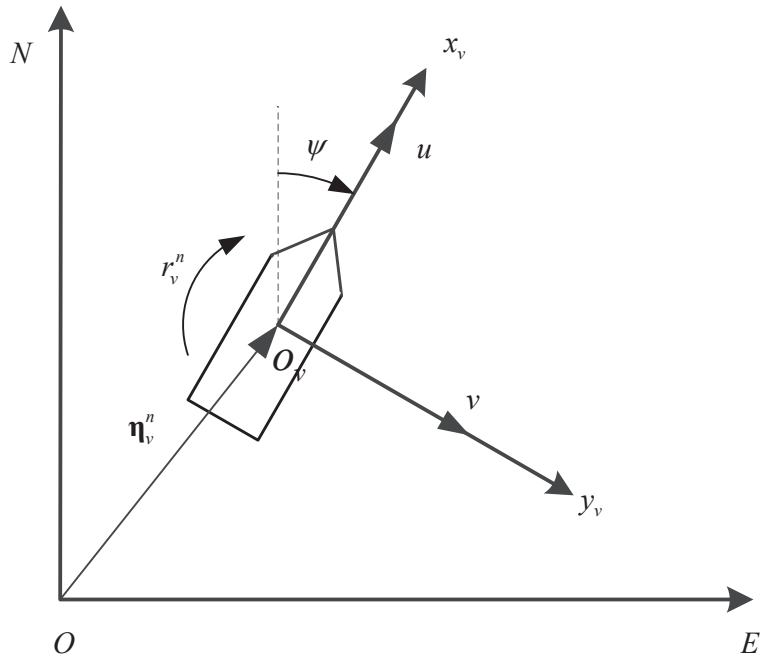

Figure 2.5: A vessel in the NE frame.

where $\boldsymbol{g}$ and $\boldsymbol{h}$ now are probability measures, or PDFs, which absorb the noise terms $\boldsymbol{w}$ and $\boldsymbol{v}$. Moreover, the $\boldsymbol{X}$ and $\boldsymbol{Y}$ are random variables. This model is named *hidden Markov model*. Equation (2.38a) describes the distribution of state vector at time $k+1$ given the state at time k as $\boldsymbol{x}_k$, where $\boldsymbol{x}_k$ is deterministic. The measurement process adopts a similar meaning. The propagation of such uncertainty is given by stochastic integral as

$$p\left(\boldsymbol{x}_{k+1}\right) = \int \boldsymbol{g}\left(\boldsymbol{x}_k, \boldsymbol{u}_k\right) p\left(\boldsymbol{x}_k\right)\, d\boldsymbol{x}. \tag{2.39}$$

It is important to clarify that the states of a system at a certain time are macroscopically deterministic. For instance, the position of the object in projectile motion is deterministic. However, our knowledge of the deterministic position is non-deterministic due to system and measurement uncertainty, such that our knowledge about the state of a system should be always described in the form $\boldsymbol{x} \sim p\left(\boldsymbol{x}\right)$.

An example will be provided to highlight the relationship between state-space model and HMM.

Example 2.3 ***Surface vessel manoeuvring model***

Consider a low-speed surface vehicle in Figure 2.5 with 3 DOFs, namely surge, sway, and yaw. The velocity of the vehicle is define in its body frame as surge speed u*,*

sway speed v, and yaw rate r. In addition, the vessel position and heading is defined in the NED frame as north position N, east position E, and heading ψ, which is with respect to the north. Define position vector $\boldsymbol{\eta} \triangleq \begin{bmatrix} N & E & \psi \end{bmatrix}^\top$, and velocity vector $\boldsymbol{\nu} \triangleq \begin{bmatrix} u & v & r \end{bmatrix}^\top$. The kinematic model of the system then is ([Fossen, 2011])

$$\begin{bmatrix} \dot{\boldsymbol{\eta}} \\ \dot{\boldsymbol{\nu}} \end{bmatrix} = \begin{bmatrix} \boldsymbol{R}(\boldsymbol{\eta})\,\boldsymbol{\nu} \\ \boldsymbol{M}^{-1}\left(\boldsymbol{C}_{RB}(\boldsymbol{\nu})\,\boldsymbol{\nu} + \boldsymbol{C}_A(\boldsymbol{\nu}_r)\,\boldsymbol{\nu}_r + \boldsymbol{D}(\boldsymbol{\nu}_r)\right) \end{bmatrix} + \begin{bmatrix} \mathbf{0} \\ \boldsymbol{M}^{-1}\boldsymbol{\tau}_{\text{thr}} \end{bmatrix} + \begin{bmatrix} \mathbf{0} \\ \boldsymbol{M}^{-1}\boldsymbol{\tau}_{\text{env}} \end{bmatrix} + \begin{bmatrix} \mathbf{0} \\ \boldsymbol{w} \end{bmatrix}, \tag{2.40}$$

where

$$\boldsymbol{R}(\boldsymbol{\eta}) = \begin{bmatrix} \cos(\psi) & -\sin(\psi) & 0 \\ \sin(\psi) & -\cos(\psi) & 0 \\ 0 & 0 & 1 \end{bmatrix} \tag{2.41}$$

is the rotation matrix, $\boldsymbol{M}$ is the mass and added mass of the vessel, $\boldsymbol{C}_{RB}(\boldsymbol{\nu})\,\boldsymbol{\nu}$ and $\boldsymbol{C}_A(\boldsymbol{\nu}_r)\,\boldsymbol{\nu}_r$ are the Coriolis force due to the vessel mass and added mass respectively, $\boldsymbol{D}(\boldsymbol{\nu}_r)$ is the nonlinear damping force, $\boldsymbol{\nu}_r$ is the vessel relative velocity with respect to the sea current, $\boldsymbol{\tau}_{\text{thr}}$ is the thruster force, $\boldsymbol{\tau}_{\text{env}}$ is the environmental force, $\boldsymbol{w}$ is the process noise representing the unmodelled dynamic and system uncertainty where assumed $\boldsymbol{w} \sim \mathcal{N}(\mathbf{0}, \boldsymbol{\Sigma}_{\boldsymbol{w}})$, $\boldsymbol{\Sigma}_{\boldsymbol{w}} \in \mathbb{R}^{3\times 3}$.

Discretizing this system at sampling time T, assuming the sampling frequency is much higher than the bandwidth of the system, such that the $\boldsymbol{\eta}$, $\boldsymbol{\nu}$, $\boldsymbol{\nu}_r$, $\boldsymbol{\tau}_{\text{thr}}$, $\boldsymbol{\tau}_{\text{env}}$, and $\boldsymbol{w}$ can be treated as constants during the sampling interval, yields

$$\begin{bmatrix} \boldsymbol{\eta}_{k+1} \\ \boldsymbol{\nu}_{k+1} \end{bmatrix} = \begin{bmatrix} \boldsymbol{\eta}_k \\ \boldsymbol{\nu}_k \end{bmatrix} + T\begin{bmatrix} \boldsymbol{R}(\boldsymbol{\eta}_k)\,\boldsymbol{\nu}_k \\ \boldsymbol{M}^{-1}\left(\boldsymbol{C}_{RB}(\boldsymbol{\nu}_k)\,\boldsymbol{\nu}_k + \boldsymbol{C}_A(\boldsymbol{\nu}_{r,k})\,\boldsymbol{\nu}_{r,k} + \boldsymbol{D}(\boldsymbol{\nu}_{r,k})\right) \end{bmatrix} + T\begin{bmatrix} \mathbf{0} \\ \boldsymbol{M}^{-1}\boldsymbol{\tau}_{\text{thr},k} \end{bmatrix} + T\begin{bmatrix} \mathbf{0} \\ \boldsymbol{M}^{-1}\boldsymbol{\tau}_{\text{env},k} \end{bmatrix} + T\begin{bmatrix} \mathbf{0} \\ \boldsymbol{w}_k \end{bmatrix}. \tag{2.42}$$

Assuming a GNSS measurement of the horizontal position of the vessel is available, the measurement equation is

$$\boldsymbol{p}_{\text{GNSS},k} = \begin{bmatrix} 1 & 0 & 0 \\ 0 & 1 & 0 \end{bmatrix} \boldsymbol{\eta}_k + \boldsymbol{v}_{\text{GNSS},k}. \tag{2.43}$$

where $\boldsymbol{v}_{\text{GNSS}}$ is the GNSS measurement noise, and assumed $\boldsymbol{v}_{\text{GNSS},k} \sim \mathcal{N}(\mathbf{0}, \boldsymbol{\Sigma}_{\text{GNSS},k})$, $\boldsymbol{\Sigma}_{\text{GNSS},k} \in \mathbb{R}^{2\times 2}$. This state-space model (2.42) and (2.43) can be transformed into HMM, such as

$$\boldsymbol{\eta}_{k+1}\,|\boldsymbol{\eta}_k, \boldsymbol{\nu}_k \sim \delta_{\boldsymbol{\eta}_{k+1}}\left(\boldsymbol{\eta}_{k+1} - \boldsymbol{\eta}_k - T\boldsymbol{R}(\boldsymbol{\eta}_k)\,\boldsymbol{\nu}_k\right) \tag{2.44a}$$

$$\boldsymbol{\nu}_{k+1}\,|\boldsymbol{\nu}_k \sim \mathcal{N}\left(T\boldsymbol{M}^{-1}\left(\boldsymbol{C}_{RB}(\boldsymbol{\nu}_k)\,\boldsymbol{\nu}_k + \boldsymbol{C}_A(\boldsymbol{\nu}_{r,k})\,\boldsymbol{\nu}_{r,k} + \boldsymbol{D}(\boldsymbol{\nu}_{r,k})\right) + T\boldsymbol{M}^{-1}\left(\boldsymbol{\tau}_{\text{thr},k} + \boldsymbol{\tau}_{\text{env},k}\right) + \boldsymbol{\nu}_k, T^2\boldsymbol{\Sigma}_\nu\right) \tag{2.44b}$$

$$\boldsymbol{p}_{\text{GNSS},k}\,|\boldsymbol{\eta}_k \sim \mathcal{N}\left(\begin{bmatrix} 1 & 0 & 0 \\ 0 & 1 & 0 \end{bmatrix} \boldsymbol{\eta}_k, \boldsymbol{\Sigma}_{\text{GNSS},k}\right), \tag{2.44c}$$

where $\delta(\cdot)$ is the Dirac measure representing the deterministic relation in the kinematic part of the vessel model. However, due to discretization error and other systematic errors, Equation (2.44a) *cannot be strict; i.e., designing an observer based on Equation* (2.44a) *always results in biased position estimation. Hence, it is common to add a small amount of white Gaussian system noise, such as using*

$$\boldsymbol{\eta}_{k+1} | \boldsymbol{\eta}_k, \boldsymbol{\nu}_k \sim \mathcal{N}\left(\boldsymbol{\eta}_k + T\boldsymbol{R}(\boldsymbol{\eta}_k)\boldsymbol{\nu}_k, \boldsymbol{\Sigma}_{\boldsymbol{\eta},k}\right), \tag{2.45}$$

instead of Equation (2.44a), where $\boldsymbol{\Sigma}_{\boldsymbol{\eta}}$ is the covariance matrix of the system noise.

□

2.3 Recursive Bayesian filtering

Having established Bayesian probability, it is now worth providing an overview of the Bayesian filtering technique. The Bayesian filtering uses Bayesian probability on the HMM (2.38) to estimate the states of the system.

2.3.1 General Form

In the following discussion, we assume that in HMM the initial time index is "0", and the distribution of $\boldsymbol{X}_0$ is known as $\boldsymbol{X}_0 \sim p(\boldsymbol{x}_0)$. And denotes the state and observation sequence up to time index k as $\mathcal{X}_k = \{\boldsymbol{x}_0, \boldsymbol{x}_1, \ldots, \boldsymbol{x}_k\}$ and $\mathcal{Y}_k = \{\boldsymbol{y}_1, \boldsymbol{y}_2, \ldots, \boldsymbol{y}_k\}$, respectively.

The purpose of filtering is to estimate the distribution of $p(\boldsymbol{x}_k | \mathcal{Y}_k)$ which is $p(\boldsymbol{x}_k | \{\boldsymbol{y}_1, \boldsymbol{y}_2, \ldots, \boldsymbol{y}_k\})$, or to extract information about $\boldsymbol{x}_k$ from the observation sequence $\{\boldsymbol{y}_1, \boldsymbol{y}_2, \ldots, \boldsymbol{y}_k\}$ based on the HMM. Following Equation (2.29), it yields

$$p(\boldsymbol{x}_k | \mathcal{Y}_k) = \frac{p(\mathcal{Y}_k | \boldsymbol{x}_k) p(\boldsymbol{x}_k)}{p(\mathcal{Y}_k)} \tag{2.46}$$

In order to construct a recursive filter, which is to derive $p(\boldsymbol{x}_k | \mathcal{Y}_k)$ from $p(\boldsymbol{x}_{k-1} | \mathcal{Y}_{k-1})$, the following partition of the observation series is usually made.

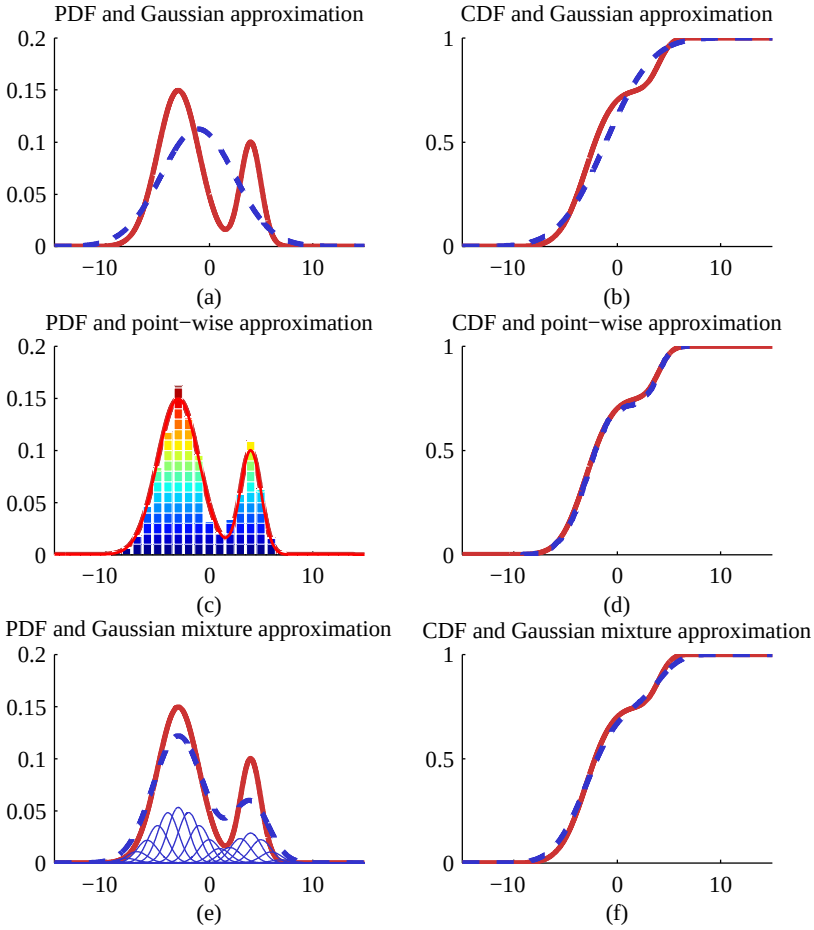

Figure 2.6: Comparisons of different approximations methods.

$$p\left(\boldsymbol{x}_k \left| \mathcal{Y}_k \right.\right) = \frac{p\left(\mathcal{Y}_k \left| \boldsymbol{x}_k \right.\right) p\left(\boldsymbol{x}_k\right)}{p\left(\mathcal{Y}_k\right)} \tag{2.47}$$

$$= \frac{p\left(\boldsymbol{y}_k, \mathcal{Y}_{k-1} \left| \boldsymbol{x}_k \right.\right) p\left(\boldsymbol{x}_k\right)}{p\left(\boldsymbol{y}_k, \mathcal{Y}_{k-1}\right)} \tag{2.48}$$

$$= \frac{p\left(\boldsymbol{y}_k \left| \mathcal{Y}_{k-1}, \boldsymbol{x}_k \right.\right) p\left(\mathcal{Y}_{k-1} \left| \boldsymbol{x}_k \right.\right) p\left(\boldsymbol{x}_k\right)}{p\left(\mathcal{Y}_{k-1}\right) p\left(\boldsymbol{y}_k \left| \mathcal{Y}_{k-1} \right.\right)} \tag{2.49}$$

$$= \frac{p\left(\boldsymbol{y}_k \left| \mathcal{Y}_{k-1}, \boldsymbol{x}_k \right.\right) p\left(\boldsymbol{x}_k \left| \mathcal{Y}_{k-1} \right.\right) p\left(\mathcal{Y}_{k-1}\right) p\left(\boldsymbol{x}_k\right)}{p\left(\mathcal{Y}_{k-1}\right) p\left(\boldsymbol{y}_k \left| \mathcal{Y}_{k-1} \right.\right) p\left(\boldsymbol{x}_k\right)} \tag{2.50}$$

$$= \frac{p\left(\boldsymbol{y}_k \left| \boldsymbol{x}_k \right.\right)}{p\left(\boldsymbol{y}_k \left| \mathcal{Y}_{k-1} \right.\right)} p\left(\boldsymbol{x}_k \left| \mathcal{Y}_{k-1} \right.\right), \tag{2.51}$$

where from Equations (2.50) to (2.51) $p\left(\boldsymbol{y}_n \left| \mathcal{Y}_{n-1}, \boldsymbol{x}_n \right.\right) = p\left(\boldsymbol{y}_n \left| \boldsymbol{x}_n \right.\right)$ because $\boldsymbol{y}_n$

and $\mathcal{Y}_{n-1}$ are independent when conditioned on $\boldsymbol{x}_n$.

This result is in the form of Bayes' rule in the sense that

- $p(\boldsymbol{x}_k|\mathcal{Y}_{k-1})$ is the prior probability, which is the prediction of current state from previous observations and usually expressed as

$$p(\boldsymbol{x}_k|\mathcal{Y}_{k-1}) = \int p(\boldsymbol{x}_k|\boldsymbol{x}_{k-1})\, p(\boldsymbol{x}_{k-1}|\mathcal{Y}_{k-1})\, d\boldsymbol{x}_{k-1} \tag{2.52}$$

  by using the law of total probability, where $p(\boldsymbol{x}_k|\boldsymbol{x}_{k-1})$ is the transition probability defined by the system Equation (2.38a) in HMM,

- $p(\boldsymbol{y}_k|\boldsymbol{x}_k)$ is the likelihood defined by the observation Equation (2.38b), and
- $p(\boldsymbol{y}_k|\mathcal{Y}_{k-1})$ corresponds to the evidence and calculated from

$$p(\boldsymbol{y}_k|\mathcal{Y}_{k-1}) = \int p(\boldsymbol{y}_k|\boldsymbol{x}_k)\, p(\boldsymbol{x}_k|\mathcal{Y}_{k-1})\, d\boldsymbol{x}_k. \tag{2.53}$$

  Substituting Equation (2.53) into Equation (2.51), it will have the form as Equation (2.28).

Except for some simplified condition, e.g. linear system with Gaussian noise, the probabilities Equations (2.52) and (2.53) are hardly analytically calculated. Hence, most of the statistical filtering methods adopt the form of (2.3.1), but are distinguished by the methods employed to calculate or approximate the terms $p(\boldsymbol{x}_k|\mathcal{Y}_{k-1})$ and $p(\boldsymbol{y}_k|\mathcal{Y}_{k-1})$. The following sections will contain a brief review of the most relevant methods that can be used to gain an overview of Bayesian filtering.

2.3.2 The Kalman Filter

The Kalman filter is one of the most popular and practical filtering techniques to be used over the past half century. The algorithm produced by [Kalman, 1960] seeks to explain the orthogonality between estimation error vector and observation vector in Euclidean space. In the following assessment, a new derivation of the Kalman filter, based on Bayesian filtering framework, is presented.

Typically, the system model considered in the Kalman filter is a time-varying linear system such as,

$$\boldsymbol{x}_{k+1} = \boldsymbol{A}_k\boldsymbol{x}_k + \boldsymbol{B}_k\boldsymbol{u}_k + \boldsymbol{w}_k \tag{2.54a}$$

$$\boldsymbol{y}_k = \boldsymbol{C}_k\boldsymbol{x}_k + \boldsymbol{D}_k\boldsymbol{u}_k + \boldsymbol{v}_k. \tag{2.54b}$$

In this system, $\boldsymbol{A}$, $\boldsymbol{B}$, $\boldsymbol{C}$, $\boldsymbol{D}$ are known matrices with appropriate dimensions, $\boldsymbol{w}_k$ and $\boldsymbol{v}_k$ are multivariate Gaussian white noise vector sequence with zero mean and covariance matrices $\boldsymbol{\Sigma}_{w,k}$ and $\boldsymbol{\Sigma}_{v,k}$, respectively. Rewriting Equation (2.54) into HMM, yields

$$\boldsymbol{x}_{k+1}\,|\boldsymbol{x}_k, \boldsymbol{u}_k \sim \mathcal{N}\left(\boldsymbol{A}_k\boldsymbol{x}_k + \boldsymbol{B}_k\boldsymbol{u}_k, \boldsymbol{\Sigma}_{w,k}\right) \tag{2.55}$$

$$\boldsymbol{y}_k\,|\boldsymbol{x}_k, \boldsymbol{u}_k \sim \mathcal{N}\left(\boldsymbol{C}_k\boldsymbol{x}_k + \boldsymbol{D}_k\boldsymbol{u}_k, \boldsymbol{\Sigma}_{v,k}\right). \tag{2.56}$$

Directly applying Equation (2.51), yields

$$p\left(\boldsymbol{x}_k\,|\mathcal{Y}_k\right) = \frac{p\left(\boldsymbol{y}_k\,|\boldsymbol{x}_k\right)}{p\left(\boldsymbol{y}_k\,|\mathcal{Y}_{k-1}\right)} \cdot p\left(\boldsymbol{x}_k\,|\mathcal{Y}_{k-1}\right) \tag{2.57}$$

$$\propto p\left(\boldsymbol{y}_k\,|\boldsymbol{x}_k\right) \cdot p\left(\boldsymbol{x}_k\,|\mathcal{Y}_{k-1}\right), \tag{2.58}$$

since $p\left(\boldsymbol{y}_k\,|\mathcal{Y}_{k-1}\right)$ is a constant. Defined by Equation (2.56), we have

$$\begin{aligned} & p\left(\boldsymbol{y}_k\,|\boldsymbol{x}_k, \boldsymbol{u}_k\right) \\ = \;& (2\pi)^{-\frac{N_y}{2}}\left|\boldsymbol{\Sigma}_{v,k}\right|^{-\frac{1}{2}} \cdot \\ & \exp\left\{-\frac{1}{2}\left(\boldsymbol{y}_k - \boldsymbol{C}_k\boldsymbol{x}_k - \boldsymbol{D}_k\boldsymbol{u}_k\right)^\top \boldsymbol{\Sigma}_{v,k}^{-1}\left(\boldsymbol{y}_k - \boldsymbol{C}_k\boldsymbol{x}_k - \boldsymbol{D}_k\boldsymbol{u}_k\right)\right\}, \end{aligned} \tag{2.59}$$

and

$$\begin{aligned} & p\left(\boldsymbol{x}_k\,|\mathcal{Y}_{k-1}\right) \\ = \;& p\left(\left(\boldsymbol{A}_{k-1}\boldsymbol{x}_{k-1} + \boldsymbol{B}_{k-1}\boldsymbol{u}_{k-1}\right)|\mathcal{Y}_{k-1}\right) \\ = \;& \mathcal{N}\left(\boldsymbol{A}_{k-1}\boldsymbol{x}_{k-1|k-1} + \boldsymbol{B}_{k-1}\boldsymbol{u}_{k-1}, \boldsymbol{A}_{k-1}\mathrm{Cov}\left[\boldsymbol{x}_{k-1|k-1}\right]\boldsymbol{A}_{k-1}^\top + \boldsymbol{\Sigma}_{w,k}\right) \\ & \exp\left\{-\frac{1}{2}\left(\boldsymbol{x}_k - \boldsymbol{A}_{k-1}\boldsymbol{x}_{k-1|k-1} - \boldsymbol{B}_{k-1}\boldsymbol{u}_{k-1}\right)^\top \cdot\right. \\ & \left.\boldsymbol{P}_{k|k-1}^{-1}\left(\boldsymbol{x}_k - \boldsymbol{A}_{k-1}\boldsymbol{x}_{k-1|k-1} - \boldsymbol{B}_{k-1}\boldsymbol{u}_{k-1}\right)\right\} \end{aligned} \tag{2.60}$$

where $\boldsymbol{x}_{k-1|k-1}$ is short for $\boldsymbol{x}_{k-1}\,|\mathcal{Y}_{k-1}$ meaning the estimation of the state at time $k-1$ given the observation up to time $k-1$, and

$$\boldsymbol{P}_{k|k-1} = \boldsymbol{A}_{k-1}\mathrm{Cov}\left[\boldsymbol{x}_{k-1|k-1}\right]\boldsymbol{A}_{k-1}^\top + \boldsymbol{\Sigma}_{w,k}. \tag{2.61}$$

Then

$$\begin{aligned} & p\left(\boldsymbol{y}_k\,|\boldsymbol{x}_k\right) p\left(\boldsymbol{x}_k\,|\mathcal{Y}_{k-1}\right) \\ = \;& (2\pi)^{-\frac{N_y}{2}}\left|\boldsymbol{\Sigma}_{v,k}\right|^{-\frac{1}{2}} \\ & \exp\left\{-\frac{1}{2}\left(\boldsymbol{y}_k - \boldsymbol{C}_k\boldsymbol{x}_k - \boldsymbol{D}_k\boldsymbol{u}_k\right)^\top \boldsymbol{\Sigma}_{v,k}^{-1}\left(\boldsymbol{y}_k - \boldsymbol{C}_k\boldsymbol{x}_k - \boldsymbol{D}_k\boldsymbol{u}_k\right)\right\} \cdot \\ & (2\pi)^{-\frac{N_y}{2}}\left|\boldsymbol{P}_{k|k-1}\right|^{-\frac{1}{2}} \exp\left\{-\frac{1}{2}\left(\boldsymbol{x}_k - \boldsymbol{A}_{k-1}\boldsymbol{x}_{k-1|k-1} - \boldsymbol{B}_{k-1}\boldsymbol{u}_{k-1}\right)^\top \cdot\right. \end{aligned}$$

$$
\begin{aligned}
& \boldsymbol{P}_{k|k-1}^{-1}\left(\boldsymbol{x}_k-\boldsymbol{A}_{k-1}\boldsymbol{x}_{k-1|k-1}-\boldsymbol{B}_{k-1}\boldsymbol{u}_{k-1}\right)\Big\} \\
= \quad & (2\pi)^{-\frac{N_y}{2}-\frac{N_x}{2}}\left|\boldsymbol{\Sigma}_{v,k}\right|^{-\frac{1}{2}}\left|\boldsymbol{P}_{k|k-1}\right|^{-\frac{1}{2}}\cdot \\
& \exp\Big\{-\frac{1}{2}\left(\boldsymbol{y}_k-\boldsymbol{C}_k\boldsymbol{x}_k-\boldsymbol{D}_k\boldsymbol{u}_k\right)^{\top}\boldsymbol{\Sigma}_{v,k}^{-1}\left(\boldsymbol{y}_k-\boldsymbol{C}_k\boldsymbol{x}_k-\boldsymbol{D}_k\boldsymbol{u}_k\right)- \\
& \frac{1}{2}\left(\boldsymbol{x}_k-\boldsymbol{A}_{k-1}\boldsymbol{x}_{k-1|k-1}-\boldsymbol{B}_{k-1}\boldsymbol{u}_{k-1}\right)^{\top}\boldsymbol{P}_{k|k-1}^{-1}\cdot \\
& \left(\boldsymbol{x}_k-\boldsymbol{A}_{k-1}\boldsymbol{x}_{k-1|k-1}-\boldsymbol{B}_{k-1}\boldsymbol{u}_{k-1}\right)\Big\} \\
= \quad & (2\pi)^{-\frac{N_x}{2}-\frac{N_y}{2}}\left|\boldsymbol{\Sigma}_{v,k}\right|^{-1}\left|\boldsymbol{P}_{k|k-1}\right|^{-\frac{1}{2}}\cdot \\
& \exp-\frac{1}{2}\Big\{\boldsymbol{x}_k^{\top}\boldsymbol{C}_k^{\top}\boldsymbol{\Sigma}_{v,k}^{-1}\boldsymbol{C}_k\boldsymbol{x}_k-\boldsymbol{x}_k^{\top}\boldsymbol{C}_k^{\top}\boldsymbol{\Sigma}_{v,k}^{-1}\left(\boldsymbol{y}_k-\boldsymbol{D}_k\boldsymbol{u}_k\right)- \\
& \left(\boldsymbol{y}_k-\boldsymbol{D}_k\boldsymbol{u}_k\right)^{\top}\boldsymbol{\Sigma}_{v,k}^{-1}\boldsymbol{C}_k\boldsymbol{x}_k+\left(\boldsymbol{y}_k-\boldsymbol{D}_k\boldsymbol{u}_k\right)^{\top}\boldsymbol{\Sigma}_{v,k}^{-1}\left(\boldsymbol{y}_k-\boldsymbol{D}_k\boldsymbol{u}_k\right)+ \\
& \boldsymbol{x}_k^{\top}\boldsymbol{P}_{k|k-1}^{-1}\boldsymbol{x}_k-\boldsymbol{x}_k^{\top}\boldsymbol{P}_{k|k-1}^{-1}\left(\boldsymbol{A}_{k-1}\boldsymbol{x}_{k-1|k-1}+\boldsymbol{B}_{k-1}\boldsymbol{u}_{k-1}\right)- \\
& \left(\boldsymbol{A}_{k-1}\boldsymbol{x}_{k-1|k-1}+\boldsymbol{B}_{k-1}\boldsymbol{u}_{k-1}\right)^{\top}\boldsymbol{P}_{k|k-1}^{-1}\boldsymbol{x}_k+ \\
& \left(\boldsymbol{A}_{k-1}\boldsymbol{x}_{k-1|k-1}+\boldsymbol{B}_{k-1}\boldsymbol{u}_{k-1}\right)^{\top}\boldsymbol{P}_{k|k-1}^{-1}\left(\boldsymbol{A}_{k-1}\boldsymbol{x}_{k-1|k-1}+\boldsymbol{B}_{k-1}\boldsymbol{u}_{k-1}\right)\Big\}.
\end{aligned}
\tag{2.62}
$$

Suppose that $\boldsymbol{x}_k\left|\mathcal{Y}_k\right. \sim \mathcal{N}\left(\hat{\boldsymbol{x}}_{k|k}, \boldsymbol{P}_{k|k}\right)$, then

$$
\begin{aligned}
p\left(\boldsymbol{x}_k\left|\mathcal{Y}_k\right.\right) &= (2\pi)^{-\frac{N_x}{2}}\left|\boldsymbol{P}_{k|k}\right|^{-\frac{1}{2}} \\
&\quad \exp\left\{-\frac{1}{2}\left(\boldsymbol{x}_k-\hat{\boldsymbol{x}}_{k|k}\right)^{\top}\boldsymbol{P}_{k|k}^{-1}\left(\boldsymbol{x}_k-\hat{\boldsymbol{x}}_{k|k}\right)\right\} \\
&= (2\pi)^{-\frac{N_x}{2}}\left|\boldsymbol{P}_{k|k}\right|^{-\frac{1}{2}}\cdot \\
&\quad \exp-\frac{1}{2}\Big\{\boldsymbol{x}_k^{\top}\boldsymbol{P}_{k|k}^{-1}\boldsymbol{x}_k-\boldsymbol{x}_k^{\top}\boldsymbol{P}_{k|k}^{-1}\hat{\boldsymbol{x}}_{k|k} \\
&\quad -\hat{\boldsymbol{x}}_{k|k}\boldsymbol{P}_{k|k}^{-1}\boldsymbol{x}_k+\hat{\boldsymbol{x}}_{k|k}^{\top}\boldsymbol{\Xi}_{k|k}^{-1}\hat{\boldsymbol{x}}_{k|k}\Big\}.
\end{aligned}
\tag{2.63}
$$

Neglecting the constant proportion factors, yields

$$
p\left(\boldsymbol{y}_k\left|\boldsymbol{x}_k\right.\right)p\left(\boldsymbol{x}_k\left|\mathcal{Y}_{k-1}\right.\right) \propto p\left(\boldsymbol{x}_k\left|\mathcal{Y}_{k-1}\right.\right). \tag{2.64}
$$

Comparing Equation (2.62) and (2.63), yields

$$
\boldsymbol{x}_k^{\top}\boldsymbol{P}_{k|k}^{-1}\boldsymbol{x}_k = \boldsymbol{x}_k^{\top}\boldsymbol{C}_k^{\top}\boldsymbol{\Sigma}_{v,k}^{-1}\boldsymbol{C}_k\boldsymbol{x}_k+\boldsymbol{x}_k^{\top}\boldsymbol{P}_{k|k-1}^{-1}\boldsymbol{x}_k \tag{2.65}
$$

$$
\begin{aligned}
-\boldsymbol{x}_k^{\top}\boldsymbol{P}_{k|k}^{-1}\hat{\boldsymbol{x}}_{k|k} =& -\boldsymbol{x}_k^{\top}\boldsymbol{C}_k^{\top}\boldsymbol{\Sigma}_{v,k}^{-1}\left(\boldsymbol{y}_k-\boldsymbol{D}_k\boldsymbol{u}_k\right) \\
& -\boldsymbol{x}_k^{\top}\boldsymbol{P}_{k|k-1}^{-1}\left(\boldsymbol{A}_{k-1}\boldsymbol{x}_{k-1|k-1}+\boldsymbol{B}_{k-1}\boldsymbol{u}_{k-1}\right)
\end{aligned}
\tag{2.66}
$$

Solving these simultaneous matrices equations, obtains

$$\begin{aligned}
\boldsymbol{P}_{k|k} =& \left(\boldsymbol{C}_k^\top \boldsymbol{\Sigma}_{v,k}^{-1} \boldsymbol{C}_k + \boldsymbol{P}_{k|k-1}^{-1}\right)^{-1} \\
=& \boldsymbol{P}_{k|k-1} - \underbrace{\boldsymbol{P}_{k|k-1}\boldsymbol{C}_k^\top \left(\boldsymbol{\Sigma}_{v,k} + \boldsymbol{C}_k \boldsymbol{P}_{k|k-1} \boldsymbol{C}_k^\top\right)^{-1}}_{\triangleq \boldsymbol{K}_k \text{ The Kalman gain}} \boldsymbol{C}_k \boldsymbol{P}_{k|k-1} \\
=& \left(\boldsymbol{I} - \boldsymbol{K}_k \boldsymbol{C}_k\right) \boldsymbol{P}_{k|k-1} \qquad (2.67) \\
\hat{\boldsymbol{x}}_{k|k} =& \boldsymbol{P}_{k|k} \left(\boldsymbol{C}_k^\top \boldsymbol{\Sigma}_{v,k}^{-1} \left(\boldsymbol{y}_k - \boldsymbol{D}_k \boldsymbol{u}_k\right) + \boldsymbol{P}_{k|k-1}^{-1} \left(\boldsymbol{A}_{k-1} \boldsymbol{x}_{k-1|k-1} + \boldsymbol{B}_{k-1} \boldsymbol{u}_{k-1}\right)\right) \\
=& \underbrace{\left(\boldsymbol{A}_{k-1} \boldsymbol{x}_{k-1|k-1} + \boldsymbol{B}_{k-1} \boldsymbol{u}_{k-1}\right)}_{\triangleq \hat{\boldsymbol{x}}_{k|k-1}} \\
& + \boldsymbol{K}_k \left(\boldsymbol{y}_k - \boldsymbol{C}_k \left(\boldsymbol{A}_{k-1} \boldsymbol{x}_{k-1|k-1} + \boldsymbol{B}_{k-1} \boldsymbol{u}_{k-1}\right) - \boldsymbol{D}_k \boldsymbol{u}_k\right) \\
=& \hat{\boldsymbol{x}}_{k|k-1} + \boldsymbol{K}_k \underbrace{\left(\boldsymbol{y}_k - \boldsymbol{C}_k \boldsymbol{x}_{k|k-1} - \boldsymbol{D}_k \boldsymbol{u}_k\right)}_{\boldsymbol{e}_k} \qquad (2.68)
\end{aligned}$$

Hence, the estimation $\boldsymbol{x}_k \,|\mathcal{Y}_k$ can be recursively obtained as

$$\boldsymbol{x}_k \,|\mathcal{Y}_k \sim \mathcal{N}\left(\hat{\boldsymbol{x}}_{k|k}, \boldsymbol{P}_{k|k}\right), \qquad (2.69)$$

where $\boldsymbol{\mu}_{k|k}, \boldsymbol{P}_{k|k}$ are calculated from the observation at current step $\boldsymbol{y}_k$ and the estimation at the last step $\boldsymbol{x}_{k-1|k-1}$ though Equations (2.67) and (2.68), and $\boldsymbol{P}_{k|k-1}$ is determined by Equation (2.61). This result coincides with the common Kalman filter formula.

Then the one step prediction is

$$\boldsymbol{x}_{k+1} \,|\boldsymbol{x}_k \sim \mathcal{N}\left(\boldsymbol{A}_k \hat{\boldsymbol{x}}_{k|k} + \boldsymbol{B}_k \boldsymbol{u}_k, \boldsymbol{A}_k \boldsymbol{P}_{k|k} \boldsymbol{A}_k^\top + \boldsymbol{\Sigma}_{w,k}\right) \qquad (2.70)$$

Remark 2.2 *The Kalman filter is constitutionally based on the property of multivariate Gaussian random vectors that an affine transformation of multivariate Gaussian random vectors is Gaussian. For instance, given* $\boldsymbol{\alpha}_1 \sim \mathcal{N}\left(\boldsymbol{\mu}_1, \boldsymbol{\Sigma}_1\right)$ *and* $\boldsymbol{\alpha}_2 \sim \mathcal{N}\left(\boldsymbol{\mu}_2, \boldsymbol{\Sigma}_2\right)$*, then*

$$\boldsymbol{A}_1 \boldsymbol{\alpha}_1 + \boldsymbol{A}_2 \boldsymbol{\alpha}_2 \sim \mathcal{N}\left(\boldsymbol{A}_1 \boldsymbol{\mu}_1 + \boldsymbol{A}_2 \boldsymbol{\mu}_2, \boldsymbol{A}_1 \boldsymbol{\Sigma}_1 \boldsymbol{A}_1^\top + \boldsymbol{A}_2 \boldsymbol{\Sigma}_2 \boldsymbol{A}_2^\top\right).$$

This results that if the initial state estimation $p\left(\boldsymbol{x}_0\right)$*, the system noise* $\boldsymbol{w}_k$*, and the measurement noise* $\boldsymbol{v}_k$ *are Gaussian distributed, the states and the measurement at any time are Gaussian distributed.*

ince its development, the Kalman filter has found wide use in control engineering and signal processing applications. There are many explanations and insights available

into this filtering technology. In addition to these, the Kalman filter can also be interpreted as a Bayesian filtering technique in linear Gaussian circumstance, as shown here.

2.3.3 Extended Kalman filter

The Kalman filter cannot be directly applied to nonlinear systems because it is not applicable to nonlinear systems in general. However, the Kalman filter can be applied to a locally linearized nonlinear system, and such an application is commonly referred to as the extended *extended Kalman filter*.

For the type of continuous nonlinear system such as

$$\dot{\boldsymbol{x}}(t) = \boldsymbol{g}(\boldsymbol{x}(t), \boldsymbol{u}(t), t) + \boldsymbol{w}(t) \tag{2.71}$$
$$\boldsymbol{y}(t) = \boldsymbol{h}(\boldsymbol{x}(t), \boldsymbol{u}(t), t) + \boldsymbol{v}(t), \tag{2.72}$$

where $\boldsymbol{g}$ and $\boldsymbol{h}$ are (nonlinear) functions, $\boldsymbol{w}(t)$ and $\boldsymbol{v}(t)$ are white Gaussian noise.

Equations (2.35) and (2.36) can be discretized as

$$\boldsymbol{x}_{k+1} = \boldsymbol{g}_k(\boldsymbol{x}_k, \boldsymbol{u}_k) + \boldsymbol{w}_k \tag{2.73}$$
$$\boldsymbol{y}_k = \boldsymbol{h}_k(\boldsymbol{x}_k, \boldsymbol{u}_k) + \boldsymbol{v}_k, \tag{2.74}$$

where k is the time index. Given the prior estimation of the states as $\boldsymbol{x}_{k-1|k-1}$, we can construct the Kalman filter, such as

$$\boldsymbol{x}_{k|k-1} = \boldsymbol{g}_{k-1}\left(\boldsymbol{x}_{k-1|k-1}, \boldsymbol{u}_k\right) \tag{2.75}$$
$$\boldsymbol{P}_{k|k-1} = \left.\frac{\partial \boldsymbol{g}_{k-1}}{\partial \boldsymbol{x}}\right|_{\boldsymbol{x}=\boldsymbol{x}_{k-1|k-1}} \boldsymbol{P}_{k-1|k-1} \left.\frac{\partial \boldsymbol{g}_{k-1}}{\partial \boldsymbol{x}}\right|_{\boldsymbol{x}=\boldsymbol{x}_{k-1|k-1}}^{\top} + \mathbb{D}\left[\boldsymbol{w}_{k-1}\right] \tag{2.76}$$
$$\boldsymbol{C}_k = \left.\frac{\partial \boldsymbol{h}_k}{\partial \boldsymbol{x}}\right|_{\boldsymbol{x}=\boldsymbol{x}_{k|k-1}} \tag{2.77}$$
$$\boldsymbol{K}_k = \boldsymbol{P}_{k|k-1}\boldsymbol{C}_k^{\top}\left(\boldsymbol{\Sigma}_{v,k} + \boldsymbol{C}_k\boldsymbol{P}_{k|k-1}\boldsymbol{C}_k^{\top}\right)^{-1}\boldsymbol{C}_k\boldsymbol{P}_{k|k-1} \tag{2.78}$$
$$\boldsymbol{x}_{k|k} = \boldsymbol{x}_{k|k-1} + \boldsymbol{K}_k\left(\boldsymbol{y}_k - \boldsymbol{h}_k\left(\boldsymbol{x}_{k|k-1}, \boldsymbol{u}_k\right)\right) \tag{2.79}$$
$$\boldsymbol{P}_{k|k} = \left(\boldsymbol{I} - \boldsymbol{K}_k\boldsymbol{C}_k\right)\boldsymbol{P}_{k|k-1} \tag{2.80}$$

Since the extended Kalman filter uses the first order linear approximation instead of the nonlinear system, the approximation error is significant when the nonlinearity of the system is strong. In statistics, the extended Kalman filter works well when the

posterior distribution of the states is close to Gaussian, such that the conditions for the Kalman filter holds approximately. If the posterior distribution is very different from the Gaussian distribution, for instance, is multimodal or heavily skewed, the estimation performance can be poor and may diverge.

Example 2.4 ***Prediction step in EKF***

Consider the following system

$$x_{k+1} = x_k^2, \tag{2.81}$$

where $x_k \sim \mathcal{N}\left(\mu, \sigma^2\right)$.

The linearization gives

$$\hat{x}_{k+1} = \hat{x}_k^2 \tag{2.82}$$

$$P_{k+1|k} = 4\hat{x}_k^2 P_{k|k}\,, \tag{2.83}$$

which means $x_{k+1|k} \sim \mathcal{N}\left(\mu_k^2, 4\mu_k^2\sigma_k^2\right)$.

Given three cases $x_k^{(1)} \sim \mathcal{N}\left(12, 4\right)$, $x_k^{(2)} \sim \mathcal{N}\left(3, 4\right)$, *and* $x_k^{(3)} \sim \text{Rayleigh}\left(1\right)$ *the linear approximations can be calculated as* $x_{k+1|k}^{(1)} \sim \mathcal{N}\left(144, 2304\right)$, $x_{k+1|k}^{(2)} \sim \mathcal{N}\left(9, 144\right)$, *and* $x_{k+1|k}^{(3)} \sim \mathcal{N}\left(452.1, 789.6\right)$ *respectively. The distributions approximated pointwisely and by linearization method are shown in Figure 2.7 and Figure 2.8. The pointwise approximation will be introduced in Chapter 2.4.1. It can be seen as a relatively accurate approximation. The means and standard deviation of the pointwise approximation are shown in Table 2.1. The approximation results confirm that when the posterior distribution is close to normal distribution as in the first case, the linear approximation is close to the real distribution. However, the linear approximation error is large when the posterior distribution is significantly different from the normal distribution.*

Table 2.1: Mean and standard deviation of the Monte Carlo and linear approximation of the posterior distribution

	method	mean	std
Case 1	pointwise	148.0	48.3
	linearization	144	48
Case 2	pointwise	13.0	12.3
	linearization	9	12
Case 3	pointwise	452.1	28.1
	linearization	451.7	18.2

With the exception of the approximation accuracy problem described in the above example, the extended Kalman filter suffers from two additional major drawbacks. The

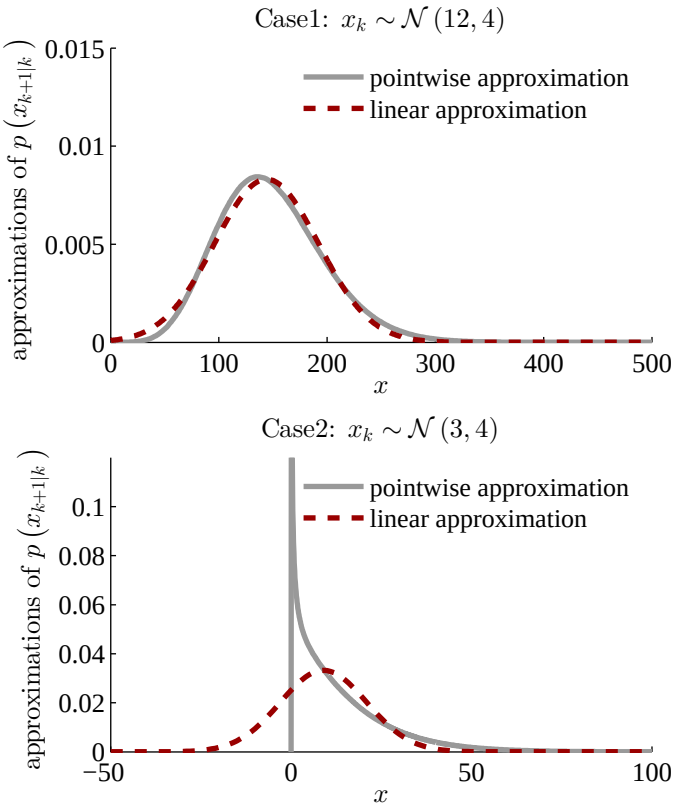

Figure 2.7: Approximation of $p\left(x_{k+1|k}\right)$, with pointwise method and linearization method, where $x_{k|k}$ subjects to Gaussian distributions.

extended Kalman filter relies on the existence of the Jacobian matrices. However, the Jacobian matrices may not be available when the system has discontinuities. Furthermore, the derivation of the Jacobian matrices is not easy when state-space is high dimensional. The resulting Jacobian matrices can be very sophisticated and hard to implement.

2.3.4 Gaussian Sum Filter

The EKF trends to use a linearized system instead of the nonlinear system dynamic, and approximates the posterior mean and variance. This seems to be a macroscopical method. It is relatively simple to calculate, but the approximation error can be large in some conditions. On the contrary, there are methods that can be used to approximate the distribution microscopically, such as the Gaussian sum filter ([Alspach and Sorenson, 1972]).

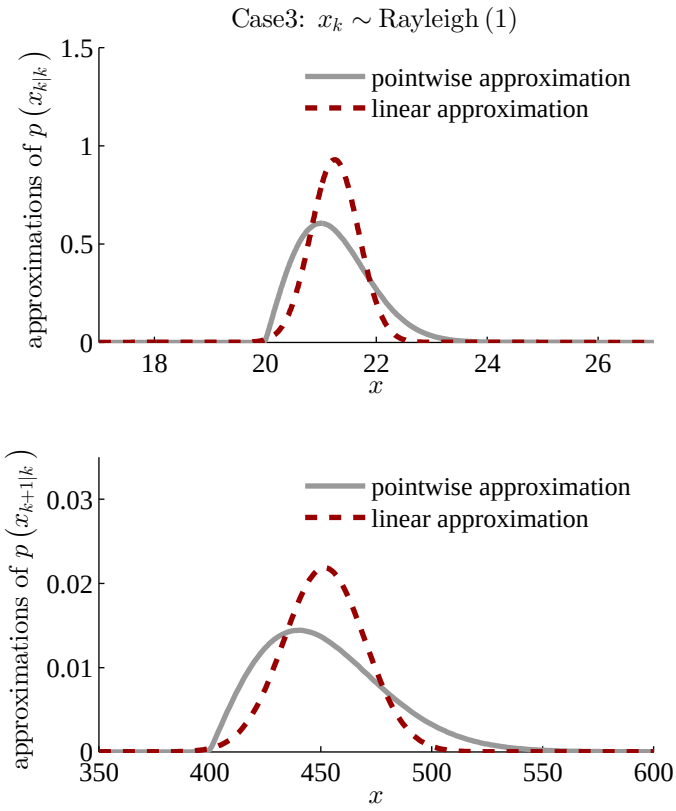

Figure 2.8: Approximation of $p\left(x_{k|k}\right)$ and $p\left(x_{k+1|k}\right)$, with pointwise method and linearization method, where $x_{k|k} \sim$ Rayleigh (1).

Notice that a distribution function $f\left(\boldsymbol{x}\right)$ can be represented by the superposition of a group of Gaussian distribution function, such as

$$f_A\left(\boldsymbol{x}\right) = \sum_{j=1}^{l} c_j \mathcal{N}\left(\boldsymbol{\mu}_j, \boldsymbol{\Sigma}_j\right), \tag{2.84}$$

where $\sum_{j=1}^{l} c_j = 1$ and $c_j \geq 0$ for all j. And $f_A\left(\boldsymbol{x}\right)$ converges uniformly to $f\left(\boldsymbol{x}\right)$ of practical concern as the number of terms l increase and the covariance $\boldsymbol{\Sigma}_j$ approaches the null matrix . In this way, a distribution function is decomposed into a group of small-scale Gaussian distributions.

If the Gaussian distributions are propagated though EKF, the sum of the processed distributions portrays the posterior distribution. [Sorenson and Alspach, 1971] described how the estimation performance of the Gaussian sum filter is better than the EKF; however, it does involve a much heavier computational load than the EKF.

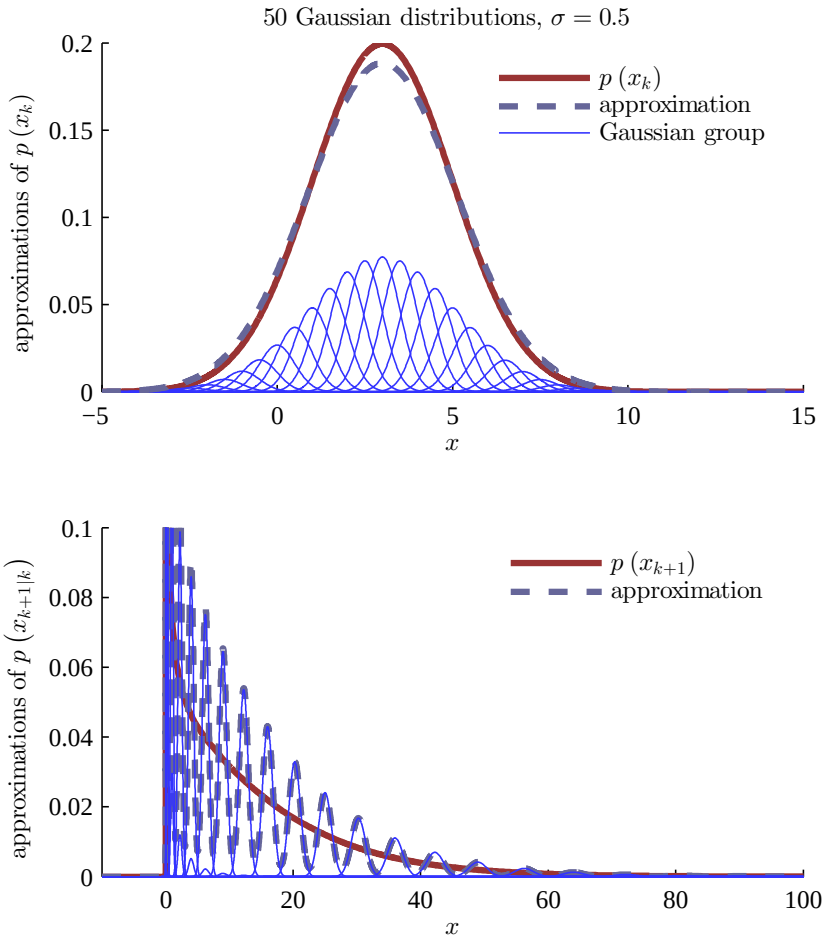

Figure 2.9: Approximation of $p\left(x_{k+1|k}\right)$ of system (2.81) using Gaussian sum method with 50 Gaussian distributions $\sigma = 0.5$.

Example 2.5 ***Prediction step in GSF***

The Gaussian sum filter was employed to deal with the second case in Example 2.4, where the distribution by linear estimation is different from the real distribution.

For convenience, all the Gaussian distributions were chosen to adopts the same standard deviation. Three setups of the Gaussian sum partition of the posterior distribution were employed: 50 Gaussian distributions with $\sigma = 0.5$, 125 Gaussian distributions with $\sigma = 0.2$, and 250 Gaussian distributions with $\sigma = 0.1$. Figure 2.9, Figures 2.10 and 2.11 respectively depict the three cases. In these figures, the axes on top are the Gaussian partition of the posterior distribution $\mathcal{N}(3, 4)$ and the axes at bottom are the

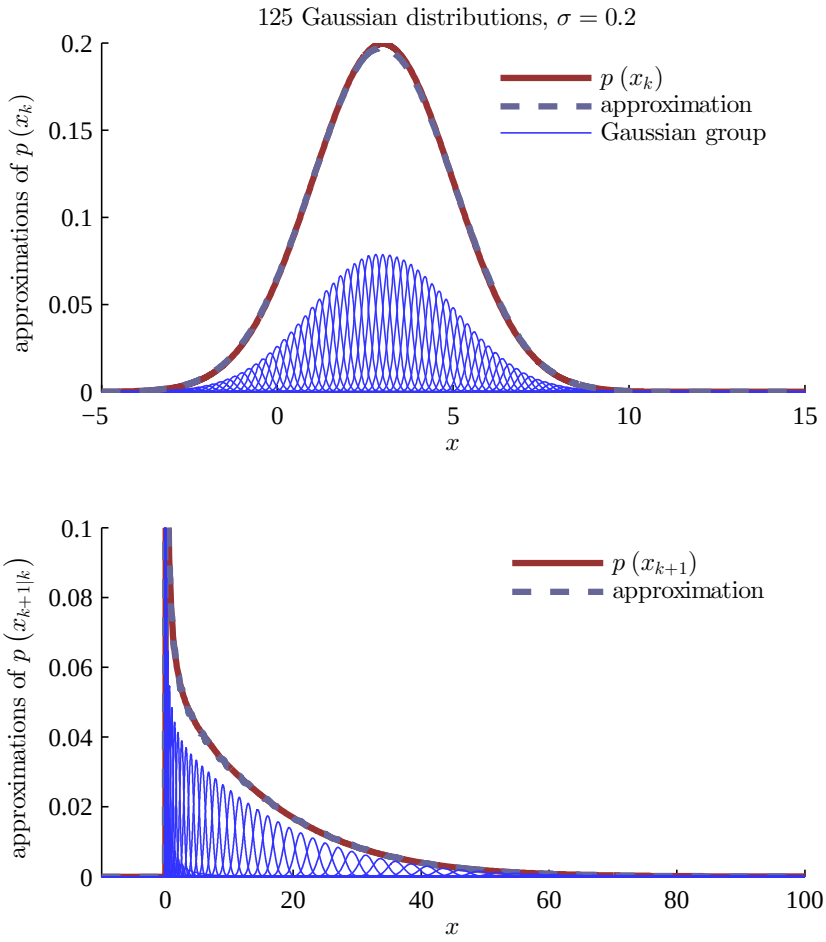

Figure 2.10: Approximation of $p\left(x_{k+1|k}\right)$ of system (2.81) using Gaussian sum method with 125 Gaussian distributions $\sigma = 0.2$.

transformed Gaussian distributions and their sum.

Table 2.2 contains a comparison of Figures 2.9, 2.10 and 2.11. It is clear that a fine Gaussian partition results in accurate approximation. There is only a slight difference between the Gaussian approximation and the pointwise approximation in Case 2. Moreover, a comparison of the information contained in Tables 2.2 and 2.1, reveals that the mean and standard deviation of the Gaussian sum filter estimated is closer to the nominal value than the EKF. This implies that when the posterior is significantly different from a Gaussian, the estimation of the Gaussian sum filter is more precise than the EKF.

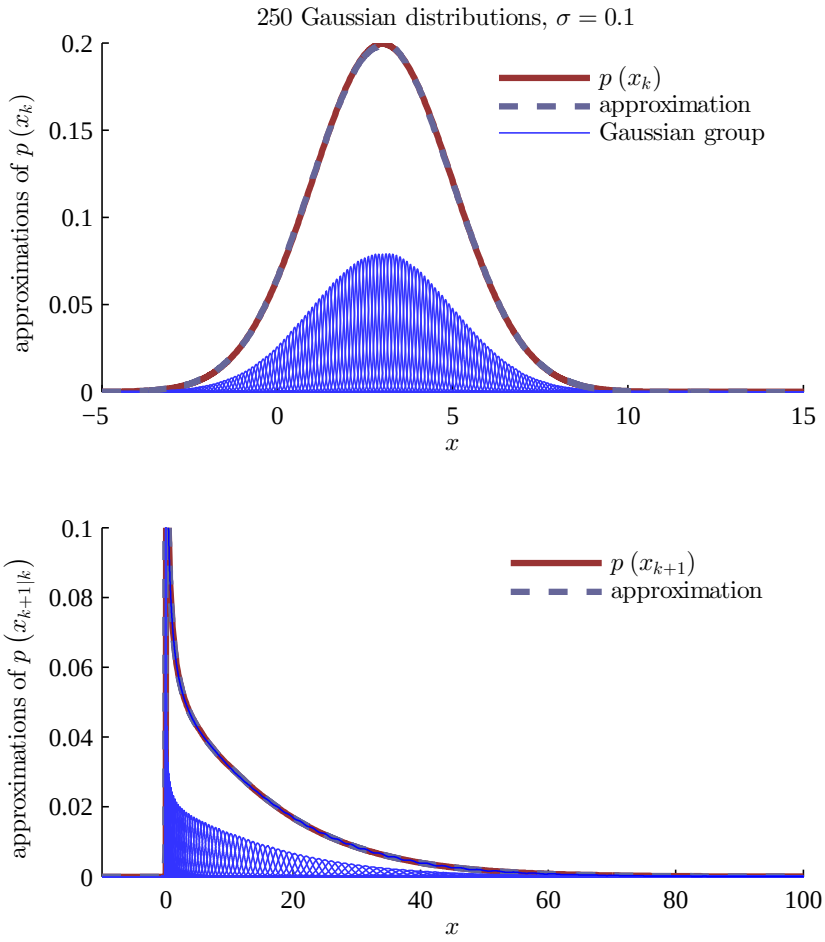

Figure 2.11: Approximation of $p\left(x_{k+1|k}\right)$ of system (2.81) using Gaussian sum method with 250 Gaussian distributions $\sigma = 0.1$.

There are a number of major drawbacks associated with the Gaussian sum filter in terms of regarding the computation approach. Firstly, partitioning a distribution into Gaussian sum is computationally heavy, even when given fixed means and covariance matrices, determining only the factors c_j. Furthermore, it is more difficult to determine the means, covariance matrices, and the factors c_j at the same time. Secondly, to propagate the Gaussian distributions though the EKF and calculate the mixture is also computationally heavy. In addition to these drawbacks, the Gaussian sum filter inherits the drawbacks of the EKF - Jacobian matrices must exist, and the derivation is complex.

Table 2.2: Mean and standard deviation of the Monte Carlo and Gaussian sum approximation of the prior and the posterior distribution

		the posterior		the prior	
	Method	mean	std	mean	std
	pointwise	3	2	13.0	12.3
Case 1	Gaussian sum 50	3.00	2.08	13.23	13.76
Case 2	Gaussian sum 125	3.00	2.03	13.05	13.38
Case 3	Gaussian sum 250	3.00	2.03	13.00	13.31

Remark 2.3 *Point mass filter (PMF) is described in the literature. PMF grids the state space and computes the posterior over this grid recursively. This research does not consider PMF; however, generally, it is understood as GSF with rectangular / uniformly-distributed bases instead of the Gaussian bases in GSF. PMF also applies to any nonlinear and non-Gaussian model. The main drawback of the PMF approach is that if it holds the density of the grid, the computational load increases exponentially as the dimensional of the state increase linearly.*

2.3.5 Unscented Kalman filter

The *unscented transformation* (UT) is based on the intuition that it is easier to approximate a probability distribution than it is to approximate an arbitrary nonlinear function or transformation ([Julier et al., 1995] [Julier and Uhlmann, 2004]). The UT uses so-called sigma points to portray a distribution and trace the propagation of the distribution. Based on UT, the so-called *unscented Kalman filter* (UKF) can be derived. The most noteworthy advantage of UKF over EKF is it represents a derivative-free method (there is no requirement to calculate Jacobians or Hessians).

The unscented transformation

To portray a distribution, a set of sigma points $\mathcal{S}$ is introduced, where $\mathcal{S}$ consists of $p+1$ vectors and they are associated with weights, such as $\mathcal{S} = \{(\boldsymbol{x}^{(i)}, W^{(i)}), i = 0, 1, \ldots, p\}$. The weights $W^{(i)}$ can be either positive or negative, but the condition

$$\sum_{i=0}^{p} W^{(i)} = 1 \tag{2.85}$$

must be satisfied. A good choice of the set of sigma points consists of a symmetric set of $2N_x + 1$ points that one lies at the center and others lies on the $\sqrt{N_x}$th covariance

contour, such as for $i = 1, \ldots, N_x$

$$\boldsymbol{x}^{(0)} = \bar{\boldsymbol{x}} \tag{2.86a}$$
$$W^{(0)} = W^{(0)} \tag{2.86b}$$
$$\boldsymbol{x}^{(i)} = \bar{\boldsymbol{x}} + \left(\sqrt{\frac{N_x}{1 - W^{(0)}} \boldsymbol{\Sigma}_x} \right)_i \tag{2.86c}$$
$$W^{(i)} = \frac{1 - W^{(0)}}{2N_x} \tag{2.86d}$$
$$\boldsymbol{x}^{(i+N_x)} = \bar{\boldsymbol{x}} - \left(\sqrt{\frac{N_x}{1 - W^{(0)}} \boldsymbol{\Sigma}_x} \right)_i \tag{2.86e}$$
$$W^{(i+N_x)} = \frac{1 - W^{(0)}}{2N_x} \tag{2.86f}$$

where $\left(\sqrt{\frac{N_x}{1-W^{(0)}} \boldsymbol{\Sigma}_x} \right)_i$ is the ith row or column of the matrix square root of $\frac{N_x}{1-W^{(0)}} \boldsymbol{\Sigma}_x$.

Once the sigma points are decided, a nonlinear transformation $\boldsymbol{z} = \boldsymbol{h}(\boldsymbol{x})$ of a random vector $\boldsymbol{x}$ with PDF $f(\boldsymbol{x})$ can be obtained, such as

1. Transform each point through the function to yield the set of transformed sigma points
$$\boldsymbol{z}^{(i)} = \boldsymbol{h}\left(\boldsymbol{x}^{(i)} \right). \tag{2.87}$$

2. The mean of the estimation is the weighted average of the transformed points
$$\bar{\boldsymbol{z}} = \sum_{i=0}^{p} W^{(i)} \boldsymbol{z}^{(i)}. \tag{2.88}$$

3. The covariance of the estimation is the weighted outer product of the transformed points
$$\boldsymbol{\Sigma}_z = \sum_{i=0}^{p} W^{(i)} \left(\boldsymbol{z}^{(i)} - \bar{\boldsymbol{z}} \right) \left(\boldsymbol{z}^{(i)} - \bar{\boldsymbol{z}} \right)^{\top}. \tag{2.89}$$

The unscented Kalman filter

Using the UT in Bayesian recursive filtering, we obtain the UKF. The UKF algorithm is given below. Detailed derivation of this algorithm can be found in a large amount of literature; for instance a study by [Julier and Uhlmann, 2004].

Recall Equations (2.73) and (2.74)

$$\boldsymbol{x}_{k+1} = \boldsymbol{g}_k\left(\boldsymbol{x}_k, \boldsymbol{u}_k\right) + \boldsymbol{w}_k \tag{2.90}$$

$$\boldsymbol{y}_k = \boldsymbol{h}_k\left(\boldsymbol{x}_k, \boldsymbol{u}_k\right) + \boldsymbol{v}_k, \tag{2.91}$$

A new state vector can be defined by augmenting the state-space with the system and measurement noise as

$$\boldsymbol{x}_{a,k} = \begin{bmatrix} \boldsymbol{x}_k \\ \boldsymbol{w}_k \\ \boldsymbol{v}_k \end{bmatrix}. \tag{2.92}$$

Then the system model can be transformed into

$$\boldsymbol{x}_{a,k+1} = \boldsymbol{g}_{a,k}\left(\boldsymbol{x}_{a,k}, \boldsymbol{u}_k\right) \tag{2.93}$$

$$\boldsymbol{y}_{a,k} = \boldsymbol{h}_{a,k}\left(\boldsymbol{x}_{a,k}, \boldsymbol{u}_k\right), \tag{2.94}$$

and sigma points of the augmented states can be created from a multivariate Gaussian distribution with mean

$$\boldsymbol{\mu}_{a,k-1} = \begin{bmatrix} \boldsymbol{\mu}_{k-1} \\ \mathbf{0} \\ \mathbf{0} \end{bmatrix} \tag{2.95}$$

and covariance matrix

$$\boldsymbol{K}_{a,k-1} = \begin{bmatrix} \boldsymbol{K}_{k-1} & \mathbf{0} & \mathbf{0} \\ \mathbf{0} & \boldsymbol{\Sigma}_{w,k-1} & \mathbf{0} \\ \mathbf{0} & \mathbf{0} & \boldsymbol{\Sigma}_{v,k-1} \end{bmatrix}. \tag{2.96}$$

Following the UT algorithm, transforms the sigma points such as

$$\boldsymbol{x}^{(i)}_{a,k|k-1} = \boldsymbol{g}\left(\boldsymbol{x}^{(i)}_{a,k-1|k-1}, \boldsymbol{u}_{k-1}\right). \tag{2.97}$$

Then the predicted mean $\hat{\boldsymbol{\mu}}_{a,k}$ and covariance $\hat{\boldsymbol{K}}_{a,k}$ can be calculated following Equations (2.88) and (2.89). Also the prediction points of the observation can be obtained as

$$\boldsymbol{y}^{(i)}_{k|k-1} = \boldsymbol{h}\left(\boldsymbol{x}^{(i)}_{k|k-1}, \boldsymbol{u}_k\right). \tag{2.98}$$

And the predicted mean $\hat{\boldsymbol{y}}_k$ and covariance $\hat{\boldsymbol{S}}_k$ can also be calculated by Equations (2.88) and (2.89).

The cross covariance matrix is

$$\boldsymbol{K}^{xy}_{k|k-1} = \sum_{i=0}^{p} W^{(i)}\left(\boldsymbol{x}^{(i)}_{k|k-1} - \boldsymbol{\mu}_{k|k-1}\right)\left(\boldsymbol{x}^{(i)}_{k|k-1} - \boldsymbol{\mu}_{k|k-1}\right)^{\top}. \tag{2.99}$$

Then use the formal Kalman filter update equations:

$$\boldsymbol{\mu}_{k|k} = \boldsymbol{\mu}_{k|k-1} + \boldsymbol{W}_k \boldsymbol{\nu}_k \tag{2.100}$$

$$\boldsymbol{K}_{k|k} = \boldsymbol{K}_{k|k-1} - \boldsymbol{W}_k \boldsymbol{S}_{k|k-1} \boldsymbol{W}_k^\top \tag{2.101}$$

where

$$\boldsymbol{\nu}_k = \boldsymbol{y}_{k|k} - \boldsymbol{y}_{k|k-1} \tag{2.102}$$

$$\boldsymbol{W}_k = \boldsymbol{K}_k^{xy} \boldsymbol{S}_{k|k-1}^{-1}. \tag{2.103}$$

2.4 Particle filter

2.4.1 Pointwise Expression of Distribution

Now is a good time to introduce the particle filter (PF). As the EKF, GSF, and UKF, the PF is also a Bayesian filtering technique; however, it is distinguished by the fact that it provides its own unique way of approximating PDFs and describing and estimating the propagation of the PDFs.

As shown in Lemma 2.1, empirical distribution defined in Definition 2.11 converges to the real distribution when the amount of samples is large enough. Compared to empirical distribution approximation, a PDF can be expressed in PF in similar fashion but with a slight difference insomuch as the PF uses "weighted" samples to construct the PDF. For instance, the distribution of a random variable $\boldsymbol{X}_k \sim f_{\boldsymbol{X}_k}(\boldsymbol{x}_k)$ can be approximated by

$$f_{\boldsymbol{X}_k}(\boldsymbol{x}_k) \approx \sum_{i=1}^{N_s} w_k^{(i)} \delta\left(\boldsymbol{x}_k - \boldsymbol{x}_k^{(i)}\right), \tag{2.104}$$

where $\left\{\left(\boldsymbol{x}_k^{(i)}, w_k^{(i)}\right), i = 1, \ldots, N_s\right\}$ are the samples and their associated weights, and the amount of samples N_s is called sample size. In this way, a pointwise approximation of the distribution is spanned by the weighted samples. The empirical distribution approximation can be seen as a special case of the "weighted" sample approximation that the weights are uniform, that is, if the "weights" $w_k^{(i)}$ are uniformly equal to $1/N_s$, the weighted sample pointwise expression degenerates to the empirical distribution.

Compared to the UKF, these weighted samples are different from the sigma points in UKF in the sense that the samples are somehow randomly chosen while the sigma points are chosen deterministically.

The pointwise expression of distribution should not be understood as distribution, and it is impossible to reconstruct the density function $f_{\boldsymbol{X}}(\boldsymbol{x})$ analytically from a pointwise expression. However, the functions, for instance the moments, of a density function can be approached by evaluating the pointwise expression. Such as the

expectation of $\boldsymbol{X}$ is approximated by

$$\begin{aligned} \mathbb{E}[\boldsymbol{X}] &= \int \boldsymbol{x} f(\boldsymbol{x}) \, d\boldsymbol{x} && (2.105) \\ &\approx \sum_{i=1}^{N_s} \boldsymbol{x}^{(i)} w_{k-1}^{(i)} \delta\left(\boldsymbol{x} - \boldsymbol{x}_k^{(i)}\right). && (2.106) \end{aligned}$$

We use the pointwise expression to simulate/describe the propagation of the distribution of the states. That is, each sample goes though the process equation, and then forms the resulting PDF as a group of weighted samples. Continuing with Equation (2.104), if the PDF of random variable $\boldsymbol{X}_{k+1} \sim \boldsymbol{g}(\boldsymbol{X}_k)$ is constructed by

$$\begin{aligned} f_{\boldsymbol{X}_{k+1}}(\boldsymbol{x}_{k+1}) &= \int \boldsymbol{g}(\boldsymbol{x}_k) f(\boldsymbol{x}_k) \, d\boldsymbol{x} \\ &\approx \sum_{i=1}^{N_s} w_{k-1}^{(i)} \delta\left(\boldsymbol{x}_{k+1} - \boldsymbol{g}\left(\boldsymbol{x}_k^{(i)}\right)\right). && (2.107) \end{aligned}$$

2.4.2 Importance Sampling and Proposal Distribution

As is the case with empirical approximation, the accuracy of the pointwise approximation increases as the sample size increases. However, how can one sample the distribution to minimize the approximation error when a small sample size is involved? Limiting the sample size is necessary since, when using PF-based observers, the sample sizes are limited by the computational capacity. This section will introduce the importance sampling technique that is employed in this thesis.

Importance Sampling

The *importance sampling* technique aims to sample the distribution in the region of "importance" in order to achieve accurate and precise approximation of a PDF that involves a limited amount of samples. This is especially important in the area of high-dimensional space, where the densities are usually sparse and the region of interest where the target lies is relatively small in terms of the entire data space [Chen, 2003]. The aim of importance sampling is to choose a proposal distribution (importance distribution) $q(\boldsymbol{x})$ in place of the true probability distribution $p(\boldsymbol{x})$, which is relatively unknown and thereby difficult to sample.

Suppose that a group of samples $\boldsymbol{x}^{(i)}, i = 1, 2, \ldots, N_s$ are drawn from the proposal $q(\boldsymbol{x})$, such that $\boldsymbol{x}^{(i)} \sim q(\boldsymbol{x})$. Then the distribution $p(\boldsymbol{x})$ can be approximated by

$$\begin{aligned} p(\boldsymbol{x}) &\approx q(\boldsymbol{x}) \sum_i \frac{p\left(\boldsymbol{x}^{(i)}\right)}{q\left(\boldsymbol{x}^{(i)}\right)} \delta\left(\boldsymbol{x}^{(i)} - \boldsymbol{x}\right) \\ &= q(\boldsymbol{x}) \sum_i w^{(i)} \delta\left(\boldsymbol{x}^{(i)} - \boldsymbol{x}\right), && (2.108) \end{aligned}$$

where $w^{(i)} \propto \frac{p\left(\boldsymbol{x}^{(i)}\right)}{q\left(\boldsymbol{x}^{(i)}\right)}$ is called *importance weights*, which are normalized according to $\sum_i w^{(i)} = 1$. A obvious requirement for the proposal $q(\boldsymbol{x})$ is that its support should cover the support of $p(\boldsymbol{x})$. Otherwise, the estimation of $p(\boldsymbol{x})$ in the region where it is not covered by the support of $q(\boldsymbol{x})$ will always be zero.

Then following Equation (2.108) the state propagation in HMM (2.34a) can be approximated as

$$\begin{aligned} p(\boldsymbol{x}_{k+1}) &= \int g(\boldsymbol{x}_{k+1}|\boldsymbol{x}_k)\, p(\boldsymbol{x}_k)\, d\boldsymbol{x}_k \\ &= \int g(\boldsymbol{x}_{k+1}|\boldsymbol{x}_k)\, \frac{p(\boldsymbol{x}_k)}{q(\boldsymbol{x}_k)} q(\boldsymbol{x}_k)\, d\boldsymbol{x}_k \\ &\approx \sum_{i=0}^{N_s} g\left(\boldsymbol{x}_k^{(i)}\right) w^{(i)} \delta\left(\boldsymbol{x}_{k+1} - \boldsymbol{x}_k^{(i)}\right). \end{aligned} \tag{2.109}$$

Example 2.6 *The purpose of this example is to compare the performance of random sample approximation of a PDF, where the samples are drawn from different proposal distributions. The objective distribution to approximate is* $\mathrm{Rayleigh}(2)$ *depicted by the solid line in Figure 2.12. The proposal distributions are:*

1. *uniform distribution on* $(-5, 15)$ *i.e.* $\mathrm{U}(-5, 15)$*, which covers, but does not concentrate on, the* $\mathrm{Rayleigh}(2)$*;*
2. *uniform distribution on* $(0, 6)$ *i.e.* $\mathrm{U}(0, 6)$*, which covers only the main part of the* $\mathrm{Rayleigh}(2)$*, but does not cover the tail;*
3. *Gaussian distribution* $\mathcal{N}(4, 1)$*, whose support is the whole space but the main part only partially covers the main part of* $\mathrm{Rayleigh}(2)$*;*
4. *Gaussian distribution* $\mathcal{N}(4, 3)$*, whose support is the whole space and main part covers the main part of* $\mathrm{Rayleigh}(2)$*;*
5. *Gaussian distribution* $\mathcal{N}(2.5, 1.7)$*, whose mean and variance are chosen close to the theoretical mean and variance of* $\mathrm{Rayleigh}(2)$*;*
6. *Gaussian distribution* $\mathcal{N}(2.5, 3)$*, whose mean is chosen close to the theoretical mean of* $\mathrm{Rayleigh}(2)$*, but with a larger coverage;*
7. *Rayleigh distribution* $\mathrm{Rayleigh}(2)$*, which is exactly the same as the distribution to be approximated,*

respectively. These distributions are shown in Figure 2.12(a). This example is intended to examine the accuracy of the approximation subject to different proposals.

Two different sample sizes, 100 *and* 10000*, are considered.* 100 *can be taken as a typical sample size when a PF runs in real-time systems, so that the approximation result is practical, while the sample size* 10000 *can be taken as a large number that shows the asymptotic behaviour of the approximation when the sample size is infinite. The results are shown in Figure 2.12(b) and 2.12(c). In each figure, the axes to the top are the CDF curve of* $\mathrm{Rayleigh}(2)$ *and the curves of empirical CDFs of the samples from different proposals. The proposal is close to the objective if their curves are close to each other, and vice versa. The axes to the bottom of the chart shows the approximation result in CDF and empirical CDFs.*

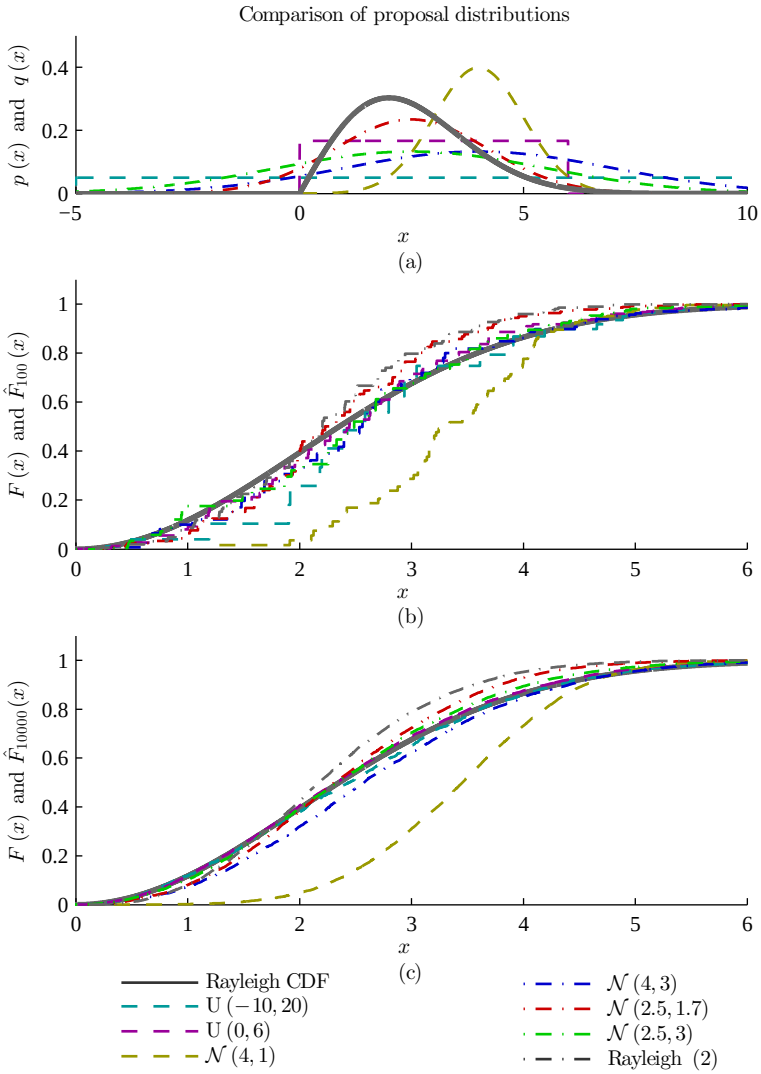

Figure 2.12: Comparison of the proposal distributions.

The rank of the approximation accuracy is shown in Table 2.3. From the results, we may conclude:

1. *If the support of the proposal does not sufficiently cover the support of distribution to be approximated, the approximation cannot be accurate, such as the result with* $\mathcal{N}(4, 1)$ *as the proposal distribution.*
2. *When the sample size is small (e.g.* 100*), too wide support of the proposal results in bad approximation, since the density of the samples on the support of*

Table 2.3: Approximation efficiency of different proposals.

Rank	**Sample size**	
	100	10000
1	$\mathcal{N}(2.5, 3)$	$\mathcal{U}(0, 6)$
2	$\mathcal{U}(0, 6)$	$\mathcal{U}(-10, 20)$
3	$\mathcal{N}(2.5, 1.7)$	$\mathcal{N}(2.5, 3)$
4	$\mathcal{N}(4, 3)$	$\mathcal{N}(2.5, 1.7)$
5	$\mathrm{Rayleigh}(2)$	$\mathrm{Rayleigh}(2)$
6	$\mathcal{U}(-10, 20)$	$\mathcal{N}(4, 3)$
7	$\mathcal{N}(4, 1)$	$\mathcal{N}(4, 1)$

the distribution to be approximated is low. This is the case with $\mathrm{U}(-10, 20)$.

3. *Using exact distribution to be approximated as the proposal does not results in the best approximation, especially at the tails of the objective distribution.*
4. *When the sample size is* 100*, using* $\mathcal{N}(2.5, 3)$*, which has the same mean as* $\mathrm{Rayleigh}(2)$ *and incorporates a slightly larger variance, the best approximation results. This is because the proposal sufficiently covers the support of the objective, and the proposal has enough samples at the tails.*
5. *When the sample size is* 10000*, proposal distributions with supports cover the support of the objective distribution and result in good approximations. But except for 1) when lacking samples at the tails, such as using* $\mathrm{Rayleigh}(2)$ *as proposal, 2) the shape of the proposal is too far away from that of the objectives.*

Remark 2.4 *It is recommended that the proposal distribution has a heavy tail so that it is insensitive to the outliers, and covers the support of* $p(\boldsymbol{x})$ *completely.*

Proposal distribution

In Example 2.6, the distribution to be estimated is known to us; as such, we can then recommend a few proposal distributions. However, since, in the HMM, the distribution to be estimated, i.e., $p(\mathcal{X}_k | \mathcal{Y}_k)$, is relatively unknown (except for the linear Gaussian case), the proposal distribution cannot be directly constructed from $p(\mathcal{X}_k | \mathcal{Y}_k)$. This means we need an approach by which we can construct the proposal based on the available information: the previous estimation $p(\mathcal{X}_{k-1} | \mathcal{Y}_{k-1})$ and the observations $\mathcal{Y}_{k-1}$. So the proposal distribution may adopt the form as a function $q(\boldsymbol{x} | \mathcal{X}_{k-1}, \mathcal{Y}_k)$. Then, the task of constructing the proposal distribution is to find the expression of $q(\boldsymbol{x} | \mathcal{X}_{k-1}, \mathcal{Y}_k)$.

According to existing literature, there are many ways to compose the proposal. Three were selected for the purposes of this research due to their importance and practical application.

Prior distribution as proposal The first choice is to directly use the prior estimation as the proposal, such as

$$q\left(\boldsymbol{x}_k^{(i)} \left| \mathcal{X}_{k-1}, \mathcal{Y}_{k-1} \right.\right) = p\left(\boldsymbol{x}_k \left| \boldsymbol{x}_{k-1}^{(i)} \right.\right), \tag{2.110}$$

so that the samples are drawn as

$$\boldsymbol{x}_k^{(i)} \sim p\left(\boldsymbol{x}_k \left| \boldsymbol{x}_{k-1}^{(i)} \right.\right). \tag{2.111}$$

The drawback of this proposal is that the current observation $\boldsymbol{y}_k$, which is the latest and most direct information of the states, is disregarded in the composition of the proposal.

EKF or UKF estimation as proposal Assuming an EKF or UKF is designed for the HMM as

$$p\left(\boldsymbol{x}_k \left| \mathcal{Y}_{k-1} \right.\right) \sim \mathcal{N}_{\mathrm{EKF}}\left(\boldsymbol{\mu}_k, \boldsymbol{\Sigma}_k\right) = \mathrm{EKF}\left(\boldsymbol{y}_k, \boldsymbol{\mu}_{k-1}, \boldsymbol{\Sigma}_{k-1}\right), \tag{2.112}$$

or

$$p\left(\boldsymbol{x}_k \left| \mathcal{Y}_{k-1} \right.\right) \sim \mathcal{N}_{\mathrm{UKF}}\left(\boldsymbol{\mu}_k, \boldsymbol{\Sigma}_k\right) = \mathrm{UKF}\left(\boldsymbol{y}_k, \boldsymbol{\mu}_{k-1}, \boldsymbol{\Sigma}_{k-1}\right), \tag{2.113}$$

respectively, where the $\boldsymbol{\mu}_{k-1}$ and $\boldsymbol{\Sigma}_{k-1}$ are the estimated mean and covariance from the PF at $k-1$; $\mathrm{EKF}\left(\cdot\right)$ and $\mathrm{UKF}\left(\cdot\right)$ are the EKF and UKF algorithm respectively as mentioned before; $\mathrm{EKF}\left(\cdot\right)$ and $\mathrm{UKF}\left(\cdot\right)$ are the resulting Gaussian distributions respectively. Then samples $\boldsymbol{x}_k^{(i)}$ can be drawn from $p\left(\boldsymbol{x}_k \left| \mathcal{Y}_{k-1} \right.\right)$.

In this case, we 1) first estimate the states with EKF or UKF, then 2) draw samples from the estimated distributions. As concluded in Remark 2.4, a preferred proposal should have long tail to cover the objective distribution. However, the resulting normal distributions from EKF and UKF do not meet this requirement.

2.4.3 Sequential Importance Sampling Partial Filter

The sequential importance sampling (SIS) partial filter algorithm is given in Algorithm 1.

We have made clear the expression of the PDF in Section 2.4.1, and then the importance sampling, which is exactly the time update in the Bayesian filtering context, is given in Section 2.4.2. It is now useful to focus on the measurement update step to complete the Bayesian filtering algorithm.

input : N_s particles from last time step $\left\{\boldsymbol{x}_{k-1}^{(i)},\ w_{k-1}^{(i)}\right\}$, which span the posterior estimation of the state at time $k-1$

$$p\left(\boldsymbol{x}_{k-1}\left|\boldsymbol{y}_{1:k-1}\right.\right) \approx \sum_{i=1}^{N_{s,k-1}} w_{k-1}^{(i)} \delta\left(\boldsymbol{x}_{k-1}-\boldsymbol{x}_{k-1}^{(i)}\right). \tag{2.114}$$

output: N_s new particles $\left\{\boldsymbol{x}_{k}^{(i)},\ w_{k}^{(i)}\right\}$, which span the posterior estimation of the state at time k

$$p\left(\boldsymbol{x}_{k}\left|\boldsymbol{y}_{1:k}\right.\right) \approx \sum_{i=1}^{N_{s,k}} w_{k}^{(i)} \delta\left(\boldsymbol{x}_{k}-\boldsymbol{x}_{k}^{(i)}\right). \tag{2.115}$$

for *each particle* **do**
  Time update:
    Drawing samples from proposal distribution obtains $\boldsymbol{x}_k^{(i)}$.
  Measurement update:
    Updating the weight of the particle obtains $w_k^{(i)}$.
end
Normalize the weights: $w_k^{(i)} = w_k^{(i)} / \sum_{j=1}^{N_s}\left(w_k^{(i)}\right)$

Algorithm 1: Sequential importance sampling particle filter

Recall the general form of recursive Bayesian filtering (2.51) that

$$\begin{aligned}
p\left(\mathcal{X}_k\left|\mathcal{Y}_k\right.\right) &= \frac{p\left(\boldsymbol{y}_k\left|\mathcal{X}_k\right.\right)}{p\left(\boldsymbol{y}_k\left|\mathcal{Y}_{k-1}\right.\right)} p\left(\mathcal{X}_k\left|\mathcal{Y}_{k-1}\right.\right) \\
&= \frac{p\left(\boldsymbol{y}_k\left|\boldsymbol{x}_k\right.\right)}{p\left(\boldsymbol{y}_k\left|\mathcal{Y}_{k-1}\right.\right)} p\left(\boldsymbol{x}_k, \mathcal{X}_{k-1}\left|\mathcal{Y}_{k-1}\right.\right) \\
&= \frac{p\left(\boldsymbol{y}_k\left|\boldsymbol{x}_k\right.\right)}{p\left(\boldsymbol{y}_k\left|\mathcal{Y}_{k-1}\right.\right)} p\left(\boldsymbol{x}_k\left|\mathcal{X}_{k-1}, \mathcal{Y}_{k-1}\right.\right) p\left(\boldsymbol{x}_k\left|\mathcal{X}_{k-1}\right.\right) \\
&= \frac{p\left(\boldsymbol{y}_k\left|\boldsymbol{x}_k\right.\right)}{p\left(\boldsymbol{y}_k\left|\mathcal{Y}_{k-1}\right.\right)} p\left(\boldsymbol{x}_k\left|\mathcal{X}_{k-1}, \mathcal{Y}_{k-1}\right.\right) p\left(\mathcal{X}_{k-1}\left|\mathcal{X}_{k-1}\right.\right) \\
&= \frac{p\left(\boldsymbol{y}_k\left|\boldsymbol{x}_k\right.\right) p\left(\boldsymbol{x}_k\left|\boldsymbol{x}_{k-1}\right.\right)}{p\left(\boldsymbol{y}_k\left|\mathcal{Y}_{k-1}\right.\right)} p\left(\mathcal{X}_{k-1}\left|\mathcal{Y}_{k-1}\right.\right) \\
&\propto p\left(\boldsymbol{y}_k\left|\boldsymbol{x}_k\right.\right) p\left(\boldsymbol{x}_k\left|\boldsymbol{x}_{k-1}\right.\right) p\left(\mathcal{X}_{k-1}\left|\mathcal{Y}_{k-1}\right.\right),
\end{aligned}$$

since the denominator $p\left(\boldsymbol{y}_k\left|\mathcal{Y}_{k-1}\right.\right)$ is a constant.

If proposal $q\left(\mathcal{X}_k\left|\mathcal{Y}_k\right.\right)$ is selected in such a way that it can be decomposed as

$$q\left(\mathcal{X}_k\left|\mathcal{Y}_k\right.\right) = q\left(\boldsymbol{x}_k\left|\mathcal{X}_{k-1}, \mathcal{Y}_k\right.\right) q\left(\mathcal{X}_{k-1}\left|\mathcal{Y}_{k-1}\right.\right) \tag{2.116}$$

Then, following $w_k^{(i)} \propto \frac{p\left(x_k^{(i)}|\mathcal{Y}_k\right)}{q\left(x_k^{(i)}|\mathcal{Y}_k\right)}$, it yields

$$\begin{aligned} w_k^{(i)} &\propto \frac{p\left(\boldsymbol{y}_k \left| \boldsymbol{x}_k^{(i)} \right.\right) p\left(\boldsymbol{x}_k^{(i)} \left| \boldsymbol{x}_{k-1}^{(i)} \right.\right) p\left(\mathcal{X}_{k-1} \left| \mathcal{Y}_{k-1} \right.\right)}{q\left(\boldsymbol{x}_k^{(i)} \left| \mathcal{X}_{k-1}, \mathcal{Y}_k \right.\right) q\left(\mathcal{X}_{k-1} \left| \mathcal{Y}_{k-1} \right.\right)} \\ &= w_{k-1}^{(i)} \frac{p\left(\boldsymbol{y}_k \left| \boldsymbol{x}_k^{(i)} \right.\right) p\left(\boldsymbol{x}_k^{(i)} \left| \boldsymbol{x}_{k-1}^{(i)} \right.\right)}{q\left(\boldsymbol{x}_k^{(i)} \left| \mathcal{X}_{k-1}, \mathcal{Y}_k \right.\right)}. \end{aligned} \tag{2.117}$$

In addition, if the proposal is chosen as $q\left(\boldsymbol{x}_k \left| \mathcal{X}_{k-1}, \mathcal{Y}_k \right.\right) = q\left(\boldsymbol{x}_k \left| \boldsymbol{x}_{k-1}, \boldsymbol{y}_k \right.\right)$, such that the proposal only depends on the states at the latest time instant, the weight update only then depends on the information from the last iteration, which is very useful and practical. In this case, the weight update adopts the form

$$w_k^{(i)} \propto w_{k-1}^{(i)} \frac{p\left(\boldsymbol{y}_k \left| \boldsymbol{x}_k^{(i)} \right.\right) p\left(\boldsymbol{x}_k^{(i)} \left| \boldsymbol{x}_{k-1}^{(i)} \right.\right)}{q\left(\boldsymbol{x}_k^{(i)} \left| \boldsymbol{x}_{k-1}^{(i)}, \boldsymbol{y}_k \right.\right)}. \tag{2.118}$$

Remark 2.5 *If use the prior distribution, which satisfies*

$$q\left(\boldsymbol{x}_k^{(i)} \left| \boldsymbol{x}_{k-1}^{(i)}, \boldsymbol{y}_k \right.\right) = p\left(\boldsymbol{x}_k^{(i)} \left| \boldsymbol{x}_{k-1}^{(i)} \right.\right) \tag{2.119}$$

as the proposal, the weights update Equation (2.118) *will follow a particularly simple form, such as*

$$w_k^{(i)} \propto w_{k-1}^{(i)} p\left(\boldsymbol{y}_k \left| \boldsymbol{x}_k^{(i)} \right.\right). \tag{2.120}$$

When compared with other proposal distributions, the former may not represent a good proposal, since it does not use the current observation, so that its shape can be relatively different from the posterior, and thereby using this proposal results in a relatively low efficiency. However, it is computationally much lighter, since it avoids the calculation of $p\left(\boldsymbol{y}_k \left| \boldsymbol{x}_k \right.\right)$ *and* $q\left(\boldsymbol{x}_k \left| \boldsymbol{x}_{k-1}, \boldsymbol{y}_k \right.\right)$*, especially when the observation relation* $p\left(\boldsymbol{y}_k \left| \boldsymbol{x}_k \right.\right)$ *is hard to calculate.*

To make good use of the proposal (2.119)*, we may 1) increase the sample size, and 2) slightly increase the modeled system noise in the HMM so that* $q\left(\boldsymbol{x}_k \left| \boldsymbol{x}_{k-1}, \boldsymbol{y}_k \right.\right) = p\left(\boldsymbol{x}_k \left| \boldsymbol{x}_{k-1} \right.\right)$ *may always covers the posterior sufficiently.*

2.4.4 Degeneracy Problem, Resampling, and Sampling Importance Resample PF

If Algorithm 1 is employed to perform recursive state estimation, a common problem emerges: the *weight degeneracy* problem. That is, after a few iterations, only one particle will have significant weight (close to 1), while the weights of other particles vanish ([Arulampalam et al., 2002]). In this condition, one particle is used to simulate

input : particles $\boldsymbol{x}_{\text{in}}^{(i)}$, uniform weights $w_{\text{in}}^{(i)}$, $i = 1, \ldots, N_s$.
output: new particles $\boldsymbol{x}_{\text{out}}^{(i)}$, new weights $w_{\text{out}}^{(i)}$, $i = 1, \ldots, N_s$.

Construct CDF from weights $w_{\text{in}}^{(i)}$, such that
    $c_1 \leftarrow 0$;
    $c_i \leftarrow c_{i-1} + w^i$;
$i \leftarrow 1$;
$u_1 \sim \mathrm{U}(0, 1/N_s)$;
for $j = 1$ **to** N_s **do**
    $u_j \leftarrow u_1 + (j-1)/N_s$;
    while $u_j > c_i$ **do**
        $i \leftarrow i + 1$
    end
    $\boldsymbol{x}_{\text{out}}^{(j)} \leftarrow \boldsymbol{x}_{\text{in}}^{(i)}$;
    $w_{\text{out}}^{(i)} \leftarrow 1/N_s$;
end

Algorithm 2: Multinomial resampling.

the propagation of the states; the other particles merely occupy the computational load but make no contribution to the estimation. The precision of the estimation is reduced and divergence occurs.

A good measure of the degeneracy is the *effective sample size* (N_{eff}), which [Liu and Chen, 1998] defined as

$$N_{\text{eff}} = \frac{N_s}{1 + \mathrm{Var}\left(w_k^{*(i)}\right)}, \tag{2.121}$$

where $w_k^{*(i)}$ is named " true weights" and $w_k^{*(i)} = \frac{p\left(\boldsymbol{x}_k^{(i)}|\mathcal{Y}_k\right)}{q\left(\boldsymbol{x}_k^{(i)}\middle|\boldsymbol{x}_{k-1}^{(i)},\mathcal{Y}_k\right)}$. Clearly, $N_{\text{eff}} \leq N_s$, and the equal sign holds only when the true weights uniformly equals to $1/N_s$. Since $p\left(\boldsymbol{x}_k^{(i)}|\mathcal{Y}_k\right)$ is unknown, a good estimation $\hat{N}_{\text{eff}}$ of the effective sample size is given by

$$\hat{N}_{\text{eff}} = \frac{1}{\sum_{i=1}^{N_s}\left(w_k^{(i)}\right)^2} \leq N_s, \tag{2.122}$$

which apparently is a measure of the unevenness of the weights.

Previous studies have shown that the effective sample size in Algorithm 1 can only decrease with time ([Doucet et al., 2000a]); as such, the means to counteract the degeneracy must be applied to keep the effective sample size high. An intuitive way to do this is to ensure that the limited particles remain focussed on the important aspect of the estimation problem by pruning those particles that have large weights and eliminating the particles that have insignificant weights. These types of methods are referred to as resampling methods in the literature. Unless specified otherwise, the resampling method applied throughout this thesis is the systematic resampling method

input : N_s particles from last time step $\left\{\boldsymbol{x}_{k-1}^{(i)},\ w_{k-1}^{(i)}\right\}$, which span the posterior estimation of the state at time $k-1$

$$p\left(\boldsymbol{x}_{k-1}\left|\boldsymbol{y}_{1:k-1}\right.\right) \approx \sum_{i=1}^{N_{s,k-1}} w_{k-1}^{(i)} \delta\left(\boldsymbol{x}_{k-1}-\boldsymbol{x}_{k-1}^{(i)}\right). \tag{2.123}$$

output: N_s new particles $\left\{\boldsymbol{x}_{k}^{(i)},\ w_{k}^{(i)}\right\}$, which span the posterior estimation of the state at time k

$$p\left(\boldsymbol{x}_{k}\left|\boldsymbol{y}_{1:k}\right.\right) \approx \sum_{i=1}^{N_{s,k}} w_{k}^{(i)} \delta\left(\boldsymbol{x}_{k}-\boldsymbol{x}_{k}^{(i)}\right). \tag{2.124}$$

for $i \leftarrow 1$ **to** N_s **do**
  // for each particle
  // *Time update:* Drawing samples from prior distribution.
  $\boldsymbol{x}_{k}^{(i)} \leftarrow \boldsymbol{x}_{k}^{(i)} \sim p\left(\boldsymbol{x}_{k}\left|\boldsymbol{x}_{k-1}^{(i)}\right.\right)$
  // *Measurement update:* Updating the weight of the particle following equation (2.120).
  $w_{k}^{(i)} \leftarrow w_{k-1}^{(i)} p\left(\boldsymbol{y}_{k}\left|\boldsymbol{x}_{k}^{(i)}\right.\right)$
end
$w_{k}^{(i)} \leftarrow w_{k}^{(i)} / \sum_{j=1}^{N_s}\left(w_{k}^{(i)}\right)$
// Normalize the weights
$w_{k}^{(i)} \leftarrow \mathrm{RESAMPLE}\left(w_{k}^{(i)}\right)$
// *Resampling:* follows Algorithm 2.

Algorithm 3: Sampling importance resample particle filter.

that was developed by [Kitagawa, 1996]. The algorithm employed for the purposes of systematic resampling is given in Algorithm 2.

By choosing the prior distribution as the proposal, and using the resampling approach, we obtain the Sampling Importance Resample Particle Filter in Algorithm 3.

Remark 2.6 *The use of EKF or UKF as proposal results in extended Kalman particle filter or unscented particle filter was discussed in detail by [Van Der Merwe et al., 2001]. However, because of their computational load per particle, these variant forms of PF are not applied in this thesis. A detailed explanation on this point is provided in the next chapter.*

2.4.5 Case Study: PF-based Navigation System

Scenario

Recalling the surface vessel model in Example 2.3, if only the kinematic part of the model is taken into consideration, the model can then be simplified as

$$\boldsymbol{\eta}_{k+1} = \boldsymbol{\eta}_k + T\boldsymbol{R}(\psi_k)\,\boldsymbol{\nu}_k + \boldsymbol{w}_k, \tag{2.125}$$

where

$$\boldsymbol{w}_k \sim \mathcal{N}(\mathbf{0}, \boldsymbol{\Sigma}_w)\,, \quad \boldsymbol{\Sigma}_w{=}\mathrm{diag}\left\{0.2 \quad 0.2 \quad \pi/180\right\}, \tag{2.126}$$

is the system noise and $T = 1s$ is the sampling time. For a pure kinematic system, the position should exactly be the integral of the velocity, so that there should be no system noise term in the kinematic equation. Nevertheless, we include the noise term to cover the uncertainty in the kinetics aspect of the system. In addition, a measurement is available, such as

$$\boldsymbol{\eta}_{k,m} = \boldsymbol{\eta}_k + \boldsymbol{v}_k, \tag{2.127}$$

where

$$\boldsymbol{v}_k \sim \mathcal{N}(\mathbf{0}, \boldsymbol{\Sigma}_v) \quad \boldsymbol{\Sigma}_v{=}\mathrm{diag}\left\{1 \quad 1 \quad 5\pi/180\right\}, \tag{2.128}$$

is the measurement noise. The vessel velocity is assumed to be constant

$$\boldsymbol{\nu} = \left[5 \quad 2 \quad -10\pi/180\right]^\top. \tag{2.129}$$

And the initial position of the vessel is at

$$\boldsymbol{\eta}_0 \sim \mathcal{N}\left(\left[-3 \quad 5 \quad -\pi/4\right]^\top, \mathrm{diag}\left\{0.5 \quad 0.5 \quad 5\pi/180\right\}\right). \tag{2.130}$$

Prediction under different sampling intervals

Firstly, we compare the accuracy of the prediction under different sampling intervals. If a shorter sampling time of $T_1 = 0.01\mathrm{s}$ is employed, the process model (2.125) transforms into

$$\boldsymbol{\eta}'_{k+1} = \boldsymbol{\eta}'_k + T_1\boldsymbol{R}(\psi'_k)\,\boldsymbol{\nu}_k + \sqrt{\frac{T_1}{T}}\boldsymbol{w}_k. \tag{2.131}$$

The propagation of the state distribution under process model (2.125) and (2.131) are shown in Figure 2.13. The distributions are shown in the 3D plot and the contour lines of the distribution and the time history of the mean of the distributions are shown in the sub-plot to the top-left. The state propagation under sampling time $T = 1\mathrm{s}$ is detailed in blue and $T_1 = 0.01\mathrm{s}$ in red. Note that the time history of the mean of the distribution with sampling time $T = 1\mathrm{s}$ is only available at time instance $k = 0, 1, 2, 3$, and is linked by straight-line segments.

For $T_1 = 0.01s$, only the distributions and contours at $k = 0,\ 100,\ 200,\ 300$ are shown in the figure. Due to the linearization and discretization error, the difference of state propagation under different sampling times becomes more significant over time.

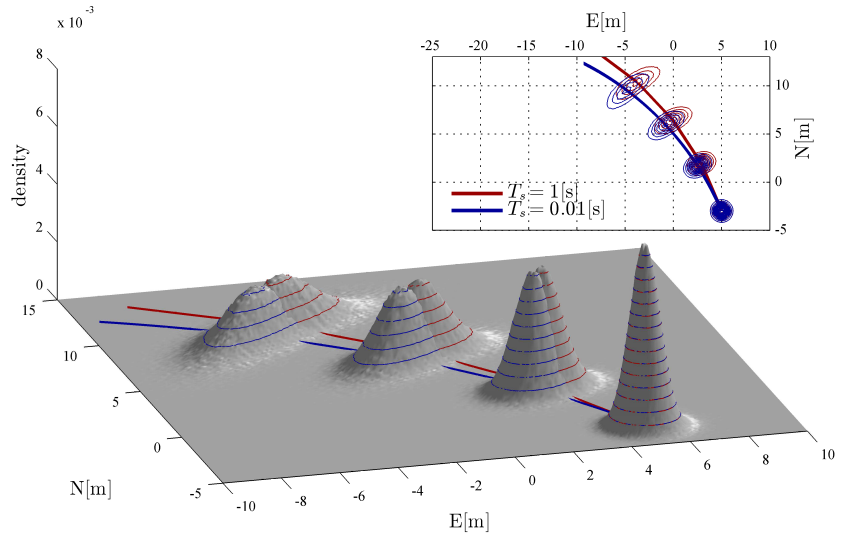

Figure 2.13: Distributions of the vessel position at time $0, 1, 2, 3$s. Sampling times used are $T = 1$s and $T_1 = 0.01$s respectively. The sub-axis shows the contour lines of the PDF and time histories of the means.

When simulating the system, the velocity is involved into the position in the body frame defined by the heading ψ_k. The state propagation cannot be accurately captured when the sampling time is long; as such, the time history of the mean position state is piece-continuous straight lines under sampling time $T_s = 1$s, while it is more curvy under sampling time $T_s = 0.01$s. However, the shape of the PDFs are almost the same under different sampling time, since the propagation of the uncertainty is dominated by the process noise, which has been scaled by the ratio $\sqrt{T_1/T}$.

Remark 2.7 *It can be concluded from the simulation that the time discretization induced significant prediction errors due to non-linearity when the sampling time is relatively long. If we use the prior distribution as the proposal in PF, such a poor prediction may entail that the proposal distribution cannot sufficiently cover the posterior distribution and the PF, therefore, will exhibit poor performance or even diverge. However, it is still possible to use the prior distribution as the proposal, especially when the non-linearity of the system is weak or the sampling is considered fast enough.*

Distributions of the state and the measurement

In the following simulation, the motion of the vessel is simulated with sampling time 0.01s*, while the observation and the estimation are made with sampling time* 1s *in order to provide a clear view of the simulation results.*

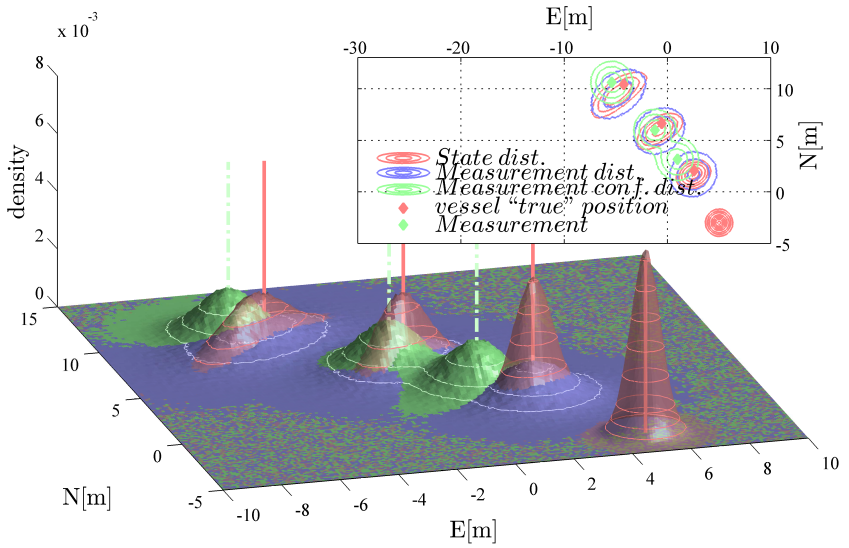

Figure 2.14: Distributions of the states and position measurement. Red surface and contour lines are from the state distribution, the blue surface and contour lines are from the measurement, and the green surface and contour lines describe the distribution of the confidence given the measurement.

Figure 2.14 shows the distribution of the states propagated from the initial condition, and also the measurements and the confidence of the measurements. The distributions of the states are simulated by propagating the initial condition through the system equation.

The distributions of the states becomes more and more flat over time as the variance of the distribution grows and the process noise pollutes the states distribution over time. Hence, measurements have to be made to maintain the required accuracy of the information or knowledge that is available pertaining to the states.

Note that the distributions of the measurement over time are simulated as a superposition of the distributions of the state and the measurement noise. For instance, the distribution of the measurement at $k = 3$ is obtained by propagating the initial states from $k = 0$ to 3, then superposed with the uncertainty of the measurement though Equation (2.127). This distribution describes the possibility at which measurements are made; i.e., given only the initial condition of the vessel, the measurement at each time step is a sample from each of the distributions of the measurement. Obviously, due to the measurement noise, the distribution of the measurement should be flatter than the distribution of the states. However, as time passes, the variance of the state distribution become larger and larger, then the measurement distribution approaches the distribution of the states.

For instance, consider a process $X_k \sim \mathcal{N}\left(\mu_{1,k}, \sigma_{1,k}^2\right)$, and an observation of it as $Y_k \,|x_k \sim \mathcal{N}\left(x_k, \sigma_2^2\right)$, where x_k is the realization of X_k, and $\sigma_{1,k}^2$ increases to infinite

over time. Then $Y_k \sim \mathcal{N}\left(\mu_{1,k}, \sigma_{1,k}^2 + \sigma_2^2\right) \overset{\sigma_{1,k}^2 \to \infty}{\to} \mathcal{N}\left(\mu_{1,k}, \sigma_{1,k}^2\right)$.

The vessel "true" positions are random samples from the serial of the distributions of the states.

The measurements are made according to Equation (2.127) given the "true" positions. Three measurements are obtained, as depicted by the green chain lines. The green surface and contour lines show the confidence of the measurement. Due to the setup of the measurement equation, the distributions of the confidence at all times are Gaussian with equal variance in each direction, due to the setup in the measurement equation. This must be understood in two ways:

View from the "true" state to the measurement: Just following the measurement relation

$$\boldsymbol{\eta}_{k,m} \sim \mathcal{N}\left(\boldsymbol{\eta}_k, \mathbb{D}\left[\boldsymbol{v}_k\right]\right), \tag{2.132}$$

this indicates that the measurements made are surrounding the "true" states subject to a Gaussian distribution. Moreover, if the observation process can be identically repeated infinite times, the resulting empirical distribution will portray the distribution in Equation (2.132). This represents the forward understanding of measurement.

View from the measurement to the "true" state: *"True" state is never available.* The measurement indicates the distribution of the "true" states. A measurement made as Equation (2.127) shows that the "true" states are located around the measurement subject to the Gaussian distribution given by the measurement equation, such as

$$\boldsymbol{\eta}_k \sim \mathcal{N}\left(\boldsymbol{\eta}_{k,m}, \mathbb{D}\left[\boldsymbol{v}_k\right]\right). \tag{2.133}$$

This is the backward understanding of measurement.

State estimation by particle filter

Applying PF Algorithm 3 to Model (2.125) and (2.127) obtains the estimated result shown in Figure 2.15, where the red surface and contour lines depicts the prior distribution $p\left(\boldsymbol{\eta}_{k|k-1}\right)$, while the yellow surface and contour lines show the posterior distribution $p\left(\boldsymbol{\eta}_{k|k}\right)$ estimated by the PF, red solid lines show the "true" vessel position, the light green chain line shows the measurement, and the light yellow dot lines show the mean of the estimation.

The time instance $k = 2, 3$ can be used to illustrate the algorithm of SIRPF. At the end of time $k = 2$, a posterior distribution $p\left(\boldsymbol{\eta}_{2|2}\right)$ was obtained, as shown in the yellow surface. This is the estimation of the distribution of the states based on a combination of the initial knowledge, and all previous measurements. Note that the weights of the particles at this stage have been resampled, so that the weights are uniform.

The time update can then be performed, where new samples are drawn from the proposal distribution. Since SIRPF is used in this simulation, the proposal is the prior

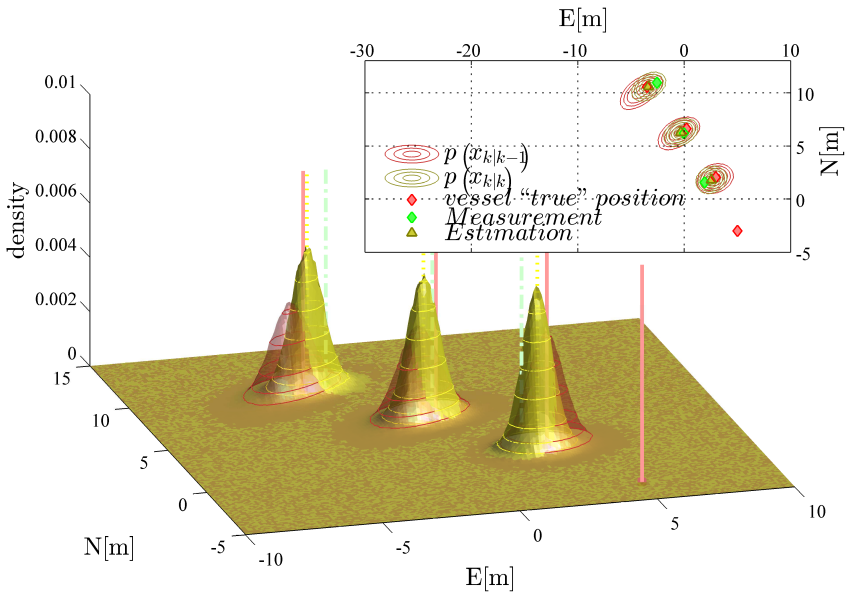

Figure 2.15: Vessel "true" position, position measurement, the prior estimation, and the posterior estimation by particle filter with sample size 10^6, the prior as proposal distribution.

distribution $p\left(\boldsymbol{\eta}_{3|2}\right)$, which is shown as the red surface obtained by pointwise propagation of the samples at $k = 2$. As previously described, the distribution of the states always propagates to a flatter one, so that the prior $p\left(\boldsymbol{\eta}_{3|2}\right)$ is flatter than the posterior $p\left(\boldsymbol{\eta}_{2|2}\right)$.

The prior $p\left(\boldsymbol{\eta}_{3|2}\right)$ has to be updated using the knowledge from the new information $\boldsymbol{\eta}_{m,3}$ according to the algorithm. The result of this measurement update is the as shown as the yellow surface, with the mean depicted by the light yellow dot line. The 2D plot clearly indicates that the variance of the posterior distribution is less than the variance of the prior. This is because the new measurement (referred to the understanding of measurement in the last sub-section) provides more accurate information of the states than the prior distribution. In addition, we see that the prior estimation is "dragged" by the measurement, and forms the posterior estimation.

At the end, resampling should be applied to acquire uniform weighted samples.

Comparison between different proposals and different sample sizes

Different proposals are used in the SISPF to compare the estimation performance in each case. The proposals used in the simulation are:

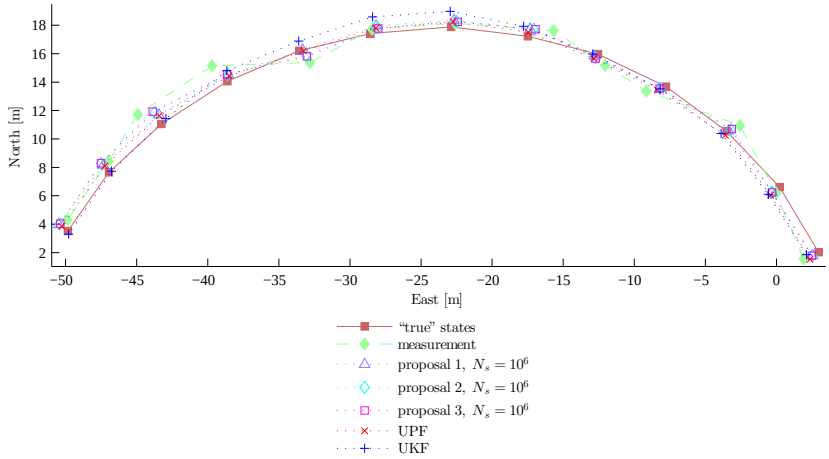

Figure 2.16: The time histories of the "true" states, the measurements, and the mean of the posterior estimation from PF from time $k = 2$ to 14.

Proposal distribution 1: The prior distribution defined by (2.127), such as

$$\begin{aligned} q_1\left(\boldsymbol{\eta}_k \left| \boldsymbol{\eta}_{k-1}\right.\right) &= p\left(\boldsymbol{\eta}_k \left| \boldsymbol{\eta}_{k-1}\right.\right) \\ &= \mathcal{N}\left(\boldsymbol{\eta}_{k-1} + T\boldsymbol{R}\left(\psi_{k-1}\right)\boldsymbol{\nu}_k, \mathbb{D}\left[\boldsymbol{w}_{k-1}\right]\right). \end{aligned}$$

Proposal distribution 2: The prior distribution with larger variance, such as

$$q_2\left(\boldsymbol{\eta}_k \left| \boldsymbol{\eta}_{k-1}\right.\right) = \mathcal{N}\left(\boldsymbol{\eta}_{k-1} + T\boldsymbol{R}\left(\psi_{k-1}\right)\boldsymbol{\nu}_k, \mathrm{diag}\left([0.4, 0.4, 5\pi/180]\right)\right).$$

Proposal distribution 3: The prior distribution with even larger variance, such as

$$q_3\left(\boldsymbol{\eta}_k \left| \boldsymbol{\eta}_{k-1}\right.\right) = \mathcal{N}\left(\boldsymbol{\eta}_{k-1} + T\boldsymbol{R}\left(\psi_{k-1}\right)\boldsymbol{\nu}_k, \mathrm{diag}\left([0.6, 0.6, 10\pi/180]\right)\right).$$

UPF (UKF as proposal): UKF proposal following Equations (2.100)-(2.103).

For Proposal 2 to 4, the time update of the weights of the particles follows

$$w_k^{(i)} = \frac{p\left(\boldsymbol{\eta}_{k,m} \left| \hat{\boldsymbol{\eta}}_k^{(i)}\right.\right) p\left(\hat{\boldsymbol{\eta}}_k^{(i)} \left| \hat{\boldsymbol{\eta}}_{k-1}^{(i)}\right.\right)}{q\left(\hat{\boldsymbol{\eta}}_k^{(i)} \left| \boldsymbol{\eta}_{k-1}^{(i)}, \boldsymbol{\eta}_{k,m}\right.\right)}. \tag{2.134}$$

The simulations last from 0 to 29 seconds. For the Proposal distributions 1-3, three different sample sizes, 10^2, 10^4 , and 10^6, are tested, while only sample size 10^2 is used in the UPF case. Figure 2.16 shows the time series of the estimation of PFs using Proposal 1-3 with sample size 10^6, the time series of the estimation of PF using Proposal 4 with sample size 10^2, and the time series of the UKF estimation. Figure 2.17 shows the time series of the estimation error of the PFs using every proposal,

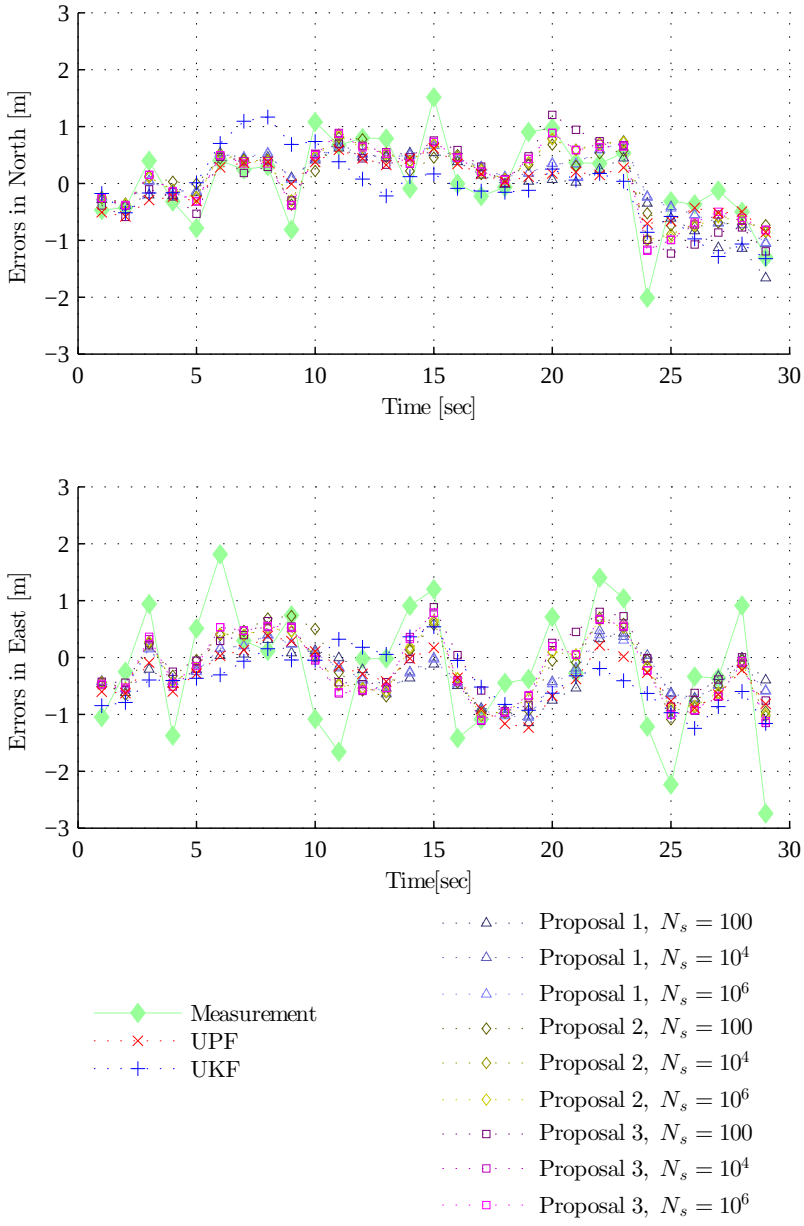

Figure 2.17: The error time histories of the measurements, and the mean of the posterior estimation from PF from time $k = 1$ to 29. The errors are defined as the difference between the signal and the "true" states.

Table 2.4: Total (estimation) errors over time for different proposals, and statistic results from repeating the simulation 10000 times.

Estimation method	**Total error in 30sec** $[\mathrm{m}]$	**10000 times average of errors** $[\mathrm{m}]$**, std. of errors** $[\mathrm{m}^2]$
(Measurement)	34.2266	36.2826, 3.5023
UKF	21.7916	25.5453, 6.4790
UPF, $N_s = 10^2$	18.4585	18.7878, 3.3206
PF, Proposal 1, $N_s = 10^2$	19.7746	36.2993, 4.4029
PF, Proposal 1, $N_s = 10^4$	18.6188	20.0016, 3.2668
PF, Proposal 1, $N_s = 10^6$	18.7194	18.3971, 3.2600
PF, Proposal 2, $N_s = 10^2$	20.9302	18.3805, 3.1805
PF, Proposal 2, $N_s = 10^4$	22.0399	20.3850, 2.8426
PF, Proposal 2, $N_s = 10^6$	21.9016	20.3775, 2.8384
PF, Proposal 3, $N_s = 10^2$	23.2608	22.4636, 3.1805
PF, Proposal 3, $N_s = 10^4$	23.5497	21.2879, 2.7947
PF, Proposal 3, $N_s = 10^6$	23.0869	21.2774, 2.7952

the UKF estimation error, and the difference between the measurement and the "true" state.

The total errors over time for the different proposals are listed in Table 2.4. The scenario in this example is repeated 10,000 times. The average errors are listed together with the standard deviation of the errors in Table 2.4. The statistical results show that the PF-based navigation performs better than the UKF-based method. And PF using UKF as the proposal exhibits better performance than PFs with other proposals, with the exception of Proposal 2. The result of Proposal 2 is unusual where the estimation error minimum appears when the number of particles is small, which is against the rule that the performance of PF benefit from the number of particles. There is no information available that can explain this and it is perhaps something that can be considered in future research.

Comparing Proposal 1, 2 and 3, the PFs with Proposal 1 give the best estimation (ignoring Proposal 2 with sample size 100), followed by the PFs using Proposal 2, and then the PFs with Proposal 3. This manifests itself as the estimation sensitivity to the measurement error grows stronger in response to the larger variations involved in the proposals. Moreover, if the proposal is chosen improperly, the larger sample size does not always result in a better estimation performance, even when the sample size is sufficiently large.

Comparing the estimation performance of PFs with different sample sizes but using the same proposal, there is a clear indication that more particles result in better estimation (ignoring Proposal 2 with sample size 100).

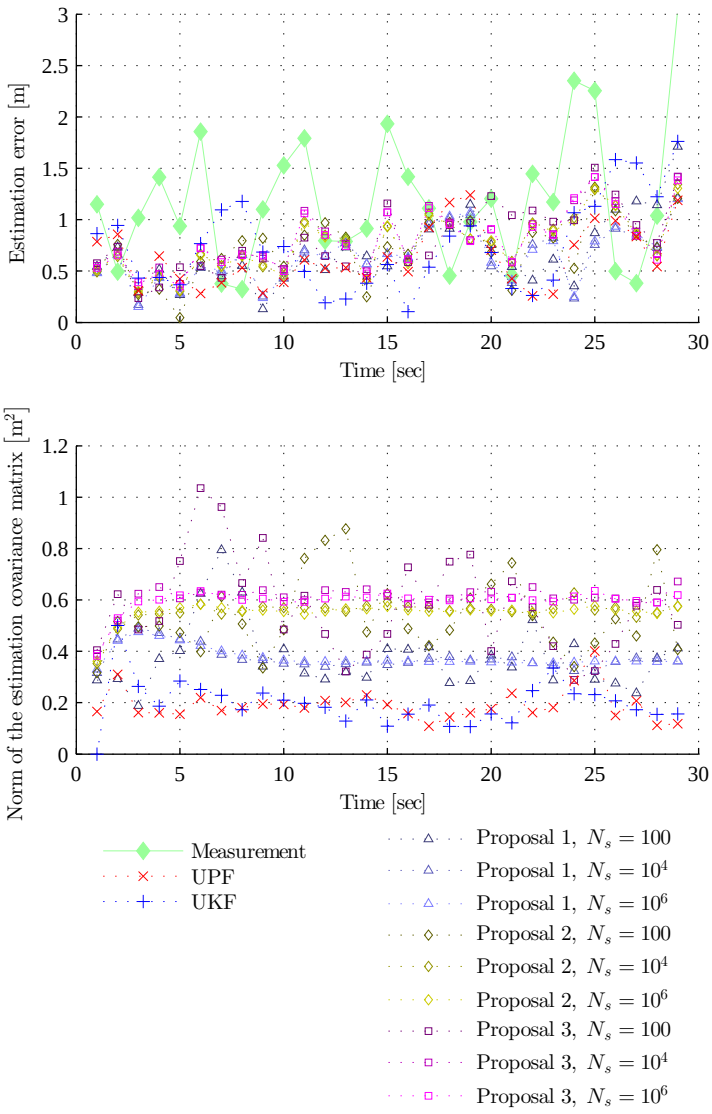

Figure 2.18: The time series of the estimation error (Euclid distance to the "true" position) and variance of the estimated distribution.

Besides the estimation error, the performance of the estimation can also be evaluated by considering its variance, or more specifically, the difference between the shape of the estimated distribution and the "true" distribution. Figure 2.18 depicts the time series of the estimation error (and the measurement error) and the time series of the norm of the estimation covariance matrix. Figure 2.19 shows the likelihood of the "true" state pertaining to the estimation (and measurement). More precisely, it shows

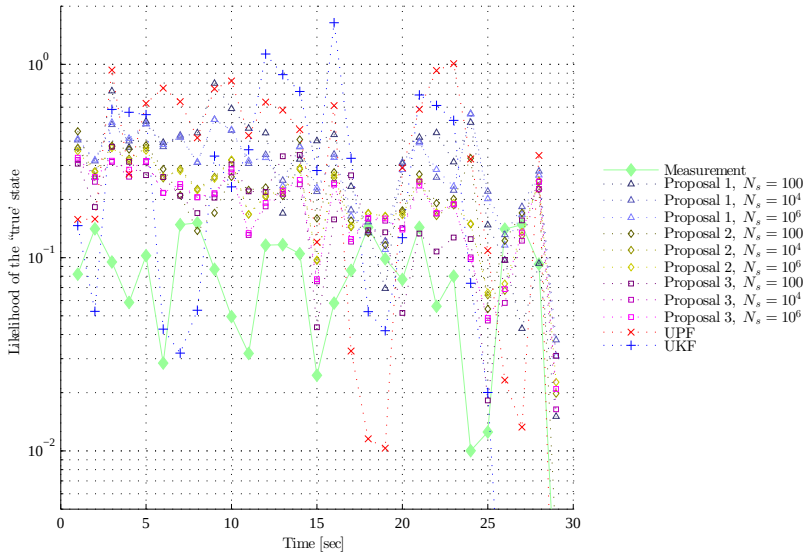

Figure 2.19: The time series of the likelihood of the "true" states.

how the "true" state manifests itself in terms of the estimated mean and covariance, e.g., Figure 2.20. This likelihood should be understood as the difference between the estimated distribution and the "true" estimation, such that a low likelihood indicates that there is a poor fit between the estimation and the reality.

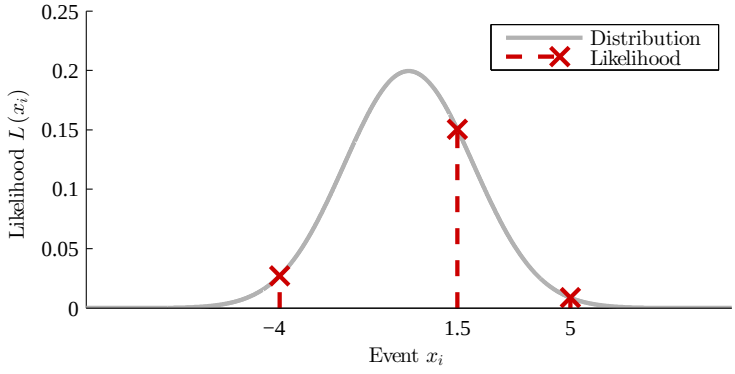

Figure 2.20: Illustration of likelihood. The events and their corresponing likelihood under a certain likelihood function.

So, from synthetically reading Figures 2.18 and 2.19, it can be concluded that:

- Considering the norm of the covariance of the position states is $0.2\mathrm{m}^2$, the UPF and UKF exhibit the smallest estimation variance; i.e., the highest precision.

However, a small estimation variance does not sufficiently lead to the highest accuracy, such that the UKF has a large estimation error.

- The size (or norm) of the (co)variance of the estimation for the PFs in Proposals 1, 2, and 3 increases in response to the size of the variances of the proposals.
- The size (or norm) of the (co)variance of the estimation for a PF depends on its sample size. The more particles used the more stable the estimation variance.
- The larger the estimation error is, the less the likelihood is, in general. For instance, since the estimation (co)variance of the PF with proposal 3 sample size 10^6 is quite stable, the likelihood almost only depends on the estimation error.
- It is hard to tell which filter has the best performance in the likelihood sense. However, the UKF and UPF performed poorly at certain times. Since the size of the variances of their estimation is small, the likelihood is quite sensitive. Moreover, PFs with small sample size may perform more poorly than those with a large sample size.

From these observations, it is possible to conclude that the PFs with Proposal 1 are recommended since their estimation error is small and the likelihood of the "true" states is relatively good. The sample size is not considered in this statement; however, the largest sample size subjecting to the restriction of the computational capacity is preferred.

Summary

Concluding from this example:

- The proposal distribution dominates the performance of the PF.
- If the model is accurate enough, the prior is a good proposal, for its computational simplicity, while the UKF proposal performs better but is computationally heavy.

2.4.6 Case Study: Wave Filtering for DP Vessel Using Particle Filter

Introduction

In this case study, we consider the wave-filtering problem for DP vessels. The source of disturbance that act on DP vessels are mainly derived from wave force, current force, and wind force. The wave force can be conceptually divided into two components: wave-frequency force and low-frequency force. The wave-frequency force tends to make DP vessels oscillate around a certain point at the wave-frequency; while the low-frequency motion induced by waves push the DP vessels to drift away. The current and wind force are usually considered to be slow varying forces ([Fossen, 2011]).

The wave-frequency wave force is strong, and dominates the resultant force. However, people always try to avoid controlling the wave-frequency induced motion of the vessel, since restricting the wave-frequency motion of the DP vessel induces wear and tear to the machinery of the thruster, and makes little contribution towards a better DP performance. Hence, it is important that appropriate methods of estimating the low-frequency motion of a DP vessel, i.e., position and velocity, are incorporated in the DP control system design. Obtaining the low-frequency motion of a vessel from the wave and noise corrupted sensor measurements is called wave filtering ([Fossen and Strand, 1999]).

The conventional method of wave filtering involves using a notch filter or a cascaded low-pass and notch filter; however, these methods induce a delay between the estimation and the real state. KF and EKF can be used for this purpose as well, where the state-space has to be augmented by the states of whitened wave motion ([Fossen, 2011]). Recent research by [Fossen and Strand, 1999] described the use of a passive nonlinear observer to perform wave filtering.

In addition to the setup described by [Fossen and Strand, 1999], we assume the DP system uses GNSS and hydroacoustic position reference (HPR) as position reference sensors, in which the update rates are generally lower than the sampling frequency of the control system.

Scenario

System Model The low-speed manoeuvring model of a vessel used in this study partially follows [Fossen and Strand, 1999], and is briefly represented by the following

$$\dot{\boldsymbol{\eta}} = \boldsymbol{R}(\boldsymbol{y})\,\boldsymbol{\nu} \tag{2.135a}$$

$$\dot{\boldsymbol{\nu}} = \boldsymbol{M}^{-1}\left(-\boldsymbol{D}\boldsymbol{\nu} + \boldsymbol{R}^{\top}(\boldsymbol{y})\,\boldsymbol{b} + \boldsymbol{\tau}\right) \tag{2.135b}$$

$$\dot{\boldsymbol{b}} = -\boldsymbol{T}^{-1}\boldsymbol{b} \tag{2.135c}$$

$$\dot{\boldsymbol{\xi}} = \boldsymbol{\Omega}\boldsymbol{\xi} + \boldsymbol{\Lambda}\boldsymbol{w} \tag{2.135d}$$

$$\boldsymbol{y} = \boldsymbol{\eta} + \boldsymbol{\eta}_w = \boldsymbol{\eta} + \boldsymbol{\Gamma}\boldsymbol{\xi}, \tag{2.135e}$$

where $\boldsymbol{\eta} = \begin{bmatrix} N & E & \psi \end{bmatrix}^{\top}$ is the low-frequency position of the vessel defined in the NED frame, $\boldsymbol{y}$ is the position of the vessel consisting of the low- and wave -frequency motion also defined in the NED frame; $\boldsymbol{R}(\boldsymbol{y})$ is the rotation matrix from the body frame of the vessel to the NED frame; $\boldsymbol{\nu} = \begin{bmatrix} u & v & r \end{bmatrix}^{\top}$ is the low-frequency velocity of the vessel defined in the body frame of the vessel; $\boldsymbol{M}$ and $\boldsymbol{D}$ are the mass and damping matrices of the vessel, $\boldsymbol{b} \in \mathbb{R}^3$ is the dynamic of the slowly varying disturbance consisting of the current and wind defined in the NED frame; $\boldsymbol{T}$ is the time constant matrix of the slowly varying disturbance dynamic; $\boldsymbol{\xi} \in \mathbb{R}^3$ is the intermediate variable of the wave dynamics; $\boldsymbol{\Omega}$ is the transition matrix of state $\boldsymbol{\xi}$; and $\boldsymbol{\Gamma}$ is the output matrix of state $\boldsymbol{\xi}$.

Wave motion Following the 2nd-order transfer function approximation of the wave-frequency motion of the vessel described in [Fossen, 2011] and [Sørensen, 2012], the dynamics of intermediate state $\boldsymbol{\xi}$ is described as

$$h(s) = \frac{2\lambda\omega_0 s}{s^2 + 2\lambda\omega_0 s + \omega_0^2}, \tag{2.136}$$

or in state-space model as

$$\begin{bmatrix} \dot{x}_{w1} \\ \dot{x}_{w2} \end{bmatrix} = \begin{bmatrix} 0 & 1 \\ -\omega_0^2 & -2\lambda\omega_0 \end{bmatrix} \begin{bmatrix} x_{w1} \\ x_{w2} \end{bmatrix} + \begin{bmatrix} 0 \\ 2\lambda\omega_0 \end{bmatrix} w, \tag{2.137}$$

where w is white driving noise. By adjusting the power of the driving noise, $\dot{x}_{w1}$ can express the wave-frequency motion in 1 DOF of the vessel. The total wave motion Equation (2.135d) is obtained by collecting three such state-space models.

Current force A vessel in the sea endures current and wind. The resulting force of the current and wind is strong, but variations in its direction and size occur relatively slowly. The resulting force of current and wind can be modeled as

$$\dot{\boldsymbol{b}} = -\boldsymbol{T}^{-1}\boldsymbol{b}, \tag{2.138}$$

where $\boldsymbol{b} \in \mathbb{R}^3$ is the resulting force of the current and wind defined in the NE frame, and $\boldsymbol{T}$ is the diagonal time constant matrix of the slowly varying disturbance dynamic.

Measurement model According to the basic requirement described in [IMCA, 1996] and also considering the common practices of DP operation, it is assumed that two global navigation satellite system (GNSS) sensors and one hydroacoustic position reference (HPR) sensor are available to the DP vessel. Additionally, it is assumed that the GNSS sensors update rate is 1Hz, and their measurement is subject to a 2-dimensional white Gaussian measurement noise with standard deviation $\text{diag}\{1/3\text{m}, 1/3\text{m}\}$ on the horizontal plane [3]. While the HPR sensor updates at 0.2Hz. The position measurement of HPR subjects to a white Gaussian measurement noise with standard deviation $\text{diag}\{1\text{m}, 1\text{m}\}$. The heading of the vessel is measured by a gyro with update rate 10Hz subject to a white Gaussian measurement noise with standard deviation $1/3\,\text{deg}$. The measurements can, therefore, be modeled as

$$\boldsymbol{p}_{\text{GNSS1},k} = \boldsymbol{C}_p\boldsymbol{y}_k + \boldsymbol{v}_{\text{GNSS1},k} \tag{2.139}$$

$$\boldsymbol{p}_{\text{GNSS2},k} = \boldsymbol{C}_p\boldsymbol{y}_k + \boldsymbol{v}_{\text{GNSS2},k} \tag{2.140}$$

$$\boldsymbol{p}_{\text{HPR},k} = \boldsymbol{C}_p\boldsymbol{y}_k + \boldsymbol{v}_{\text{HPR},k} \tag{2.141}$$

$$\psi_{\text{gyro},y} = \boldsymbol{C}_\psi\boldsymbol{y}_k + v_{\text{gyro},y}, \tag{2.142}$$

where k is the time index; $\boldsymbol{p}_{\text{GNSS1}}$, $\boldsymbol{p}_{\text{GNSS2}}$, $\boldsymbol{p}_{\text{HPR}}$ are the position measurement vectors, each of them consisting of North and East position measurement of the vessel;

[3] We only consider the GNSS measurement on the horizontal plane in this application.

ψ_{gryo} is the vessel heading measurement from the gyro; $\boldsymbol{v}_{\text{GNSS1}}, \boldsymbol{v}_{\text{GNSS2}}, \boldsymbol{v}_{\text{HPR}}, v_{\text{gyro}}$ are the four measurement noise terms corresponding to the description above; and $\boldsymbol{C}_p = \left[\begin{smallmatrix} 1 & 0 & 0 \\ 0 & 1 & 0 \end{smallmatrix}\right]$ and $\boldsymbol{C}_\psi = \begin{bmatrix} 0 & 0 & 1 \end{bmatrix}$ are the output matrices. Note that the position and heading measurements are made with respect to the resulting position $\boldsymbol{y}$, which consists of the wave-frequency motion.

Particle filter design

Compared with Equation (2.135), the model used in particle filter design has to take into account two factors:

- discrete time model,
- driving noise.

Since the highest update rate of the sensors is 10Hz, and the dynamic of a surface vessel is much lower than this value, it is good to have a discrete-time model with sampling time 10Hz. Since the system dynamics are much lower than the sampling frequency, it is possible, and also convenient, to use time-difference directly instead of time-derivative, such as

$$p\left(\boldsymbol{\eta}_{k+1}\right) = \mathcal{N}\left(\boldsymbol{\eta}_k + T_s \boldsymbol{R}\left(\boldsymbol{y}_k\right) \boldsymbol{\nu}_k, \operatorname{Cov}\left[\boldsymbol{w}_{\eta,k}\right]\right), \tag{2.143a}$$

$$p\left(\boldsymbol{\nu}_{k+1}\right) = \mathcal{N}\left(\boldsymbol{\nu}_k + T_s \boldsymbol{M}^{-1}\left(-\boldsymbol{D}\boldsymbol{\nu}_k + \boldsymbol{R}^\top\left(\boldsymbol{y}_k\right) \boldsymbol{b}_k + \boldsymbol{\tau}_k\right), \operatorname{Cov}\left[\boldsymbol{w}_{\nu,k}\right]\right), \tag{2.143b}$$

$$p\left(\boldsymbol{b}_{k+1}\right) = \mathcal{N}\left(\boldsymbol{b}_k - T_s \boldsymbol{T}_b^{-1} \boldsymbol{b}_k, \operatorname{Cov}\left[\boldsymbol{w}_{b,k}\right]\right), \tag{2.143c}$$

$$p\left(\boldsymbol{\xi}_{k+1}\right) = \mathcal{N}\left(\boldsymbol{\xi}_k + T_s \boldsymbol{\Omega}\boldsymbol{\xi}_k, \operatorname{Cov}[\boldsymbol{\Lambda}\boldsymbol{w}_{\xi,k}\boldsymbol{\Lambda}^\top]\right), \tag{2.143d}$$

$$p\left(\boldsymbol{y}_{\text{GNSS1},k}\right) = \mathcal{N}\left(\boldsymbol{C}_p \boldsymbol{y}_k + \boldsymbol{d}_{\text{GNSS},k} + \boldsymbol{b}_{\text{GNSS},k}, \operatorname{Cov}\left[\boldsymbol{v}_{\text{GNSS1},k}\right]\right) \tag{2.143e}$$

$$p\left(\boldsymbol{y}_{\text{GNSS2},k}\right) = \mathcal{N}\left(\boldsymbol{C}_p \boldsymbol{y}_k + \boldsymbol{d}_{\text{GNSS},k} + \boldsymbol{b}_{\text{GNSS},k}, \operatorname{Cov}\left[\boldsymbol{v}_{\text{GNSS2},k}\right]\right) \tag{2.143f}$$

$$p\left(\boldsymbol{y}_{\text{HPR},k}\right) = \mathcal{N}\left(\boldsymbol{C}_p \boldsymbol{y}_k, \operatorname{Cov}\left[\boldsymbol{v}_{\text{HPR},k}\right]\right) \tag{2.143g}$$

$$p\left(\boldsymbol{\psi}_{\text{gyro},k}\right) = \mathcal{N}\left(\boldsymbol{C}_\psi \boldsymbol{y}_k, \operatorname{Var}[v_{\text{gyro}}]\right). \tag{2.143h}$$

where T_s is the sampling time.

The particle filter follows the SIR PF Algorithm 3. Due to the fact that the update rates of the sensors are different, the measurement update of the particle filter behaves in such a manner that whenever a new measurement is obtained by a sensor, its corresponding measurement model in (2.142) is used to update the weights of the particles.

Simulation and result

The simulation was performed in MATLAB/ SIMULINK with components from the MSS toolbox [Fossen and Perez]. The mass and damping matrices of the vessel are

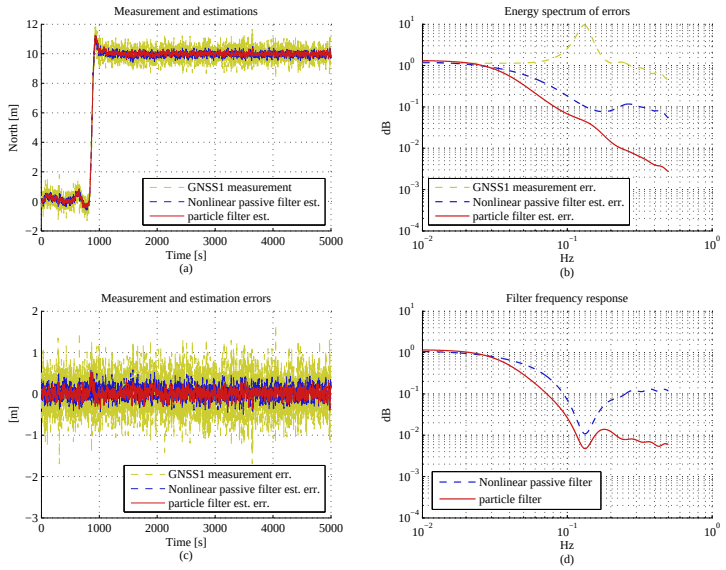

Figure 2.21: The performance of PF-based wave filtering and nonlinear passive filter. (a) shows the GNSS measurement and the estimations; (b) is the energy spectrum of the measurement and estimation errors; (c) shows the measurement error and the estimation error; (d) shows the frequency response of the filters by comparing the energy spectrums.

set to

$$\boldsymbol{M} = \begin{bmatrix} 5.3122 \times 10^6 & 0 & 0 \\ 0 & 8.2831 \times 10^6 & 0 \\ 0 & 0 & 3.7454 \times 10^9 \end{bmatrix}$$

and

$$\boldsymbol{D} = \begin{bmatrix} 5.0242 \times 10^4 & 0 & 0 \\ 0 & 2.7229 \times 10^5 & 4.3933 \times 10^6 \\ 0 & 4.3933 \times 10^6 & 4.1894 \times 10^8 \end{bmatrix},$$

which are adapted from the vessel *Northern Clipper*, as described by [Fossen and Strand, 1999]. The vessel is controlled by a properly tuned nonlinear PID controller. The position and velocity signals from the vessel are directly used as feedback, such that the offline observers do not affect the performance of the control system.

In the simulation the wave motion of the vessel is simulated by Equation (2.137) , with $w_0 = 0.8$ and $\lambda = 0.1$. GNSS and HPR measurements are simulated by combining the vessel total position with proper noise. The vessel suffers from current and wind environmental disturbance, and the resulting force is simulated as $\begin{bmatrix} 1 \times 10^4 & 8 \times 10^3 \end{bmatrix}$ N from the North and East direction, respectively.

The position feedback used in the controller is $\boldsymbol{\eta}$, so that the PF and the nonlinear passive filter are working offline. The simulation lasts 5000 seconds. The vessel is commanded to change the heading from 0deg to 30deg at 500s, then to change the position to 10m North and 10m East at 800s.

Figure 2.21 compares the the estimations of the passive nonlinear observer and the particle filters. Figure 2.21 (a) (c) show the time domain performance of the navigation filters. The PF based wave filter exhibits smaller estimation error, and the performance during the transient is acceptable. Figure 2.21 (b) (d) show the filtering performance in frequency domain. Both the PF and nonlinear passive filter can significantly suppress the wave-frequency disturbance. PF-based wave-filtering for DP vessel can accurately estimate the position of the vessel even when there is strong external disturbance from both ocean current and wave. In addition, PF-based wave-filtering is suitable for DP vessels because it is able to merge multiple measurements.

Summary

PF-based wave filtering for the DP vessel can accurately estimate the position of the vessel, even when there is strong external disturbance from both ocean current and wave. In addition, PF-based wave filtering is suitable for DP vessels because it is able to merge multiple measurements.

2.5 Conclusion

This chapter reviewed basic concepts in probability and stochastics, especially the Bayesian filtering technique. The Kalman filter, extended Kalman filter, Gaussian sum filter, unscented Kalman filter were reviewed, as too was the particle filter algorithm. One illustrative case was presented to provide an overview of the use of the particle filter in terms of a navigation problem. The application of the particle filter within a wave-filtering problem involving the DP vessel was also studied.

Chapter 3

Fault Diagnosis with Particle Filter

“真実はいつも一つ！”
(*“There is only one truth!”*)

— 工藤新一 (Kudo·Shinichi)

3.1 Introduction

According to [Gustafsson, 2001, Chapter 10], a linear system with possible faults can be modeled as a time variant linear system[1]

$$\boldsymbol{x}_{k+1} = \boldsymbol{A}_k(\delta_k)\,\boldsymbol{x}_k + \boldsymbol{B}_{u,k}(\delta_k)\,\boldsymbol{u}_k + \boldsymbol{B}_{w,k}(\delta_k)\,\boldsymbol{w}_k \tag{3.1a}$$
$$\boldsymbol{y}_k = \boldsymbol{C}_k(\delta_k)\,\boldsymbol{x}_k + \boldsymbol{D}_{u,k}(\delta_k)\,\boldsymbol{u}_k + \boldsymbol{D}_{v,k}(\delta_k)\,\boldsymbol{v}_k \tag{3.1b}$$
$$\boldsymbol{w}_k \sim \mathcal{N}\left(\boldsymbol{\mu}_{w,k}(\delta_k), \boldsymbol{Q}_k(\delta_k)\right) \tag{3.1c}$$
$$\boldsymbol{v}_k \sim \mathcal{N}\left(\boldsymbol{\mu}_{v,k}(\delta_k), \boldsymbol{R}_k(\delta_k)\right). \tag{3.1d}$$

In this model,

- $\boldsymbol{x} \in \mathbb{R}^{N_x}$ is the *state* vector;
- $\boldsymbol{y} \in \mathbb{R}^{N_y}$ is the *measurement* / *observation* vector;

[1] The notations in [Gustafsson, 2001] have been modified to ensure consistency with this thesis.

- $\boldsymbol{A} \in \mathbb{R}^{N_x \times N_x}$ is the *state transition matrix*;
- $\boldsymbol{B}_u \in \mathbb{R}^{N_x \times N_u}$ is the *input matrix*;
- $\boldsymbol{B}_w \in \mathbb{R}^{N_x \times N_w}$ is the *noise input matrix*;
- $\boldsymbol{C} \in \mathbb{R}^{N_y \times N_x}$ is the *measurement matrix*;
- $\boldsymbol{D}_u \in \mathbb{R}^{N_y \times N_u}$ is the *direct input to measurement transition matrix*;
- $\boldsymbol{w}$ and $\boldsymbol{v}$ are the *system noise* vector and *measurement noise* vector, and are assumed to be white and Gaussian distributed;
- δ is the *system mode parameter*;
- k denotes *the time index*, such that if the sampling is evenly made with time interval T, then the time is $t = kT$.

All the parameter matrices can be time-varying and conditioned on the system mode parameter δ, which makes δ essential to this model. It is named the system mode parameter because the system switches its behaviour (mode) in response to δ changes providing not all the parameter matrices depend on δ in a trivial manner.

The model (3.1) is linear Gaussian; as such it coincides with most of the assumptions associated with the Kalman filter, except for the system mode parameter δ. As such, the Kalman filter is still valid for model (3.1) assuming that δ is known. However, in FD problems δ is unknown, and is the objective to detect and diagnose. For these features of the model, a Kalman filter-bank-based FD scheme was provided by [Gustafsson, 2001, Chapter 10], where the FD problem is reformed as an estimation problem of the time series $\delta_{1:k}$, such as to obtain the maximum a posteriori estimator

$$\left\{\hat{\delta}_{1:k}\right\}_{\mathrm{MAP}} = \arg\max_{\delta_{1:k}} p\left(\delta_{1:k} \left| \boldsymbol{x}_1, \boldsymbol{y}_{1:k} \right.\right). \tag{3.2}$$

However, this model has its limitations. These are as follows:

1. The model is linear, but the systems in the real world are nonlinear in general. In addition, as described in previous research [Zhao et al., 2012b], in some extreme cases there is a requirement to handle a nonlinear measurement problem. As such, it is necessary to extend this model to nonlinear circumstances.
2. The noise terms are assumed Gaussian in the model; however, this is not always the case in the real world. According to [Zhao et al., 2012a], although we can whiten a coloured noise by states argumentation, a Rice distributed measurement noise and a Gaussian mixture driving noise remains.

This chapter proposes a particle-filter-based fault diagnosis method. Focusing on the limitations of model (3.1), a generalized system model is defined as a combination of a hidden Markov model and a Markov chain in Section 3.2. Following this, several modelling examples are provided in Section 3.2.1. Then, a modified particle filter algorithm is proposed to estimate the system states and system mode in the generalized model in Section 3.4. A case study is described in Section 3.7 to validate the proposed algorithm. The conclusion of this paper follows.

3.2 Switching Mode Hidden Markov Model

Recall the HMM model Equation (2.38) as

$$\boldsymbol{X}_{k+1} | \boldsymbol{x}_k, \boldsymbol{u}_k \sim \boldsymbol{g}_k (\boldsymbol{x}_k, \boldsymbol{u}_k) \tag{3.3}$$
$$\boldsymbol{Y}_k | \boldsymbol{x}_k, \boldsymbol{u}_k \sim \boldsymbol{h}_k (\boldsymbol{x}_k, \boldsymbol{u}_k) . \tag{3.4}$$

Following the idea that system mode parameters can be employed to represent the behaviour of the system, we can augment the model with system mode parameter vector $\boldsymbol{\delta}$, such as

$$\Pr \left(\boldsymbol{\Delta}_{k+1} = \boldsymbol{\delta}^j \middle| \boldsymbol{\Delta}_k = \boldsymbol{\delta}^i \right) = p_{ij,k} \tag{3.5}$$
$$\begin{aligned} \boldsymbol{X}_{k+1} | (\boldsymbol{X}_k = \boldsymbol{x}_k, \boldsymbol{u}_k, \boldsymbol{\Delta}_k) &\sim p (\boldsymbol{x}_{k+1} | \boldsymbol{x}_k, \boldsymbol{u}_k, \boldsymbol{\Delta}_k) \\ &= f_k (\boldsymbol{x}_k, \boldsymbol{u}_k, \boldsymbol{\Delta}_k) \end{aligned} \tag{3.6}$$
$$\begin{aligned} \boldsymbol{Y}_k | (\boldsymbol{X}_k = \boldsymbol{x}_k, \boldsymbol{u}_k, \boldsymbol{\Delta}_k) &\sim p (\boldsymbol{y}_k | \boldsymbol{x}_k, \boldsymbol{u}_k, \boldsymbol{\Delta}_k) \\ &= h_k (\boldsymbol{x}_k, \boldsymbol{u}_k, \boldsymbol{\Delta}_k) . \end{aligned} \tag{3.7}$$

Equation (3.5) is the *system mode transition Markov chain*, defining how the system transfers between system modes, where

- $\boldsymbol{\Delta} = \begin{bmatrix} \Delta^{f^{(1)}} & \Delta^{f^{(2)}} & \cdots & \Delta^{f^{(N_m)}} \end{bmatrix}^\top$ is a *discrete random variable* defining the *system mode*, where the components $\Delta^{f^{(p)}} \in \{0, \quad 1\}$, $(p \in \{1, \ldots, N_m\})$ denote whether the fault "$f^{(p)}$" occurs in the system. Hence, $\boldsymbol{\Delta} \in \{0, 1\}^{N_m}$ describes the condition of all the faults in the system, where N_m is the number of all possible faults in the system. For instance, $\boldsymbol{\Delta} = \begin{bmatrix} 0 & \cdots & 0 \end{bmatrix}^\top$ is the fault-free case.
- $\boldsymbol{\delta}^i$, $\boldsymbol{\delta}^j$ are realizations of $\boldsymbol{\Delta}$, representing two system modes. Since $\boldsymbol{\Delta} \in \{0, 1\}^{N_m}$, the cardinality of the set of all possible $\boldsymbol{\delta}$ is 2^{N_m}, representing all possible system modes. We assign $\boldsymbol{\delta}^{m^{(q)}}$, $\left(q = 0, \ldots, 2^{N_m} - 1\right)$ to all these realizations in a certain order. Especially, $\boldsymbol{\delta}^{m^{(0)}} = \begin{bmatrix} 0 & \cdots & 0 \end{bmatrix}^\top$.

Equation (3.6) is the *system equation*; Eequation (3.7) is the *measurement equation*, where the variables follows their definitions in HMM.

This model is a generalization of the model (3.1) since this model can describe the nonlinear systems, and covers the non-Gaussian noise conditions. For instance, the model (3.1) is covered by switching mode HMM and can be written as

$$p\left(\boldsymbol{x}_{k+1}\left|\boldsymbol{x}_k, \boldsymbol{u}_k, \boldsymbol{\delta}_k\right.\right) = \mathcal{N}\left(\boldsymbol{A}_k\left(\boldsymbol{\delta}_k\right)\boldsymbol{x}_k + \boldsymbol{B}_{u,k}\left(\boldsymbol{\delta}_k\right)\boldsymbol{u}_k + \boldsymbol{B}_{w,k}\left(\boldsymbol{\delta}_k\right)\boldsymbol{\mu}_{w,k},\right.$$
$$\left.\boldsymbol{B}_{w,k}\left(\boldsymbol{\delta}_k\right)\boldsymbol{w}_k\boldsymbol{B}_{w,k}^{\top}\left(\boldsymbol{\delta}_k\right)\right) \tag{3.8}$$

$$p\left(\boldsymbol{y}_k\left|\boldsymbol{x}_k, \boldsymbol{u}_k, \boldsymbol{\delta}_k\right.\right) = \mathcal{N}\left(\boldsymbol{C}_k\left(\boldsymbol{\delta}_k\right)\boldsymbol{x}_k + \boldsymbol{D}_{u,k}\left(\boldsymbol{\delta}_k\right)\boldsymbol{u}_k + \boldsymbol{B}_{v,k}\left(\boldsymbol{\delta}_k\right)\boldsymbol{\mu}_{v,k},\right.$$
$$\left.\boldsymbol{B}_{v,k}\left(\boldsymbol{\delta}_k\right)\boldsymbol{v}_k\boldsymbol{B}_{v,k}^{\top}\left(\boldsymbol{\delta}_k\right)\right), \tag{3.9}$$

It should be highlighted that although this model is very general, it is not universal, for instance, the model (3.2) is discrete, but physical systems are always continuous. Discretization has to be applied to the physical systems to fit the model. This results in a discretization error, as described in Section 2.4.5.

Remark 3.1 *In the switching mode HMM, we implicitly assume that system mode $\boldsymbol{\Delta}$ is independent from the system state $\boldsymbol{x}$, such that the state neither induces nor affects mode transition. This assumption is good in many cases. However, sometimes we need to consider the fact that extreme condition of the states may induce physical faults. This problem is not considered this problem in this paper. A number of works, such as those by [Funiak and Williams, 2003] discuss the interaction between the system states and the system mode. It may be useful for future research to include consideration of the reaction from the state on the system mode to describe the behaviour of the failures in more detail.*

Remark 3.2 *Since this model is time discrete, the time when the system mode transition occurs is also discretized. This means that whenever the mode transition happens within a sampling interval, it is viewed as having occurred at the sampling instant. If the sampling time is long, this may induce a divergence of the continuous reality and the discrete model. However, in the case of a computer-controlled system that incorporates a short sampling time, this discretization error is perceived to be negligible.*

3.2.1 Modelling Examples

Modelling a system into the form (3.2) is not difficult. Knowledge and methods of modelling a system into state-space model can be directly inherited. In terms of nonlinearity and non-Gaussian noise, it is possible to inherit the nonlinearity of the system directly rather than linearizing the system as would be the case with the extended Kalman filter, and the general model is compatible with non-Gaussian noise by manufacturing the mappings. In general, the modelling process is close to mathematically describing the nature of the systems. This section includes some examples that describe how the systems, with their possible faults, are modelled in the form of a switching mode HMM. These examples are furthered enlightened by the examples of [Gustafsson, 2001, Section 10.2].

Example 3.1 Changing DC Level in White Noise

One-time Changing Mean Model *Consider the case of an unknown DC component embedded in white Gaussian noise. Suppose that we want to test the hypothesis that the DC component has changed at some unknown time. We can model the signal by*

$$y_k = \theta_1 - \sigma(k-l+1)\,\theta_1 + \sigma(k-l+1)\,\theta_2 + v_k, \tag{3.10}$$

where $\sigma(\cdot)$ is the step function, θ_1 and θ_2 are the known DC components embedded in the white noise before and after the change, l is the change time, and v_k is the white measurement noise. If all possible change instants are to be considered, the variable l takes its value from the set $\{0, 1, \cdots, k-1, k\}$, where $l = k$ should be interpreted as no change yet.

We can rewrite (3.10) *as*

$$y_k = \boldsymbol{\Delta}_k \begin{bmatrix} \theta_1 \\ \theta_2 \end{bmatrix} + v_k, \tag{3.11}$$

where the system mode parameter $\boldsymbol{\Delta}_k = \begin{bmatrix} \Delta^1 & \Delta^2 \end{bmatrix} \in \left\{ \begin{bmatrix} 1 & 0 \end{bmatrix}, \begin{bmatrix} 0 & 1 \end{bmatrix} \right\}$. Define $\boldsymbol{\delta}^0 = \begin{bmatrix} 1 & 0 \end{bmatrix}$, and $\boldsymbol{\delta}^1 = \begin{bmatrix} 0 & 1 \end{bmatrix}$. This model is in the form of (3.2) *in the sense that*

$$Y_k \sim p(y_k \,|\boldsymbol{\Delta}_k) = \boldsymbol{\Delta}_k \begin{bmatrix} \mathcal{N}(\theta_1, \mathrm{Var}(v_k)) \\ \mathcal{N}(\theta_2, \mathrm{Var}(v_k)) \end{bmatrix}. \tag{3.12}$$

However the model (3.11) *is not equivalent to* (3.10)*, because the system mode in* (3.11) *can switch multiple times between δ^0 and δ^1, while it can only change once in* (3.10)*. As such, some restriction must be assigned to the system mode parameter in* (3.11)*, such that $\boldsymbol{\Delta}$ can only change from δ^0 to δ^1, but never goes backwards. This can be mathematically described by the following Markov chain (See also Figure 3.1), that*

$$\Pr\left(\boldsymbol{\Delta}_k = \boldsymbol{\delta}^0 \,\middle|\, \boldsymbol{\Delta}_{k-1} = \boldsymbol{\delta}^0\right) = p_{00} \tag{3.13a}$$
$$\Pr\left(\boldsymbol{\Delta}_k = \boldsymbol{\delta}^1 \,\middle|\, \boldsymbol{\Delta}_{k-1} = \boldsymbol{\delta}^0\right) = p_{01} = 1 - p_{00} \tag{3.13b}$$
$$\Pr\left(\boldsymbol{\Delta}_k = \boldsymbol{\delta}^0 \,\middle|\, \boldsymbol{\Delta}_{k-1} = \boldsymbol{\delta}^1\right) = p_{10} \tag{3.13c}$$
$$\Pr\left(\boldsymbol{\Delta}_k = \boldsymbol{\delta}^1 \,\middle|\, \boldsymbol{\Delta}_{k-1} = \boldsymbol{\delta}^1\right) = p_{11} = 1 - p_{10}, \tag{3.13d}$$

where p_{00} is the probability that the value of the DC component remains the same between the time steps, and p_{01} is the probability that the value of the DC component will change from θ_1 to θ_2 between time steps. So are the transition probabilities p_{10} and p_{11}.

Until now, the combined model of (3.11) *and* (3.13) *is almost equivalent to* (3.10)*. However, the combined model of* (3.11) *and* (3.13) *is more precise because it also defines the system mode transition probabilities. On the contrary, in model* (3.10) *the probability of the mode switching is undefined, which means the prior knowledge, such as p_{00} and p_{01}, is not modeled.*

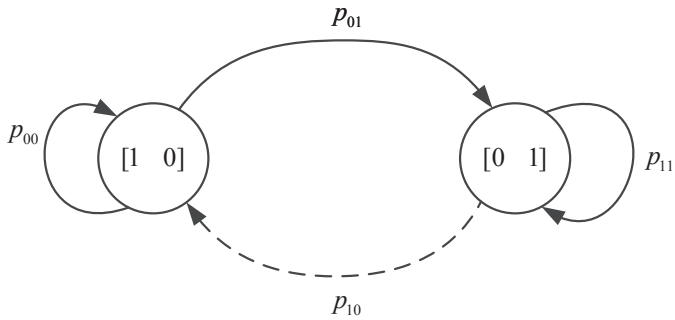

Figure 3.1: The Markov chain of mode transition.

Segmentation in changing mean model *If we extend the above scenario to a more general case by losing the assumptions of previous knowledge of the DC values and the number of changes in the DC level. In this case, it is convenient to take the DC level as the system state, and thereby model the signal as*

$$\boldsymbol{\Theta}_k \sim p\left(\theta_{k+1}\left|\theta_k, \boldsymbol{\Delta}_k\right.\right) = \boldsymbol{\Delta}_k \begin{bmatrix} \rho\left(\theta_{k+1} - \theta_k\right) \\ U\left(\theta_{\inf}, \theta_{\sup}\right) \end{bmatrix} \tag{3.14}$$

$$\boldsymbol{Y}_k \sim p\left(y_k\left|\theta_k\right.\right) = \mathcal{N}\left(\theta_k, \mathrm{Var}\left(v_k\right)\right), \tag{3.15}$$

where $\rho(\cdot)$ is the Dirac function, $U\left(\theta_{\inf}, \theta_{\sup}\right)$ is an uniform distribution on $\theta_{\inf}$ and $\theta_{\sup}$, and $\boldsymbol{\Delta}_k$ follows the definition in the previous example. $\boldsymbol{\delta}^0 \triangleq \begin{bmatrix} 1 & 0 \end{bmatrix}$ indicates there is no change at time k, while $\boldsymbol{\delta}^1 \triangleq \begin{bmatrix} 0 & 1 \end{bmatrix}$ represents there is a change at time k.

The mode transition can be defined according to the frequency of the mode change, such as

$$\Pr\left(\boldsymbol{\Delta}_k = \boldsymbol{\delta}^0\right) = p_1 \tag{3.16}$$

$$\Pr\left(\boldsymbol{\Delta}_k = \boldsymbol{\delta}^1\right) = p_2 = 1 - p_1. \tag{3.17}$$

Example 3.2 Signal drifting

It is common to have a measurement signal that may drift away from its real value. For example, when the GNSS signal is subject to ionosphere disturbance it may drift slowly. Assuming three characteristics of the drifting being 1) the drifting may happen at any time without foreboding, 2) the drift is slow rather than representing an abrupt change, 3) once drift occurs the signal never returns to the normal condition, we may

Table 3.1: The Markov chain for the mode transition in Example 3.2.

		$\boldsymbol{\Delta}_k$	
	Pr	$\boldsymbol{\delta}^0$	$\boldsymbol{\delta}^1$
$\boldsymbol{\Delta}_{k+1}$	$\boldsymbol{\delta}^0$	p_{00}	0
	$\boldsymbol{\delta}^1$	p_{01}	1

use the following equations to model the signal drifting

$$p\left(d_{k+1}\right) \sim \boldsymbol{\Delta}_k \begin{bmatrix} \mathcal{N}\left(d_k + d^0, \sigma_d^2\right) \\ \rho\left(0\right) \end{bmatrix} \tag{3.18a}$$

$$p\left(y_k\right) \sim \mathcal{N}\left(d_k, \sigma_v^2\right), \tag{3.18b}$$

where d^0 is the unknown drifting speed with PDF $p\left(d^0\right)$, σ_d^2 is the variance of the drifting speed, $\boldsymbol{\Delta}_k \in \left\{\boldsymbol{\delta}^0, \quad \boldsymbol{\delta}^1\right\}$, such that $\boldsymbol{\delta}^0 = \begin{bmatrix} 0 & 1 \end{bmatrix}$ represents fault-free mode, and $\boldsymbol{\delta}^1 = \begin{bmatrix} 1 & 0 \end{bmatrix}$ represents a drift in the signal. In addition, the mode transition can be defined as pre the information contained in Table 3.1, where the transition probabilities should be defined according to the reality. Due to Assumption 3, a drifted signal will not return to normal.

Example 3.3 Decayed output

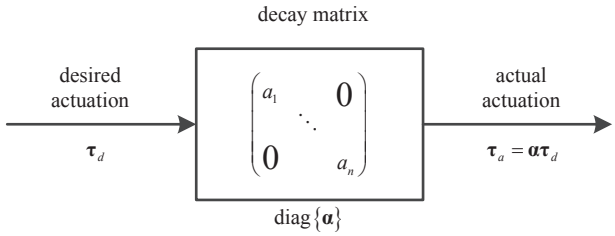

Figure 3.2: Decayed output.

The output from actuators in a control system can be less than the desired value. This input reduction may occur suddenly, and changes may be relatively small. Denoting the desired output by $\boldsymbol{x}$, and the actual output as $\boldsymbol{y}$, this fault can be modelled as

$$p\left(\boldsymbol{\alpha}_{k+1} \left| \boldsymbol{\alpha}_k, \boldsymbol{\Delta}_k \right.\right) = \boldsymbol{\Delta}_k \begin{bmatrix} \mathbf{1} \\ g\left(\boldsymbol{\alpha}_k\right) \end{bmatrix} \tag{3.19}$$

$$p\left(\boldsymbol{\tau}_{a,k} \left| \boldsymbol{\tau}_{d,k}, \boldsymbol{\alpha}_k \right.\right) = \mathrm{diag}\left\{\boldsymbol{\alpha}_k\right\} \boldsymbol{\tau}_{d,k}, \tag{3.20}$$

where $\boldsymbol{\alpha}$ is a vector, of witch the entries are between 0 and 1, indicating the reduction rate of each channel of the system output. The dynamic of $\boldsymbol{\alpha}$ is modelled in (3.19)*, where PDF $g(\boldsymbol{\alpha}_k)$ can be designed in the manner that ensures the entries in $\boldsymbol{\alpha}_{k+1}$ are less than or equal to the ones in $\boldsymbol{\alpha}_k$, to capture the behaviour of the decay. $\boldsymbol{\Delta}_k = \begin{bmatrix}\Delta^1 & \Delta^2\end{bmatrix} \in \left\{\begin{bmatrix}0 & 1\end{bmatrix}, \begin{bmatrix}1 & 0\end{bmatrix}\right\}$, where $\boldsymbol{\delta}^0 \triangleq \begin{bmatrix}1 & 0\end{bmatrix}$ confirms that the input channels are fault-free, and $\boldsymbol{\delta}^1 \triangleq \begin{bmatrix}0 & 1\end{bmatrix}$ denotes input reduction.*

Assuming this aging problem is irreversible if maintenance is not carried out, the mode transition Markov chain can be designed as

$$\Pr\left(\boldsymbol{\Delta}_{k+1} = \boldsymbol{\delta}^0 \,\middle|\, \boldsymbol{\Delta}_k = \boldsymbol{\delta}^0\right) = p_{00} \tag{3.21a}$$
$$\Pr\left(\boldsymbol{\Delta}_{k+1} = \boldsymbol{\delta}^1 \,\middle|\, \boldsymbol{\Delta}_k = \boldsymbol{\delta}^0\right) = p_{01} \tag{3.21b}$$
$$\Pr\left(\boldsymbol{\Delta}_{k+1} = \boldsymbol{\delta}^0 \,\middle|\, \boldsymbol{\Delta}_k = \boldsymbol{\delta}^1\right) = 0 \tag{3.21c}$$
$$\Pr\left(\boldsymbol{\Delta}_{k+1} = \boldsymbol{\delta}^0 \,\middle|\, \boldsymbol{\Delta}_k = \boldsymbol{\delta}^1\right) = 1. \tag{3.21d}$$

Example 3.4 Missing measurement

It is common for some time instances measurements to be missing in some applications, typically due to sensor failure. A suitable model for this situation is

$$p\left(\boldsymbol{x}_{k+1} \,|\boldsymbol{x}_k, \boldsymbol{u}_k\right) = \boldsymbol{g}_k\left(\boldsymbol{x}_k, \boldsymbol{u}_k\right) \tag{3.22}$$
$$p\left(\boldsymbol{y}_k \,|\boldsymbol{x}_k, \boldsymbol{u}_k, \boldsymbol{\Delta}_k\right) = \boldsymbol{\Delta}_k \begin{bmatrix} \boldsymbol{h}_k\left(\boldsymbol{x}_k, \boldsymbol{u}_k\right) \\ \mathcal{N}\left(\mathbf{0}, \boldsymbol{\infty}\right) \end{bmatrix}, \tag{3.23}$$

where $\boldsymbol{\Delta}_k \in \left\{\begin{bmatrix}1 & 0\end{bmatrix}, \begin{bmatrix}0 & 1\end{bmatrix}\right\}$, and the missing measurement is modeled as a sample from distribution $\mathcal{N}\left(\mathbf{0}, \boldsymbol{\infty}\right)$, which gives no information.[2]

In practice, whether the measurement is missing for a certain period can be deterministically observed, so that the mode transition in this case will not be modelled as a Markov chain. However, the outliers of measurements, which are also a common failure mode of the measurement signal, are modelled in the following example.

Example 3.5 Measurement outliers

Outliers are interpreted as samples from a measurement signal that lie abnormally far from the other values. Mathematically, they can be seen as samples from a distribution that exhibits much larger variance than standard, such as

$$y_k = \boldsymbol{\Delta}_k \begin{bmatrix} N\left(x_k, \sigma_k^2\right) \\ N\left(x_k, \sigma_{o,k}^2\right) \end{bmatrix}, \tag{3.24}$$

[2]The notation $\mathcal{N}\left(\mathbf{0}, \boldsymbol{\infty}\right)$ is rough. It is used here to make sure the observer handling this measurement will not encounter any "missing" measurements. Practically, using an uniform distribution on a wide base is also valid, and computationally easier.

where x_k is the mean of the measurement, σ_k^2 is the variance of the measurement in fault-free condition, $\sigma_{o,k}^2$ is the variance of the measurement outliers and conceptually $\sigma_{o,k}^2 \gg \sigma_k^2$, and $\boldsymbol{\Delta}_k \in \left\{ \begin{bmatrix} 1 & 0 \end{bmatrix}, \quad \begin{bmatrix} 0 & 1 \end{bmatrix} \right\}$.

3.2.2 Discussion Regarding the HMM

A augmented system state vector, which consists of the system state vector and the system mode parameter, can be defined as

$$\boldsymbol{\xi}_k = \begin{bmatrix} \boldsymbol{\delta}_k^\top & \boldsymbol{x}_k^\top \end{bmatrix}^\top . \tag{3.25}$$

Then the system can be written as

$$\begin{aligned} p\left(\boldsymbol{\xi}_{k+1} \left| \boldsymbol{\xi}_k, \boldsymbol{u}_k \right.\right) &= \Pr\left(\boldsymbol{\Delta}_{k+1} = \boldsymbol{\delta}^i \left| \boldsymbol{\Delta}_k = \boldsymbol{\delta}^j \right.\right) \cdot p\left(\boldsymbol{x}_{k+1} \left| \boldsymbol{\xi}_k, \boldsymbol{u}_k \right.\right) \\ &= p_{ji,k} \cdot f_k\left(\boldsymbol{\xi}_k, \boldsymbol{u}_k\right) \qquad (3.26a) \\ p\left(\boldsymbol{y}_k \left| \boldsymbol{\xi}_k, \boldsymbol{u}_k \right.\right) &= h_k\left(\boldsymbol{\xi}_k, \boldsymbol{u}_k\right). \qquad (3.26b) \end{aligned}$$

Model (3.26) will be used in the following derivation of the PF based FD algorithm.

3.3 Understanding the Behaviour of Switching Mode HMM

3.3.1 Internal View

Figure 3.3 (a) shows the behaviour of a system with possible faults starting from known mode and states. The system is assumed to propagate in two modes at each time step, such that at each time step there are two possible paths for states to propagate. However, the system states can only propagate following a certain path over time, which is depicted in Figure 3.3 as the solid line. The dashed line is the other possible path. The observation is drawn from the states, if we do not consider the faults in the observation.

If the system mode can transfer infinite times between the two modes, the possible paths of the system mode increase exponentially. However, among the large amount of possible system mode paths, the system has only actually followed one path. As shown in Figure 3.3, the solid line represents the path that the system has followed, and all additional measurements are based on that.

Remark 3.3 *The switching mode HMM considered is a discrete-time mode that represents a discretized approximation of the real world. Therefore, a latent assumption made in this interpretation is that the system mode transitions only occur at the*

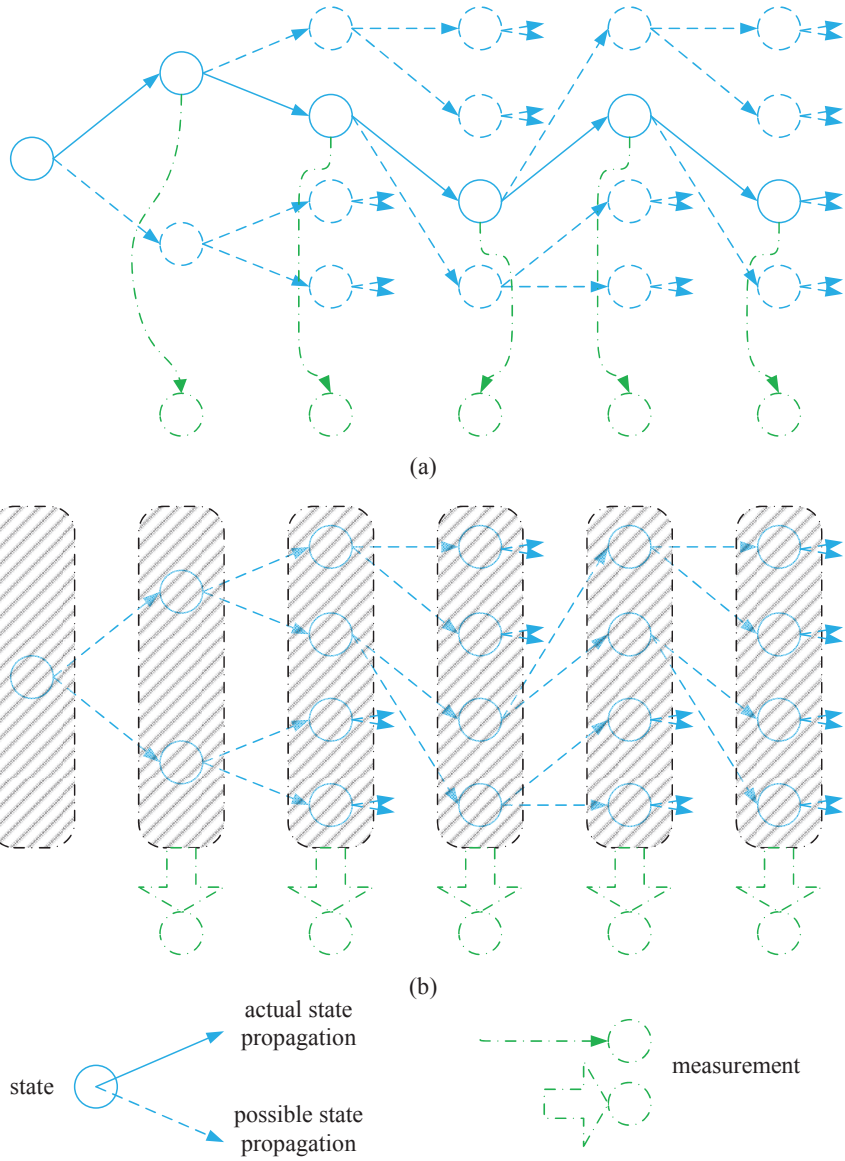

Figure 3.3: Principle of using PF for fault detection on switching mode HMM. (a) shows the actual propagation of the states depending on the system mode, and the measurement from these states. (b) shows the propagation of the states in the particle filter, where the states propagates along all possible paths, and the measurements are made from all possible conditions.

sampling instances, rather than between sampling instances, as shown in Figure 3.4. This assumption is valid when the sampling frequency is high so that shifting the time instances when the mode transitions occur would not result in significant differences

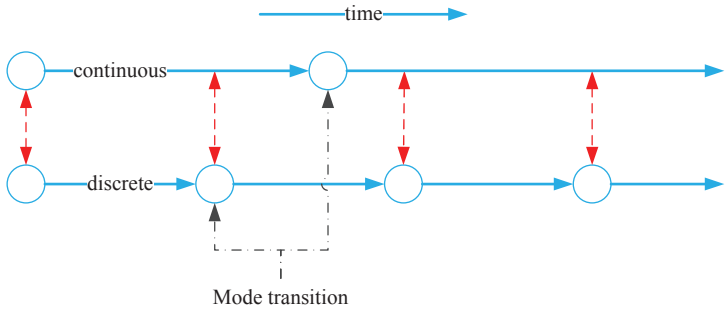

Figure 3.4: Mode transition in continuous and discrete systems.

to the propagation of the states.

3.3.2 External View

If we observe the system from outside, the system mode transitions are unknown. Figure 3.3 (b) can roughly describe the cognizance of the system as, due to the system mode, transitions are concealed to the observers; as such, it is only possible to claim that

1. all the states propagation paths are possible;
2. there is only one "true" path;
3. the observation is from the true path.

Thus, the principle of conducting FD on switching mode HMM is to identify, or estimate, the true system path given all the possible system mode transitions and the observation series. The algorithm of using PF to conduct FD on switching mode HMM is given in the following.

3.4 Algorithm of Using PF for FD on Switching Mode HMM

3.4.1 PF Algorithm

The algorithm of the PF proposed in Algorithm 4 is adapted from the SIR PF. In fact, different Monte Carlo methods, for instance those described by [Arulampalam et al., 2002] and [Chen, 2003], can be employed to solve the estimation problem in Model (3.26). Given its simplicity, the SIRPF presented here should be taken as a prototype. 3.5 shows the process of the proposed PF algorithm, and the concept of mode specified probability space. The steps of the algorithm will be reviewed in the following section.

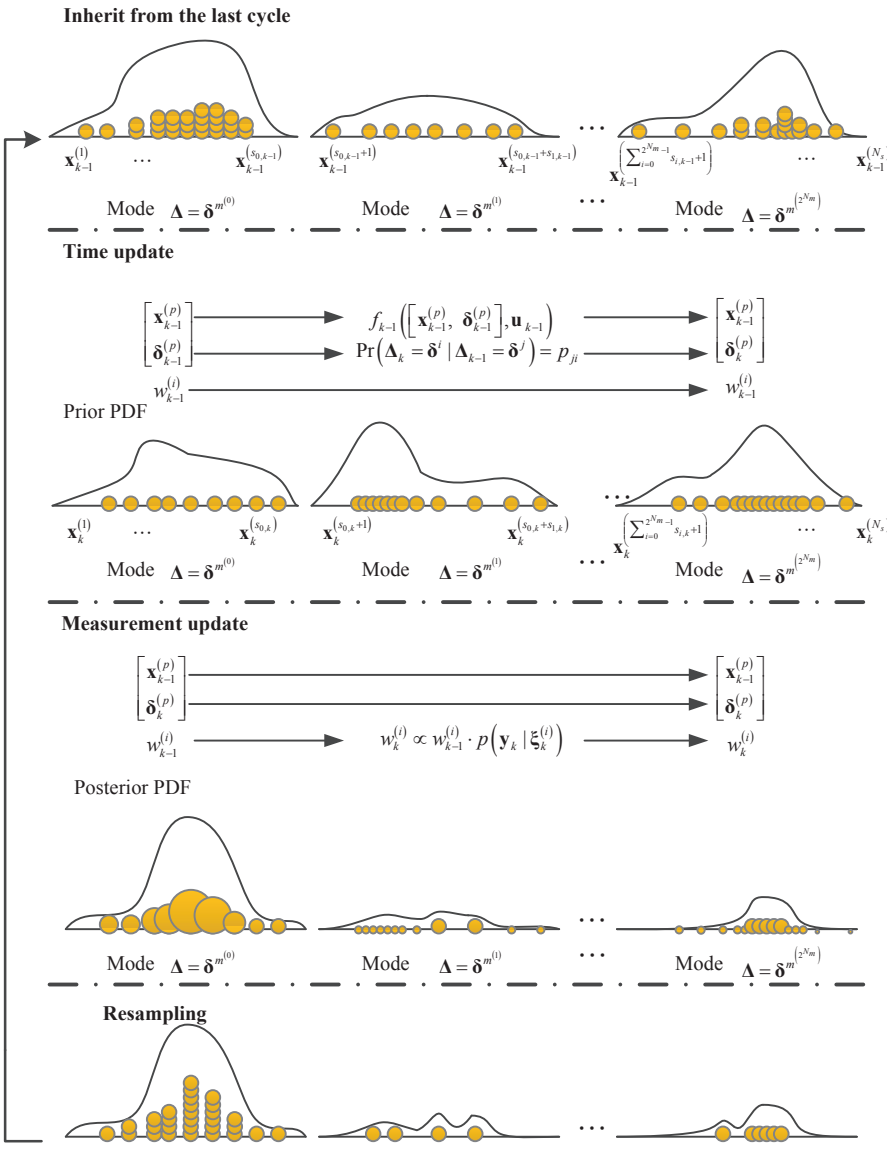

Figure 3.5: One cycle of the PF, divided into three steps by chain lines. These steps correspond to the inheritance, time update and measurement update respectively. The resampling step is not included in this figure. For the purpose of depicting the replacement of the particles in the time update steps, the particles are conceptually ordered 1–N_s from left to right in the inherit step of the figure.

Inheriting from the last cycle

At time k, the particle filter inherits $p\left(\boldsymbol{\xi}_{k-1}|\boldsymbol{y}_{1:k-1}\right)$, which is the estimation of the posterior distribution of the system extended states given the observation up to time $k-1$. A conceptual description of the posterior is presented in Figure 3.5. Because the system contains both continuous states and discrete states, the posterior density should be understood as a combination of 2^{N_m} scaled distributions subjecting to different system modes. For instance, the posterior distribution of $\boldsymbol{x}_{k-1}$ in mode $\boldsymbol{\delta}^{m^{(q)}}$ is

$$\begin{aligned} & p\left(\boldsymbol{x}_{k-1}\left|\boldsymbol{\Delta}_{k-1}=\boldsymbol{\delta}^{m^{(q)}},\boldsymbol{y}_{1:k-1}\right.\right) \\ = & \frac{p\left(\boldsymbol{x}_{k-1},\boldsymbol{\Delta}_{k-1}=\boldsymbol{\delta}^{m^{(q)}}\left|\boldsymbol{y}_{1:k-1}\right.\right)}{\Pr\left(\boldsymbol{\Delta}_{k-1}=\boldsymbol{\delta}^{m^{(q)}}\left|\boldsymbol{y}_{1:k-1}\right.\right)} \\ \approx & \frac{\sum_{i=1}^{N_s} w_{k-1}^{(i)}\cdot\rho\left(\boldsymbol{x}_{k-1}-\boldsymbol{x}_{k-1}^{(i)}\right)\cdot\rho_{\boldsymbol{\delta}^{m^{(q)}},\boldsymbol{\delta}_{k-1}^{(i)}}}{\sum_{q=0}^{2^{N_m}-1} w_{k-1}^{(i)}\cdot\rho_{\boldsymbol{\delta}^{m^{(q)}},\boldsymbol{\delta}_{k-1}^{(i)}}}, \end{aligned} \tag{3.27}$$

where N_s is the number of particles, $\rho(\cdot)$ is the Dirac function, and $\rho_{s,t}$ is the Kronecker delta function. When $q=1$, the distribution in Equation (3.27) spans the distribution $p\left(\boldsymbol{x}_{k-1}\left|\boldsymbol{\Delta}_{k-1}=\boldsymbol{\delta}^{m^{(1)}},\boldsymbol{y}_{1:k-1}\right.\right)$ to the top-left of Figure 3.5. Thereby, the posterior distribution $p\left(\boldsymbol{\xi}_{k-1}|\boldsymbol{y}_{1:k-1}\right)$ is obtained by total probability and conditional probability, such as

$$\begin{aligned} & p\left(\boldsymbol{\xi}_{k-1}|\boldsymbol{y}_{1:k-1}\right) \\ = & \sum_{q=1}^{2^{N_m}} p\left(\boldsymbol{x}_{k-1}\left|\boldsymbol{\Delta}_{k-1}=\boldsymbol{\delta}_{k-1}^{m^{(q)}},\boldsymbol{y}_{1:k-1}\right.\right) \\ \approx & \sum_{q=1}^{2^{N_m}}\left(\sum_{i=1}^{N_s} w_{k-1}^{(i)}\cdot\rho\left(\boldsymbol{x}_{k-1}-\boldsymbol{x}_{k-1}^{(i)}\right)\cdot\rho_{\boldsymbol{\delta}^{m^{(q)}},\boldsymbol{\delta}_{k-1}^{(i)}}\right). \end{aligned} \tag{3.28}$$

Time update

The purpose of the *time update* process is to obtain the a priori estimation of the states as $q\left(\boldsymbol{\xi}_k\left|\boldsymbol{\xi}_{0:k-1},\boldsymbol{y}_{1:k}\right.\right)$. In the PF context, this process is performed by drawing samples from the *importance density*. The SIR PF uses the most convenient distribution $p\left(\boldsymbol{\xi}_k\left|\boldsymbol{\xi}_{k-1}^{(i)}\right.\right)$ as the importance density.

There is dependence in the system equation (3.26a). Hence, the time update process has to be divided into two steps: the *system mode time update*, and the *system states time update*. Intuitively the system mode should be updated first, and then the system states should be updated, since they are mode dependent. That is, for each particle, it is necessary to firstly determine its mode at current time instance by propagating the system mode of a particle though the system mode transition Markov Chain in Equation (3.5), then obtain the system mode at current time step, and finally determine

the system states by drawing sample from Equation (3.6). As such, the distribution that the samples are drawn from is equivalent to

$$\begin{aligned} & p\left(\boldsymbol{\xi}_k \left| \boldsymbol{\xi}_{k-1}^{(i)}, \boldsymbol{u}_k \right.\right) \\ = \quad & p\left(\left[\boldsymbol{x}_k, \boldsymbol{\delta}_k\right]^\top \left| \left[\boldsymbol{x}_{k-1}^{(i)}, \boldsymbol{\delta}_{k-1}^{(i)}\right]^\top, \boldsymbol{u}_k \right.\right) \\ = \quad & p\left(\boldsymbol{x}_k \left| \left[\boldsymbol{x}_{k-1}^{(i)}, \boldsymbol{\delta}_{k-1}^{(i)}\right]^\top, \boldsymbol{u}_k \right.\right) \cdot \Pr\left(\boldsymbol{\delta}_k \left| \left[\boldsymbol{x}_{k-1}^{(i)}, \boldsymbol{\delta}_{k-1}^{(i)}\right]^\top, \boldsymbol{u}_k \right.\right) \\ = \quad & p\left(\boldsymbol{x}_k \left| \left[\boldsymbol{x}_{k-1}^{(i)}, \boldsymbol{\delta}_{k-1}^{(i)}\right]^\top, \boldsymbol{u}_k \right.\right) \cdot \Pr\left(\boldsymbol{\delta}_k \left| \boldsymbol{\delta}_{k-1}^{(i)}, \boldsymbol{u}_k \right.\right), \end{aligned} \tag{3.29}$$

where $\Pr\left(\boldsymbol{\delta}_k \left| \left[\boldsymbol{x}_{k-1}^{(i)}, \boldsymbol{\delta}_{k-1}^{(i)}\right]^\top, \boldsymbol{u}_k \right.\right) = \Pr\left(\boldsymbol{\delta}_k \left| \boldsymbol{\delta}_{k-1}^{(i)}, \boldsymbol{u}_k \right.\right)$, because $\boldsymbol{\delta}_k$ is independent from $\boldsymbol{x}_k$. At the end of the time update step, the we obtained new positions $\boldsymbol{\xi}_k^{(i)}$ of the particles.

Remark 3.4 *In this circumstance, it is preferable to use as many particles as possible, while keeping computational load for each particle as low as possible. Different PF algorithms are mainly distinguished by the importance densities selected, such as the extended particle filter (EPF) and the unscented particle filter (UPF) ([van der Merwe et al., 2001]). For instance, [Caron et al., 2007] recommended the use of EKF or UKF estimation as the importance density in order to reduce the sample size, and thereby reduce the computational load. However, using EKF or UKF increases the computational load for each particle; as such, the sample size has to be reduced if the total computational load is restricted. In our case, because the proposed algorithm simulates the system mode transition by propagating the particles through the Markov chain, a certain amount of particles are necessary to adequately capture the behaviour of the system mode. This is against the principle of EPF or UPF. Hence, the author recommends the use of a simple algorithm, such as SIR PF, to reduce the computation for each particle; however, they should be employed in combination with a large sample size.*

Measurement update

At this step, the particle weights will be updated according to the observation at the current time instance k. The weights are updated following the Baye's law that when one particle's prior $\boldsymbol{\xi}_k^{(i)}$ is supported by the observation, the weight of the particle should increase, and vice versa.

Given the observation at current time as $\boldsymbol{y}_k$, and chosen the importance density $p\left(\boldsymbol{\xi}_k \left| \boldsymbol{\xi}_{k-1}^{(i)} \right.\right)$, it yields

$$w_k^{(i)} \propto w_{k-1}^{(i)} \cdot p\left(\boldsymbol{y}_k \left| \boldsymbol{\xi}_k^{(i)}, \boldsymbol{u}_k \right.\right), \tag{3.30}$$

where $p\left(\boldsymbol{y}_k \left| \boldsymbol{\xi}_k^{(i)}, \boldsymbol{u}_k \right.\right)$ is defined by (3.26b).

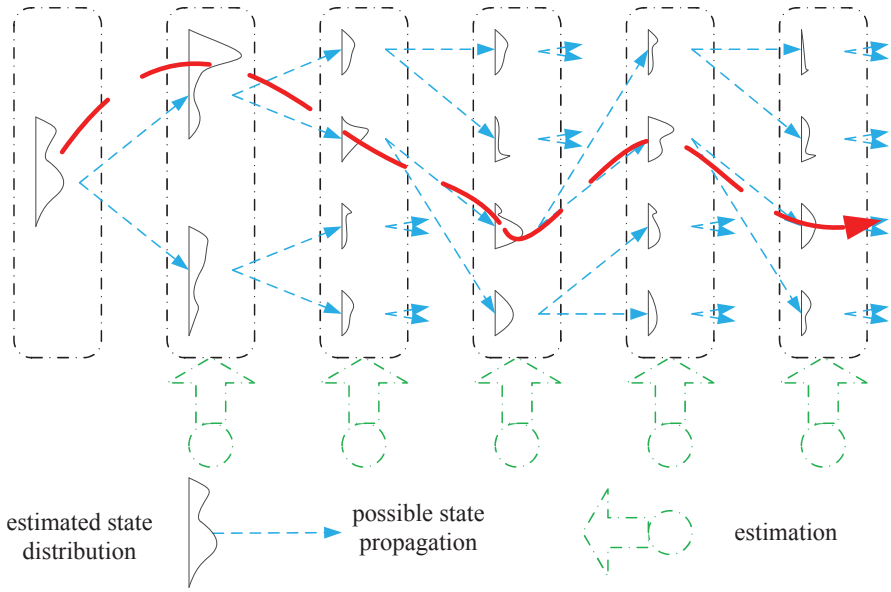

Figure 3.6: The estimation of the PF on switching mode HMM. The distributions in this figure are not realistic.

Resampling

It is common to employ a resample step in the PF algorithm to counteract the degeneracy, for example, as per the resample methods proposed in *multinomial resampling* in [Smith and Gelfand, 1992], *residual resampling* in [Liu, 1996], and *systematic resampling* in [Carpenter et al., 1999]. These methods are suitable for use in the switching mode HMM circumstance.

Remark 3.5 *Regarding the resampling step, we recommend using an adaptive resampling method in Section 3.5.1. The new method is suitable for PF working in switching mode condition, and is good at handling the case that some system mode has little marginal probability mass. However, the drawback is the new method results in a variable sample size.*

3.4.2 Fault Diagnosis Algorithm

It is concluded that the system is working in mode $\boldsymbol{\delta}^{m^{(q)}}$, when the mode $\boldsymbol{\Delta}_k = \boldsymbol{\delta}^{m^{(q)}}$ has the largest marginal probability mass, such as

$$\max_i \Pr\left(\boldsymbol{\Delta}_k = \boldsymbol{\delta}^{m^{(i)}} | \boldsymbol{y}_{1:k}\right) = q, \tag{3.31}$$

input : $N_{s,k-1}$ particles from last time step $\left\{\boldsymbol{x}_{k-1}^{(i)},\ w_{k-1}^{(i)}\right\}$, which span the posterior estimation of the state at time $k-1$

$$\begin{aligned} & p\left(\boldsymbol{\xi}_{k-1}|\boldsymbol{y}_{1:k-1}\right) \\ \approx & \sum_{q=1}^{2^{N_m}}\left(\sum_{i=1}^{N_{s,k-1}} w_{k-1}^{(i)}\cdot\rho\left(\boldsymbol{x}_{k-1}-\boldsymbol{x}_{k-1}^{(i)}\right)\cdot\rho_{\boldsymbol{\delta}^{m^{(q)}},\boldsymbol{\delta}_{k-1}^{(i)}}\right). \end{aligned}$$

output: $N_{s,k}$ new particles $\left\{\boldsymbol{x}_{k}^{(i)},\ w_{k}^{(i)}\right\}$, which span the posterior estimation of the state at time k

$$\begin{aligned} & p\left(\boldsymbol{\xi}_{k}|\boldsymbol{y}_{1:k}\right) \\ \approx & \sum_{q=1}^{2^{N_m}}\left(\sum_{i=1}^{N_{s,k}} w_{k}^{(i)}\cdot\rho\left(\boldsymbol{x}_{k}-\boldsymbol{x}_{k}^{(i)}\right)\cdot\rho_{\boldsymbol{\delta}^{m^{(q)}},\boldsymbol{\delta}_{k}^{(i)}}\right). \end{aligned}$$

//for each particle
for $i \leftarrow 1$ **to** $N_{s,k-1}$ **do**
// *Time update:* Drawing samples from the proposal distribution.

$$\begin{aligned} \boldsymbol{\xi}_k^{(i)} \leftarrow \boldsymbol{\xi}_k^{(i)} &\sim p\left(\boldsymbol{\xi}_k\left|\boldsymbol{\xi}_{k-1}^{(i)},\boldsymbol{u}_k\right.\right) \\ &= p\left(\boldsymbol{x}_k\left|\left[\boldsymbol{x}_{k-1}^{(i)},\boldsymbol{\delta}_{k-1}^{(i)}\right]^{\top},\boldsymbol{u}_k\right.\right)\cdot\Pr\left(\boldsymbol{\delta}_k\left|\boldsymbol{\delta}_{k-1}^{(i)},\boldsymbol{u}_k\right.\right) \end{aligned}$$

// *Measurement update:*
$w_k^{(i)} \leftarrow w_{k-1}^{(i)} p\left(\boldsymbol{y}_k\left|\boldsymbol{x}_k^{(i)},\boldsymbol{u}_k\right.\right)$
end
// Normalize the weights
$w_k^{(i)} \propto w_{k-1}^{(i)}\cdot p\left(\boldsymbol{y}_k\left|\boldsymbol{\xi}_k^{(i)},\boldsymbol{u}_k\right.\right)$
// *Resampling:* follows Algorithm 2 or Algorithm 5.
$w_k^{(i)}, i\in\{1,N_{s,k}\} \leftarrow \mathrm{RESAMPLE}\left(w_k^{(i)}\right), i\in\{1,N_{s,k-1}\}$

Algorithm 4: SIRPF for FD on switching mode HMM.

where $i \in \left\{0,\ldots,2^{N_m}-1\right\}$. This mode $\boldsymbol{\delta}^{m^{(q)}}$ is named *significant mode*. The probability mass is obtained by marginalizing the distribution $p\left(\boldsymbol{\xi}_k|\boldsymbol{y}_{1:k}\right)$, such as

$$\Pr\left(\boldsymbol{\Delta}_k=\boldsymbol{\delta}^{m^{(q)}}|\boldsymbol{y}_{1:k}\right)\approx\sum_{i=1}^{N_{s,k}} w_k^{(j)}\rho_{\boldsymbol{\delta}^{m^{(q)}},\boldsymbol{\delta}_k^{(i)}}. \tag{3.32}$$

Then the fault detection is performed intuitively: once the observed significant mode is different from the fault-free mode, the fault is detected. The estimated system mode at this time gives the failure mode as a fault isolation result. In addition, the size of

the fault can be obtained by the state estimation of the PF.

There can be alternative ways to deduce the failure mode. One may define threshold $H_{\boldsymbol{\delta}^{m^{(q)}}} \in (0,1)$ for each system mode $\boldsymbol{\delta}^{m^{(q)}},\ q \in \left\{1,\ldots,2^{N_m}-1\right\}$. Once the estimated marginal mass $\Pr\left(\boldsymbol{\Delta}_k = \boldsymbol{\delta}^{m^{(q)}} |\boldsymbol{y}_{1:k}\right)$ of a mode $\boldsymbol{\delta}^{m^{(q)}}$ exceeds the threshold $H_{\boldsymbol{\delta}^{m^{(q)}}}$ is captured, the system should be considered to have failed in the corresponding failure mode. Although this method requires designing $2^{N_m}-1$ thresholds, it allows the possibility to tune the sensitivity of the detector; for instance, tuning according to the requirements of mean-time-to-detection and false-alarm-rate.

The so-called CUSUM algorithm motivates another way; e.g. [Blanke et al., 2006]. One may take the time cumulation of the marginal mass of the modes as indicators, and detect the faults by judging the behaviour of the indicators. This method is especially practical when the mode has little "into" probability in the mode transition Markov chain.

3.5 Relevant Topics

3.5.1 Adaptive Resampling Algorithm

Vanishing of the particles in rare modes

If the sample size of the PF were infinite, the estimation of the extended states would be accurate and precise. The accuracy and precision are obtained if there are always sufficient particles in each system mode.

However, the sample size cannot be infinite. With the exception of the suboptimal estimation performance, this results in some modes exhibiting very small marginalized probability so that the particles in these mode will unfortunately vanish after the resampling. For instance, a system has two modes $\boldsymbol{\delta}^1$ and $\boldsymbol{\delta}^2$, and the transition probabilities are $\Pr_{11} = 0.9999$, $\Pr_{12} = 0.0001$, $\Pr_{21} = 1$, and $\Pr_{22} = 0$. If the sample size of the PF working on this system is 100, the particles representing the mode $\boldsymbol{\delta}^2$ are probably not able to "survive" the resampling if the mode $\boldsymbol{\delta}^2$ is not very strongly supported by the observation. When particles in a system mode vanish, the information carried by these particles is lost. This phenomenon deteriorates the FD performance when trying to capture a slowly developing failure mode that rarely occurs.

Although this problem is induced by the insufficiency of particles in PF, it is not suitable for solving the problem by increasing the sample size. One may consider in the system (3.26), assuming that one mode has the marginal mass $\Pr\left(\Delta_k^{f^{(q)}} = 1\right) = 0.0001$ $(q \in \{1,\ldots,N_m\})$, when this mode rarely occurs in the system. It is common to use more than 100 particles to accurately describe the distribution, which is representative of the distribution as we found out in Section 2.4.5. So, if using 100 particles, which is a very low value, representing the density $p\left(\boldsymbol{x}_k \left| \Delta_k^{f^{(q)}} = 1\right.\right)$, in

average, $\frac{100}{0.0001} = 10^7$ particles in total are needed to describe the whole density $p(\boldsymbol{\xi}_k|\boldsymbol{y}_{1:k})$. This large amount of particles is computationally unbearable.

An alternative method involves manufacturing the resampling algorithm so that the it is able to generate suitable amounts of particles for each system mode and counteract the vanishing problem, thereby restraining the information loss. Because the probability of a fault occurring in a system is generally low, the particles in these modes will have very light weights. With a standard resampling method, these light-weighted particles are unlikely to survive. Thus, the suitable amounts of particles regenerated by the resampling algorithm should entail that the computational cost is not too high, and the particles from these system modes, which are unlikely to occur, are still adequately representative of the conditional density of the states in these system modes.

For this reason, an adaptive resampling method can be applied that results in sufficient samples for the modes with small marginal probability mass and, in the meanwhile, restricts the total numbers of particles. It is essential that this modified resampling algorithm is able to adaptively determine the number of samples in each system mode in accordance to their significance, and allow a compromise between the computational complexity and the estimation performance.

The adaptive resampling algorithm

At first, define $\breve{N}_s$ as the minimum number of particles required for representing a system mode; e.g., 20 for a system with high sampling frequency, and 100 for system with relatively low sampling frequency. This will result in at least $\breve{N}_s N_m$ particles in the PF. As such, if there are too many modes in the system, a large amount of particles cannot be avoided.

Then, consider those system modes with significant marginal probability mass. Define $\tilde{N}_s$ as the number of particles suitable for the estimation with respect to the estimation accuracy and precision, and that $\breve{N}_s(N_m - 1) + \tilde{N}_s$ should be an acceptable sample size for computing. Then assign the $\tilde{N}_s$ particles to each system mode according to their marginal probability mass, such as

$$N_{s,k}^{(\boldsymbol{\delta}^{(q)})} = \left\lceil \Pr\left(\boldsymbol{\Delta}_k = \boldsymbol{\delta}^{(q)}|\boldsymbol{y}_{1:k}\right) \cdot \tilde{N}_s \right\rceil, \tag{3.33}$$

where $N_{s,k}^{(\boldsymbol{\delta}^{(q)})}$ is the number of particles required in mode $\boldsymbol{\delta}^{(q)}$ in the resampling step, and $\lceil a \rceil$ is the minimum integer which is larger than a. For any $N_{s,k}^{(\boldsymbol{\delta}^{(q)})} \leq \breve{N}_s$, compulsorily assign $\breve{N}_s$ to $N_{s,k}^{(\boldsymbol{\delta}^{(q)})}$.

After assigning the number of samples $N_{s,k}^{(\boldsymbol{\delta}^{(q)})}$, resampling can be performed mode-specifically with any standard method. Resulting from the adaptive resampling, it obtains a group of particles with uneven weights $\Pr(\boldsymbol{\Delta}_k = \boldsymbol{\delta}^{(q)}|\boldsymbol{y}_{1:k})/N_{s,k}^{(\boldsymbol{\delta}^{(q)})}$, depending on the modes $\boldsymbol{\delta}^{(q)}$ that the particles belong to. This algorithm is summarized in Algorithm 5.

input : particles $\boldsymbol{x}_{\text{in}}^{(i)}$, weights $w_{\text{in}}^{(i)}$, $i = 1, \ldots, N_{s,\text{in}}$.
output: new particles $\boldsymbol{x}_{\text{out}}^{(i)}$, new weights $w_{\text{out}}^{(i)}$, $i = 1, \ldots, N_{s,\text{out}}$.

for $q = 1$ **to** N_m **do**
  $N_{s,k}^{(\boldsymbol{\delta}^{(q)})} \leftarrow \left\lceil \Pr\left(\boldsymbol{\Delta}_k = \boldsymbol{\delta}^{(q)} | \boldsymbol{y}_{1:k}\right) \cdot \tilde{N}_s \right\rceil$
  if $N_{s,k}^{(\boldsymbol{\delta}^{(q)})} \leq \breve{N}_s$ **then**
    $N_{s,k}^{(\boldsymbol{\delta}^{(q)})} \leftarrow \breve{N}_s$
  end
  Construct CDF from weights $w_{\text{in}}^{(i)}$ whose corresponding particle $\boldsymbol{x}_{\text{in}}$ is in mode $\boldsymbol{\delta}^{(q)}$, such that
    $c_1 \leftarrow 0$;
    $c_i \leftarrow c_{i-1} + w^i$;
  $i \leftarrow 1$;
  $u_1 \sim \text{U}\left(0, 1/N_{s,k}^{(\boldsymbol{\delta}^{(q)})}\right)$;
  for $j = 1$ **to** $N_{s,k}^{(\boldsymbol{\delta}^{(q)})}$ **do**
    $u_j \leftarrow u_1 + (j-1)/N_{s,k}^{(\boldsymbol{\delta}^{(q)})}$;
    while $u_j > c_i$ **do**
      $i \leftarrow i + 1$
    end
    $\boldsymbol{x}_{\text{out}}^{(j,\boldsymbol{\delta}^{(q)})} \leftarrow \boldsymbol{x}_{\text{in}}^{(i)}$;
    $w_{\text{out}}^{(j,\boldsymbol{\delta}^{(q)})} \leftarrow \Pr\left(\boldsymbol{\Delta}_k = \boldsymbol{\delta}^{(q)} | \boldsymbol{y}_{1:k}\right)/N_{s,k}^{(\boldsymbol{\delta}^{(q)})}$;
  end
end

Algorithm 5: Adaptive resampling.

It then can be used to derive the lower boundary of the estimated effective sample size as

$$\begin{aligned} \hat{N}_{eff} &= \frac{1}{\sum_{i=1}^{N_{s,k}} \left(w_k^{(i)}\right)^2} \\ &= \frac{1}{\sum_{p=1}^{2^{N_m}} \left(\Pr\left(\boldsymbol{\Delta}_k = \boldsymbol{\delta}^{(p)} | \boldsymbol{y}_{1:k}\right)^2 / N_{s,\boldsymbol{\delta}^{(p)},k}\right)}, \end{aligned} \tag{3.34}$$

where $N_{s,k} = \sum_{p=1}^{2^{N_m}} N_{s,\boldsymbol{\delta}^{(p)},k}$ is the number of particles at time k. Since $N_{s,\boldsymbol{\delta}^{(p)},k} \geq \Pr\left(\boldsymbol{\Delta}_k = \boldsymbol{\delta}^{(p)} | \boldsymbol{y}_{1:k}\right) \cdot \tilde{N}_s$,

$$\frac{\Pr\left(\boldsymbol{\Delta}_k = \boldsymbol{\delta}^{(p)} | \boldsymbol{y}_{1:k}\right)^2}{N_{s,\boldsymbol{\delta}^{(p)},k}} \leq \frac{\Pr\left(\boldsymbol{\Delta}_k = \boldsymbol{\delta}^{(p)} | \boldsymbol{y}_{1:k}\right)}{\tilde{N}_s}, \tag{3.35}$$

for each $\boldsymbol{\delta}^{(p)}$. Thereby,

$$\sum_{p=1}^{2^{N_m}} \frac{\Pr\left(\boldsymbol{\Delta}_k = \boldsymbol{\delta}^{(p)} | \boldsymbol{y}_{1:k}\right)^2}{N_{s,\boldsymbol{\delta}^{(p)},k}} \leq \frac{1}{\tilde{N}_s} \sum_{p=1}^{2^{N_m}} \Pr\left(\boldsymbol{\Delta}_k = \boldsymbol{\delta}^{(p)} | \boldsymbol{y}_{1:k}\right) \leq \frac{1}{\tilde{N}_s}. \tag{3.36}$$

Substituting this into the above Equation 3.34, yields

$$\hat{N}_{eff} \geq \tilde{N}_s. \tag{3.37}$$

Thus, the proposed adaptive resampling method can keep the effective sample size larger than or equal to $\tilde{N}_s$.

The least efficient case occurs when one of the modes has the posterior probability 1. For instance, if there are $N_m = 24$ modes in the system, and setting $\tilde{N}_s = 1000$, $\breve{N}_s = 100$. In the worst case, we still have $\breve{N}_s (N_m - 1) + \tilde{N}_s$ particles in the system; however, $\breve{N}_s (N_m - 1)$ of them have null weights. This makes the effective sample size $\hat{N}_{eff} = \tilde{N}_s = 1000$, and computation was wasted on the other $\breve{N}_s (N_m - 1) = 2300$ particles.

3.5.2 Rao-Blackwellization

Rao-Blackwellization, which is based on the Rao-Blackwell theorem [Lehmann and Casella, 1998], is a marginalization technique that can be applied to PFs to make the most of the advantage of the optimal linear filtering method (e.g., KF), and thereby improve the estimation performance ([Doucet et al., 2000a] [Andrieu and Doucet, 2002] [Schon et al., 2005]). These studies used Rao-Blackwellization to separate the linear part of a system from the nonlinear part, before applying a Kalman filtering to estimate the linear part and apply particle filter to the nonlinear part.

Rao-Blackwellization can be applied in the proposed PF algorithm. To give a brief example, if, in Model (3.2), the mappings $f(\cdot, \boldsymbol{\delta})$ and $h(\cdot, \boldsymbol{\delta})$ are linear and result in normal distributions, under each mode, the states estimation can be solved optimally by KF. Thus, in the time update step, we still firstly propagate the system mode through the Markov chain obtaining $\boldsymbol{\delta}_k^{(i)}$. Then we can perform the Kalman filter on the linear part of the system, and obtain the estimation of $\boldsymbol{x}_k$, as

$$p\left(\boldsymbol{x}_k^{(i)} \middle| \boldsymbol{y}_k, \boldsymbol{x}_{k-1}^{(i)}, \boldsymbol{u}_k, \boldsymbol{\delta}_k^{(i)}\right) = \mathcal{N}\left(\boldsymbol{\mu}_k^{(i)}, \left(\boldsymbol{\sigma}_k^{(i)}\right)^2\right), \tag{3.38}$$

where $\boldsymbol{\mu}_k^{(i)}$ and $\left(\boldsymbol{\sigma}_k^{(i)}\right)^2$ are the estimated mean and variance from KF, $\mathcal{N}(\cdot)$ denotes normal distribution.

Finally, we can perform the particle filter measurement update to obtain new weights based on $\boldsymbol{y}_k$ and also the estimated $\boldsymbol{\mu}_k^{(i)}$ and $\left(\boldsymbol{\sigma}_k^2\right)^{(i)}$, as

$$w_k^{(i)} \propto w_{k-1}^{(i)} p\left(\boldsymbol{y}_k \middle| \boldsymbol{\mu}_k^{(i)}, \left(\boldsymbol{\sigma}_k^{(i)}\right)^2, \boldsymbol{u}_k, \boldsymbol{\delta}_k^{(i)}\right). \tag{3.39}$$

Remark 3.6 *The Kalman filter is not the only filter that can be used in the Rao-Blackwellization approach. In the event that parts of the system exhibit nonlinearity that is not significant, EKF or UKF can be applied to these parts in a similar way. For instance, as reported in [Caron et al., 2007], the nonlinear state evolution is covered by EKF or UKF, and only left the mode switching of the sensors to handle by the PF. However, as discussed in [Karlsson et al., 2005], the computational complexity should be examined carefully.*

3.5.3 Mode Ambiguity

It is possible that two or more system modes become somehow significant at the same time. This is raised by the ambiguity of the system and observation mappings in different modes, such as the mappings $f_k\left(\cdot, \boldsymbol{\delta}^{(p)}\right)$ and $h_k\left(\cdot, \boldsymbol{\delta}^{(p)}\right)$ overlaps in a large part with another mappings pairs $f_k\left(\cdot, \boldsymbol{\delta}^{(q)}\right)$ and $h_k\left(\cdot, \boldsymbol{\delta}^{(q)}\right)$ in a different system mode.

Example 3.6 *Considering we have an observation series which can be a zero-mean Gaussian white noise, or a Gaussian noise with mean at θ, where $\theta \in [-10, 10]$. We can model the system as*

$$P\left(y_k\right) = \boldsymbol{\Delta}_k \begin{bmatrix} \mathcal{N}\left(0, \sigma^2\right) \\ \mathcal{N}\left(\theta, \sigma^2\right) \end{bmatrix}, \tag{3.40}$$

where σ^2 is the measurement variance, and $\theta \sim \mathcal{U}\left(\theta_{\inf}, \theta_{\sup}\right)$. Then the CDF of Y if θ is unknown, is given by

$$\begin{aligned} p\left(y_k \left| \boldsymbol{\Delta}_k = \begin{bmatrix} 0 & 1 \end{bmatrix}\right.\right) &= \int_{-\infty}^{+\infty} f_Y\left(y - \tau \left| \theta \right.\right) f_\Theta\left(\theta\right) d\tau \\ &= \frac{1}{\theta_{\sup} - \theta_{\inf}} \int_{\tau \in [\theta_{\inf}, \theta_{\sup}]} \gamma_{N(0,\sigma^2)}\left(y_k\right) d\tau \\ &= \frac{1}{\theta_{\sup} - \theta_{\inf}} \left\{\Gamma_{N(0,\sigma^2)}\left(y - \theta_{\inf}\right) - \Gamma_{N(0,\sigma^2)}\left(y - \theta_{\sup}\right)\right\}, \end{aligned} \tag{3.41}$$

where $\gamma_{N(0,\sigma^2)}\left(\cdot\right)$, and $\Gamma_{N(0,\sigma^2)}\left(\cdot\right)$ are the PDF and CDF of Gaussian variable with zero mean and variance σ^2, respectively. Let's assume $\theta_{\sup} = 10$, $\theta_{\inf} = -10$, and $\sigma^2 = 1$ yields the prior densities shown in Figure 3.7. In this case, if getting a measurement locates in a small range around zero, for instance $[-2, 2]$, it supports both of the two system modes, and thereby the PF delivers an ambiguous result.

Better modeling can reduce this ambiguity. The main idea is to reduce the overlapping of the priors distributions of each system mode. In the previous example, it can be more accurate and reasonable to use the density

$$f_\Theta\left(\theta\right) = \begin{cases} \frac{1}{\theta_{\sup} - \theta_{\inf} - 2\sigma} & \theta \in [\theta_{\inf}, -\sigma] \cup [\sigma, \theta_{\sup}] \\ 0 & \textit{otherwise} \end{cases}, \tag{3.42}$$

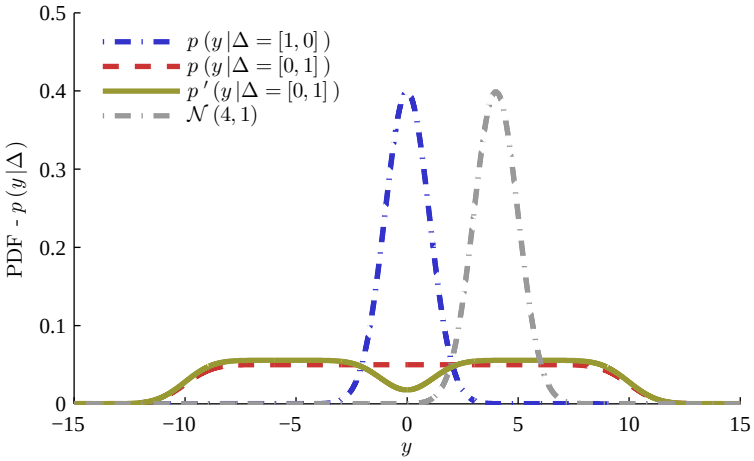

Figure 3.7: The probability densities of the measurement in two system modes, respectively.

instead of $\theta \sim U(\theta_{\inf}, \theta_{\sup})$ *to represents the randomness of the DC component. Then it yields a new prior of the PDF of the measurement that*

$$\begin{aligned} P'\left(y_k \left| \delta_k = \Delta^2 \right.\right) &= \frac{1}{\theta_{\sup} - \theta_{\inf} - 2\sigma} \\ &\cdot \left\{ \phi_{N(0,\sigma^2)}(y - \theta_{\inf}) - \phi_{N(0,\sigma^2)}(y + \sigma) \right. \\ &\left. + \phi_{N(0,\sigma^2)}(y - \sigma) - \phi_{N(0,\sigma^2)}(y - \theta_{\sup}) \right\}. \end{aligned} \quad (3.43)$$

These modified densities are also shown in Figure 3.7. Although there is still an overlap between the densities, the situation is much better than before.

Thus, one possible method of minimizing the ambiguity involves reducing the overlap of the densities. This is a modelling problem and requires a good inspection of the system and its failure modes. The Jensen-Shannon divergence can be evaluated numerically; e.g., as per the work of [Nielsen, 2010] and [Fuglede and Topsoe, 2004], to measure the difference. This yields

$$\mathrm{JSD}\left(p\left(y \left| \boldsymbol{\Delta} = \begin{bmatrix} 1 & 0 \end{bmatrix}\right.\right) \middle\| p\left(y \left| \boldsymbol{\Delta} = \begin{bmatrix} 0 & 1 \end{bmatrix}\right.\right)\right) \approx 16.57, \quad (3.44)$$

$$\mathrm{JSD}\left(p\left(y \left| \boldsymbol{\Delta} = \begin{bmatrix} 1 & 0 \end{bmatrix}\right.\right) \middle\| p'\left(y \left| \boldsymbol{\Delta} = \begin{bmatrix} 0 & 1 \end{bmatrix}\right.\right)\right) \approx 19.11. \quad (3.45)$$

As a comparison, the Jensen-Shannon divergence between $p\left(y \left| \boldsymbol{\Delta} = \begin{bmatrix} 1 & 0 \end{bmatrix}\right.\right)$ *and* $\mathcal{N}(4,1)$ *is* 16.

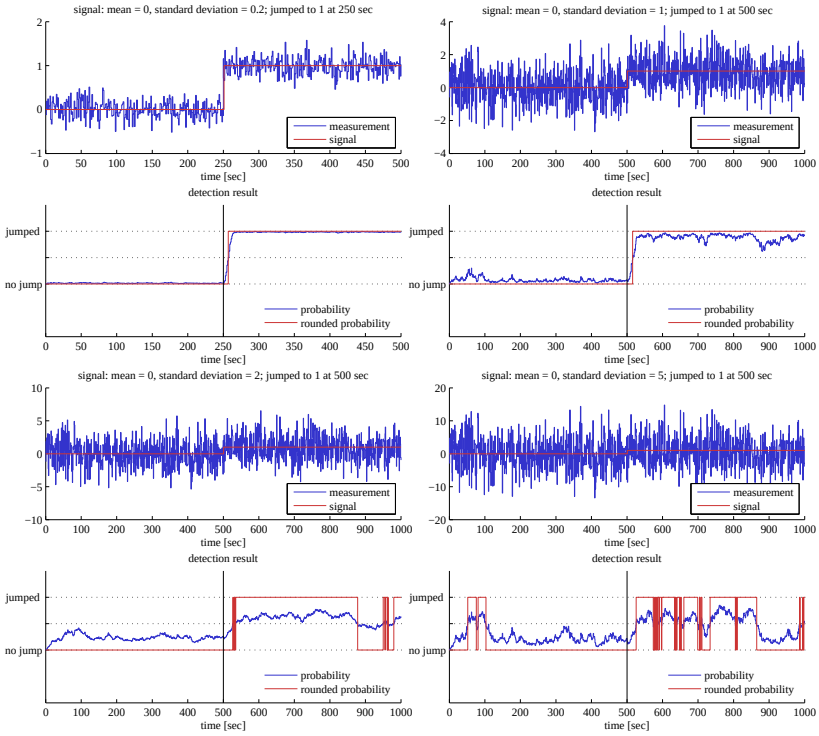

Figure 3.8: Detection of one-time changing mean model.

3.6 Study Cases: Examples of Diagnosis for Basic Anomalies

In this section, the PFFD algorithm is applied to diagnose the anomalies identified in Section 3.2.1. In all the examples in this section, the PFs run with 1,000 particles.

3.6.1 Changing DC Level in White Noise

One-time Changing Mean Model

In this example, we use PF to detect a change of a signal (following the model in Example 3.1), which is embedded in white Gaussian noise. The size of the change is 1, but we assume four different standard deviation of the noise in each cases.

Figure 3.8 indicated the detection result of a size 1 jump embedded in white Gaussian noise of different variance. Two axes in a quarter is a group that depicts the signal and diagnosis, respectively. The signal in the four groups adopts measurement noise with standard deviation 0.2, 1, 2, and 5, respectively.

The model running in the particle filter follows Equation (3.12). In the first two cases, where the signal-to-noise rate is high, the time-to-detection[3] is short, and the detection result is uniform. This means that the rounded probability always indicates "jumped" after the jump is detected. Hence, in these cases, the PFFD algorithm can effectively detect the change. When the standard deviation of the measurement noise is 2, the detection result is nonuniform, such that when the jumped measurement signal behaves close to the zero-mean condition (around 900[sec]), the PFFD indicates "fault-free." This phenomenon is significant in the fourth case, where the signal-to-noise rate is very low. Compared with the first and second cases, the time-to-detection in this case is longer, the diagnosis is nonuniform, and a false alarm occurs.

Segmentation in changing mean model

The result of diagnosis of the segmentation in changing mean model is shown in Figure 3.9, where the DC level embedded in the white noise is 0, 0, 2, 4, 10, and 0 in each 200 second period, as shown in sub-figure (a). The standard deviation of the measurement noise is 1, as depicted by the blue curve in Figure 3.7, where the prior probability of the DC level is depicted by the green curve in Figure 3.7.

The model runs in the particle filter follows Equation (3.1). Figure 3.9(a) shows the DC signal, the measurement signal, and the estimated DC levels. Because the transition probability is designed in such a way that the estimation "sticky" to the previous estimation, it takes some time for the estimation to adjust to a new DC level after the DC level changes. The further the DC level is away from 0, the more precise and accurate the estimation is; for instance, the DC level at 10 spans from $1000\,\mathrm{sec}$ to $1200\,\mathrm{sec}$. This can also be seen in Figure 3.9(b), which indicates most of the particles work in non-zero mean mode, thus providing a better estimation. Moreover, as per the last example, the change of DC level is detected as long as the sample size of the particles of the non-zero-mean mode exceeds the sample size of the particles of the zero-mean mode. Figure 3.9(c) shows the time sequence of the posterior distributions.

3.6.2 Signal Drifting

The result of the diagnosis of signal drifting is shown in Figure 3.10. The signal in drifting is shown in Figure 3.10(a) and two estimations of the signal from PF and a noise driven KF, respectively. Their estimation error is also shown together. The estimations of the drifting speed are shown in Figure 3.10(b), and the estimated posterior distribution of the drifting speed is shown in Figure 3.10(d). The sequence of the sample size is shown in 3.10(c).

The model runs in the particle filter follows Equation (3.18). There is no significant difference between the signal tracking performance of the PF and KF in general. The PF performs estimates the drifting speed better because it responses faster to drifting speed changes, and the estimation is more stable in the stationary segments of the drifting speed. The model used in the PF is Equation (3.18), hence in the time range

[3]Time-to -detect is defined as the time between a change or a failure happens and the it is detected.

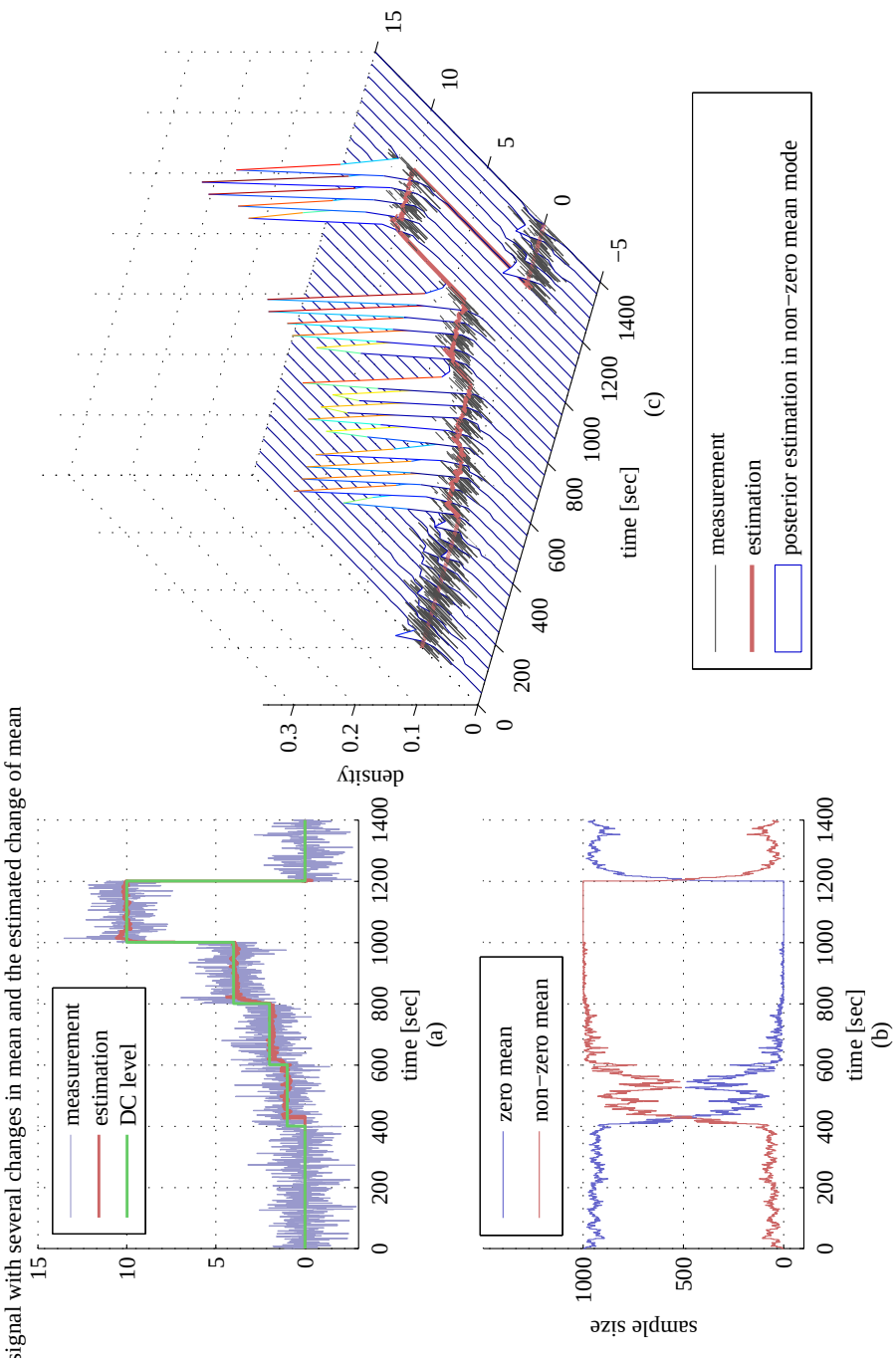

Figure 3.9: Segmentation in changing mean model.

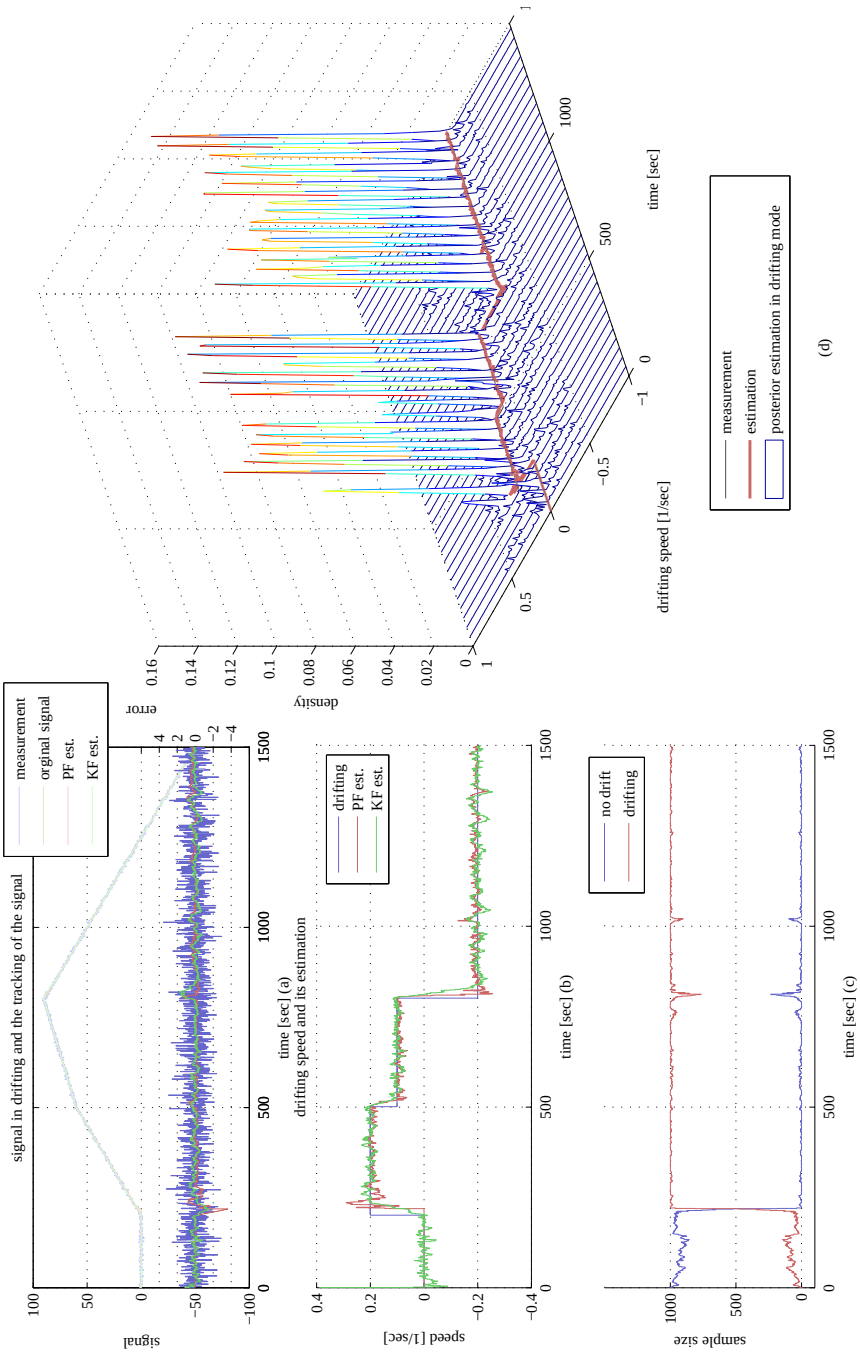

Figure 3.10: Detection and estimation of signal drifting.

from $0\,\mathrm{sec}$ to $200\,\mathrm{sec}$, when the sample size of the no-drifting mode dominates, the estimation of the drifting speed is identically 0. The reason the dynamic of the PF estimation is faster than the KF estimation is due to the fact that the prior density $p\left(d^0\right)$ is set to be uniform distribution on $\begin{bmatrix}-1 & 1\end{bmatrix}$. On the other hand, in the station segments of the drifting speed, the PF estimation of the drifting speed exhibits less variance than the KF estimation due to the fact that the variance of the driving noise of the PF is less than the KF. So by separating the system into two modes, the PF can switch between different dynamics.

Some small peeks around 0 can be observed in Figure 3.10(d) in the time range from 0 sec to 200 sec. These are due to the samples transferring from non-drifting mode to drifting mode. The sample size indicates the drifting in the signal correctly, with the exception of the c.a., 15 sec after the first change in drifting speed. This 15 sec delay is die to the fact that it takes time for the particles to transfer from non-drifting mode to drifting mode.

3.6.3 Missing Measurement

An illustrative example of a missing measurement is shown in Figure 3.11, where the signal drifting model in Example 3.6.2 is used. However, instead of a uniform sampled measurement series, the measurement in this case study is modelled as non-uniformly sampled measurement, and may be lost from time to time. The measurement is performed every 3, 4 or 5 seconds, and the three gaps can be observed in the figure.

The position and speed estimation of the particle filter is good in general, even when the measurement is lost. This is due to the fact that the speed happens to be constant when the position measurement is lost. However, the variance of the position and speed estimation increases during the measurement missing as 1σ upper and lower boundaries parts from each other, due to the lack of new information that can be used to update the estimation. In this condition, only the system time update runs in each time step, and system noise accumulates. This increases the variance of the estimation.

This phenomenon can be observed more clearly in Figure 3.12, where the measurement in this case is non-uniformly sampled. The sampling time subjects to a uniform distribution on $\begin{bmatrix}180 & 220\end{bmatrix}$. After the sudden change of the speed, the estimation by the particle filter cannot track the true state immediately, due to lack of measurement (information). However, after about two measurements the particle filter adjusts itself to the true state, and results in a relatively good estimation.

Comparing Figure 3.11 with 3.12, one can find that the variance of the position estimation is lower when the update rate of the measurement is high, since it depends on the information obtained from the observation. And thereby, the position estimation in the first case is much smoother.

Figure 3.11 reveals a dramatic increase in the variance of the speed estimation after the sudden change in speed; e.g., after 200 sec and 800 sec. This is because, as in Example 3.6.2, the "speed" state in the particle filter may adopt a "jump" behaviour instead of a continuous dynamic. Once, the "jump" occurs in the particle filter to

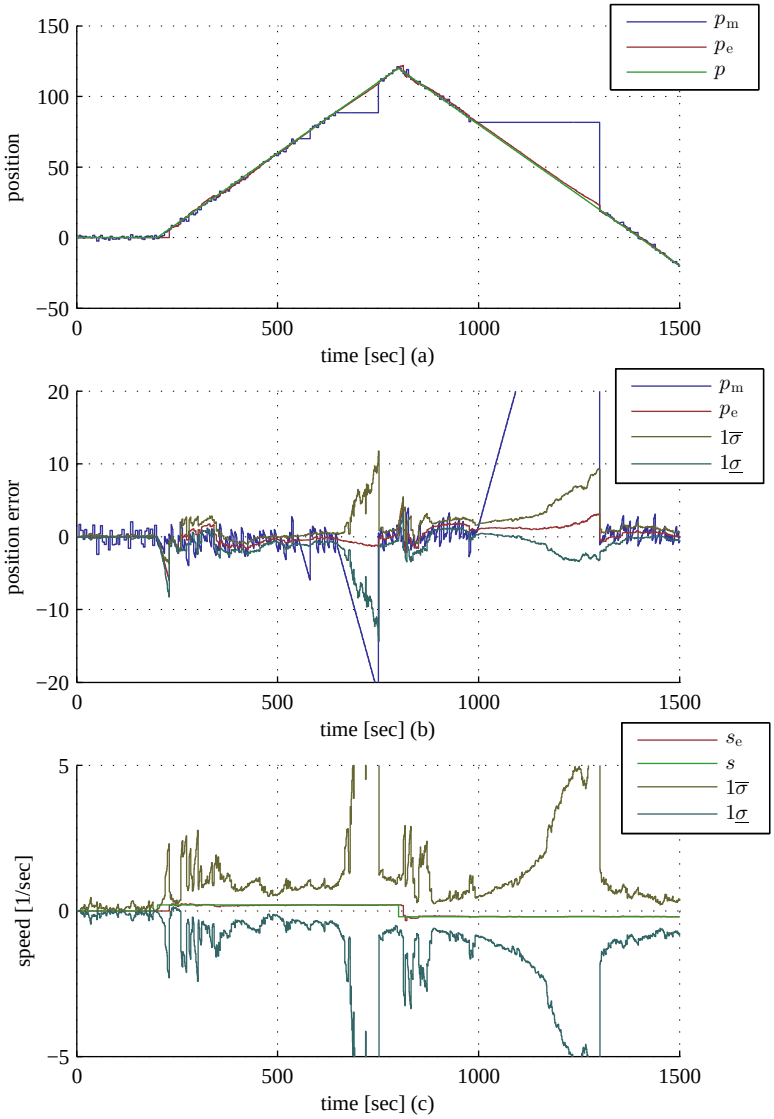

Figure 3.11: Simulation of handling missing measurement. The 1σ upper and lower boundaries of the position and speed estimation are shown as the curves $1\overline{\sigma}$ and $1\underline{\sigma}$, respectively.

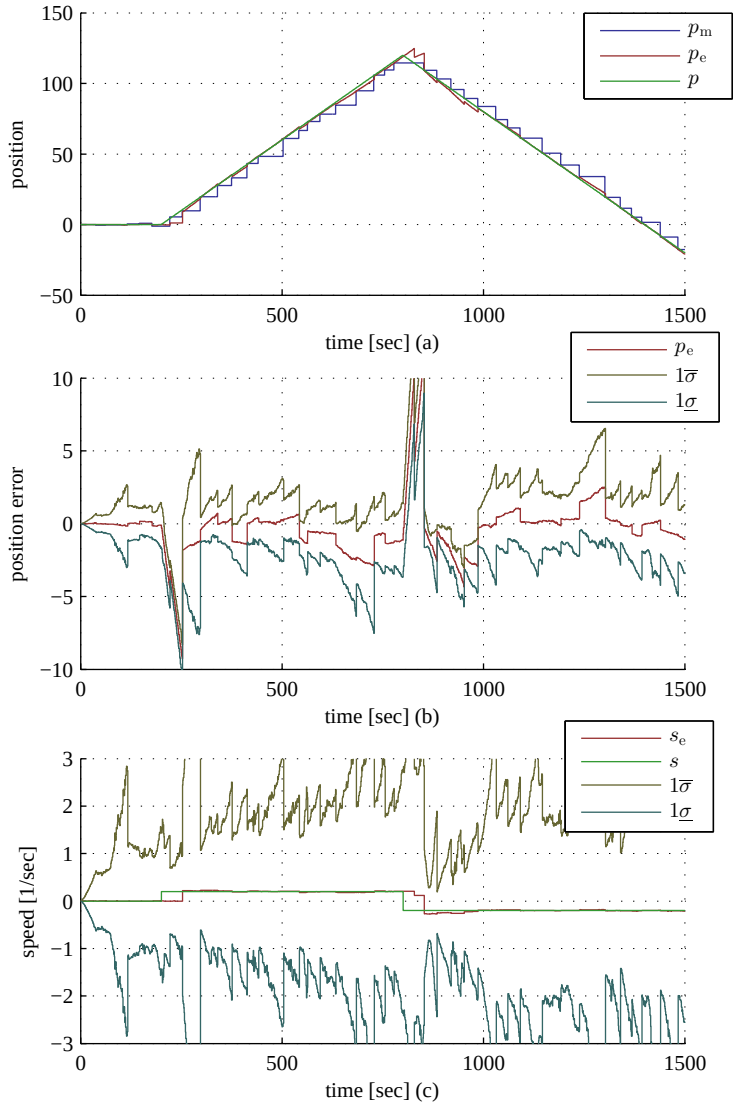

Figure 3.12: Simulation of handling missing measurement. The 1σ upper and lower boundaries of the position and speed estimation are shown as the curves $1\overline{\sigma}$ and $1\underline{\sigma}$, respectively.

Table 3.2: List of failure modes.

Failure mode	GNSS 1	GNSS 2	HPR
Bias	$\Delta^{\mathrm{GNSS,B}}$		-
Drifting	$\Delta^{\mathrm{GNSS,D}}$		-
Outliers	$\Delta^{\mathrm{GNSS1,O}}$	$\Delta^{\mathrm{GNSS2,O}}$	$\Delta^{\mathrm{HPR,O}}$

capture the fast change of the speed, the variance of the estimation increases quite rapidly.

3.7 Study Case: PF for Fault Diagnosis and Robust Navigation of DP Vessels

3.7.1 Scenario

In industrial control systems, the typical failure modes in measurements are as follows:

bias - the measurement has a constant-like bias relative to the true signal;

drift - the measurement drifts off relative to the true signal, either by a stochastic process or deterministically (ramp);

outliers - a sample from a measurement signal that lies abnormally far from the other values; and

increased noise - the variance of the measurement noise increases.

For safety and reliability, sensor redundancy is often required in industry applications. This involves the installation of multiple sensors to measure the same system output or state. The fault diagnosis in this case should focus on monitoring and identifying the conditions of sensors. In this case study, we continue with the PF-based wave filtering problem described in Section 2.4.6; moreover, we assume that failures may occur in the sensors. The PF will be designed to diagnose the faults in addition to performing its original task of state estimation and filtering.

3.7.2 Analysis and Modelling of Failure Modes

Following the models of fault-free behaviours of GNSS and HPR described in (2.142), the deviated models when GNSS or HPR are faulty are given in the following.

GNSS Faults

According to [Bhatti, 2007], 23 failure modes may occur in GNSS due to different mechanisms. In PF-based fault diagnosis, the modelling of the failure modes

is focused on the behaviour of the measurement from a GNSS perspective instead of studying the mechanisms. This entails that the 23 failure modes of the GNSS can be summarized into bias (named "range error" in [Bhatti, 2007]), drifting, and outliers.

GNSS Bias Several faults result from bias failure modes. The sizes of the bias depend on the failure, and can range from a few meters to a few kilometres. For DP operations, GNSS bias tens of meters in size can be critical, since they can be hard to detect, and induce the risk of drive-off of the DP vessel. How the bias occurs in a GNSS signal is not clear. It can be assumed that the process by which the bias occurs in a GNSS signal adopts two ways: abrupt jump and drifting. Abrupt jump can be modelled as

$$\boldsymbol{y}_{\mathrm{GNSS},k} = \boldsymbol{y}_k + \boldsymbol{v}_{\mathrm{GNSS},k} + \boldsymbol{b}_k, \tag{3.46}$$

where $\boldsymbol{p}_{\mathrm{GNSS}}$ is the GNSS measurement, $\boldsymbol{p}$ is the position vector, k is the time index, $\boldsymbol{v}$ is the measurement noise, and $\boldsymbol{b}$ is the bias term. The bias term $\boldsymbol{b}$ in the case of abrupt jump performs as $\boldsymbol{b}_k = \mathbf{0},\ k < l$, and $\boldsymbol{b}_k = \boldsymbol{b}^0 \neq \mathbf{0},\ k \geq l$, where l is the time instant when bias occurs. An abrupt jump in the GNSS signal of a DP vessel is highly suspicious and can be detected with less difficulty. However, the drifting problem of GNSS is more difficult to detect and more risky to DP operations.

GNSS Drifting [Bhatti, 2007] described GNSS drifting, the behaviour of the GNSS signal when drifting occurs is not clarified. By judging the mechanisms of the failure modes, it is reasonable to assume two kinds of drifting on the signal: deterministic ramp and random increasing. In both cases, the drifting speed is also of importance. A fast drift can be easier to detect. Hence, ramp-type drifting is modelled as

$$\boldsymbol{d}_{k+1} = \begin{cases} \mathbf{0} & , k < l \\ \boldsymbol{d}_k + \boldsymbol{r}_d & , k \geq l \quad |\boldsymbol{d}_k| < |\boldsymbol{d}_{\mathrm{MAX}}| \\ \boldsymbol{d}_k & , k \geq l \quad |\boldsymbol{d}_k| \geq |\boldsymbol{d}_{\mathrm{MAX}}| \end{cases} \tag{3.47}$$

$$\boldsymbol{y}_{\mathrm{GNSS},k} = \boldsymbol{y}_k + \boldsymbol{v}_k + \boldsymbol{d}_k, \tag{3.48}$$

where $\boldsymbol{r}_d$ is a constant representing the speed of drifting. While, for stochastic-process-type drifting, a suitable prior distribution $p(\boldsymbol{r}_d)$ of the speed of drifting can be designed instead of using a constant drifting speed in the deterministic drifting case, This should ensure that the drifting term $\boldsymbol{d}$ adopts a desired behaviour. However, a constant can be seen as a random variable from a distribution given by Dirac delta function, so that the models of these two types of drifting can be uniformly formulated.

Outliers

For several reasons, such as the aging of the electric circuit and multipath, outliers in the measurement are frequently encountered, and these manifest themselves as mea-

Table 3.3: The Markov chain for the transition of combined modes of GNSS sensors - $\boldsymbol{\Delta}^{\mathrm{GNSS}} = \begin{bmatrix}\Delta^{\mathrm{GNSS,B}} & \Delta^{\mathrm{GNSS,D}}\end{bmatrix}^{\top}$

				$\boldsymbol{\delta}^{(m)}$		
			$\Delta^{\mathrm{GNSS,D}}$	0	1	0
			$\Delta^{\mathrm{GNSS,B}}$	0	0	1
		$\Pr_{\boldsymbol{\delta}^{(m)}\boldsymbol{\delta}^{(n)}}$				
$\boldsymbol{\delta}^{(n)}$	$\Delta^{\mathrm{GNSS,D}}$	$\Delta^{\mathrm{GNSS,B}}$	-	-	-	-
	0	0	-	0.80	0.20	0.10
	1	0	-	0.10	0.75	0.05
	0	1	-	0.10	0.05	0.85

sured values that lie far away from others. Through assessing the appearance on the measurement signal, the outliers are always modelled as a sample from a distribution with much larger variance than the normal measurements. In our case, the outliers in GNSS and HPR are modelled as

$$\boldsymbol{y}_{\mathrm{GNSS},k} = \boldsymbol{y}_k + \boldsymbol{v}_{\mathrm{GNSS,O},k}, \tag{3.49}$$

and

$$\boldsymbol{y}_{\mathrm{HPR},k} = \boldsymbol{y}_k + \boldsymbol{v}_{\mathrm{HPR,O},k}, \tag{3.50}$$

respectively. And conceptually, $\|\mathrm{Cov}\left[\boldsymbol{v}_{*,\mathrm{O},k}\right]\| \gg \|\mathrm{Cov}\left[\boldsymbol{v}_{*,k}\right]\|$.

3.7.3 Particle Filter Design

In addition to the use of PF as a navigation filter, as described in Section 2.4.6, mode transitions should be designed to allow the particles to run in abnormal modes to accommodate sensor failures.

We assume that the GNSS bias and drifting are induced by external problems, such as ionosphere changes; as such, all GNSS receivers suffer from the same fault at the same time, and the faults in both GNSS sensors are of the same size. While the outliers are generally due to internal problems relating to a sensor or multipath phenomenon, the occurrences of the failure in each sensor are independent. The design of the mode transition should take these features of the fault into account. For instance, the outliers may occur as a combination of bias or drifting; however, bias and drifting cannot happen at the same time. Hence, the mode transition Markov chain of the GNSS is designed as Tables 3.3 and 3.4.

For the HPR sensor, we augment the state-space with a state representing the random excursion term, such as the Equations (3.51h) and (3.51k), so that the HPR excursion problem is not treated as a fault but estimated to be a state by the particle filter. Hence, the HPR sensor has the only failure mode being the outliers. Its mode transition is as pre the information presented in Table 3.5.

Table 3.4: The Markov chain for the transition of the GNSS mode $\Delta^{\mathrm{GNSS},i,\mathrm{O}}$

		$\boldsymbol{\delta}^{(m)}$		
	Pr_{mn}	$\Delta^{\mathrm{GNSS},i,\mathrm{O}}$	0	1
$\boldsymbol{\delta}^{(n)}$	$\Delta^{\mathrm{GNSS},i,\mathrm{O}}$	-	-	-
	0	-	0.70	1.00
	1	-	0.30	0.00

Table 3.5: The Markov chain for the transition of HPR mode $\Delta^{\mathrm{HPR,O}}$

		$\boldsymbol{\delta}^{(m)}$		
	Pr_{mn}	$\Delta^{\mathrm{HPR,O}}$	0	1
$\boldsymbol{\delta}^{(n)}$	$\Delta^{\mathrm{HPR,O}}$	-	-	-
	0	-	0.70	1.00
	1	-	0.30	0.00

To sum up, the resulting model runs in the particle filter is shown in Equation (3.51), where $\boldsymbol{y}_k = \boldsymbol{\eta}_k + \boldsymbol{\Gamma}\boldsymbol{\xi}_k$ is the vessel position as the superposition of vessel low- and wave-frequency motion, $\boldsymbol{C} = \begin{bmatrix}\boldsymbol{I}_{2\times 2} & \boldsymbol{0}_{2\times 1}\end{bmatrix}$ is the measurement matrix, $\mathcal{U}\left(\begin{bmatrix}-20 & 20\end{bmatrix}^2\right)$ is a 2-dimensional uniform distribution on the square area $\begin{bmatrix}-20 & 20\end{bmatrix}\times\begin{bmatrix}-20 & 20\end{bmatrix}$, and so does $\mathcal{U}\left(\begin{bmatrix}-0.2 & 0.2\end{bmatrix}^2\right)$ Some parts of this model, such as the behaviour of the sensors, depend on the system mode.

3.7.4 Simulation and Result

Three scenarios were employed to verify the performance of the PF-based fault tolerant navigation. In these simulations, the failures in the position reference sensors are triggered at 250 sec. The three scenarios correspond to bias, drifting, and outlier failure modes respectively. The results are shown in Figures 3.13, 3.14, and 3.15 respectively. In each figure, the four axes in the left column denote the position measurement and estimation, and the failure and the estimation of failure in each direction, respectively. In the right column, the first axis shows the vessel position and the position reference; the second axis shows the time history of the significant mode, which is rounded from the marginal density in the third axis and is also the conclusion of the mode estimation of the PF; the third axis is the marginal density in each system mode; and the fourth axis shows the sample size in each system mode.

In Figure 3.13, both of the GNSS signals jumped to 8 m to the north and 9 m to the west. As shown, the marginal density is dominated by the GNSS bias mode after triggering the failure, which means the PF detects the failure immediately. The PF also estimates the failure size precisely, as the estimated failure size is very similar to the actual failure size. As depicted in the position and reference axis, the vessel position follows the reference nicely, this means the vessel is able to maintain position

$$p\left(\boldsymbol{\eta}_{k+1}\right) = \mathcal{N}\left(\boldsymbol{\eta}_k + T_s \boldsymbol{R}\left(\boldsymbol{y}_k\right)\left(\boldsymbol{\nu}_k + \boldsymbol{R}^{\top}\left(\boldsymbol{y}_k\right)\boldsymbol{\nu}_{c,k}\right), \mathrm{Cov}\left[\boldsymbol{w}_{\eta,k}\right]\right), \tag{3.51a}$$

$$p\left(\boldsymbol{\nu}_{k+1}\right) = \mathcal{N}\left(\boldsymbol{\nu}_k + T_s \boldsymbol{M}^{-1}\left(-\boldsymbol{D}\boldsymbol{\nu}_k + \boldsymbol{\tau}_k\right), \mathrm{Cov}\left[\boldsymbol{w}_{\nu,k}\right]\right), \tag{3.51b}$$

$$p\left(\boldsymbol{\nu}_{c,k+1}\right) = \mathcal{N}\left(\boldsymbol{\nu}_{c,k} - T_s \boldsymbol{T}_c^{-1}\boldsymbol{\nu}_{c,k}, \mathrm{Cov}\left[\boldsymbol{w}_{c,k}\right]\right), \tag{3.51c}$$

$$p\left(\boldsymbol{\xi}_{k+1}\right) = \mathcal{N}\left(\boldsymbol{\xi}_k + T_s \boldsymbol{\Omega}\boldsymbol{\xi}_k, \mathrm{Cov}\left[\boldsymbol{\Lambda}\boldsymbol{w}_{\xi,k}\boldsymbol{\Lambda}^{\top}\right]\right), \tag{3.51d}$$

$$p\left(\boldsymbol{b}_{\mathrm{GNSS},k+1}\right) = \begin{cases} \rho\left(\boldsymbol{0}\right) & , \ \Delta_{k+1}^{\mathrm{GNSS,B}} = 0 \\ \mathcal{U}\left(\begin{bmatrix}-20 & 20\end{bmatrix}^2\right) & , \ \Delta_{k}^{\mathrm{GNSS,B}} = 0 \quad \Delta_{k+1}^{\mathrm{GNSS,B}} = 1 \\ \mathcal{N}\left(T_s \boldsymbol{T}_{b,\mathrm{GNSS}}^{-1}\boldsymbol{b}_{\mathrm{GNSS},k}, \mathrm{Cov}\left[\boldsymbol{w}_{b,\mathrm{GNSS},k}\right]\right) & , \ \Delta_{k}^{\mathrm{GNSS,B}} = 1 \quad \Delta_{k+1}^{\mathrm{GNSS,B}} = 1 \end{cases}, \tag{3.51e}$$

$$p\left(\boldsymbol{r}_{\mathrm{GNSS,d},k+1}\right) = \begin{cases} \rho\left(\boldsymbol{0}\right) & , \ \Delta_{k+1}^{\mathrm{GNSS,D}} = 0 \\ \mathcal{U}\left(\begin{bmatrix}-0.2 & 0.2\end{bmatrix}^2\right) & , \ \Delta_{k}^{\mathrm{GNSS,D}} = 0 \quad \Delta_{k+1}^{\mathrm{GNSS,D}} = 1 \\ \mathcal{N}\left(T_s \boldsymbol{T}_{r,\mathrm{GNSS}}^{-1}\boldsymbol{r}_{\mathrm{GNSS,d},k}, \mathrm{Cov}\left[\boldsymbol{w}_{r,\mathrm{GNSS},k}\right]\right) & , \ \Delta_{k}^{\mathrm{GNSS,D}} = 1 \quad \Delta_{k+1}^{\mathrm{GNSS,D}} = 1 \end{cases}, \tag{3.51f}$$

$$p\left(\boldsymbol{d}_{\mathrm{GNSS},k+1}\right) = \begin{cases} \rho\left(\boldsymbol{0}\right) & , \Delta_{k+1}^{\mathrm{GNSS,D}} = 0 \\ \rho\left(T_s \boldsymbol{d}_{\mathrm{GNSS},k} + \boldsymbol{r}_{\mathrm{GNSS,d},k}\right) & , \Delta_{k+1}^{\mathrm{GNSS,D}} = 1 \end{cases}, \tag{3.51g}$$

$$p\left(\boldsymbol{b}_{\mathrm{HPR},k+1}\right) = \mathcal{N}\left(T_s \boldsymbol{T}_{b,\mathrm{HPR}}^{-1}\boldsymbol{b}_{\mathrm{HPR},k}, \mathrm{Cov}\left[\boldsymbol{w}_{b,\mathrm{HPR},k}\right]\right), \tag{3.51h}$$

$$p\left(\boldsymbol{y}_{\mathrm{GNSS1},k}\right) = \begin{cases} \mathcal{N}\left(\boldsymbol{C}\boldsymbol{y}_k + \boldsymbol{d}_{\mathrm{GNSS},k} + \boldsymbol{b}_{\mathrm{GNSS},k}, \mathrm{Cov}\left[\boldsymbol{v}_{\mathrm{GNSS1},k}\right]\right) & , \Delta_{k}^{\mathrm{GNSS1,O}} = 0 \\ \mathcal{N}\left(\boldsymbol{C}\boldsymbol{y}_k + \boldsymbol{d}_{\mathrm{GNSS},k} + \boldsymbol{b}_{\mathrm{GNSS},k}, \mathrm{Cov}\left[\boldsymbol{v}_{\mathrm{GNSS1,O},k}\right]\right) & , \Delta_{k}^{\mathrm{GNSS1,O}} = 1 \end{cases}, \tag{3.51i}$$

$$p\left(\boldsymbol{y}_{\mathrm{GNSS2},k}\right) = \begin{cases} \mathcal{N}\left(\boldsymbol{C}\boldsymbol{y}_k + \boldsymbol{d}_{\mathrm{GNSS},k} + \boldsymbol{b}_{\mathrm{GNSS},k}, \mathrm{Cov}\left[\boldsymbol{v}_{\mathrm{GNSS2},k}\right]\right) & , \Delta_{k}^{\mathrm{GNSS2,O}} = 0 \\ \mathcal{N}\left(\boldsymbol{C}\boldsymbol{y}_k + \boldsymbol{d}_{\mathrm{GNSS},k} + \boldsymbol{b}_{\mathrm{GNSS},k}, \mathrm{Cov}\left[\boldsymbol{v}_{\mathrm{GNSS2,O},k}\right]\right) & , \Delta_{k}^{\mathrm{GNSS2,O}} = 1 \end{cases}, \tag{3.51j}$$

$$p\left(\boldsymbol{y}_{\mathrm{HPR},k}\right) = \mathcal{N}\left(\boldsymbol{C}\boldsymbol{y}_k + \boldsymbol{b}_{\mathrm{HPR}}, \mathrm{Cov}\left[\boldsymbol{v}_{\mathrm{HPR}}\right]\right), \tag{3.51k}$$

$$p\left(\psi_{\mathrm{gyro},k}\right) = \begin{bmatrix}0 & 0 & 1\end{bmatrix}\boldsymbol{y}_k + v_{\mathrm{gyro}}. \tag{3.51l}$$

even when there is a bias failure in the GNSS sensors.

In Figure 3.14, both of the GNSS signals drift with the speed $[0.15\mathrm{m/s}, -0.1\mathrm{m/s}]$ in the N-E frame. This drifting speed is rather slow and, therefore, the failure is hard to detect. The result shows that it takes about 22 s for the PF to detect the failure where the vessel has drifted off course $[3.3\mathrm{m}, 2.2\mathrm{m}]$. After the failure is detected, the size of the drift can be precisely estimated. Taking the estimation of the drift into the vessel navigation, the vessel can follow the reference within a 5 m zone with some oscillation. This is because, following the failure, the only effective position reference is the HPR, which is less precise and offers low update frequency.

In Figure 3.15, the outliers are triggered on the sensor GNSS1. When the position signal is an outlier, the marginal density of the GNSS outliers mode becomes high, and the PF will reject the current measurement.

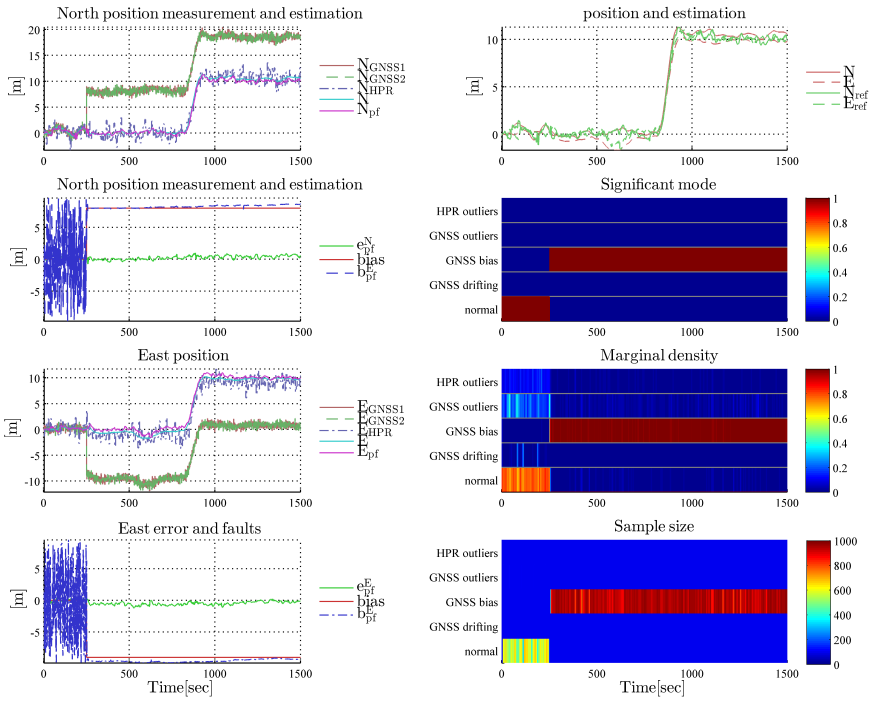

Figure 3.13: The performance of PF base FDD for DP vessel with GPSS bias.

3.8 Conclusion

This chapter described the use of a PF-based algorithm for fault diagnosis that was built on a switching mode hidden Markov model. Examples were given to illustrate and validate the proposed algorithm. A PF-based DP system fault tolerant design was also proposed. The simulation results confirmed that the performance of the fault diagnosis was generally good and that the proposed algorithm provided robust and efficient state estimation.

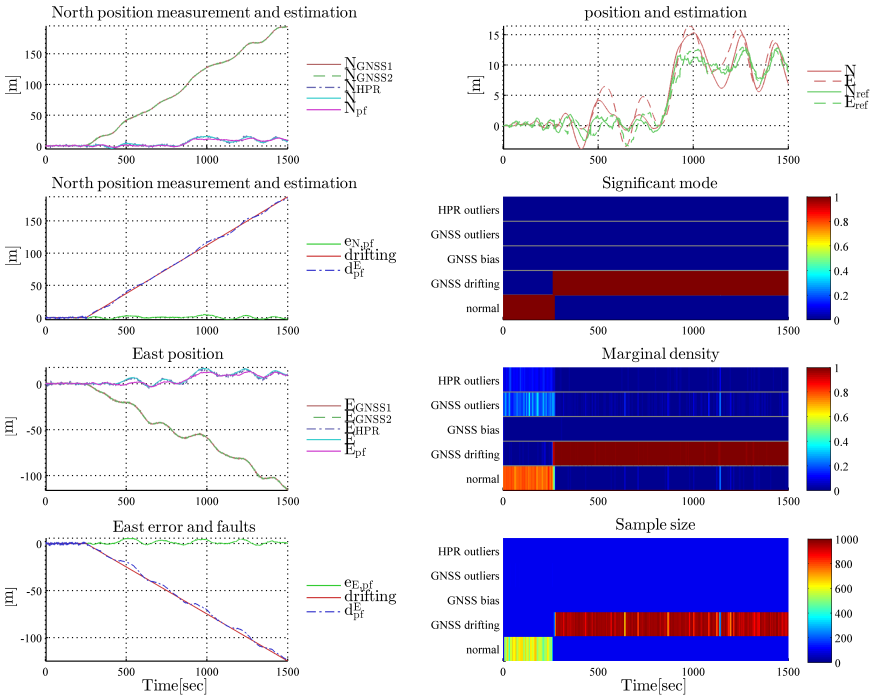

Figure 3.14: The performance of PF base FDD for DP vessel with GPSS drifting.

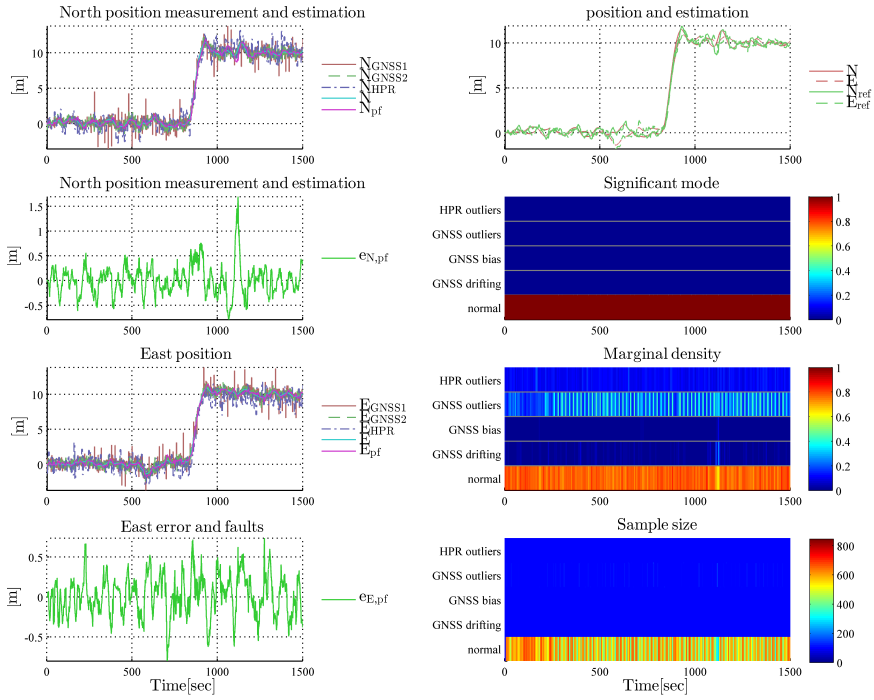

Figure 3.15: The performance of PF base FDD for DP vessel with GPSS outliers.

Chapter 4

Application: Particle Filter for Robust Navigation of Underwater Robot

> “ *‘From a drop of water,’ said the writer, ‘a logician could infer the possibility of an Atlantic or a Niagara without having seen or heard of one or the other. So all life is a great chain, the nature of which is known whenever we are shown a single link of it. Like all other arts, the Science of Deduction and Analysis is one which can only be acquired by long and patient study nor is life long enough to allow any mortal to attain the highest possible perfection in it. Before turning to those moral and mental aspects of the matter which present the greatest difficulties, let the enquirer begin by mastering more elementary problems. Let him, on meeting a fellow-mortal, learn at a glance to distinguish the history of the man, and the trade or profession to which he belongs. Puerile as such an exercise may seem, it sharpens the faculties of observation, and teaches one where to look and what to look for. By a man’s finger nails, by his coat-sleeve, by his boot, by his trouser knees, by the callosities of his forefinger and thumb, by his expression, by his shirt cuffs ’* ”
>
> – Conan Doyle, “*Study in Scarlet*”.

4.1 Introduction

This chapter describes the validation of the particle filter-based fault diagnosis method proposed in the last chapter through applying the method to the robust navigation problem of an underwater robot, where 10 failure modes of sensors and thrusters are considered. Closed-loop full-scale experimental results show that the proposed

Figure 4.1: ROV Minerva. *Photo: Mauro Candeloro.*

method is robust, can diagnose faults effectively, and can provide good state estimation, even in cases where multiple faults occur.

The structure of this chapter is as follows. Firstly, Section 4.2 presents the model of the ROV for the experiment, while its failure modes are analysed and modelled in Section 4.3. The proposed PF-based FD method is employed to design an ROV observer in Section 4.4, and finally the results from an ROV sea trial are presented in Section 4.5.

4.2 ROV manoeuvring Model

4.2.1 The ROV Minerva

The ROV Minerva, as shown in Figure 4.1, is a SUB-fighter 7500 ROV that was constructed by Sperre AS for NTNU in 2003. It is powered from, and communicates with, a surface vessel through a 600 m umbilical cable. Minerva is usually deployed from the NTNU research vessel RV Gunnerus, which is part of the NTNU AUR-Lab. The specifications of the sensors and other instruments employed in the equipment are provided in Table 4.1.

The thruster arrangement is shown in Figure 4.3. The starboard and port thrusters are oriented 10° towards the centreline. The side thruster has two propellers, one at each end, but it has the same power rating as the other thrusters – which in open water is rated to 300–340N. All thrusters have fixed pitch propellers.

A Kongsberg HiPAP 500, which is a high precision hydroacoustic positioning reference (HPR) system, is used to measure the position of the ROV relative to the transducer on the surface vessel. NaviPac is an integrated navigation software that was produced by EIVA. It outputs the position of the ROV in UTM coordinates based on the measurements from the HiPAP, the GNSS, and the MRU of the surface vessel. A Doppler velocity log (DVL) is installed to measure the ROV velocity in addition to an Xsens MTi, which is used as an IMU. The depth is provided by the HPR and is also measured by a pressure gauge. More details of the vehicle and its control system can be found in [Dukan et al., 2011].

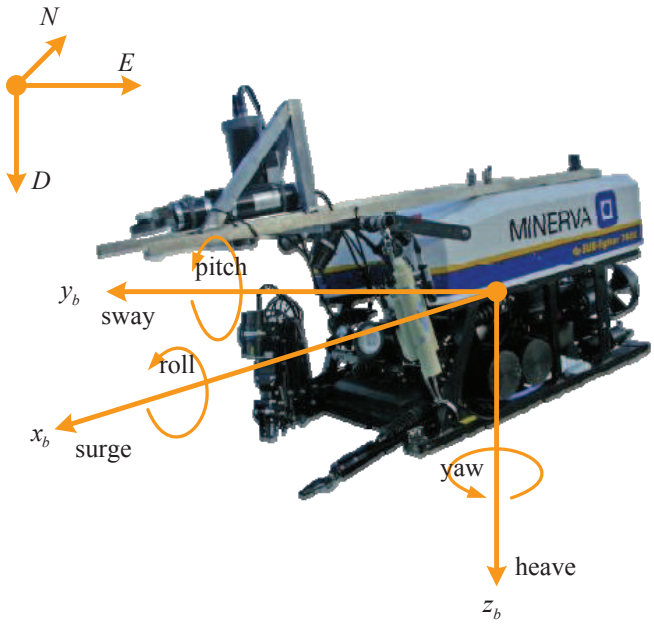

Figure 4.2: ROV Minerva and the notations of its kinematics. *Photo: Johanna Jarnegren.*

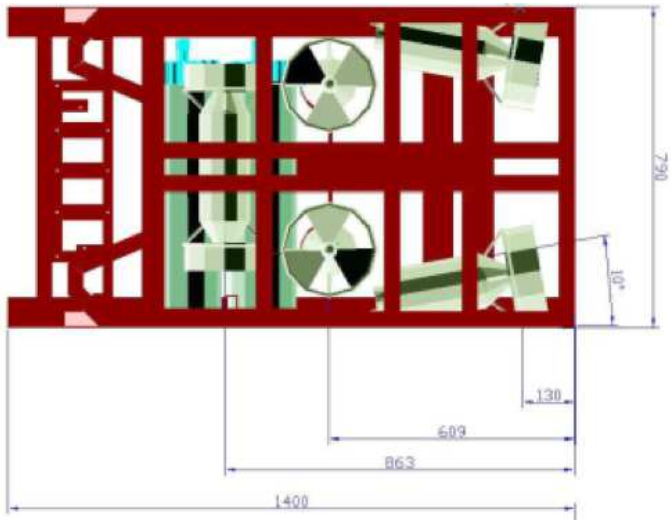

Figure 4.3: Overview of thruster configuration (Drawing from: [Dukan et al., 2011]).

Table 4.1: ROV Minerva specifications

Dimensions	LWH: $144 \times 82 \times 81\mathrm{cm}$
Weight (air)	$485\mathrm{kg}$
Payload	$\approx 20\mathrm{kg}$
Max depth	$700\mathrm{m}$
Thrusters	Horizontal: $2 \times 2000\mathrm{W}$
	Vertical: $2 \times 2000\mathrm{W}$
	Lateral: $1 \times 2000\mathrm{W}$
Max speed	Horizontal: $2.0\mathrm{knot}$
	Vertical: $1.2\mathrm{knot}$
	Lateral: $1.3\mathrm{knot}$
	Turn rate: $60^\circ/\mathrm{s}$
Sensors	$100\mathrm{bar}$ pressure gauge
	Xsens MTi
	Kongsberg HiPAP 500
	Teledyne RDI Workhorse Doppler velocity log

Table 4.2: Notations for ROV model.

DOF		**Force and moment**	**Linear and angular velocities**	**Positions and Euler angles**
1	motion in x direction (surge)	X	u	x
2	motion in y direction (sway)	Y	v	y
3	motion in z direction (heave)	Z	w	z
4	rotation about x axis (roll)	K	p	ϕ
5	rotation about y axis (pitch)	M	q	θ
6	rotation about z axis (yaw)	N	r	ψ

4.2.2 Kinematics

Adopting the notations of [Fossen, 2011], based on the SNAME[1] formulation, the kinematics are described by the degrees-of-freedom (DOFs) in Table 4.2 and the body-fixed reference frame is shown in Figure 4.2. Since the ROV is designed to be passive and stable in the roll and pitch DOFs, the dynamics in these DOFs are ignored (assuming the roll and pitch angles are zero). In this case, the kinematic model of the ROV is given by the 4-DOF model

$$\dot{\boldsymbol{\eta}} = \boldsymbol{R}(\psi)\,\boldsymbol{\nu}, \tag{4.1}$$

where $\boldsymbol{\eta} = \begin{bmatrix} N & E & D & \psi \end{bmatrix}^\top$ is the ROV position and heading in the NED (North-East-Down) reference frame, $\boldsymbol{\nu} = \begin{bmatrix} u & v & w & r \end{bmatrix}^\top$ is the body-fixed velocity and yaw rate vector, and

$$\boldsymbol{R}(\psi) = \begin{bmatrix} \cos(\psi) & -\sin(\psi) & 0 & 0 \\ \sin(\psi) & \cos(\psi) & 0 & 0 \\ 0 & 0 & 1 & 0 \\ 0 & 0 & 0 & 1 \end{bmatrix} \tag{4.2}$$

is the rotation matrix which transforms a vector in the ROV body frame to the NED frame.

4.2.3 Kinetics

According to [Fossen, 2011] and [Dukan et al., 2011], the motion of the ROV can be described by the model

$$\begin{aligned} \boldsymbol{M}\dot{\boldsymbol{\nu}} &= -\boldsymbol{C}_{\mathrm{RB}}(\boldsymbol{\nu})\,\boldsymbol{\nu} - \boldsymbol{C}_{\mathrm{A}}(\boldsymbol{\nu}_{\mathrm{r}})\,\boldsymbol{\nu}_{\mathrm{r}} \\ &\quad -\boldsymbol{D}_{\mathrm{NL}}(\boldsymbol{\nu}_{\mathrm{r}})\,\boldsymbol{\nu}_{\mathrm{r}} - \boldsymbol{D}_{\mathrm{L}}\boldsymbol{\nu}_{\mathrm{r}} \\ &\quad -\boldsymbol{g}(\boldsymbol{\eta}) + \boldsymbol{\tau} + \boldsymbol{w}_{\nu} \qquad (4.3) \\ \dot{\boldsymbol{\nu}}_{\mathrm{c}} &= -\boldsymbol{T}_{\mathrm{c}}^{-1}\boldsymbol{\nu}_{\mathrm{c}} + \boldsymbol{w}_{\mathrm{c}}, \qquad (4.4) \end{aligned}$$

where $\boldsymbol{M} \in \mathbb{R}^{4\times4}$ is the combined rigid body and added mass matrix, $\boldsymbol{C}_{\mathrm{RB}}(\boldsymbol{\nu}) \in \mathbb{R}^{4\times4}$ is the rigid body Coriolis and centripetal matrix, $\boldsymbol{C}_{\mathrm{A}}(\boldsymbol{\nu}_{\mathrm{r}}) \in \mathbb{R}^{4\times4}$ is the added mass Coriolis and centripetal matrix, $\boldsymbol{D}_{\mathrm{NL}}(\boldsymbol{\nu}_{\mathrm{r}}) \in \mathbb{R}^{4\times4}$ and $\boldsymbol{D}_{\mathrm{L}} \in \mathbb{R}^{4\times4}$ are the nonlinear and linear hydrodynamic damping matrices, $\boldsymbol{g}(\boldsymbol{\eta}) \in \mathbb{R}^4$ is the restoring force vector, $\boldsymbol{\tau} = \begin{bmatrix} X & Y & Z & N \end{bmatrix}^\top$ is the control force and moment, and $\boldsymbol{w}_{\nu}$ is process noise. Moreover, $\boldsymbol{\nu}_{\mathrm{r}} = \boldsymbol{\nu} - \begin{bmatrix} \boldsymbol{\nu}_{\mathrm{c}}^\top & 0 & 0 \end{bmatrix}^\top$ is the relative velocity vector with respect to the ocean current. The current velocity $\boldsymbol{\nu}_{\mathrm{c}} \in \mathbb{R}^2$ can be modelled as the Markov process (4.4), in accordance with [Fossen, 2011], where $\boldsymbol{T}_{\mathrm{c}} \in \mathbb{R}^{4\times4}$ is a diagonal matrix of positive time constants representing the dynamic of the current, and $\boldsymbol{w}_{\mathrm{c}} \in \mathbb{R}^2$ is process noise.

[1] Society of Naval Architects and Marine Engineers.

4.2.4 Thruster Control

The ROV motion is controlled by thrusters, for which the rotational speed must be set and controlled. However, the speed control is unfortunately only open-loop due to the lack of rotational speed sensors. In our FDPF design we include the thruster system in the ROV model to account for faults in the thruster control system.

The thruster control described by [Dukan et al., 2011] should be briefly recalled. The desired generalized force vector $\boldsymbol{\tau}_{\mathrm{d}}$ must be allocated as a rotational speed for each thruster. The thruster speed vector $\boldsymbol{n}$ is defined as

$$\boldsymbol{n} = \begin{bmatrix} n_{\mathrm{l}} & n_{\mathrm{vp}} & n_{\mathrm{vs}} & n_{\mathrm{p}} & n_{\mathrm{s}} \end{bmatrix}^{\top}, \tag{4.5}$$

where n_{l}, n_{vp}, n_{vs}, n_{p}, n_{s} are the rotational speed of the lateral, vertical port, vertical starboard, port and starboard thrusters, respectively. As all thrusters are fixed, the thrust vector can be written

$$\boldsymbol{\tau} = \boldsymbol{T}\boldsymbol{K}\boldsymbol{u}, \tag{4.6}$$

where $\boldsymbol{T} \in \mathbb{R}^{4\times 5}$ is the thrust configuration matrix that depends only on thruster position and orientation, $\boldsymbol{K} \in \mathbb{R}^{5\times 5}$ is a diagonal gain matrix, and the control input is

$$\boldsymbol{u} = \begin{bmatrix} |n_{\mathrm{l}}|\, n_{\mathrm{l}} & |n_{\mathrm{vp}}|\, n_{\mathrm{vp}} & |n_{\mathrm{vs}}|\, n_{\mathrm{vs}} & |n_{\mathrm{p}}|\, n_{\mathrm{p}} & |n_{\mathrm{s}}|\, n_{\mathrm{s}} \end{bmatrix}^{\top}. \tag{4.7}$$

The control input $\boldsymbol{u} = \boldsymbol{u}_d$ is found by taking the inverse of Equation (4.6), that is,

$$\boldsymbol{u}_d = \boldsymbol{K}^{-1}\boldsymbol{T}^{\dagger}\boldsymbol{\tau}_{\mathrm{d}}, \tag{4.8}$$

where $\boldsymbol{T}^{\dagger} = \boldsymbol{T}^{\top}\left(\boldsymbol{T}\boldsymbol{T}^{\top}\right)^{-1}$ is the pseudo inverse of $\boldsymbol{T}$. This gives the actual applied thrust input by the model

$$\boldsymbol{\tau} = \boldsymbol{T}\boldsymbol{K}\boldsymbol{u} = \boldsymbol{T}\boldsymbol{K}\left(\boldsymbol{K}^{-1}\boldsymbol{T}^{\dagger}\boldsymbol{\tau}_{\mathrm{d}}\right), \tag{4.9}$$

assuming the actual propeller speeds follow the commanded speeds exactly. Obviously, this introduces some uncertainty into the model, including a small time delay between $\boldsymbol{\tau}_{\mathrm{d}}$ and $\boldsymbol{\tau}$ due to thruster dynamics.

4.2.5 Sensor Model

Hydroacoustic position reference (HPR) system

The HPR system determines the position of an underwater target by using acoustic sound waves in the water to measure its distance and direction. It follows that the measurement is obtained originally in spherical coordinates and then transformed to Cartesian coordinates. Hence, the position measurement in each Cartesian direction is correlated.

The HPR suffers from various error sources, such as ray bending, orientation change of the transducer, and variation of sound velocity in the water column. As such, it is

difficult to analyse the behaviour of the HPR due to its time-varying nature. In this design, the HPR measurement was considered to be a vector with the North and East positions, whose covariance is time varying, and the covariance of the measurement noise was estimated recursively from historical data. Note that since the pressure gauge depth sensor provides more reliable measurements than the HPR measurement in depth, the depth component in the HPR measurement was not used. Let $\boldsymbol{p}_{\mathrm{A},i} = [N_{\mathrm{A},i}\ E_{\mathrm{A},i}]^\top$ denote the ROV position at instant i, $\bar{\boldsymbol{p}}_{\mathrm{A}}$ is the moving window average of $\boldsymbol{p}_{\mathrm{A}}$, and $\tilde{\boldsymbol{p}}_A = \boldsymbol{p}_{\mathrm{A}} - \bar{\boldsymbol{p}}_{\mathrm{A}}$ is the error vector. The estimate of the covariance $\boldsymbol{\Sigma}_{\mathrm{A}}$ is correspondingly

$$\begin{aligned}\boldsymbol{\Sigma}_{\mathrm{A},k} &= \frac{1}{N+1}\sum_{i=k-N}^{k}\left(\tilde{\boldsymbol{p}}_{\mathrm{A},i}(\tilde{\boldsymbol{p}}_{\mathrm{A},i})^\top\right)\\ &= \frac{N}{N+1}\left(\boldsymbol{\Sigma}_{\mathrm{A},k-1} + \frac{1}{N}\left(\tilde{\boldsymbol{p}}_{\mathrm{A},k}\right)\left(\tilde{\boldsymbol{p}}_{\mathrm{A},k}\right)^\top\right),\end{aligned} \tag{4.10}$$

where N is the tunable time window length. The HPR measurement $\boldsymbol{p}_{\mathrm{A}}$ is then subjected to a multivariate Gaussian distribution with a time-varying covariance,

$$p\left(\boldsymbol{p}_{\mathrm{A},k}\,|\boldsymbol{\eta}_k\right) = \mathcal{N}\left(\begin{bmatrix}\boldsymbol{I}_{2\times2} & \boldsymbol{0}_{2\times2}\end{bmatrix}\boldsymbol{\eta}_k, \boldsymbol{\Sigma}_{\mathrm{A},k}\right), \tag{4.11}$$

where $\mathcal{N}$ denotes the Gaussian distribution function.

Doppler velocity log (DVL)

The DVL measures the velocity of the ROV in 3D space with respect to the water or with respect to the seabed. We adopt the latter setup in this design and use only the two horizontal components in its measurement. The DVL measurement is first decomposed in the "instrument frame" of the DVL, and it is then transformed into the ROV body frame according to

$$\boldsymbol{v}_{\mathrm{D}} = \boldsymbol{R}_{\mathrm{DVL}}^{\mathrm{ROV}}\left(\boldsymbol{v}_{\mathrm{D}}^{\mathrm{DVL}} + r\boldsymbol{b}_{\mathrm{DVL}}^{\mathrm{ROV}}\right), \tag{4.12}$$

where $\boldsymbol{v}_{\mathrm{D}}^{\mathrm{DVL}}$ is the velocity measurement vector in the DVL instrument frame, $\boldsymbol{R}_{\mathrm{DVL}}^{\mathrm{ROV}}$ is the constant rotation matrix from the DVL instrument frame to the ROV body frame, $\boldsymbol{b}_{\mathrm{DVL}}^{\mathrm{ROV}}$ is the offset between the origins of the two frames expressed in ROV body frame, and $\boldsymbol{v}_{\mathrm{D}}$ is the resulting velocity measurement of the ROV in its body frame. Because this offset correction requires the yaw rate r of the ROV, it can potentially be the source of a common mode failure. However, as the offset is small and the yaw rate is generally low, we choose to neglect the noise and uncertainty involved in this transformation and express the DVL measurement simply as $\boldsymbol{v}_{\mathrm{D}} = \begin{bmatrix}u_{\mathrm{D}} & v_{\mathrm{D}}\end{bmatrix}^\top$; that is, the velocities along the x and y axes of the ROV body frame. Assuming the DVL measurement noise in each direction are independent identically normally distributed, the DVL velocity measurement $\boldsymbol{v}_{\mathrm{D},k}$ can be seen as a multivariate normally distributed random vector with expectation $\begin{bmatrix}\boldsymbol{I}_{2\times2} & \boldsymbol{0}_{2\times2}\end{bmatrix}\boldsymbol{\nu}_k$, and covariance matrix $\boldsymbol{\sigma}_{\mathrm{D}}^2\boldsymbol{I}$, where $\boldsymbol{\sigma}_{\mathrm{D}}^2$ is the variance of the DVL measurement noise vector. This gives the resulting DVL measurement $\boldsymbol{v}_{\mathrm{D},k}$ expressed as

$$p\left(\boldsymbol{v}_{\mathrm{D},k}\,|\boldsymbol{\nu}_k\right) = \mathcal{N}\left(\begin{bmatrix}\boldsymbol{I}_{2\times2} & \boldsymbol{0}_{2\times2}\end{bmatrix}\boldsymbol{\nu}_k, \boldsymbol{\sigma}_{\mathrm{D}}^2\boldsymbol{I}\right). \tag{4.13}$$

$$\dot{\boldsymbol{\eta}} = \boldsymbol{R}(\psi)\,\boldsymbol{\nu} \tag{4.16a}$$

$$\begin{aligned}\boldsymbol{M}\dot{\boldsymbol{\nu}} = &-\boldsymbol{C}_{\mathrm{RB}}(\boldsymbol{\nu})\,\boldsymbol{\nu} - \boldsymbol{C}_{\mathrm{A}}(\boldsymbol{\nu}_{\mathrm{r}})\,\boldsymbol{\nu}_{\mathrm{r}} \\ &- \boldsymbol{D}_{\mathrm{NL}}(\boldsymbol{\nu}_{\mathrm{r}})\,\boldsymbol{\nu}_{\mathrm{r}} - \boldsymbol{D}_{\mathrm{L}}\boldsymbol{\nu} \\ &- \boldsymbol{g}(\boldsymbol{\eta}) + \boldsymbol{T}\boldsymbol{K}\left(\boldsymbol{K}^{-1}\boldsymbol{T}^{\dagger}\boldsymbol{\tau}_{\mathrm{d}}\right) \\ &+ \boldsymbol{w}_{\nu}\end{aligned} \tag{4.16b}$$

$$\dot{\boldsymbol{\nu}}_{\mathrm{c}} = -\boldsymbol{T}_{\mathrm{c}}^{-1}\boldsymbol{\nu}_{\mathrm{c}} + \boldsymbol{w}_{\mathrm{c}}, \tag{4.16c}$$

$$p\left(\boldsymbol{p}_{\mathrm{A},k}\,|\boldsymbol{\eta}_k\right) = \mathcal{N}\left(\left[\boldsymbol{I}_{2\times 2}\;\boldsymbol{0}_{2\times 2}\right]\boldsymbol{\eta}_k, \boldsymbol{\Sigma}_{\mathrm{A},k}\right) \tag{4.16d}$$

$$p\left(\boldsymbol{v}_{\mathrm{D},k}\,|\boldsymbol{\nu}_k\right) = \mathcal{N}\left(\left[\boldsymbol{I}_{2\times 2}\;\boldsymbol{0}_{2\times 2}\right]\boldsymbol{\nu}_k, \boldsymbol{\sigma}_{\mathrm{D}}^2\boldsymbol{I}\right). \tag{4.16e}$$

$$p\left(D_{\mathrm{P},k}\,|\boldsymbol{\eta}_k\right) = \mathcal{N}\left(\begin{bmatrix}0 & 0 & 1 & 0\end{bmatrix}\boldsymbol{\eta}_k, \sigma_{\mathrm{P}}^2\right). \tag{4.16f}$$

$$\psi_{\mathrm{M}} = \begin{bmatrix}0 & 0 & 0 & 1\end{bmatrix}\boldsymbol{\eta} \tag{4.16g}$$

Inertial measurement unit (IMU) as heading sensor

The Xsens MTi is used as an IMU, which provides measurements from three-axis rate gyros, accelerometers and magnetometers. The heading ψ and yaw rate r of the ROV were estimated by the nonlinear complementary filter by [Mahony et al., 2008], and further examined by [Fossen, 2011]. This estimation is accurate and reliable; as such, the dynamic of the estimation error can be ignored and a basic assumption is made that the heading of the ROV is directly obtained as

$$\psi_{\mathrm{M}} = \begin{bmatrix}0 & 0 & 0 & 1\end{bmatrix}\boldsymbol{\eta}. \tag{4.14}$$

Depth sensor

The pressure gauge depth sensor is reliable and accurate, and it is modeled as

$$p\left(D_{\mathrm{P},k}\,|\boldsymbol{\eta}_k\right) = \mathcal{N}\left(\begin{bmatrix}0 & 0 & 1 & 0\end{bmatrix}\boldsymbol{\eta}_k, \sigma_{\mathrm{P}}^2\right), \tag{4.15}$$

where D_{P} is the measured depth from the pressure gauge, and σ_{P}^2 is the variance of the measurement noise.

4.2.6 Resulting ROV Model

Collecting the ROV kinematics (4.1), kinetics (4.3), thruster control (4.9), current (4.4), and the measurements (4.11), (4.13), (4.15) and (4.14), we obtain the ROV model (4.16).

This model can be discretized and transformed into an HMM according to

$$p\left(\boldsymbol{x}_{k+1}\,|\boldsymbol{x}_k, \boldsymbol{\tau}_{\mathrm{d},k}\right) = f\left(\boldsymbol{x}_k, \boldsymbol{\tau}_{\mathrm{d},k}\right) \tag{4.17}$$

$$p\left(\boldsymbol{y}_k\,|\boldsymbol{x}_k\right) = h\left(\boldsymbol{x}_k\right). \tag{4.18}$$

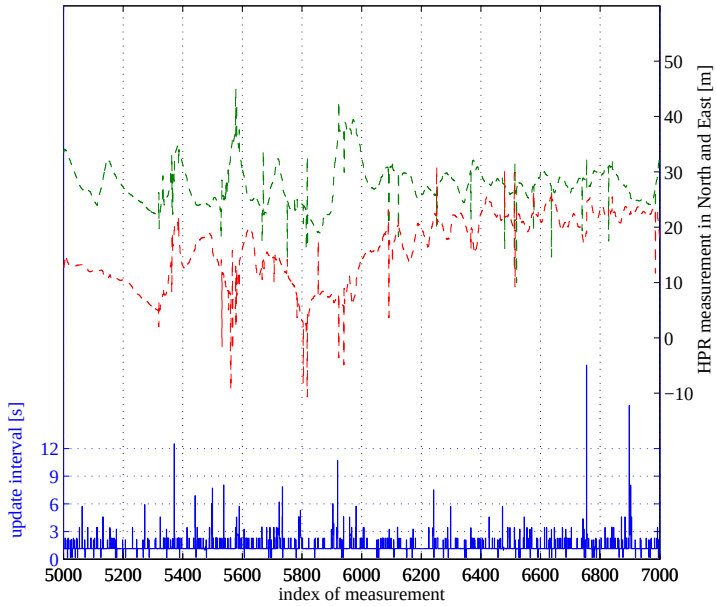

Figure 4.4: A segment of the HPR measurement and its update interval, with the measurement index along the horizontal axis, when the ROV was performing slow manoeuvres and station keeping.

where $\boldsymbol{x} = \begin{bmatrix}\boldsymbol{\eta} & \boldsymbol{\nu} & \boldsymbol{\nu}_{\mathrm{c}}\end{bmatrix}^{\top} \in \mathbb{R}^{11}$, $\boldsymbol{y} = \begin{bmatrix}\boldsymbol{p}_{\mathrm{A}} & \boldsymbol{v}_{\mathrm{D}} & D_{\mathrm{P}} & \psi_{\mathrm{M}}\end{bmatrix} \in \mathbb{R}^{7}$, and $f(\cdot)$ and $h(\cdot)$ are the mappings corresponding to (4.16).

4.3 Anomaly Analysis

When a system suffers from faults, its behaviour will differ from its fault-free condition. Besides faults, anomalies, such as sensor dropouts and outliers, also lead to deviation from the fault-free behaviour. The phenomena that causes abnormal behaviours are referred to anomalies. This section discusses the anomalies observed in the ROV sea trials. We will model the concluded anomalies from this analysis as faults, which then becomes the failure modes in the switching mode HMM (4.2.6).

4.3.1 Mode $\Delta^{\mathrm{HPR},1}$ – HPR dropout

The HPR measurement model provided in (4.16d) is valid when the ROV is in shallow water in witch the HPR holds a nearly constant update rate. It is known that the HPR

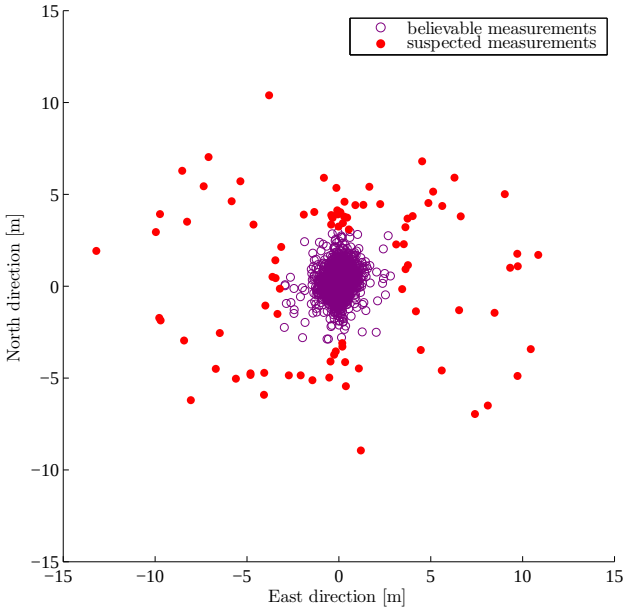

Figure 4.5: Termwise differences of the HPR measurements. A few extremely large differences that were out of the axis range were ignored.

update rate depends on the slant range between the transponder and the transducer. As such, when the ROV dives down to deeper water the HPR update rate becomes nonuniform and lower than the nominal rate. This phenomenon was observed in the ROV sea trials as shown in Figure 4.4. When the ROV depth was operating around $80\mathrm{m}$, the HPR update intervals were larger than 2 seconds in general and, in some extreme cases, it reached 18 seconds. This update rate is too low for a high-precision ROV positioning control system and will significantly reduce the responsiveness of the system if these measurement are used directly. Hence, the navigation observer should accommodate the nonuniform update rate of the HPR and output a reliable data stream of the position estimate even when the HPR measurement drops out for tens of seconds. The HPR dropouts are modelled as

$$p\left(\boldsymbol{p}_{\mathrm{A},k}\,|\boldsymbol{x}_k\right) = \mathcal{N}\left(\begin{bmatrix}0 & 0\end{bmatrix}^\top, \sigma^2_{\mathrm{A,d}}\boldsymbol{I}\right). \tag{4.19}$$

where $\boldsymbol{\sigma}_{\mathrm{A,d}}$ is assigned to a very large positive number that represents the fact that the current measurement is uninformative.

4.3.2 Mode $\Delta^{\mathrm{HPR},2}$ – HPR Measurement Outliers

Figure 4.4 shows that the HPR measurement exhibits outliers. This becomes more visible in the scatter plot in Figure 4.5, which shows the termwise differences of the HPR measurement series of Figure 4.4. Since the velocity of the ROV is low, the

termwise differences should be close to zero when the system is fault-free. Hence, the HPR measurements with large termwise differences from their successors are suspected (the time interval between two measurements should also be taken into account) outliers. In [Gustafsson, 2001], the outliers are seen as samples from another process whose noise variance is significantly greater than the one in the normal case, motivating the distribution

$$p\left(\boldsymbol{p}_{\mathrm{A},k}\,|\boldsymbol{x}_k\right) = \mathcal{N}\left(\begin{bmatrix}\boldsymbol{I}_{2\times 2} & \boldsymbol{0}_{2\times 2}\end{bmatrix}\boldsymbol{x}_k, \sigma^2_{\mathrm{A,o}}\boldsymbol{I}\right), \tag{4.20}$$

where $\sigma^2_{\mathrm{A,o}}\boldsymbol{I}$ is the covariance of the outlier distribution, conceptually chosen as $\left\|\sigma^2_{\mathrm{A,o}}\boldsymbol{I}\right\| \gg \|\boldsymbol{\Sigma}_{\mathrm{A}}\|$.

4.3.3 Mode $\Delta^{\mathrm{DVL},1}$ – DVL Dropout

When the DVL loses sea bottom tracking, it reports a sentinel maximum velocity that indicates a lost velocity measurement. Along the same lines as the HPR dropout, the DVL dropout is modelled as

$$p\left(\boldsymbol{v}_{\mathrm{D},k}\,|\boldsymbol{\nu}_k\right) = \mathcal{N}\left(\begin{bmatrix}0 & 0\end{bmatrix}^\top, \boldsymbol{\sigma}^2_{\mathrm{D,d}}\boldsymbol{I}\right). \tag{4.21}$$

4.3.4 DVL Bias

As described in the model of the DVL, the velocity measurement is conducted in the instrument frame and then transformed to the body frame, using the lever arm between the body and instrument frame and the corresponding orientation of the instrument frame. An alignment error of the instrument frame, that is, a deviation between the actual (installed) orientation and the configured orientation of the frame, and an error in the lever arm will cause a bearing and offset error of the measured velocity with respect to the actual velocity of the ROV, where the size of this error depends also on the ROV velocity. This problem has been observed in sea trials and should be included as an anomaly of the DVL. Since this error is unknown and time varying, a 1st-order Markov process can be used to model a DVL bias, that is

$$\dot{\boldsymbol{b}}_{\mathrm{DVL}} = -\boldsymbol{T}^{-1}_{\mathrm{DVL}}\boldsymbol{b}_{\mathrm{DVL}} + \boldsymbol{w}_{\mathrm{DVL}}, \tag{4.22}$$

where $\boldsymbol{b}_{\mathrm{DVL}} \in \mathbb{R}^2$ is the resulting bias of the DVL measurement, $\boldsymbol{T}_{\mathrm{DVL}}$ is a 2×2 diagonal time constant matrix, and $\boldsymbol{w}_{\mathrm{DVL}} \in \mathbb{R}^2$ is the driving noise of this process. It follows that the DVL measurement is biased from the ROV velocity according to

$$p\left(\boldsymbol{v}_{\mathrm{D},k}\,|\boldsymbol{\nu}_k, \boldsymbol{b}_{\mathrm{DVL}}\right) = \mathcal{N}\left(\begin{bmatrix}\boldsymbol{I}_{2\times 2} & \boldsymbol{0}_{2\times 2}\end{bmatrix}\boldsymbol{\nu}_k + \boldsymbol{b}_{\mathrm{DVL}}, \boldsymbol{\sigma}^2_{\mathrm{D}}\boldsymbol{I}\right). \tag{4.23}$$

4.3.5 Modes $\Delta^{\mathrm{THR},t,1}$ and $\Delta^{\mathrm{THR},t,2}$ – Insufficient Thrust and Zero Thrust

Thruster faults can have severe consequence on the ROV positioning control system, and relevant designs have been reported to prevent these; for example, the EKF-based

thruster fault detection in [Alessandri et al., 1999] and the fault accommodation design in [Omerdic and Roberts, 2004].

As described in Section 4.2.4, the ROV Minerva is installed with speed-commanded thrusters. Unfortunately, the speeds of the thrusters are not measured, and the propellers are therefore controlled in open-loop, implying an unknown error between the commanded and actual speeds of the thrusters. However, such thruster anomalies can be categorized into the following list of failure modes (Note: A more comprehensive description can be found in [Antonelli, 2003]):

1. The actual speed is slightly lower than the commanded speed, e.g. due to an aging problem of a propeller. Such a failure mode is typically small in size and can be very hard to detect by fault diagnosis. However, it can easily be handled by a robust controller, which alleviates this task from the FD design.

2. The actual speed is much lower than the commanded value, e.g. due to the propeller operations being restricted by seaweed or other objects. In this condition, the thrust loss becomes severe. This failure mode can be referred to as *insufficient thrust*, and assigned mode $\Delta^{\mathrm{THR},t,1}$ where $t \in \{\mathrm{l}, \mathrm{vp}, \mathrm{vs}, \mathrm{p}, \mathrm{s}\}$ is the index of thrusters.

3. The actual speed is zero; e.g., due to an object blocking the propeller, loss of power supply, or the fuse breaking. This is the most severe case. This failure mode is labelled *zero thrust*, assigned mode $\Delta^{\mathrm{THR},t,2}$.

We augment the state space with the vector $\begin{bmatrix} a_{\mathrm{l},k} & a_{vp,k} & a_{\mathrm{vs},k} & a_{\mathrm{p},k} & a_{\mathrm{s},k} \end{bmatrix} \in [0,1]^5$ to model the thrust loss according to these failure modes. This will represent the ratio between the desired control input $\boldsymbol{u}_{\mathrm{d},k} \in \mathbb{R}^{5\times 1}$ and the actual control input $\boldsymbol{u}_k \in \mathbb{R}^{5\times 1}$, using $\boldsymbol{u}_k = \mathrm{diag}\left\{\boldsymbol{\alpha}_k\right\} \boldsymbol{u}_{\mathrm{d},k}$. It follows that for the fault-free case all entries of $\boldsymbol{\alpha}_k$ are 1, for insufficient thrust one or more entries of $\boldsymbol{\alpha}_k$ are between 0 and 1, and for zero thrust one or more entries of $\boldsymbol{\alpha}_k$ are zero. Inserting this into the thruster model yields

$$\begin{aligned} \boldsymbol{\tau} &= \boldsymbol{T}\boldsymbol{K}\boldsymbol{u} \\ &= \boldsymbol{T}\boldsymbol{K}\mathrm{diag}\left\{\boldsymbol{\alpha}_k\right\}\left(\boldsymbol{K}^{-1}\boldsymbol{T}^{\dagger}\boldsymbol{\tau}_{\mathrm{d}}\right) \\ &= \boldsymbol{T}\mathrm{diag}\left\{\boldsymbol{\alpha}_k\right\}\boldsymbol{T}^{\dagger}\boldsymbol{\tau}_{\mathrm{d}}. \end{aligned} \tag{4.24}$$

4.3.6 Simultaneous Faults

The system model will transform to a combination of the corresponding models when faults happen simultaneously. Since there are 14 different failure modes modelled in the system, there may be be 2^{14} combinations of failure modes (including single fault cases and the fault-free case). However, some failure modes exclude others for the same equipment. For instance, the HPR can experience a fault-free, dropout, or outlier condition at any point in time. Hence, a particle in the filter representing the system mode of the HPR needs to have three states as opposed to 2^3 states. As a result, considering the exclusiveness among the failure modes, there can be a maxi-

Table 4.3: The Markov chain for the transition of modes $\Delta^{\mathrm{HPR},1}$ and $\Delta^{\mathrm{HPR},2}$.

			$\boldsymbol{\delta}^{(m)}$			
			$\Delta^{\mathrm{HPR},1}$	0	1	0
		$p_{\boldsymbol{\delta}^{(m)}\boldsymbol{\delta}^{(n)}}$	$\Delta^{\mathrm{HPR},2}$	0	0	1
$\boldsymbol{\delta}^{(n)}$	$\Delta^{\mathrm{HPR},1}$	$\Delta^{\mathrm{HPR},2}$	-	-	-	-
	0	0	-	0.75	0.75	0.75
	1	0	-	N/A	N/A	N/A
	0	1	-	0.25	0.25	0.25

mum of $3\,(\mathrm{HPR}) \times 3\,(\mathrm{DVL}) \times 3^5\,(\mathrm{Thrusters}) = 2187$ combinations of failure modes (including single fault cases and the fault-free case).

4.4 Navigation System Design

4.4.1 Separating the Heave and Yaw DOFs

Work by [Fossen, 2011] indicated that, for the ROV kinematic equation (4.16a) and kinetic equation (4.16b), the heave DOF is not coupled with the other three DOFs. Hence, the heave DOF is separately controlled and observed, and a KF is designed for this purpose. On the other hand, the faults of MTi have never been encountered in previous ROV sea trails; as such, they are not considered in this navigation design. And as mentioned, the heading of the ROV is estimated and used as an input to the particle filter.

4.4.2 Mode Transitions

Since the failure modes discussed in Section 4.3 are induced by different mechanisms, it is reasonable to assume that they are independent from each other. Hence, the mode transition Markov chain can also be designed independently for each equipment and then assembled. Table 4.3 shows the mode transition probabilities for the HPR failure modes, using

$$\Pr\left(\begin{bmatrix}\Delta_{k+1}^{\mathrm{HPR},1} & \Delta_{k+1}^{\mathrm{HPR},2}\end{bmatrix}^\top = \boldsymbol{\delta}^{(n)} \,\middle|\, \begin{bmatrix}\Delta_{k}^{\mathrm{HPR},1} & \Delta_{k}^{\mathrm{HPR},2}\end{bmatrix}^\top = \boldsymbol{\delta}^{(m)}\right) = p_{\boldsymbol{\delta}^{(m)}\boldsymbol{\delta}^{(n)}}. \tag{4.25}$$

The transition probabilities for $\begin{bmatrix}\Delta^{\mathrm{HPR},1} & \Delta^{\mathrm{HPR},2}\end{bmatrix} = [1\ 0]$ are not considered in this Markov chain since the system adopts the HPR dropout mode whenever the HPR measurement is not available in the last sampling interval. The probability of the HPR measurement being an outlier is set to 0.25, which is much higher than the rate of outliers in the experimental data; however, this probability is selected to balance the detectability and fault alarm rate.

Table 4.4: The Markov chain for the transition of modes $\Delta^{\mathrm{THR},t,1}$ and $\Delta^{\mathrm{THR},t,2}$, $t \in \{\mathrm{l}, \mathrm{vp}, \mathrm{vs}, \mathrm{p}, \mathrm{s}\}$.

				$\boldsymbol{\delta}^{(m)}$		
			$\Delta^{\mathrm{THR},t,1}$	0	1	0
		$p_{\boldsymbol{\delta}^{(m)}\boldsymbol{\delta}^{(n)}}$	$\Delta^{\mathrm{THR},t,2}$	0	0	1
	$\Delta^{\mathrm{THR},t,1}$	$\Delta^{\mathrm{THR},t,2}$	-	-	-	-
$\boldsymbol{\delta}^{(n)}$	0	0	-	0.4	0.4	0.4
	1	0	-	0.4	0.4	0.4
	0	1	-	0.2	0.2	0.2

For the DVL failure modes - $\Delta^{\mathrm{DVL},1}$ and $\Delta^{\mathrm{DVL},2}$, the DVL dropout is handled in the same way as the HPR dropout; that is, the DVL measurement adopts (4.21) whenever its measurement is not available, while the DVL bias has been modelled as an additional state of the system. Hence, there is no probabilistic mode switching for the DVL.

The mode transition probabilities for the thruster modes are given in Table 4.4, using

$$\Pr\left(\left[\Delta_{k+1}^{\mathrm{HPR},1} \quad \Delta_{k+1}^{\mathrm{HPR},2}\right]^{\top} = \boldsymbol{\delta}^{(n)} \,\middle|\, \left[\Delta_{k}^{\mathrm{HPR},1} \quad \Delta_{k}^{\mathrm{HPR},2}\right]^{\top} = \boldsymbol{\delta}^{(m)}\right) = p_{\boldsymbol{\delta}^{(m)}\boldsymbol{\delta}^{(n)}}. \tag{4.26}$$

The total mode transition Markov chain is then obtained by combining the two Markov chains (4.25) and (4.26), assuming they are independent.

4.4.3 Switching Mode HMM for the ROV

The system mode vector is first constructed

$$\boldsymbol{\Delta} = \left[\Delta^{\mathrm{HPR},1} \quad \Delta^{\mathrm{HPR},2} \quad \Delta^{\mathrm{DVL},1} \quad \boldsymbol{\Delta}^{\mathrm{THR},1} \quad \boldsymbol{\Delta}^{\mathrm{THR},2}\right]^{\top}, \tag{4.27}$$

where $\boldsymbol{\Delta}^{\mathrm{THR},1}$ and $\boldsymbol{\Delta}^{\mathrm{THR},2}$ are vectors consisting of three components representing the condition of the three horizontal thrusters. The mode transition Markov chain subjects to the combination of Equations (4.25) and (4.26), that is,

$$\Pr\left(\boldsymbol{\Delta}_{k+1} = \boldsymbol{\delta}^{j} \,\middle|\, \boldsymbol{\Delta}_{k+1} = \boldsymbol{\delta}^{i}\right) = p_{ij}. \tag{4.28}$$

Augmenting the DVL bias state (4.22), (4.23) and the model of the thruster failure modes into (4.16), yields the overall model (4.29), where $\rho(\cdot)$ is the Dirac delta function.

By separating heave DOF from the model, and using the heading estimation $\psi_{\mathrm{M},k}$ from the nonlinear complementary filter as input to the particle filter, the model (4.29) can then be shrunk and discretized as the switching mode HMM

$$p\left(\boldsymbol{x}_{k+1} \,|\boldsymbol{x}_k, \psi_{\mathrm{M},k}, \boldsymbol{\tau}_{\mathrm{d},k}, \boldsymbol{\delta}_k\right) = f^{*}\left(\boldsymbol{x}_k, \psi_{\mathrm{M},k}, \boldsymbol{\tau}_{\mathrm{d},k}, \boldsymbol{\delta}_k\right) \tag{4.30}$$

$$p\left(\boldsymbol{y}_k \,|\boldsymbol{x}_k, \boldsymbol{\delta}_k\right) = h^{*}\left(\boldsymbol{x}_k, \boldsymbol{\delta}_k\right). \tag{4.31}$$

$$\dot{\boldsymbol{\eta}} = \boldsymbol{R}(\psi)\,\boldsymbol{\nu} \tag{4.29a}$$

$$\begin{aligned}\boldsymbol{M}\dot{\boldsymbol{\nu}} =& -\boldsymbol{C}_{\mathrm{RB}}(\boldsymbol{\nu})\,\boldsymbol{\nu} - \boldsymbol{C}_{\mathrm{A}}(\boldsymbol{\nu}_{\mathrm{r}})\,\boldsymbol{\nu}_{\mathrm{r}} - \boldsymbol{D}_{\mathrm{NL}}(\boldsymbol{\nu}_{\mathrm{r}})\,\boldsymbol{\nu}_{\mathrm{r}} - \boldsymbol{D}_{\mathrm{L}}\boldsymbol{\nu} \\ & - \boldsymbol{g}(\boldsymbol{\eta}) + \boldsymbol{T}\mathrm{diag}\{\boldsymbol{\alpha}_k\}\left(\boldsymbol{T}^{\dagger}\boldsymbol{\tau}_{\mathrm{d}}\right) + \boldsymbol{w}_{\nu}\end{aligned} \tag{4.29b}$$

$$\dot{\boldsymbol{\nu}}_{\mathrm{c}} = -\boldsymbol{T}_{\mathrm{c}}^{-1}\boldsymbol{\nu}_{\mathrm{c}} + \boldsymbol{w}_{\mathrm{c}}, \tag{4.29c}$$

$$\dot{\boldsymbol{b}}_{\mathrm{DVL}} = -\boldsymbol{T}_{b_{\mathrm{DVL}}}^{-1}\boldsymbol{b}_{\mathrm{DVL}} + \boldsymbol{w}_{b_{\mathrm{DVL}}} \tag{4.29d}$$

$$p\left(a_{\mathrm{t},k}\right) = \begin{cases} \rho\left(a_{\mathrm{t},k}-1\right) & ,\begin{bmatrix}\Delta^{\mathrm{THR,t,1}} & \Delta^{\mathrm{THR,t,2}}\end{bmatrix} = \begin{bmatrix}0 & 0\end{bmatrix} \\ U(0,1) & ,\begin{bmatrix}\Delta^{\mathrm{THR,t,1}} & \Delta^{\mathrm{THR,t,2}}\end{bmatrix} = \begin{bmatrix}1 & 0\end{bmatrix} \\ \rho\left(a_{\mathrm{t},k}\right) & ,\begin{bmatrix}\Delta^{\mathrm{THR,t,1}} & \Delta^{\mathrm{THR,t,2}}\end{bmatrix} = \begin{bmatrix}0 & 1\end{bmatrix}\end{cases},\ t \in \{\mathrm{l},\mathrm{p},\mathrm{s}\}. \tag{4.29e}$$

$$p\left(\boldsymbol{p}_{\mathrm{A}}\,|\boldsymbol{\eta}\right) = \begin{cases} \mathcal{N}\left(\begin{bmatrix}\boldsymbol{I} & \boldsymbol{0}\end{bmatrix}\boldsymbol{\eta}, \boldsymbol{\Sigma}_{\mathrm{A}}\right) & ,\begin{bmatrix}\Delta^{\mathrm{HPR},1} & \Delta^{\mathrm{HPR},2}\end{bmatrix} = \begin{bmatrix}0 & 0\end{bmatrix} \\ \mathcal{N}\left(\begin{bmatrix}0 & 0\end{bmatrix}^{\top}, \sigma_{\mathrm{A,d}}^2\boldsymbol{I}\right) & ,\begin{bmatrix}\Delta^{\mathrm{HPR},1} & \Delta^{\mathrm{HPR},2}\end{bmatrix} = \begin{bmatrix}1 & 0\end{bmatrix} \\ \mathcal{N}\left(\begin{bmatrix}\boldsymbol{I} & \boldsymbol{0}\end{bmatrix}\boldsymbol{\eta}, \sigma_{\mathrm{A,o}}^2\boldsymbol{I}\right) & ,\begin{bmatrix}\Delta^{\mathrm{HPR},1} & \Delta^{\mathrm{HPR},2}\end{bmatrix} = \begin{bmatrix}0 & 1\end{bmatrix}\end{cases} \tag{4.29f}$$

$$p\left(\boldsymbol{v}_{\mathrm{D}}\,|\boldsymbol{\nu}\right) = \begin{cases} \mathcal{N}\left(\begin{bmatrix}\boldsymbol{I} & \boldsymbol{0}\end{bmatrix}\boldsymbol{\nu} + \boldsymbol{b}_{\mathrm{DVL}}, \sigma_{\mathrm{D}}^2\boldsymbol{I}\right) & ,\Delta^{\mathrm{DVL},1} = 0 \\ \mathcal{N}\left(\begin{bmatrix}0 & 0\end{bmatrix}^{\top}, \sigma_{\mathrm{D,d}}^2\boldsymbol{I}\right) & ,\Delta^{\mathrm{DVL},1} = 1\end{cases} \tag{4.29g}$$

$$p\left(\psi_{\mathrm{M},k}\,|\boldsymbol{\eta}_k\right) = \rho\left(\psi_{\mathrm{M},k} - \begin{bmatrix}0 & 0 & 0 & 1\end{bmatrix}\boldsymbol{\eta}_k\right), \tag{4.29h}$$

where $\boldsymbol{x} = \begin{bmatrix}\boldsymbol{p}_k & \boldsymbol{v}_k & \boldsymbol{v}_{\mathrm{c},k} & \boldsymbol{b}_{\mathrm{DVL,k}}\end{bmatrix}$, $\boldsymbol{y} = \begin{bmatrix}\boldsymbol{p}_{\mathrm{A,k}} & \boldsymbol{v}_{\mathrm{D,k}}\end{bmatrix}$, and $f^*(\cdot)$ and $h^*(\cdot)$ are the mappings corresponding to (4.29).

4.5 Full-scale Test Campaign

The full-scale test was performed on October 17-18, 2012, in Trondheimsfjord, Trondheim, Norway. The test focused on the performance of the proposed FDPF-based navigation filter in terms of real environment disturbance, real sensor measurement, and its cooperation with the ROV control system and the ROV itself.

4.5.1 Setup

System structure

The FDPF-based navigation filter is deployed in the control system of the ROV Minerva. The architecture of the ROV control system was described in [Dukan et al., 2011] and is depicted in Figure 4.6. Referring to this figure, the control system is realized in the cRIO digital controller by National Instruments and the Host PC located in the ROV control center onboard the RV Gunnerus, with communication of command and feedback signals through an umbilical connection. The user interface control panel that runs on the Host PC, which is connected to the controller through Ethernet, is used to command and monitor the ROV. Besides the FDPF-based navigation filter, a Kalman-filter-based navigation filter ([Dukan et al., 2011]), runs in parallel, but in open-loop, as comparison.

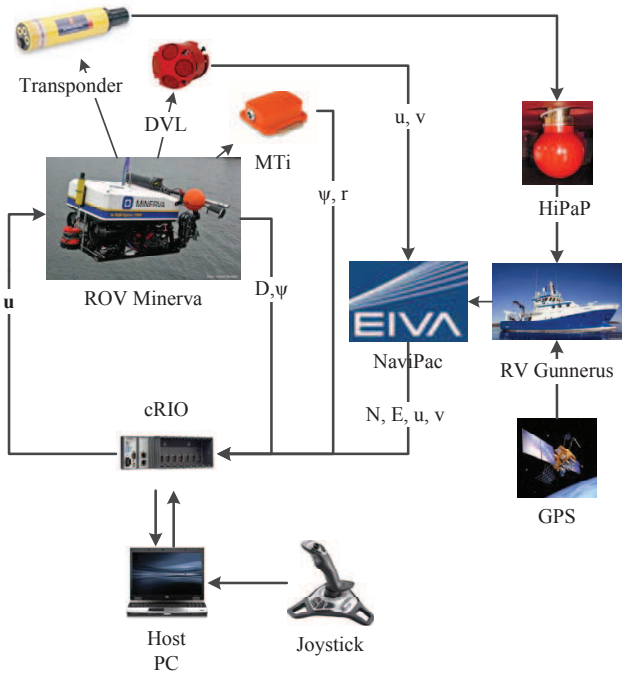

Figure 4.6: ROV control system architecture: Signal communication overview.

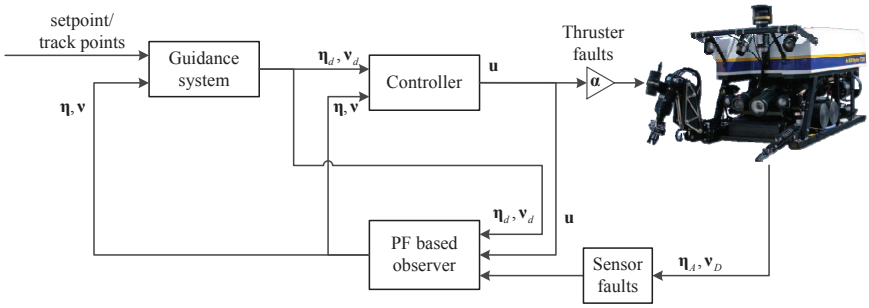

Figure 4.7: ROV control system architecture: Block diagram of the control system. Note that the functionality has been implemented to trigger the thruster and sensors failure modes to ensure that the failure testing more predictable and practical.

Triggering faults

Functionality has been implemented to manually set the relevant thruster and sensor failure modes, as per Figure 4.7, and the list is as following:

- HPR outliers: A random number is added to the current HPR measurement, taken from a 2-dimensional multivariate normal distribution with zero mean and tunable variance.

Table 4.5: Particle filter parameters in the experiment

Parameter			**Value**
Item	notation	unit	
System noise - velocity	$\boldsymbol{w}_v$	$[\mathrm{m/s}]$	$\sim \mathcal{N}(\mathbf{0}, 0.002\boldsymbol{I})$
Time constant - current	$\boldsymbol{T}_c$	$[\mathrm{s}]$	$0.01\boldsymbol{I}$
Driving noise - current	$\boldsymbol{w}_c$	$[\mathrm{m/s}]$	$\sim \mathcal{N}(\mathbf{0}, 0.01\boldsymbol{I})$
Time constant - DVL bias	$\boldsymbol{T}_{b_{\mathrm{DVL}}}$	$[\mathrm{s}]$	$0.01\boldsymbol{I}$
Driving noise - DVL bias	$\boldsymbol{w}_{b_{\mathrm{DVL}}}$	$[\mathrm{m/s}]$	$\sim \mathcal{N}(\mathbf{0}, 0.01\boldsymbol{I})$
Measurement noise variance - DVL	σ_{D}	$[\mathrm{m^2/s^2}]$	$(0.02)^2$
Measurement noise covariance - HPR[2]	$\boldsymbol{\Sigma}_{\mathrm{A}}$	$[\mathrm{m^2}]$	$(0.2\boldsymbol{I})^2$
Measurement noise covariance - HPR outliers	$\boldsymbol{\Sigma}_{\mathrm{A,o}}$	$[\mathrm{m^2}]$	$(3\boldsymbol{I})^2$

- HPR dropout: Short-term (e.g., less than 10 sec) dropout of the HPR happens frequently in normal operation. Long-term dropout is triggered such that the HPR measurement is frozen to the last value.
- DVL dropout: The DVL measurement is frozen to the last value.
- DVL bias: A tunable constant bias is added to the DVL measurement.
- Loss of thrust: The thruster failure modes are activated by setting the gain $\boldsymbol{\alpha}_k$ in $\boldsymbol{u}_k = \mathrm{diag}\{\boldsymbol{\alpha}_k\}\,\boldsymbol{u}_{\mathrm{d},k}$.

Parameters

In the test trial 200 particles were used in the PF. The mode transition Markov chain probabilities are shown in Tables 4.3 and 4.4. Other parameters were set according to Table 4.5.

4.5.2 Discussion of the Results

Figures 4.8 to 4.19 show the results from the ROV sea trial according to the notations listed in Table 4.6.

Basic Navigation

The output from the use of the FDPF for state estimation of the ROV are shown in Figures 4.8 and 4.9. In this test the ROV was controlled to move counter-clockwise along a triangular path in three straight-line segments, with heading along the path. As can be observed, the HPR measurement suffered from outliers, and its update rate

[2]In some experiment cases, the covariance of the HPR measurements noise $\boldsymbol{\Sigma}_{\mathrm{A}}$ is set to this constant instead on update online though Equation 4.10.

Table 4.6: Notations in the experimental results figures

Notation	Meaning
N, E	North and East position.
u, v	Surge and sway velocity.
subscript $\square_{\mathrm{e}}$	FDPF estimate.
subscript $\square_{\mathrm{d}}$	Desired position/velocity from the guidance system.
subscript $\square_{\mathrm{o}}$	Measurement without triggered failure modes.
subscript $\square_{\mathrm{off}}$	Estimation from the sector heading KF in open-loop [Dukan et al., 2011]).
$1\bar{\sigma}$	1σ upper bound of the FDPF estimate.
$1\underline{\sigma}$	1σ lower bound of the FDPF estimate.

is much lower than the sampling frequency of the control system. However, the state estimate produced by the FDPF was generally good, which verifies its effectiveness as a state observer exposed to a non-uniform measurement update rate and measurement outliers. The state estimation performance of the particle filter was similar to the Kalman filter, but a small high-frequency oscillation was observed due to tuning.

Outliers

The state estimation will be affected if the outliers in the measurements are not detected and handled. For instance, an outlier was triggered, as shown in Figure 4.10 and detected by the FDPF. Hence, the FDPF state estimate was not affected, while the estimate of the open-loop KF was displaced. Outliers of different sizes were triggered during an ROV position-keeping test trial, and the statistics of the outlier detection were calculated as presented in Figure 4.12. Obviously, the detection rate increased as the size of the outliers became larger. The smaller sized outliers, on the other hand, exhibited a lower detection rate. This is mainly due to the long update interval of the HPR, which resulted in increasing uncertainty of the actual ROV position and less possibility of distinguishing small outliers from the measurement. This phenomenon can be more explicitly observed in Figure 4.13, making it clear that a small outlier in the measurement $2\mathrm{m}$ in size, for example, can not be distinguished from a fault-free measurement.

Figure 4.11 shows a typical response of outlier detection during an ROV position-keeping experiment. The FDPF detected the majority of the large-sized outliers but struggled to detect the smaller ones, especially when the outlier was slightly larger but close to the 1σ boundary.

HPR dropout

Figure 4.13 shows the performance of the FDPF when the HPR dropped out for about 30 sec while the ROV was moving straight in an eastern direction. As previously

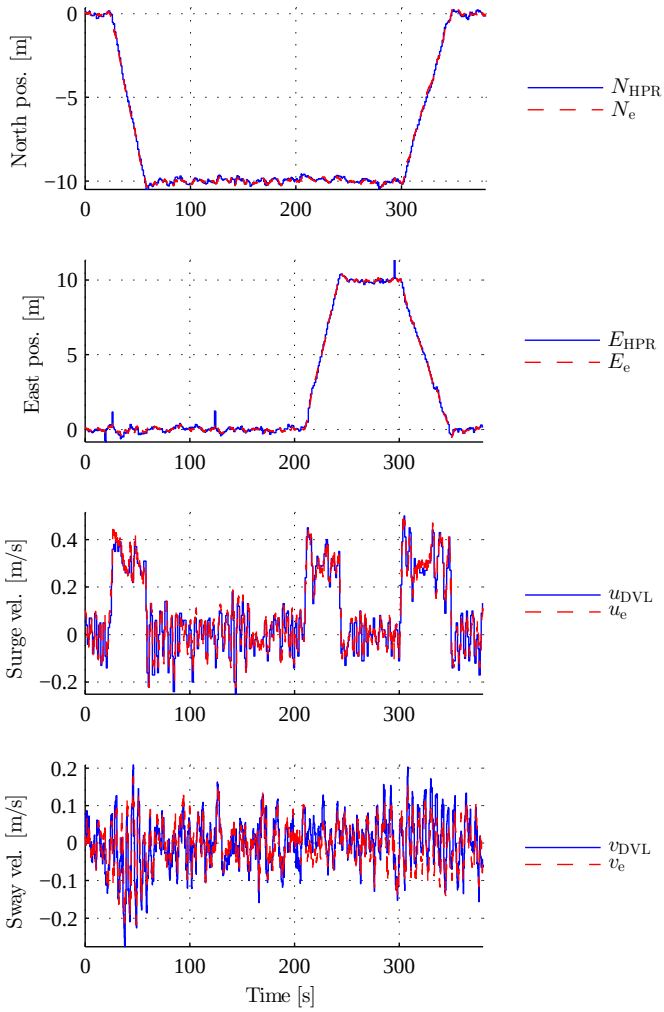

Figure 4.8: Basic state estimation results when the ROV followed a triangular path with heading along the path. No faults occurred during this test. Note that the outliers seen in the position measurement were detected and handled by the FDPF.

discussed, the HPR dropout does not have to be diagnosed, since it is handled within the non-uniform sampling interval mechanism, even for such a long interval. All the while, the FDPF outputs a steady stream of position estimates. In state-of-the-art observers, this is typically achieved by entering a "dead-reckoning" mode, see [Sørensen, 2012], such that the position is estimated open-loop based on the thrust force and, possibly, velocity measurement. When the position measurement drops out for the ROV here, the variance of the estimation cannot be reduced by new position information and the uncertainty of the estimation grows due to system noise. This is observed by by the increasing distance between the upper and lower 1σ bounds. The

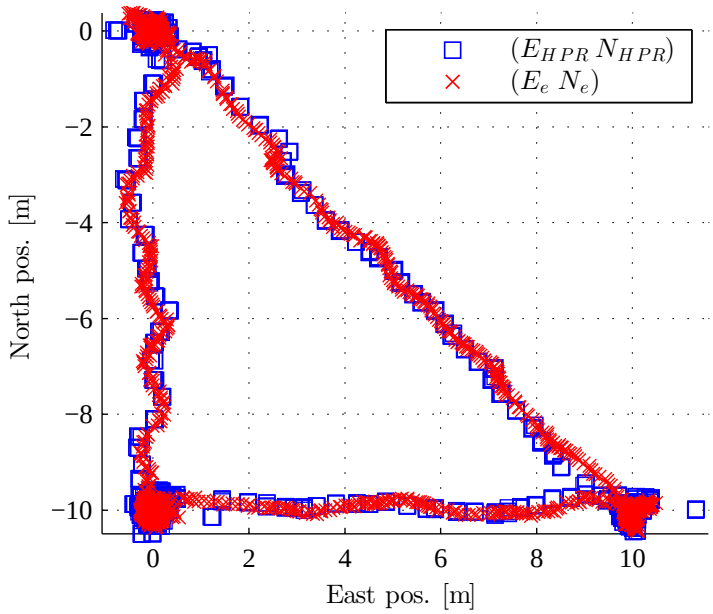

Figure 4.9: 2D plot of the position measurement PF estimate.

estimated position during the dropout is shown to be close to the original fault-free measurement, and this confirms the good "dead-reckoning" capability of the FDPF.

DVL dropout

When the DVL drops out, the state estimation is based on the thrust force command and the HPR measurement. The performance of the FDPF is for this case presented in Figure 4.14. The output shows that the estimated velocity was satisfactorily close to the original fault-free measured velocity during the DVL dropout. Similar to the HPR dropout case, the variance of the velocity estimation started to increase during the DVL dropout. However, this increase only lasted for approximately three seconds, at which point it seemed to settle at a stationary value. This can be explained by the Bayesian properties of the PF, in that the particles with estimated velocity that are significantly different from the actual velocity will not be supported by the observations since these will also yield a large difference between the estimated position and the measured position. This is a back propagation of information principle for the PF.

DVL bias

In the sea trial, a DVL bias was triggered in the ROV surge direction while the ROV was in position-keeping operation. The bias was first increased slowly in steps before being decreased back to 0. The corresponding experimental responses are shown in

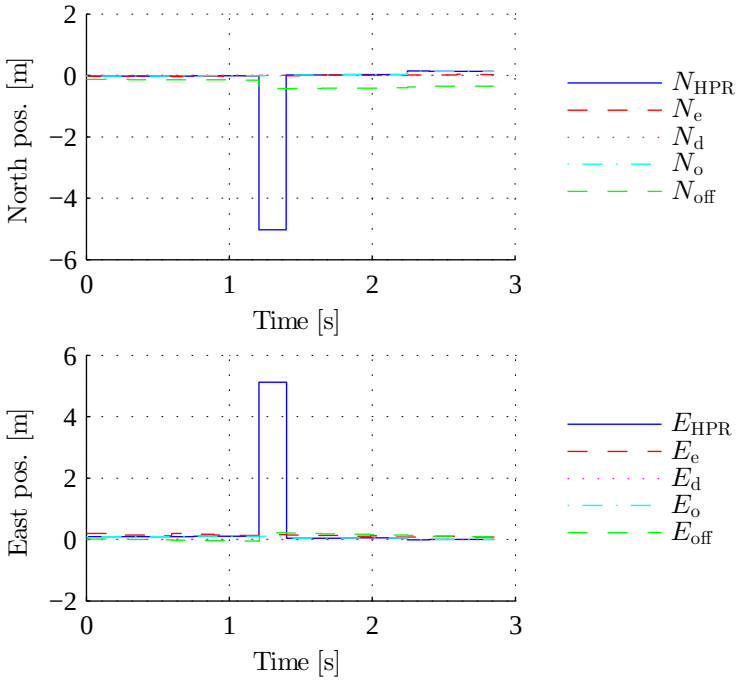

Figure 4.10: Comparison of the position estimates by the PF and KF after triggering an outlier in the position measurement. The size of the outlier was about 7 meters.

Figure 4.15 and in more detail in Figure 4.16. The bias estimate is close to the value of the manually triggered failure mode, especially if taking the variances of the DVL measurement noise and the system noise into account. This indicates that the DVL bias was well diagnosed by the proposed algorithm.

Insufficient thrust and zero thrust

The reduced-thrust failure mode was tested by decreasing the thrust from the two surge-directed thrusters to a certain percentage, as shown in the third graph in Figure 4.17, in such a way as to avoid the ROV from spinning in a potentially dangerous manner. The estimation and detection results from the test are shown in Figure 4.17, in which the responses of the offline KF are also compared. This illustrates the effect of using a faulty control input to a "nominal" state observer where, in this case, the KF estimates rapidly diverged from the true state when the failure modes were triggered, even with fault-free position and velocity sensors. The use of the FDPF, which is designed to detect and handle such cases, resulted in good state estimates during these failure modes, confirming the robustness of the proposed navigation algorithm.

Investigating the detection result in the fourth graph in Figure 4.17 during the (middle) position-keeping period of this test, shows that there were many false detections. The

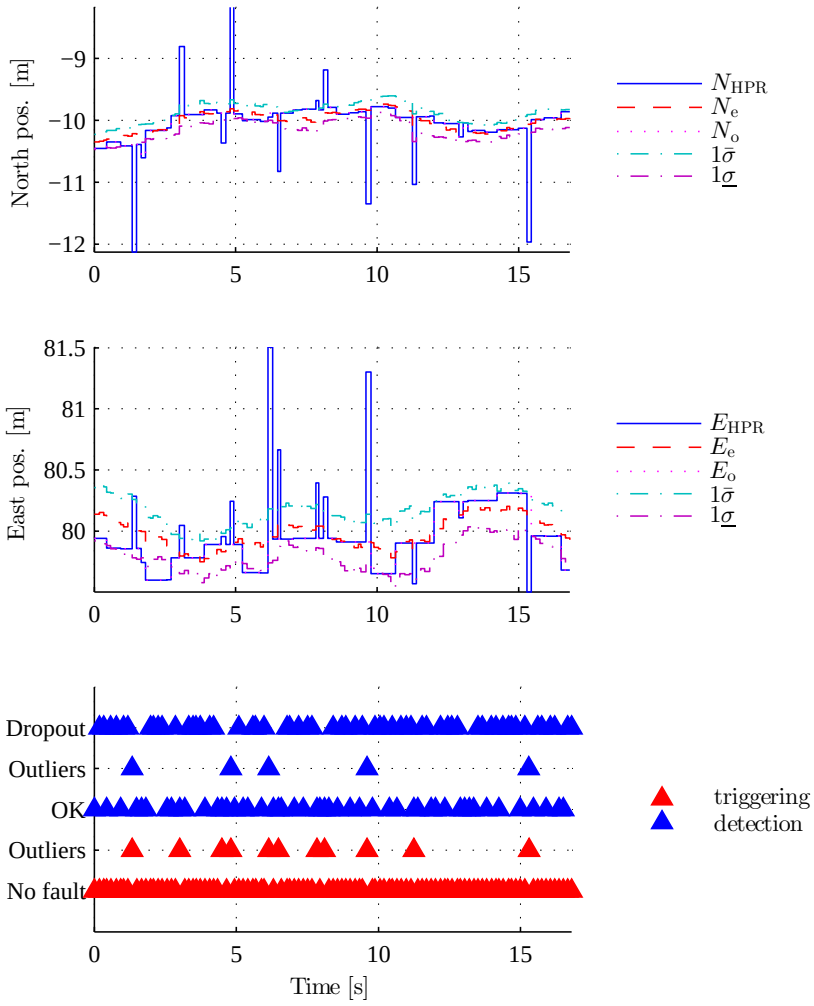

Figure 4.11: Position estimation and outliers detection result by the PF, when the ROV was performing position keeping. The third plot shows the time serial of fault triggering and detection.

reasons for this, when performing position-keeping or low speed manoeuvring, is the small utilized thrust forces that result in an insignificant difference between the fault-free condition and the insufficient/zero thrust failure mode. Hence, it becomes difficult to correctly detect these thrust failure modes in such operations; although the effect of such false detections on the control performance is negligible.

The FDPF failed to provide a distinct detection of the failure modes when the reduced thrust was triggered. The detection was only manifested in that the zero thrust and insufficient thrust modes seemed to appear more frequently than the fault-free conditions. However, the last graph of Figure 4.17 shows the time cumulations of the zero

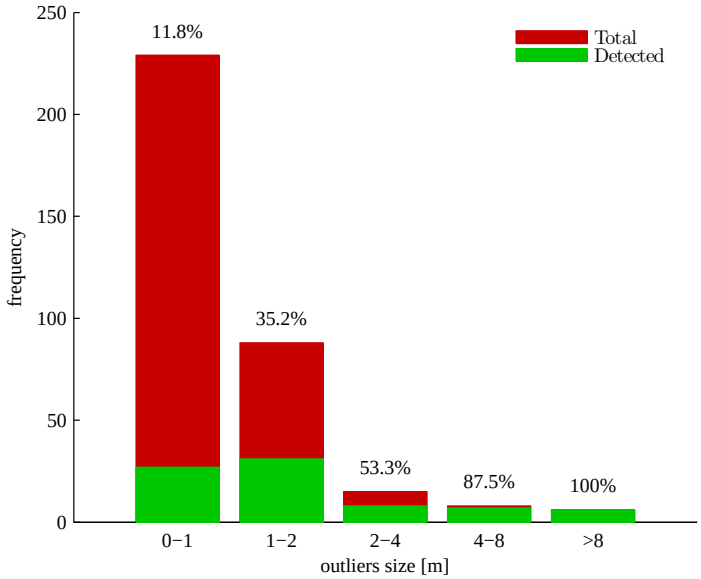

Figure 4.12: Detection success of the outliers classified by their size (offset from the original true measurement).

thrust and insufficient thrust modes, which are adjusted by regression constants to ensure they stay close to zero during, for example, the ROV position-keeping period. During the fault, on the other hand, it obviously increased. Thresholding methods can be applied to these cumulations to give a more correct detection result.

Multiple failure modes

Two combinations of multiple failure modes were tested. Figure 4.18 shows the state estimation when the DVL drops out during a period of HPR dropout. When both the HPR and DVL are lost, the FDPF estimates the states only based on the command to the thrusters. At the end of the 30 sec HPR dropout interval, the position estimate had deviated approximately 1 m from the measurement, while the velocity estimate was generally good. The variance of the velocity estimation increased rapidly when both sensors were lost, since no new information to update the filter was received.

The other multiple failure mode test assessed the system response to HPR outliers during a DVL dropout period, and the results are shown in Figure 4.19. When HPR outliers occur during a DVL dropout, the variance of the position estimate becomes large, and this makes detection of outliers increasingly difficult. The results were consistent with the results from the single failure HPR outliers case in that the majority of large-sized outliers were detected well but smaller outliers were detected less efficiently. However, the position and velocity estimation was, again, generally good. In this case, one should also notice that the variance of the velocity estimation did not

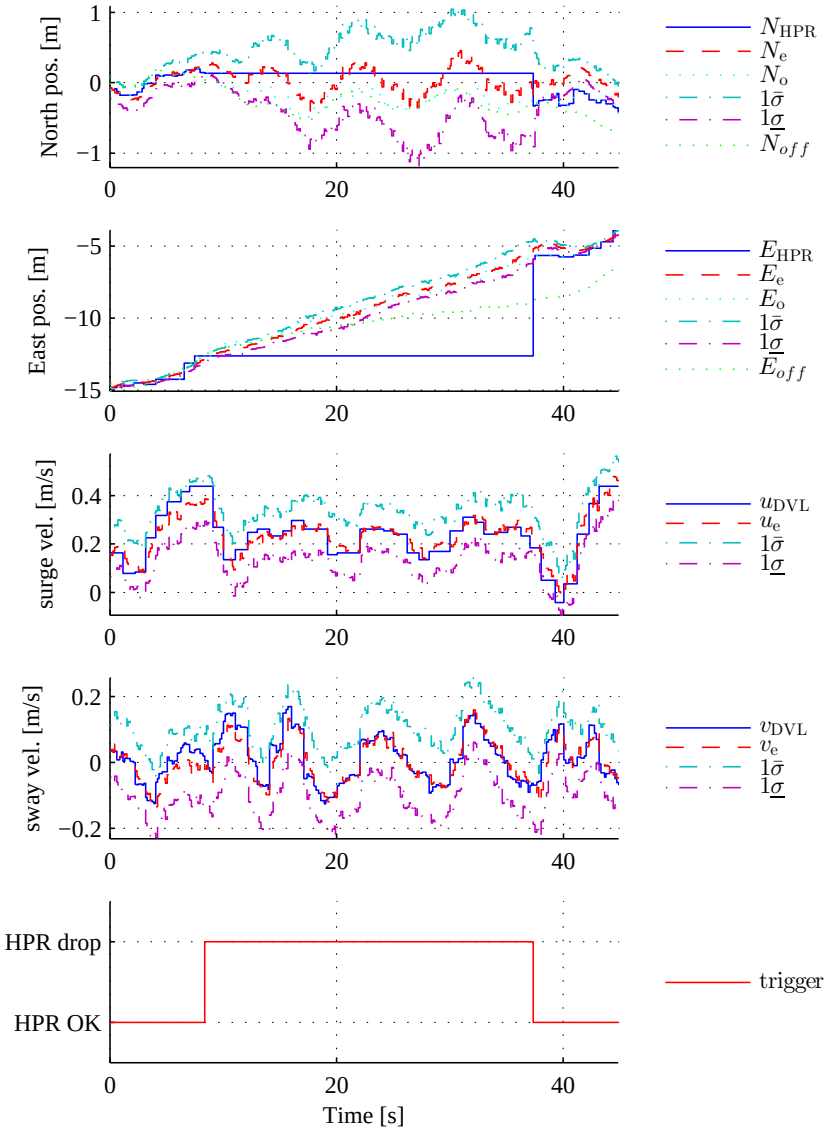

Figure 4.13: Position and velocity measurements and state estimate responses during sensor dropouts when the ROV was moving straight forward: Responses when triggering HPR dropout.

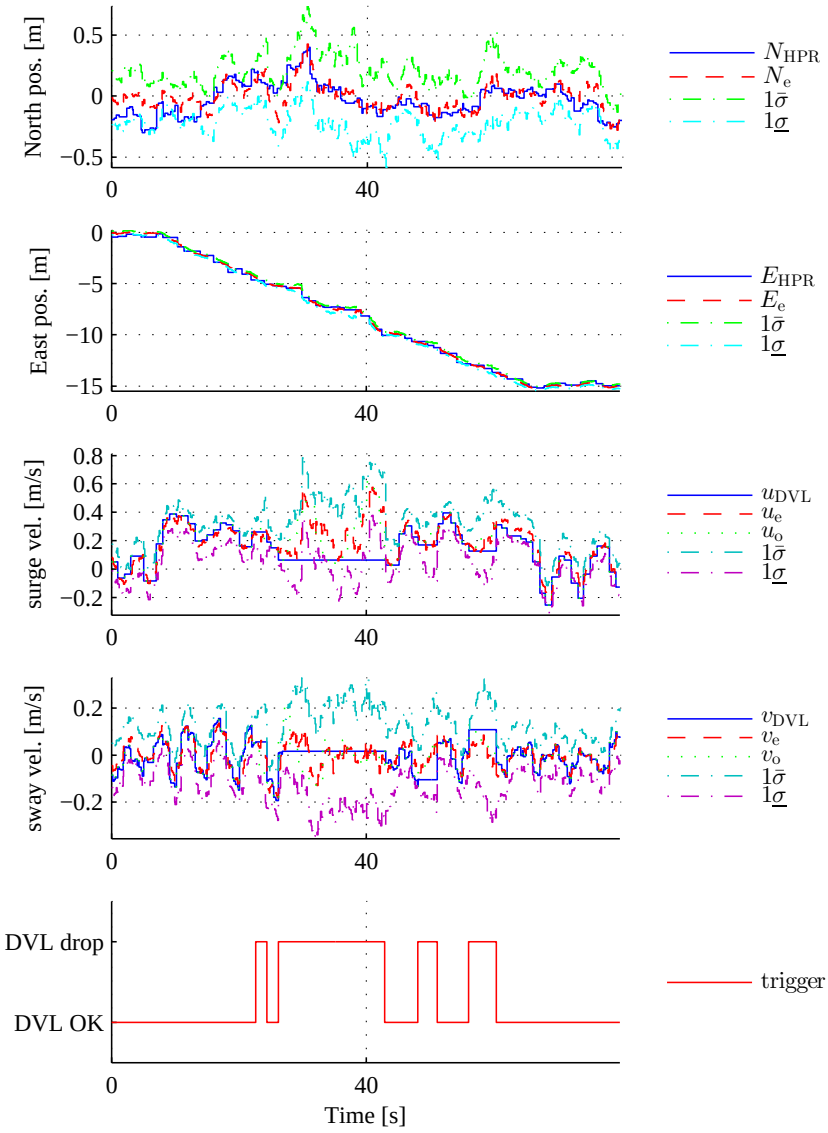

Figure 4.14: Position and velocity measurements and state estimate responses during sensor dropouts when the ROV was moving straight forward: Responses when triggering DVL dropout.

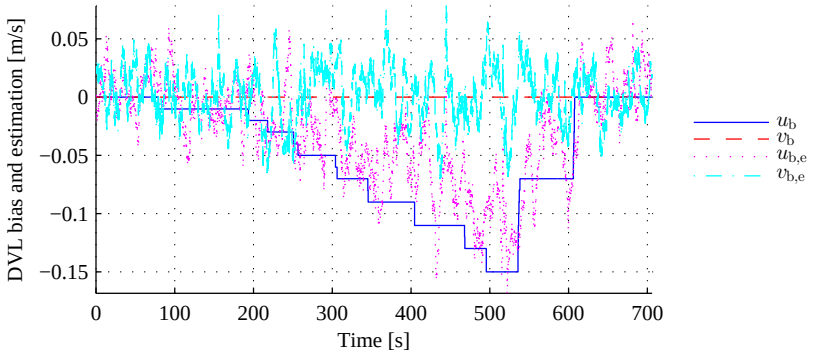

Figure 4.15: The triggered DVL bias and its estimate.

increase as much as in the previous multiple failure case (but more than the fault-free case) since the information from the HPR was backward propagated to the velocity estimation through the system model.

4.6 Conclusion

In this chapter, the proposed particle filter-based algorithm was applied for fault diagnosis (FDPF) to robustify the navigation of an ROV, in which case the navigation sensors and thrusters are vulnerable and fault diagnosis is essential. The design was tested in a full-scale ROV sea trial. The design process and test responses have been presented and discussed in detail in this paper. The experimental results confirmed that the performance of the fault diagnosis was generally good and that the proposed algorithm provided robust and efficient state estimation for the ROV under different combinations of failure modes, signal artefacts and disturbances.

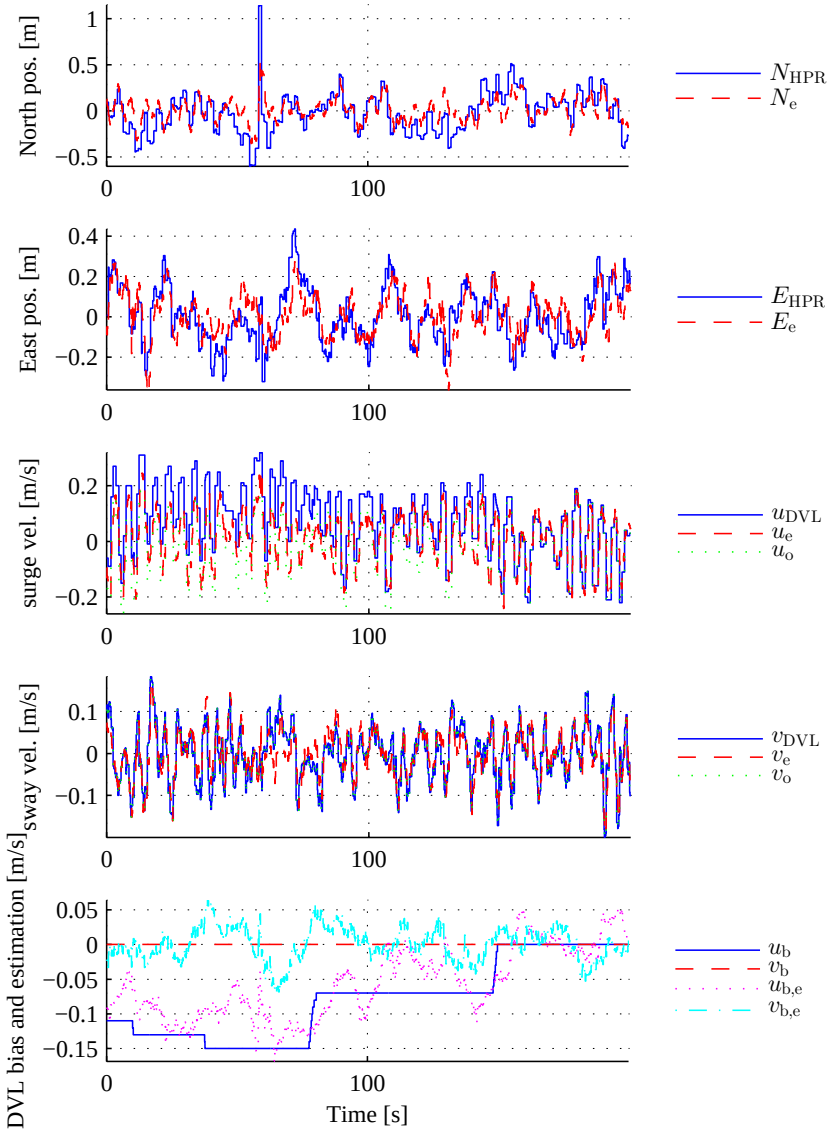

Figure 4.16: Measured and estimated position and velocity with DVL bias, where the last graph shows the triggered DVL bias and its estimate.

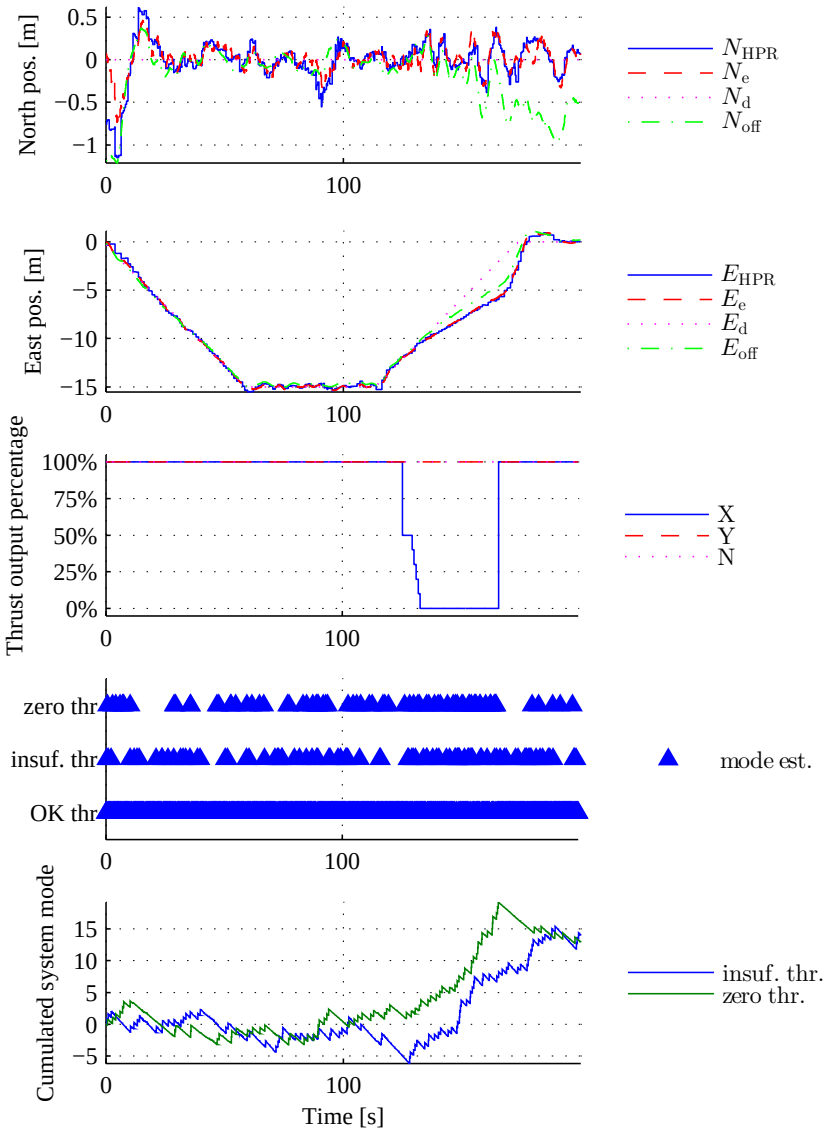

Figure 4.17: The first two graphs show the measured and estimated position and velocity during an insufficient thrust failure modes, the third graph shows the size of the triggered failure modes, the fourth graph shows the detection result, and the last graph shows the cumulative system mode.

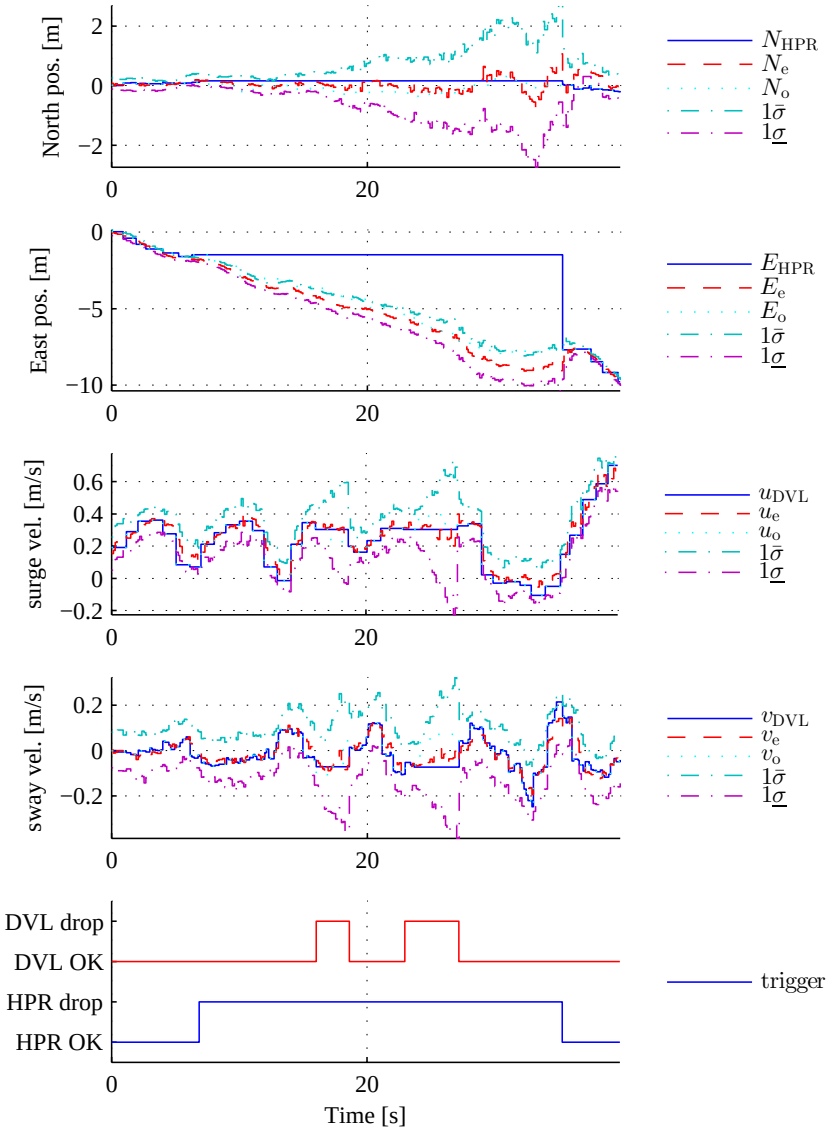

Figure 4.18: Test results for simultaneous HPR and DVL dropout.

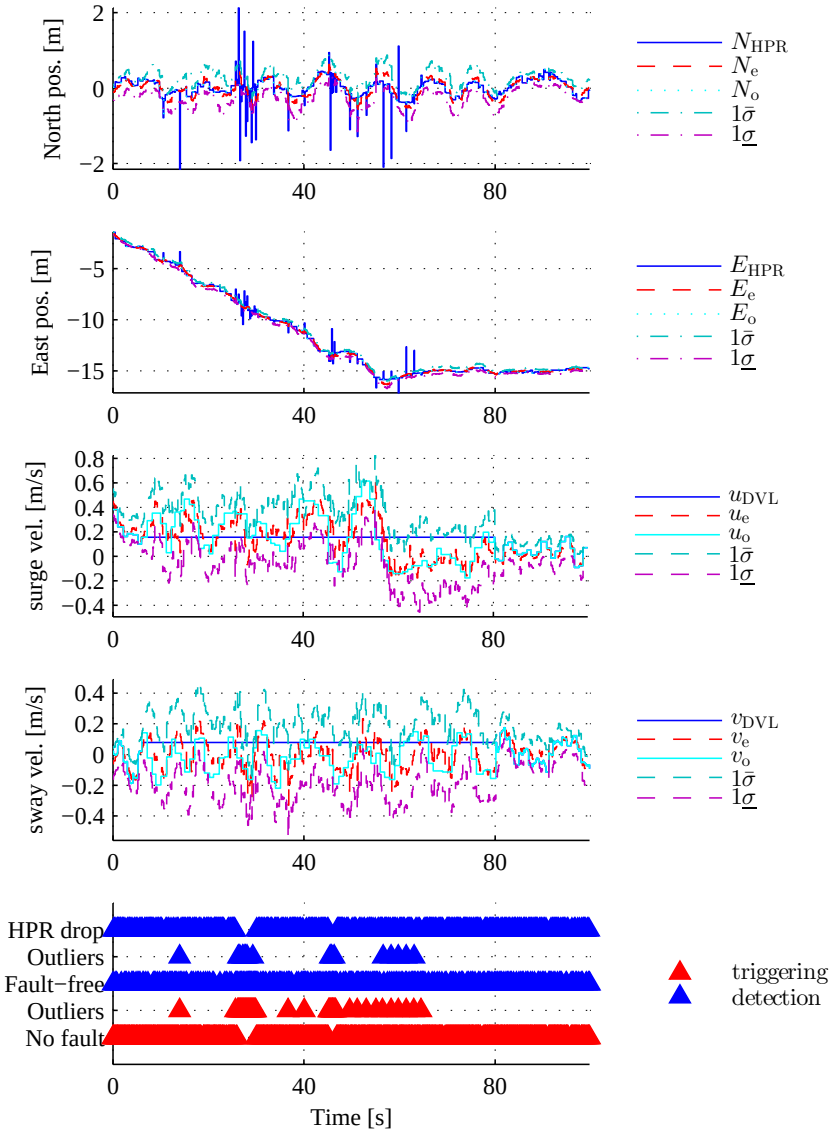

Figure 4.19: Test results for simultaneous HPR outliers during DVL dropout.

Chapter 5

Conclusion and Future Work

This thesis studied the possibility of using a particle filter as a failure observer to detect and diagnose failures in nonlinear systems. The paper briefly reviewed existing filtering technology and introduced the particle filter. Then the particle filter was studied and extensively employed in fault detection and diagnosis (FDD) on a mode-switching hidden Markov model (HMM). The system mode was used to denote the status of the system: fault-free or in a predefined failure mode. Following this, the FDD problem was transformed into an estimation problem. The outputs revealed system failures can be detected as long as the system mode and system states are correctly estimated.

The PF-based FDD method is practical. Two applications of this method were reviewed in detail. In the case of PF-based DP fault tolerant navigation, the PF-based navigation effectively detected and tolerated the common failure modes of the DP position reference sensors. At the same time, the wave filtering performance of the PF-based navigation was better than the conventional method.

The PF-based ROV robust navigation approach takes into consideration the whole ROV, from the actuator to the sensors. The experiment showed that the PF-based navigation scheme is capable of detecting and diagnosing the failure modes of the position and velocity measurements, and the failures in the thrusters of the ROV.

The main advantage of the PF-based FDD is its flexibility. Since PF-based FDD copes with switching mode HMM, which is very general, we can inherit most of the modelling experience from the previous work, and simply transfer it into a switching mode HMM. In addition, because of the flexibility of the system, the modification work is not significant when the system design changes. For examples, if a new sensor is added to the system under consideration, only the measurement mapping and the mode transition Markov chain need augmenting, and the whole FDD scheme does not need to be redesigned.

Another feature of the PF-based FDD is that it synthesizes fault detection and diagnosis tasks into a single process. As previously pointed out, FDD is performed by estimating the system mode and states.

Sensor fusion is a common problem that should be taken into consideration when performing FDD. In this thesis, in the DP navigation study case, the fusion of three position reference sensors was considered; in the ROV navigation study case, fusion of position and velocity sensor was considered. Moreover, the results indicated that there is significant potential to fuse a larger amount of sensors with PF. It is easy and favourable to use PF to handle the sensor fusion problem.

Two issues need to be resolved to make better use of this method:

1. The probabilities in system mode transition Markov Chain (3.5) need proper tuning. It has been observed in simulations that these probabilities affect the sensitivity of the PF-based FDD. That is, when the probability that a system will transfer from fault-free mode to a failure mode is low, the PF is insensitive to the failure mode. This may lead to misdetection, especially when the failure mode occurs isolated in time, as is the case with outliers. On the other hand, when the transition probability from the fault-free mode to a failure mode is high, the PF may be over sensitive to the failure mode. This can result in a misdiagnosis or sometimes further divergence of the estimation. Hence, it is important to develop a proper design process for the transition matrix.
2. This thesis briefly studied the efficiency problem of the PF. However, the efficiency of PF when it is running on switching mode HMM was not studied. The questions regarding this can be:
   (a) If sampling importance resample PF is still applied, what type of proposal distribution is particularly suitable for FDD on switching mode HMM?
   (b) Are any other PF algorithms suitable for FDD on switching mode HMM?
   (c) When the number of system modes increases, is there a requirement to use a larger sample size to promote acceptable FDD performance? If so, what is an appropriate sample size?

Bibliography

Hajime Akashi and Hiromitsu Kumamoto. Random sampling approach to state estimation in switching environments. *Automatica*, 13(4):429 – 434, 1977. ISSN 0005-1098. doi: 10.1016/0005-1098(77)90028-0. URL http://www.sciencedirect.com/science/article/pii/0005109877900280.

A. Alessandri, M. Caccia, and G. Veruggio. Fault detection of actuator faults in unmanned underwater vehicles. *Control Engineering Practice*, 7 (3):357 – 368, 1999. ISSN 0967-0661. doi: 10.1016/S0967-0661(98) 00169-5. URL http://www.sciencedirect.com/science/article/pii/S0967066198001695.

D.L. Alspach and H.W. Sorenson. Nonlinear bayesian estimation using gaussian sum approximations. *Automatic Control, IEEE Transactions on*, 17(4):439–448, 1972. ISSN 0018-9286. doi: 10.1109/TAC.1972.1100034.

Christophe Andrieu and Arnaud Doucet. Particle filtering for partially observed gaussian state space models. *Journal of the Royal Statistical Society: Series B (Statistical Methodology)*, 64(4):827–836, 2002. ISSN 1467-9868. doi: 10.1111/1467-9868.00363. URL http://dx.doi.org/10.1111/1467-9868.00363.

Anonymous. Incident timeline: Bibby offshore dsv loses dp in 30 knots with divers below. Webpage, September 2012. URL http://gcaptain.com/forum/offshore/9854-incident-timeline-bibby-offshore-dsv-loses-dp-30-a.html.

Gianluca Antonelli. A survey of fault detection/tolerance strategies for auvs and rovs. In Fabrizio Caccavale and Luigi Villani, editors, *Fault Diagnosis and Fault Tolerance for Mechatronic Systems:Recent Advances*, volume 1 of *Springer Tracts in Advanced Robotics*, pages 109–127. Springer Berlin Heidelberg, 2003. ISBN 978-3-540-44159-5. doi: 10.1007/3-540-45737-2_4. URL http://dx.doi.org/10.1007/3-540-45737-2_4.

M.S. Arulampalam, S. Maskell, N. Gordon, and T. Clapp. A tutorial on particle filters for online nonlinear/non-gaussian bayesian tracking. *Signal Processing, IEEE Transactions on*, 50(2):174 –188, feb 2002. ISSN 1053-587X. doi: 10.1109/78.978374.

AUR-Lab. Applied underwater robotics laboratory - aur-lab, May 2013. URL http://www.ntnu.no/aur-lab.

Thomas Bak, Rafal Wisniewski, and Mogens Blanke. Autonomous attitude determination and control system for the ?rsted satellite. In *In proc.: IEEE Aerospace Applications Conference*, 1996. doi: 10.1.1.50.2495.

Bjørn Inge Bakken and Terje Olsen Smedvig. Risk associated with drive-off/drift-off when drilling on dp. In *DYNAMIC POSITIONING CONFERENCE*, 2001.

Anwer Bashi, Vesselin P. Jilkov, and X. Rong Li. Fault detection for systems with multiple unknown modes and similar units and its application to hvac. *IEEE Transactions on Control Systems Technology*, 19(5):957–968, September 2011. ISSN 1063-6536. doi: 10.1109/TCST.2010.2062183. URL http://ieeexplore.ieee.org/xpls/abs_all.jsp?arnumber=5565517http://ieeexplore.ieee.org/lpdocs/epic03/wrapper.htm?arnumber=5565517.

W. Y. Bhatti, U. I. Ochieng. Failure modes and models for integrated gps/ins systems. *JOURNAL OF NAVIGATION*, 60:327–348, 2007. URL http://journals.cambridge.org/download.php?file=%2FNAV%2FNAV60_02%2FS0373463307004237a.pdf&code=d2819002c9c0fef4e051a6bcc1b17fc3.

M. Blain, S. Lemieux, and R. Houde. Implementation of a rov navigation system using acoustic/doppler sensors and kalman filtering. In *OCEANS 2003. Proceedings*, volume 3, pages 1255 –1260 Vol.3, sept. 2003. doi: 10.1109/OCEANS.2003.178033.

M. Blanke. Diagnosis and fault-tolerant control for ship station keeping. In *Intelligent Control, 2005. Proceedings of the 2005 IEEE International Symposium on, Mediterrean Conference on Control and Automation*, pages 1379 –1384, june 2005. doi: 10.1109/.2005.1467217.

Mogens Blanke, Roozbeh Izadi-Zamanabadi, and Tako F. Lootsma. Fault monitoring and re-configurable control for a ship propulsion plant. *International Journal of Adaptive Control and Signal Processing*, 12(8):671–688, 1998. ISSN 1099-1115. doi: 10.1002/(SICI)1099-1115(199812)12:8<671::AID-ACS531>3.0.CO;2-J. URL http://dx.doi.org/10.1002/(SICI)1099-1115(199812)12:8<671::AID-ACS531>3.0.CO;2-J.

Mogens Blanke, M. Kinnaert, J. Lunze, and M. Staroswiecki. *Diagnosis and Fault-Tolerant Control*. Springer Berlin Heidelberg, 2006.

R. Bono, G. Bruzzone, and M. Caccia. Rov actuator fault diagnosis through servo-amplifiers' monitoring: an operational experience. In *OCEANS '99 MTS/IEEE. Riding the Crest into the 21st Century*, volume 3, pages 1318 –1324 vol.3, 1999. doi: 10.1109/OCEANS.1999.800185.

O. Cappe, S.J. Godsill, and E. Moulines. An overview of existing methods and recent advances in sequential monte carlo. *Proceedings of the IEEE*, 95(5):899–924, 2007. ISSN 0018-9219. doi: 10.1109/JPROC.2007.893250.

F. Caron, M. Davy, E. Duflos, and P. Vanheeghe. Particle filtering for multisensor data fusion with switching observation models: Application to land vehicle positioning.

Signal Processing, IEEE Transactions on, 55(6):2703 –2719, june 2007. ISSN 1053-587X. doi: 10.1109/TSP.2007.893914.

J. Carpenter, P. Clifford, and P. Fearnhead. Improved particle filter for nonlinear problems. *Radar, Sonar and Navigation, IEE Proceedings* -, 146(1):2 –7, feb 1999. ISSN 1350-2395. doi: 10.1049/ip-rsn:19990255.

Zhe Chen. Bayesian filtering: From kalman filters to particle filters, and beyond. Technical report, McMaster University, 2003. URL `http://www.cse.buffalo.edu/~peter/refs/DataAssimilation/GenRefsTutorials/Chen_2003.pdf`.

C. Chin. Dynamic positioning simulation, thrust optimization design and control of a drill ship under disturbances and faulty thruster. *SIMULATION*, 88(11):1338–1349, Oct 2012. doi: 10.1177/0037549712450345. URL `http://dx.doi.org/10.1177/0037549712450345`.

Roger Cornes and Thomas R Stockton. Fmea as an integral part of vessel design and construction: Producing a fault tolerant dp vessel. In *DYNAMIC POSITIONING CONFERENCE*, 1998.

Harald Cramer. *Mathematical Methods of Statistics*. Princeton University Press, 1999.

N. de Freitas. Rao-blackwellised particle filtering for fault diagnosis. In *Aerospace Conference Proceedings, 2002. IEEE*, volume 4, pages 4–1767–4–1772 vol.4, 2002. doi: 10.1109/AERO.2002.1036890.

F. J. Deegan. Collection of dp vessel disconnect data. In *DYNAMIC POSITIONING CONFERENCE*, 1998.

DNV. Review of methods for demonstrating redundancy in dynamic positioning systems for the offshore industry. Technical report, DNV Consulting, 2004.

A. Doucet, A. Logothetis, and V. Krishnamurthy. Stochastic sampling algorithms for state estimation of jump markov linear systems. *Automatic Control, IEEE Transactions on*, 45(2):188 –202, feb 2000a. ISSN 0018-9286. doi: 10.1109/9.839943.

Arnaud Doucet and A.M. Johansen. *The Oxford Handbook of Nonlinear Filtering*, chapter A tutorial on particle filtering and smoothing: Fifteen years later, pages 1–39. Number December. Cambridge University Press, Cambridge, 2009.

Arnaud Doucet, Nando de Freitas, Kevin Murphy, and Stuart Russell. Rao-blackwellised particle filtering for dynamic bayesian networks. In *Proceedings of the Sixteenth Conference on Uncertainty in Artificial Intelligence*, 2000b.

Arnaud Doucet, Nando de Freitas, and Neil Gordon, editors. *Sequential Monte Carlo Methods in Practice*. Springer, 2001.

F. Dukan, M. Ludvigsen, and A.J. Sorensen. Dynamic positioning system for a small size rov with experimental results. In *OCEANS, 2011 IEEE - Spain*, pages 1 –10, june 2011. doi: 10.1109/Oceans-Spain.2011.6003399.

Shaoji Fang and Mogens Blanke. Fault monitoring and fault recovery control for position moored tanker. *International Journal of Applied*

Mathematics and Computer Science, 21(3):467–478, 2011. ISSN 1641-876X. URL http://orbit.dtu.dk/fedora/objects/orbit:56419/datastreams/file_4054188/content.

Shaoji Fang, Bernt J. Leira, and Mogens Blanke. Position mooring control based on a structural reliability criterion. *Structural Safety*, 41:97–106, Mar 2013. doi: 10.1016/j.strusafe.2012.10.008. URL http://dx.doi.org/10.1016/j.strusafe.2012.10.008.

K.M. Fauske, F. Gustafsson, and O. Hegrenaes. Estimation of auv dynamics for sensor fusion. In *Information Fusion, 2007 10th International Conference on*, pages 1 –6, july 2007. doi: 10.1109/ICIF.2007.4408044.

V. Filaretov, A. Zhirabok, and A. Zuev. The development of the adaptive diagnostic system for navigation sensors of autonomous underwater vehicles. In *Mechatronics and Automation (ICMA), 2012 International Conference on*, pages 1704 –1709, aug. 2012. doi: 10.1109/ICMA.2012.6284393.

Thor I. Fossen. *Handbook of Marine Craft Hydrodynamics and Motion Control*. John Wiley & Sons Ltd, UK, 2011. ISBN 9781119991496.

Thor I. Fossen and Tristan Perez. Marine systems simulator (mss). webpage. URL http://www.marinecontrol.org/.

Thor I Fossen and Jann Peter Strand. Passive nonlinear observer design for ships using lyapunov methods: full-scale experiments with a supply vessel. *Automatica*, 35(1):3 – 16, 1999. ISSN 0005-1098. doi: 10.1016/S0005-1098(98)00121-6. URL http://www.sciencedirect.com/science/article/pii/S0005109898001216.

Mingyu Fu, JiPeng Ning, and Yushi Wei. Fault-tolerant control of dynamic positioning vessel by means of a virtual thruster. In *Mechatronics and Automation (ICMA), 2011 International Conference on*, pages 1706–1710, 2011. doi: 10.1109/ICMA.2011.5986367.

B. Fuglede and F. Topsoe. Jensen-shannon divergence and hilbert space embedding. In *Information Theory, 2004. ISIT 2004. Proceedings. International Symposium on*, page 31, june-2 july 2004. doi: 10.1109/ISIT.2004.1365067.

S. Funiak and B.C. Williams. Multi-modal particle filtering for hybrid systems with autonomous mode transitions. In *Proceeding of Workshop on Principles of Diagnosis*, 2003. URL http://www.cs.cmu.edu/afs/.cs.cmu.edu/Web/People/sfuniak/pubs/funiak-williams-dx03final.pdf.

R. Galeazzi, M. Blanke, and N. K. Poulsen. Early detection of parametric roll resonance on container ships. *Control Systems Technology, IEEE Transactions on*, PP (99):1, 2012. ISSN 1063-6536. doi: 10.1109/TCST.2012.2189399.

K. Garg, L. Weingarth, and S. Shah. Dynamic positioning power plant system reliability and design. In *Petroleum and Chemical Industry Conference Europe Conference Proceedings (PCIC EUROPE), 2011*, pages 1–10, 2011.

N.J. Gordon, D.J. Salmond, and A.F.M. Smith. Novel approach to nonlinear/non-gaussian bayesian state estimation. *Radar and Signal Processing, IEE Proceedings F*, 140(2):107 –113, apr 1993. ISSN 0956-375X. URL http://ieeexplore.ieee.org/xpls/abs_all.jsp?arnumber=210672&tag=1.

F. Gustafsson. Particle filter theory and practice with positioning applications. *Aerospace and Electronic Systems Magazine, IEEE*, 25(7):53–82, 2010. ISSN 0885-8985. doi: 10.1109/MAES.2010.5546308.

Fredrik Gustafsson. *Adaptive Filtering and Change Detection*. John Wiley & Sons, Ltd, Chichester, UK, 1 edition, 2001. ISBN 0-470-84161-3.

J.E. Handschin. Monte carlo techniques for prediction and filtering of non-linear stochastic processes. *Automatica*, 6(4):555 – 563, 1970. ISSN 0005-1098. doi: 10.1016/0005-1098(70)90010-5. URL http://www.sciencedirect.com/science/article/pii/0005109870900105.

Ian Harper. An fmea is for life. In *DYNAMIC POSITIONING CONFERENCE*, 2008.

H. Henao, G. A. Capolino, M. Ferandez-Cabanas, and M. Garcia-Melero. An improved signal processing-based fault detection technique for induction machine drives. In *Industrial Electronics Society, 2003. IECON '03. The 29th Annual Conference of the IEEE*, volume 2, pages 1386–1389 Vol.2, 2003. doi: 10.1109/IECON.2003.1280260.

Sajid Hussain and Hossam A. Gabbar. A novel method for real time gear fault detection based on pulse shape analysis. *Mechanical Systems and Signal Processing*, 25(4):1287 – 1298, 2011. ISSN 0888-3270. doi: 10.1016/j.ymssp.2010.11.013. URL http://www.sciencedirect.com/science/article/pii/S0888327010004164.

IMCA. Guidelines for vessel with dynamic positioning systems, June 1996. URL http://www.imca-int.com/documents/divisions/marine/docs/IMCAM113.pdf.

IMCA. Guidelines for the design and operation of dynamically positioned vessels, 1999.

IMCA. Guidance on failure modes & effects analyses (fmeas), 2002.

Rolf Isermann. *Fault-diagnosis systems: an introduction from fault detection to fault tolerance*. Springer Verlag, 1 edition, 2006. ISBN 978-3-540-24112-6. URL http://eu.wiley.com/WileyCDA/WileyTitle/productCd-EHEP002052.html.

Nils Albert Jenssen and Øyvind Hauge. Dp performance and incident analyses. In *DYNAMIC POSITIONING CONFERENCE*, 2002.

Tor A. Johansen and Asgeir J. Sørensen. Experiences with hil simulator testing of power management systems. In *DYNAMIC POSITIONING CONFERENCE*, 2009.

Tor A. Johansen, Thor I. Fossen, and Bjørnar Vik. Hardware-in-the-loop testing of dp systems. In *DYNAMIC POSITIONING CONFERENCE*, 2005.

S.J. Julier and J.K. Uhlmann. Unscented filtering and nonlinear estimation. *Proceedings of the IEEE*, 92(3):401 – 422, mar 2004. ISSN 0018-9219. doi: 10.1109/JPROC.2003.823141.

S.J. Julier, J.K. Uhlmann, and H.F. Durrant-Whyte. A new approach for filtering nonlinear systems. In *American Control Conference, Proceedings of the 1995*, volume 3, pages 1628–1632 vol.3, 1995. doi: 10.1109/ACC.1995.529783.

V. Kadirkamanathan, P. Li, M.H. Jaward, and S.G. Fabri. A sequential monte carlo filtering approach to fault detection and isolation in nonlinear systems. In *Decision and Control, 2000. Proceedings of the 39th IEEE Conference on*, volume 5, pages 4341–4346 vol.5, 2000. doi: 10.1109/CDC.2001.914586.

V. Kadirkamanathan, P. Li, M. H. Jaward, and S. G. Fabri. Particle filtering-based fault detection in non-linear stochastic systems. *International Journal of Systems Science*, 33(4):259–265, Jan 2002. doi: 10.1080/00207720110102566. URL http://dx.doi.org/10.1080/00207720110102566.

R. E. Kalman. A new approach to linear filtering and prediction problems. *Transactions of the ASME Journal of Basic Engineering*, 82(82 (Series D)):35–45, 1960. URL http://www.cs.unc.edu/~welch/kalman/media/pdf/Kalman1960.pdf.

R. Karlsson and F. Gustafsson. Bayesian surface and underwater navigation. *Signal Processing, IEEE Transactions on*, 54(11):4204 –4213, nov. 2006. ISSN 1053-587X. doi: 10.1109/TSP.2006.881176.

R. Karlsson, T. Schon, and F. Gustafsson. Complexity analysis of the marginalized particle filter. *Signal Processing, IEEE Transactions on*, 53(11):4408 – 4411, nov. 2005. ISSN 1053-587X. doi: 10.1109/TSP.2005.857061.

James C Kinsey and Louis L Whitcomb. Preliminary field experience with the dvlnav integrated navigation system for oceanographic submersibles. *Control Engineering Practice*, 12(12):1541 – 1549, 2004. ISSN 0967-0661. doi: 10.1016/j.conengprac.2003.12.010. URL http://www.sciencedirect.com/science/article/pii/S0967066103002843. <ce:title>Guidance and control of underwater vehicles</ce:title>.

J.C. Kinsey, R.M. Eustice, and L.L. Whitcomb. A survey of underwater vehicle navigation: Recent advances and new challenges. In *IFAC Conference of Manoeuvering and Control of Marine Craft*, 2006.

Genshiro Kitagawa. Monte carlo filter and smoother for non-gaussian nonlinear state space models. *Journal of Computational and Graphical Statistics*, 5(1):pp. 1–25, 1996. ISSN 10618600. URL http://www.jstor.org/stable/1390750.

Xenofon Koutsoukos, James Kurien, and Feng Zhao. Monitoring and diagnosis of hybrid systems using particle filtering methods. In *International Symposium on Mathematical Theory of Networks and Systems*, 2002.

E.L. Lehmann and George Casella. *Theory of Point Estimation*. Springer, 1998.

Ping Li and Visakan Kadirkamanathan. Particle filtering based likelihood ratio approach to fault diagnosis in nonlinear stochastic systems. *IEEE TRANSACTIONS ON SYSTEMS, MAN, AND CYBERNETICSŮPART C: APPLICATIONS AND REVIEWS*, 31:337–343, 2001.

Jun S. Liu and Rong Chen. Sequential monte carlo methods for dynamic systems. *Journal of the American Statistical Association*, 93:1032–1044, 1998. doi: 10.1.1.56.1897.

JunS. Liu. Metropolized independent sampling with comparisons to rejection sampling and importance sampling. *Statistics and Computing*, 6:113–119, 1996. ISSN 0960-3174. doi: 10.1007/BF00162521. URL http://dx.doi.org/10.1007/BF00162521.

R. Mahony, T. Hamel, and J.-M. Pflimlin. Nonlinear complementary filters on the special orthogonal group. *Automatic Control, IEEE Transactions on*, 53(5):1203–1218, june 2008. ISSN 0018-9286. doi: 10.1109/TAC.2008.923738.

Cybernetics Marine. The software problem ++. Technical report, Marine Cybernetics, 2004.

N. Meskin, E. Naderi, and K. Khorasani. A multiple model-based approach for fault diagnosis of jet engines. *IEEE Transactions on Control Systems Technology*, 21(1):254–262, January 2013. ISSN 1063-6536. doi: 10.1109/TCST.2011.2177981. URL http://ieeexplore.ieee.org/lpdocs/epic03/wrapper.htm?arnumber=6119240.

Ruben Morales-Menendez, Nando de Freitas, and David Poole. Real-time monitoring of complex industrial processes with particle filters. In *Advances in Neural Information Processing Systems*, pages 1433–1440, 2002.

Frank Nielsen. A family of statistical symmetric divergences based on jensen's inequality. *Computing Research Repository - CORR*, abs/1009.4004:0, 2010. URL http://arxiv.org/abs/1009.4004.

Edin Omerdic and Geoff Roberts. Thruster fault diagnosis and accommodation for open-frame underwater vehicles. *Control Engineering Practice*, 12 (12):1575 – 1598, 2004. ISSN 0967-0661. doi: 10.1016/j.conengprac.2003.12.014. URL http://www.sciencedirect.com/science/article/pii/S0967066103002892. <ce:title>Guidance and control of underwater vehicles</ce:title>.

Doug Phillips and Blake Miller. Dp systems Ű fail to test or test to fail? In *DYNAMIC POSITIONING CONFERENCE*, 2000.

T. Schon, F. Gustafsson, and P.-J. Nordlund. Marginalized particle filters for mixed linear/nonlinear state-space models. *Signal Processing, IEEE Transactions on*, 53 (7):2279 – 2289, july 2005. ISSN 1053-587X. doi: 10.1109/TSP.2005.849151.

Lan Shang and Guangjun Liu. Sensor and actuator fault detection and isolation for a high performance aircraft engine bleed air temperature control system. *IEEE Transactions on Control Systems Technology*, 19(5):1260–1268, September 2011. ISSN

1063-6536. doi: 10.1109/TCST.2010.2076353. URL http://ieeexplore.ieee.org/lpdocs/epic03/wrapper.htm?arnumber=5749704.

Xiaocheng Shi, Xingyan Sun, Mingyu Fu, Youzhen Chen, and Wenbo Xie. Federated filter for multi-sensor data fusion of dynamic positioning ship. In *Automation and Logistics (ICAL), 2012 IEEE International Conference on*, pages 13–18, 2012. doi: 10.1109/ICAL.2012.6308162.

A. F. M. Smith and A. E. Gelfand. Bayesian statistics without tears: A Sampling-Resampling perspective. *The American Statistician*, 46(2):84–88, May 1992. ISSN 00031305. doi: 10.2307/2684170. URL http://dx.doi.org/10.2307/2684170.

A. J. Sørensen. *Marine Control Systems: Propulsion and Motion Control Systems of Ships and Ocean Structures*. Department of Marine Technology at the Norwegian University of Science and Technology, Trondheim, Norway, 2nd edition, 2012. URL http://www.marin.ntnu.no/~assor/publications/marcyb.pdf.

Asgeir J. Sørensen. A survey of dynamic positioning control systems. *Annual Reviews in Control*, 35(1):123 – 136, 2011. ISSN 1367-5788. doi: 10.1016/j.arcontrol.2011.03.008. URL http://www.sciencedirect.com/science/article/pii/S1367578811000095.

H.W. Sorenson and D.L. Alspach. Recursive bayesian estimation using gaussian sums. *Automatica*, 7(4):465 – 479, 1971. ISSN 0005-1098. doi: 10.1016/0005-1098(71)90097-5. URL http://www.sciencedirect.com/science/article/pii/0005109871900975.

J. Spjtvold and T.A. Johansen. Fault tolerant control allocation for a thruster-controlled floating platform using parametric programming. In *Decision and Control, 2009 held jointly with the 2009 28th Chinese Control Conference. CDC/CCC 2009. Proceedings of the 48th IEEE Conference on*, pages 3311–3317, 2009. doi: 10.1109/CDC.2009.5400701.

S. Thrun, Langford. J., and V. Verma. Risk sensitive particle filters. In *Advances in Neural Information Processing Systems 14*. MIT Press, 2002.

R. Van Der Merwe, A. Doucet, N. De Freitas, and E. Wan. The unscented particle filter. *Advances in Neural Information Processing Systems*, pages 584–590, 2001. URL http://www.markirwin.net/stat220/Refs/upf2000.pdf.

Rudolph van der Merwe, Nando de Freitas, Arnaud Doucet, and Eric Wan. The unscented particle filter. In *Advances in Neural Information Processing Systems 13*, November 2001. URL http://citeseerx.ist.psu.edu/viewdoc/summary?doi=10.1.1.32.9011.

A.W. Van der Vaart. *Asymptotic statistics*, volume 3. Cambridge university press, 2000.

V. Verma, G. Gordon, R. Simmons, and S. Thrun. Real-time fault diagnosis [robot fault diagnosis]. *Robotics Automation Magazine, IEEE*, 11(2):56–66, 2004. ISSN 1070-9932. doi: 10.1109/MRA.2004.1310942.

Vandi Verma, John Langford, and Reid Simmons. Non-parametric fault identification for space rovers. In *Proceeding of International Symposium on Artificial Intelligence, Robotics and Automation in Space (i-SAIRAS)*, 2001.

Vandi Verma, Sebastian Thrun, Reid Simmons, Carnegie Mellon, and University. Variable resolution particle filter. In *In Proceedings of the International Joint Conference on Artificial intelligence (IJCAI)*, 2003.

Wikipedia. Dynamic positioning — wikipedia, the free encyclopedia, 2013. URL `http://en.wikipedia.org/w/index.php?title=Dynamic_positioning&oldid=553467613`. [Online; accessed 6-May-2013].

N. Eva Wu, Sudha Thavamani, Youmin Zhang, and Mogens Blanke. Sensor fault masking of a ship propulsion system. *Control Engineering Practice*, 14(11):1337–1345, Nov 2006. doi: 10.1016/j.conengprac.2005.09.003. URL `http://dx.doi.org/10.1016/j.conengprac.2005.09.003`.

Youmin Zhang, N. Eva Wu, and Bin Jiang. Fault detection and isolation applied and to a and ship propulsion and benchmark. In *Proceedings of the 17th World Congress The International Federation of Automatic Control*, 2009.

Bo Zhao, M. Blanke, and R. Skjetne. Particle filter rov navigation using hydroacoustic position and speed log measurements. In *American Control Conference (ACC), 2012*, pages 6209 –6215, june 2012a. URL `http://ieeexplore.ieee.org/xpl/articleDetails.jsp?reload=true&arnumber=6315511&contentType=Conference+Publications`.

Bo Zhao, M. Blanke, and R. Skjetne. Particle filter based fault-tolerant rov navigation using hydro-acoustic position and doppler velocity measurements. In *9th IFAC Conference on Manoeuvring and Control of Marine Craft*, 2012b. URL `http://orbit.dtu.dk/fedora/objects/orbit:116653/datastreams/file_fb6537f3-4149-4a6a-9f8f-45c8016d342f/content`.

Bo Zhao, Roger Skjetne, and Mogens Blanke. Particle filter and for fault and diagnosis and robust navigation of underwater robot. *IEEE Transactions on control systems technology (Submitted)*, (NTNU.(mb@elektro.dtu.dk)), 2013.

Previous PhD theses published at the Department of Marine Technology
(earlier: Faculty of Marine Technology)
NORWEGIAN UNIVERSITY OF SCIENCE AND TECHNOLOGY

Report No.	Author	Title
	Kavlie, Dag	Optimization of Plane Elastic Grillages, 1967
	Hansen, Hans R.	Man-Machine Communication and Data-Storage Methods in Ship Structural Design, 1971
	Gisvold, Kaare M.	A Method for non-linear mixed-integer programming and its Application to Design Problems, 1971
	Lund, Sverre	Tanker Frame Optimalization by means of SUMT-Transformation and Behaviour Models, 1971
	Vinje, Tor	On Vibration of Spherical Shells Interacting with Fluid, 1972
	Lorentz, Jan D.	Tank Arrangement for Crude Oil Carriers in Accordance with the new Anti-Pollution Regulations, 1975
	Carlsen, Carl A.	Computer-Aided Design of Tanker Structures, 1975
	Larsen, Carl M.	Static and Dynamic Analysis of Offshore Pipelines during Installation, 1976
UR-79-01	Brigt Hatlestad, MK	The finite element method used in a fatigue evaluation of fixed offshore platforms. (Dr.Ing. Thesis)
UR-79-02	Erik Pettersen, MK	Analysis and design of cellular structures. (Dr.Ing. Thesis)
UR-79-03	Sverre Valsgård, MK	Finite difference and finite element methods applied to non-linear analysis of plated structures. (Dr.Ing. Thesis)
UR-79-04	Nils T. Nordsve, MK	Finite element collapse analysis of structural members considering imperfections and stresses due to fabrication. (Dr.Ing. Thesis)
UR-79-05	Ivar J. Fylling, MK	Analysis of towline forces in ocean towing systems. (Dr.Ing. Thesis)
UR-80-06	Nils Sandsmark, MM	Analysis of Stationary and Transient Heat Conduction by the Use of the Finite Element Method. (Dr.Ing. Thesis)
UR-80-09	Sverre Haver, MK	Analysis of uncertainties related to the stochastic modeling of ocean waves. (Dr.Ing. Thesis)
UR-81-15	Odland, Jonas	On the Strength of welded Ring stiffened cylindrical Shells primarily subjected to axial Compression
UR-82-17	Engesvik, Knut	Analysis of Uncertainties in the fatigue Capacity of Welded Joints
UR-82-18	Rye, Henrik	Ocean wave groups
UR-83-30	Eide, Oddvar Inge	On Cumulative Fatigue Damage in Steel Welded Joints
UR-83-33	Mo, Olav	Stochastic Time Domain Analysis of Slender Offshore Structures
UR-83-34	Amdahl, Jørgen	Energy absorption in Ship-platform impacts
UR-84-37	Mørch, Morten	Motions and mooring forces of semi submersibles as determined by full-scale measurements and theoretical analysis
UR-84-38	Soares, C. Guedes	Probabilistic models for load effects in ship structures
UR-84-39	Aarsnes, Jan V.	Current forces on ships
UR-84-40	Czujko, Jerzy	Collapse Analysis of Plates subjected to Biaxial Compression and Lateral Load

Report No.	Author	Title
UR-85-46	Alf G. Engseth, MK	Finite element collapse analysis of tubular steel offshore structures. (Dr.Ing. Thesis)
UR-86-47	Dengody Sheshappa, MP	A Computer Design Model for Optimizing Fishing Vessel Designs Based on Techno-Economic Analysis. (Dr.Ing. Thesis)
UR-86-48	Vidar Aanesland, MH	A Theoretical and Numerical Study of Ship Wave Resistance. (Dr.Ing. Thesis)
UR-86-49	Heinz-Joachim Wessel, MK	Fracture Mechanics Analysis of Crack Growth in Plate Girders. (Dr.Ing. Thesis)
UR-86-50	Jon Taby, MK	Ultimate and Post-ultimate Strength of Dented Tubular Members. (Dr.Ing. Thesis)
UR-86-51	Walter Lian, MH	A Numerical Study of Two-Dimensional Separated Flow Past Bluff Bodies at Moderate KC-Numbers. (Dr.Ing. Thesis)
UR-86-52	Bjørn Sortland, MH	Force Measurements in Oscillating Flow on Ship Sections and Circular Cylinders in a U-Tube Water Tank. (Dr.Ing. Thesis)
UR-86-53	Kurt Strand, MM	A System Dynamic Approach to One-dimensional Fluid Flow. (Dr.Ing. Thesis)
UR-86-54	Arne Edvin Løken, MH	Three Dimensional Second Order Hydrodynamic Effects on Ocean Structures in Waves. (Dr.Ing. Thesis)
UR-86-55	Sigurd Falch, MH	A Numerical Study of Slamming of Two-Dimensional Bodies. (Dr.Ing. Thesis)
UR-87-56	Arne Braathen, MH	Application of a Vortex Tracking Method to the Prediction of Roll Damping of a Two-Dimension Floating Body. (Dr.Ing. Thesis)
UR-87-57	Bernt Leira, MK	Gaussian Vector Processes for Reliability Analysis involving Wave-Induced Load Effects. (Dr.Ing. Thesis)
UR-87-58	Magnus Småvik, MM	Thermal Load and Process Characteristics in a Two-Stroke Diesel Engine with Thermal Barriers (in Norwegian). (Dr.Ing. Thesis)
MTA-88-59	Bernt Arild Bremdal, MP	An Investigation of Marine Installation Processes – A Knowledge-Based Planning Approach. (Dr.Ing. Thesis)
MTA-88-60	Xu Jun, MK	Non-linear Dynamic Analysis of Space-framed Offshore Structures. (Dr.Ing. Thesis)
MTA-89-61	Gang Miao, MH	Hydrodynamic Forces and Dynamic Responses of Circular Cylinders in Wave Zones. (Dr.Ing. Thesis)
MTA-89-62	Martin Greenhow, MH	Linear and Non-Linear Studies of Waves and Floating Bodies. Part I and Part II. (Dr.Techn. Thesis)
MTA-89-63	Chang Li, MH	Force Coefficients of Spheres and Cubes in Oscillatory Flow with and without Current. (Dr.Ing. Thesis
MTA-89-64	Hu Ying, MP	A Study of Marketing and Design in Development of Marine Transport Systems. (Dr.Ing. Thesis)
MTA-89-65	Arild Jæger, MH	Seakeeping, Dynamic Stability and Performance of a Wedge Shaped Planing Hull. (Dr.Ing. Thesis)
MTA-89-66	Chan Siu Hung, MM	The dynamic characteristics of tilting-pad bearings
MTA-89-67	Kim Wikstrøm, MP	Analysis av projekteringen for ett offshore projekt. (Licenciat-avhandling)
MTA-89-68	Jiao Guoyang, MK	Reliability Analysis of Crack Growth under Random Loading, considering Model Updating. (Dr.Ing. Thesis)

Report No.	Author	Title
MTA-89-69	Arnt Olufsen, MK	Uncertainty and Reliability Analysis of Fixed Offshore Structures. (Dr.Ing. Thesis)
MTA-89-70	Wu Yu-Lin, MR	System Reliability Analyses of Offshore Structures using improved Truss and Beam Models. (Dr.Ing. Thesis)
MTA-90-71	Jan Roger Hoff, MH	Three-dimensional Green function of a vessel with forward speed in waves. (Dr.Ing. Thesis)
MTA-90-72	Rong Zhao, MH	Slow-Drift Motions of a Moored Two-Dimensional Body in Irregular Waves. (Dr.Ing. Thesis)
MTA-90-73	Atle Minsaas, MP	Economical Risk Analysis. (Dr.Ing. Thesis)
MTA-90-74	Knut-Ariel Farnes, MK	Long-term Statistics of Response in Non-linear Marine Structures. (Dr.Ing. Thesis)
MTA-90-75	Torbjørn Sotberg, MK	Application of Reliability Methods for Safety Assessment of Submarine Pipelines. (Dr.Ing. Thesis)
MTA-90-76	Zeuthen, Steffen, MP	SEAMAID. A computational model of the design process in a constraint-based logic programming environment. An example from the offshore domain. (Dr.Ing. Thesis)
MTA-91-77	Haagensen, Sven, MM	Fuel Dependant Cyclic Variability in a Spark Ignition Engine – An Optical Approach. (Dr.Ing. Thesis)
MTA-91-78	Løland, Geir, MH	Current forces on and flow through fish farms. (Dr.Ing. Thesis)
MTA-91-79	Hoen, Christopher, MK	System Identification of Structures Excited by Stochastic Load Processes. (Dr.Ing. Thesis)
MTA-91-80	Haugen, Stein, MK	Probabilistic Evaluation of Frequency of Collision between Ships and Offshore Platforms. (Dr.Ing. Thesis)
MTA-91-81	Sødahl, Nils, MK	Methods for Design and Analysis of Flexible Risers. (Dr.Ing. Thesis)
MTA-91-82	Ormberg, Harald, MK	Non-linear Response Analysis of Floating Fish Farm Systems. (Dr.Ing. Thesis)
MTA-91-83	Marley, Mark J., MK	Time Variant Reliability under Fatigue Degradation. (Dr.Ing. Thesis)
MTA-91-84	Krokstad, Jørgen R., MH	Second-order Loads in Multidirectional Seas. (Dr.Ing. Thesis)
MTA-91-85	Molteberg, Gunnar A., MM	The Application of System Identification Techniques to Performance Monitoring of Four Stroke Turbocharged Diesel Engines. (Dr.Ing. Thesis)
MTA-92-86	Mørch, Hans Jørgen Bjelke, MH	Aspects of Hydrofoil Design: with Emphasis on Hydrofoil Interaction in Calm Water. (Dr.Ing. Thesis)
MTA-92-87	Chan Siu Hung, MM	Nonlinear Analysis of Rotordynamic Instabilities in High-speed Turbomachinery. (Dr.Ing. Thesis)
MTA-92-88	Bessason, Bjarni, MK	Assessment of Earthquake Loading and Response of Seismically Isolated Bridges. (Dr.Ing. Thesis)
MTA-92-89	Langli, Geir, MP	Improving Operational Safety through exploitation of Design Knowledge – an investigation of offshore platform safety. (Dr.Ing. Thesis)
MTA-92-90	Sævik, Svein, MK	On Stresses and Fatigue in Flexible Pipes. (Dr.Ing. Thesis)
MTA-92-91	Ask, Tor Ø., MM	Ignition and Flame Growth in Lean Gas-Air Mixtures. An Experimental Study with a Schlieren System. (Dr.Ing. Thesis)

Report No.	Author	Title
MTA-86-92	Hessen, Gunnar, MK	Fracture Mechanics Analysis of Stiffened Tubular Members. (Dr.Ing. Thesis)
MTA-93-93	Steinebach, Christian, MM	Knowledge Based Systems for Diagnosis of Rotating Machinery. (Dr.Ing. Thesis)
MTA-93-94	Dalane, Jan Inge, MK	System Reliability in Design and Maintenance of Fixed Offshore Structures. (Dr.Ing. Thesis)
MTA-93-95	Steen, Sverre, MH	Cobblestone Effect on SES. (Dr.Ing. Thesis)
MTA-93-96	Karunakaran, Daniel, MK	Nonlinear Dynamic Response and Reliability Analysis of Drag-dominated Offshore Platforms. (Dr.Ing. Thesis)
MTA-93-97	Hagen, Arnulf, MP	The Framework of a Design Process Language. (Dr.Ing. Thesis)
MTA-93-98	Nordrik, Rune, MM	Investigation of Spark Ignition and Autoignition in Methane and Air Using Computational Fluid Dynamics and Chemical Reaction Kinetics. A Numerical Study of Ignition Processes in Internal Combustion Engines. (Dr.Ing. Thesis)
MTA-94-99	Passano, Elizabeth, MK	Efficient Analysis of Nonlinear Slender Marine Structures. (Dr.Ing. Thesis)
MTA-94-100	Kvålsvold, Jan, MH	Hydroelastic Modelling of Wetdeck Slamming on Multihull Vessels. (Dr.Ing. Thesis)
MTA-94-102	Bech, Sidsel M., MK	Experimental and Numerical Determination of Stiffness and Strength of GRP/PVC Sandwich Structures. (Dr.Ing. Thesis)
MTA-95-103	Paulsen, Hallvard, MM	A Study of Transient Jet and Spray using a Schlieren Method and Digital Image Processing. (Dr.Ing. Thesis)
MTA-95-104	Hovde, Geir Olav, MK	Fatigue and Overload Reliability of Offshore Structural Systems, Considering the Effect of Inspection and Repair. (Dr.Ing. Thesis)
MTA-95-105	Wang, Xiaozhi, MK	Reliability Analysis of Production Ships with Emphasis on Load Combination and Ultimate Strength. (Dr.Ing. Thesis)
MTA-95-106	Ulstein, Tore, MH	Nonlinear Effects of a Flexible Stern Seal Bag on Cobblestone Oscillations of an SES. (Dr.Ing. Thesis)
MTA-95-107	Solaas, Frøydis, MH	Analytical and Numerical Studies of Sloshing in Tanks. (Dr.Ing. Thesis)
MTA-95-108	Hellan, Øyvind, MK	Nonlinear Pushover and Cyclic Analyses in Ultimate Limit State Design and Reassessment of Tubular Steel Offshore Structures. (Dr.Ing. Thesis)
MTA-95-109	Hermundstad, Ole A., MK	Theoretical and Experimental Hydroelastic Analysis of High Speed Vessels. (Dr.Ing. Thesis)
MTA-96-110	Bratland, Anne K., MH	Wave-Current Interaction Effects on Large-Volume Bodies in Water of Finite Depth. (Dr.Ing. Thesis)
MTA-96-111	Herfjord, Kjell, MH	A Study of Two-dimensional Separated Flow by a Combination of the Finite Element Method and Navier-Stokes Equations. (Dr.Ing. Thesis)
MTA-96-112	AEsøy, Vilmar, MM	Hot Surface Assisted Compression Ignition in a Direct Injection Natural Gas Engine. (Dr.Ing. Thesis)
MTA-96-113	Eknes, Monika L., MK	Escalation Scenarios Initiated by Gas Explosions on Offshore Installations. (Dr.Ing. Thesis)
MTA-96-114	Erikstad, Stein O., MP	A Decision Support Model for Preliminary Ship Design. (Dr.Ing. Thesis)

Report No.	Author	Title
MTA-96-115	Pedersen, Egil, MH	A Nautical Study of Towed Marine Seismic Streamer Cable Configurations. (Dr.Ing. Thesis)
MTA-97-116	Moksnes, Paul O., MM	Modelling Two-Phase Thermo-Fluid Systems Using Bond Graphs. (Dr.Ing. Thesis)
MTA-97-117	Halse, Karl H., MK	On Vortex Shedding and Prediction of Vortex-Induced Vibrations of Circular Cylinders. (Dr.Ing. Thesis)
MTA-97-118	Igland, Ragnar T., MK	Reliability Analysis of Pipelines during Laying, considering Ultimate Strength under Combined Loads. (Dr.Ing. Thesis)
MTA-97-119	Pedersen, Hans-P., MP	Levendefiskteknologi for fiskefartøy. (Dr.Ing. Thesis)
MTA-98-120	Vikestad, Kyrre, MK	Multi-Frequency Response of a Cylinder Subjected to Vortex Shedding and Support Motions. (Dr.Ing. Thesis)
MTA-98-121	Azadi, Mohammad R. E., MK	Analysis of Static and Dynamic Pile-Soil-Jacket Behaviour. (Dr.Ing. Thesis)
MTA-98-122	Ulltang, Terje, MP	A Communication Model for Product Information. (Dr.Ing. Thesis)
MTA-98-123	Torbergsen, Erik, MM	Impeller/Diffuser Interaction Forces in Centrifugal Pumps. (Dr.Ing. Thesis)
MTA-98-124	Hansen, Edmond, MH	A Discrete Element Model to Study Marginal Ice Zone Dynamics and the Behaviour of Vessels Moored in Broken Ice. (Dr.Ing. Thesis)
MTA-98-125	Videiro, Paulo M., MK	Reliability Based Design of Marine Structures. (Dr.Ing. Thesis)
MTA-99-126	Mainçon, Philippe, MK	Fatigue Reliability of Long Welds Application to Titanium Risers. (Dr.Ing. Thesis)
MTA-99-127	Haugen, Elin M., MH	Hydroelastic Analysis of Slamming on Stiffened Plates with Application to Catamaran Wetdecks. (Dr.Ing. Thesis)
MTA-99-128	Langhelle, Nina K., MK	Experimental Validation and Calibration of Nonlinear Finite Element Models for Use in Design of Aluminium Structures Exposed to Fire. (Dr.Ing. Thesis)
MTA-99-129	Berstad, Are J., MK	Calculation of Fatigue Damage in Ship Structures. (Dr.Ing. Thesis)
MTA-99-130	Andersen, Trond M., MM	Short Term Maintenance Planning. (Dr.Ing. Thesis)
MTA-99-131	Tveiten, Bård Wathne, MK	Fatigue Assessment of Welded Aluminium Ship Details. (Dr.Ing. Thesis)
MTA-99-132	Søreide, Fredrik, MP	Applications of underwater technology in deep water archaeology. Principles and practice. (Dr.Ing. Thesis)
MTA-99-133	Tønnessen, Rune, MH	A Finite Element Method Applied to Unsteady Viscous Flow Around 2D Blunt Bodies With Sharp Corners. (Dr.Ing. Thesis)
MTA-99-134	Elvekrok, Dag R., MP	Engineering Integration in Field Development Projects in the Norwegian Oil and Gas Industry. The Supplier Management of Norne. (Dr.Ing. Thesis)
MTA-99-135	Fagerholt, Kjetil, MP	Optimeringsbaserte Metoder for Ruteplanlegging innen skipsfart. (Dr.Ing. Thesis)
MTA-99-136	Bysveen, Marie, MM	Visualization in Two Directions on a Dynamic Combustion Rig for Studies of Fuel Quality. (Dr.Ing. Thesis)
MTA-2000-137	Storteig, Eskild, MM	Dynamic characteristics and leakage performance of liquid annular seals in centrifugal pumps. (Dr.Ing. Thesis)

Report No.	Author	Title
MTA-2000-138	Sagli, Gro, MK	Model uncertainty and simplified estimates of long term extremes of hull girder loads in ships. (Dr.Ing. Thesis)
MTA-2000-139	Tronstad, Harald, MK	Nonlinear analysis and design of cable net structures like fishing gear based on the finite element method. (Dr.Ing. Thesis)
MTA-2000-140	Kroneberg, André, MP	Innovation in shipping by using scenarios. (Dr.Ing. Thesis)
MTA-2000-141	Haslum, Herbjørn Alf, MH	Simplified methods applied to nonlinear motion of spar platforms. (Dr.Ing. Thesis)
MTA-2001-142	Samdal, Ole Johan, MM	Modelling of Degradation Mechanisms and Stressor Interaction on Static Mechanical Equipment Residual Lifetime. (Dr.Ing. Thesis)
MTA-2001-143	Baarholm, Rolf Jarle, MH	Theoretical and experimental studies of wave impact underneath decks of offshore platforms. (Dr.Ing. Thesis)
MTA-2001-144	Wang, Lihua, MK	Probabilistic Analysis of Nonlinear Wave-induced Loads on Ships. (Dr.Ing. Thesis)
MTA-2001-145	Kristensen, Odd H. Holt, MK	Ultimate Capacity of Aluminium Plates under Multiple Loads, Considering HAZ Properties. (Dr.Ing. Thesis)
MTA-2001-146	Greco, Marilena, MH	A Two-Dimensional Study of Green-Water Loading. (Dr.Ing. Thesis)
MTA-2001-147	Heggelund, Svein E., MK	Calculation of Global Design Loads and Load Effects in Large High Speed Catamarans. (Dr.Ing. Thesis)
MTA-2001-148	Babalola, Olusegun T., MK	Fatigue Strength of Titanium Risers – Defect Sensitivity. (Dr.Ing. Thesis)
MTA-2001-149	Mohammed, Abuu K., MK	Nonlinear Shell Finite Elements for Ultimate Strength and Collapse Analysis of Ship Structures. (Dr.Ing. Thesis)
MTA-2002-150	Holmedal, Lars E., MH	Wave-current interactions in the vicinity of the sea bed. (Dr.Ing. Thesis)
MTA-2002-151	Rognebakke, Olav F., MH	Sloshing in rectangular tanks and interaction with ship motions. (Dr.Ing. Thesis)
MTA-2002-152	Lader, Pål Furset, MH	Geometry and Kinematics of Breaking Waves. (Dr.Ing. Thesis)
MTA-2002-153	Yang, Qinzheng, MH	Wash and wave resistance of ships in finite water depth. (Dr.Ing. Thesis)
MTA-2002-154	Melhus, Øyvin, MM	Utilization of VOC in Diesel Engines. Ignition and combustion of VOC released by crude oil tankers. (Dr.Ing. Thesis)
MTA-2002-155	Ronæss, Marit, MH	Wave Induced Motions of Two Ships Advancing on Parallel Course. (Dr.Ing. Thesis)
MTA-2002-156	Økland, Ole D., MK	Numerical and experimental investigation of whipping in twin hull vessels exposed to severe wet deck slamming. (Dr.Ing. Thesis)
MTA-2002-157	Ge, Chunhua, MK	Global Hydroelastic Response of Catamarans due to Wet Deck Slamming. (Dr.Ing. Thesis)
MTA-2002-158	Byklum, Eirik, MK	Nonlinear Shell Finite Elements for Ultimate Strength and Collapse Analysis of Ship Structures. (Dr.Ing. Thesis)
IMT-2003-1	Chen, Haibo, MK	Probabilistic Evaluation of FPSO-Tanker Collision in Tandem Offloading Operation. (Dr.Ing. Thesis)
IMT-2003-2	Skaugset, Kjetil Bjørn, MK	On the Suppression of Vortex Induced Vibrations of Circular Cylinders by Radial Water Jets. (Dr.Ing. Thesis)
IMT-2003-3	Chezhian, Muthu	Three-Dimensional Analysis of Slamming. (Dr.Ing. Thesis)

Report No.	Author	Title
IMT-2003-4	Buhaug, Øyvind	Deposit Formation on Cylinder Liner Surfaces in Medium Speed Engines. (Dr.Ing. Thesis)
IMT-2003-5	Tregde, Vidar	Aspects of Ship Design: Optimization of Aft Hull with Inverse Geometry Design. (Dr.Ing. Thesis)
IMT-2003-6	Wist, Hanne Therese	Statistical Properties of Successive Ocean Wave Parameters. (Dr.Ing. Thesis)
IMT-2004-7	Ransau, Samuel	Numerical Methods for Flows with Evolving Interfaces. (Dr.Ing. Thesis)
IMT-2004-8	Soma, Torkel	Blue-Chip or Sub-Standard. A data interrogation approach of identity safety characteristics of shipping organization. (Dr.Ing. Thesis)
IMT-2004-9	Ersdal, Svein	An experimental study of hydrodynamic forces on cylinders and cables in near axial flow. (Dr.Ing. Thesis)
IMT-2005-10	Brodtkorb, Per Andreas	The Probability of Occurrence of Dangerous Wave Situations at Sea. (Dr.Ing. Thesis)
IMT-2005-11	Yttervik, Rune	Ocean current variability in relation to offshore engineering. (Dr.Ing. Thesis)
IMT-2005-12	Fredheim, Arne	Current Forces on Net-Structures. (Dr.Ing. Thesis)
IMT-2005-13	Heggernes, Kjetil	Flow around marine structures. (Dr.Ing. Thesis
IMT-2005-14	Fouques, Sebastien	Lagrangian Modelling of Ocean Surface Waves and Synthetic Aperture Radar Wave Measurements. (Dr.Ing. Thesis)
IMT-2006-15	Holm, Håvard	Numerical calculation of viscous free surface flow around marine structures. (Dr.Ing. Thesis)
IMT-2006-16	Bjørheim, Lars G.	Failure Assessment of Long Through Thickness Fatigue Cracks in Ship Hulls. (Dr.Ing. Thesis)
IMT-2006-17	Hansson, Lisbeth	Safety Management for Prevention of Occupational Accidents. (Dr.Ing. Thesis)
IMT-2006-18	Zhu, Xinying	Application of the CIP Method to Strongly Nonlinear Wave-Body Interaction Problems. (Dr.Ing. Thesis)
IMT-2006-19	Reite, Karl Johan	Modelling and Control of Trawl Systems. (Dr.Ing. Thesis)
IMT-2006-20	Smogeli, Øyvind Notland	Control of Marine Propellers. From Normal to Extreme Conditions. (Dr.Ing. Thesis)
IMT-2007-21	Storhaug, Gaute	Experimental Investigation of Wave Induced Vibrations and Their Effect on the Fatigue Loading of Ships. (Dr.Ing. Thesis)
IMT-2007-22	Sun, Hui	A Boundary Element Method Applied to Strongly Nonlinear Wave-Body Interaction Problems. (PhD Thesis, CeSOS)
IMT-2007-23	Rustad, Anne Marthine	Modelling and Control of Top Tensioned Risers. (PhD Thesis, CeSOS)
IMT-2007-24	Johansen, Vegar	Modelling flexible slender system for real-time simulations and control applications
IMT-2007-25	Wroldsen, Anders Sunde	Modelling and control of tensegrity structures. (PhD Thesis, CeSOS)
IMT-2007-26	Aronsen, Kristoffer Høye	An experimental investigation of in-line and combined inline and cross flow vortex induced vibrations. (Dr. avhandling, IMT)

Report No.	Author	Title
IMT-2007-27	Gao, Zhen	Stochastic Response Analysis of Mooring Systems with Emphasis on Frequency-domain Analysis of Fatigue due to Wide-band Response Processes (PhD Thesis, CeSOS)
IMT-2007-28	Thorstensen, Tom Anders	Lifetime Profit Modelling of Ageing Systems Utilizing Information about Technical Condition. (Dr.ing. thesis, IMT)
IMT-2008-29	Berntsen, Per Ivar B.	Structural Reliability Based Position Mooring. (PhD-Thesis, IMT)
IMT-2008-30	Ye, Naiquan	Fatigue Assessment of Aluminium Welded Box-stiffener Joints in Ships (Dr.ing. thesis, IMT)
IMT-2008-31	Radan, Damir	Integrated Control of Marine Electrical Power Systems. (PhD-Thesis, IMT)
IMT-2008-32	Thomassen, Paul	Methods for Dynamic Response Analysis and Fatigue Life Estimation of Floating Fish Cages. (Dr.ing. thesis, IMT)
IMT-2008-33	Pákozdi, Csaba	A Smoothed Particle Hydrodynamics Study of Two-dimensional Nonlinear Sloshing in Rectangular Tanks. (Dr.ing.thesis, IMT/ CeSOS)
IMT-2008-34	Grytøyr, Guttorm	A Higher-Order Boundary Element Method and Applications to Marine Hydrodynamics. (Dr.ing.thesis, IMT)
IMT-2008-35	Drummen, Ingo	Experimental and Numerical Investigation of Nonlinear Wave-Induced Load Effects in Containerships considering Hydroelasticity. (PhD thesis, CeSOS)
IMT-2008-36	Skejic, Renato	Maneuvering and Seakeeping of a Singel Ship and of Two Ships in Interaction. (PhD-Thesis, CeSOS)
IMT-2008-37	Harlem, Alf	An Age-Based Replacement Model for Repairable Systems with Attention to High-Speed Marine Diesel Engines. (PhD-Thesis, IMT)
IMT-2008-38	Alsos, Hagbart S.	Ship Grounding. Analysis of Ductile Fracture, Bottom Damage and Hull Girder Response. (PhD-thesis, IMT)
IMT-2008-39	Graczyk, Mateusz	Experimental Investigation of Sloshing Loading and Load Effects in Membrane LNG Tanks Subjected to Random Excitation. (PhD-thesis, CeSOS)
IMT-2008-40	Taghipour, Reza	Efficient Prediction of Dynamic Response for Flexible amd Multi-body Marine Structures. (PhD-thesis, CeSOS)
IMT-2008-41	Ruth, Eivind	Propulsion control and thrust allocation on marine vessels. (PhD thesis, CeSOS)
IMT-2008-42	Nystad, Bent Helge	Technical Condition Indexes and Remaining Useful Life of Aggregated Systems. PhD thesis, IMT
IMT-2008-43	Soni, Prashant Kumar	Hydrodynamic Coefficients for Vortex Induced Vibrations of Flexible Beams. PhD thesis, CeSOS
IMT-2009-43	Amlashi, Hadi K.K.	Ultimate Strength and Reliability-based Design of Ship Hulls with Emphasis on Combined Global and Local Loads. PhD Thesis, IMT
IMT-2009-44	Pedersen, Tom Arne	Bond Graph Modelling of Marine Power Systems. PhD Thesis, IMT
IMT-2009-45	Kristiansen, Trygve	Two-Dimensional Numerical and Experimental Studies of Piston-Mode Resonance. PhD thesis, CeSOS
IMT-2009-46	Ong, Muk Chen	Applications of a Standard High Reynolds Number Model and a Stochastic Scour Prediction Model for Marine Structures. PhD-thesis, IMT

Report No.	Author	Title
IMT-2009-47	Hong, Lin	Simplified Analysis and Design of Ships subjected to Collision and Grounding. PhD-thesis, IMT
IMT-2009-48	Koushan, Kamran	Vortex Induced Vibrations of Free Span Pipelines, PhD thesis, IMT
IMT-2009-49	Korsvik, Jarl Eirik	Heuristic Methods for Ship Routing and Scheduling. PhD-thesis, IMT
IMT-2009-50	Lee, Jihoon	Experimental Investigation and Numerical in Analyzing the Ocean Current Displacement of Longlines. Ph.d.-Thesis, IMT.
IMT-2009-51	Vestbøstad, Tone Gran	A Numerical Study of Wave-in-Deck Impact usin a Two-Dimensional Constrained Interpolation Profile Method, Ph.d.thesis, CeSOS.
IMT-2009-52	Bruun, Kristine	Bond Graph Modelling of Fuel Cells for Marine Power Plants. Ph.d.-thesis, IMT
IMT-2009-53	Holstad, Anders	Numerical Investigation of Turbulence in a Sekwed Three-Dimensional Channel Flow, Ph.d.-thesis, IMT.
IMT-2009-54	Ayala-Uraga, Efren	Reliability-Based Assessment of Deteriorating Ship-shaped Offshore Structures, Ph.d.-thesis, IMT
IMT-2009-55	Kong, Xiangjun	A Numerical Study of a Damaged Ship in Beam Sea Waves. Ph.d.-thesis, IMT/CeSOS.
IMT-2010-56	Kristiansen, David	Wave Induced Effects on Floaters of Aquaculture Plants, Ph.d.-thesis, CeSOS.
IMT-2010-57	Ludvigsen, Martin	An ROV-Toolbox for Optical and Acoustic Scientific Seabed Investigation. Ph.d.-thesis IMT.
IMT-2010-58	Hals, Jørgen	Modelling and Phase Control of Wave-Energy Converters. Ph.d.thesis, CeSOS.
IMT-2010-59	Shu, Zhi	Uncertainty Assessment of Wave Loads and Ultimate Strength of Tankers and Bulk Carriers in a Reliability Framework. Ph.d. Thesis, IMT/ CeSOS
IMT-2010-60	Shao, Yanlin	Numerical Potential-Flow Studies on Weakly-Nonlinear Wave-Body Interactions with/without Small Forward Speed, Ph.d.thesis, CeSOS.
IMT-2010-61	Califano, Andrea	Dynamic Loads on Marine Propellers due to Intermittent Ventilation. Ph.d.thesis, IMT.
IMT-2010-62	El Khoury, George	Numerical Simulations of Massively Separated Turbulent Flows, Ph.d.-thesis, IMT
IMT-2010-63	Seim, Knut Sponheim	Mixing Process in Dense Overflows with Emphasis on the Faroe Bank Channel Overflow. Ph.d.thesis, IMT
IMT-2010-64	Jia, Huirong	Structural Analysis of Intect and Damaged Ships in a Collission Risk Analysis Perspective. Ph.d.thesis CeSoS.
IMT-2010-65	Jiao, Linlin	Wave-Induced Effects on a Pontoon-type Very Large Floating Structures (VLFS). Ph.D.-thesis, CeSOS.
IMT-2010-66	Abrahamsen, Bjørn Christian	Sloshing Induced Tank Roof with Entrapped Air Pocket. Ph.d.thesis, CeSOS.
IMT-2011-67	Karimirad, Madjid	Stochastic Dynamic Response Analysis of Spar-Type Wind Turbines with Catenary or Taut Mooring Systems. Ph.d.-thesis, CeSOS.
IMT-2011-68	Erlend Meland	Condition Monitoring of Safety Critical Valves. Ph.d.-thesis, IMT.

Report No.	Author	Title
IMT-2011-69	Yang, Limin	Stochastic Dynamic System Analysis of Wave Energy Converter with Hydraulic Power Take-Off, with Particular Reference to Wear Damage Analysis, Ph.d. Thesis, CeSOS.
IMT-2011-70	Visscher, Jan	Application of Particla Image Velocimetry on Turbulent Marine Flows, Ph.d.Thesis, IMT.
IMT-2011-71	Su, Biao	Numerical Predictions of Global and Local Ice Loads on Ships. Ph.d.Thesis, CeSOS.
IMT-2011-72	Liu, Zhenhui	Analytical and Numerical Analysis of Iceberg Collision with Ship Structures. Ph.d.Thesis, IMT.
IMT-2011-73	Aarsæther, Karl Gunnar	Modeling and Analysis of Ship Traffic by Observation and Numerical Simulation. Ph.d.Thesis, IMT.
IMT-2011-74	Wu, Jie	Hydrodynamic Force Identification from Stochastic Vortex Induced Vibration Experiments with Slender Beams. Ph.d.Thesis, IMT.
IMT-2011-75	Amini, Hamid	Azimuth Propulsors in Off-design Conditions. Ph.d.Thesis, IMT.
IMT-2011-76	Nguyen, Tan-Hoi	Toward a System of Real-Time Prediction and Monitoring of Bottom Damage Conditions During Ship Grounding. Ph.d.thesis, IMT.
IMT-2011-77	Tavakoli, Mohammad T.	Assessment of Oil Spill in Ship Collision and Grounding, Ph.d.thesis, IMT.
IMT-2011-78	Guo, Bingjie	Numerical and Experimental Investigation of Added Resistance in Waves. Ph.d.Thesis, IMT.
IMT-2011-79	Chen, Qiaofeng	Ultimate Strength of Aluminium Panels, considering HAZ Effects, IMT
IMT-2012-80	Kota, Ravikiran S.	Wave Loads on Decks of Offshore Structures in Random Seas, CeSOS.
IMT-2012-81	Sten, Ronny	Dynamic Simulation of Deep Water Drilling Risers with Heave Compensating System, IMT.
IMT-2012-82	Berle, Øyvind	Risk and resilience in global maritime supply chains, IMT.
IMT-2012-83	Fang, Shaoji	Fault Tolerant Position Mooring Control Based on Structural Reliability, CeSOS.
IMT-2012-84	You, Jikun	Numerical studies on wave forces and moored ship motions in intermediate and shallow water, CeSOS.
IMT-2012-85	Xiang, Xu	Maneuvering of two interacting ships in waves, CeSOS
IMT-2012-86	Dong, Wenbin	Time-domain fatigue response and reliability analysis of offshore wind turbines with emphasis on welded tubular joints and gear components, CeSOS
IMT-2012-87	Zhu, Suji	Investigation of Wave-Induced Nonlinear Load Effects in Open Ships considering Hull Girder Vibrations in Bending and Torsion, CeSOS
IMT-2012-88	Zhou, Li	Numerical and Experimental Investigation of Station-keeping in Level Ice, CeSOS
IMT-2012-90	Ushakov, Sergey	Particulate matter emission characteristics from diesel enignes operating on conventional and alternative marine fuels, IMT
IMT-2013-1	Yin, Decao	Experimental and Numerical Analysis of Combined In-line and Cross-flow Vortex Induced Vibrations, CeSOS
IMT-2013-2	Kurniawan, Adi	Modelling and geometry optimisation of wave energy converters, CeSOS

Report No.	Author	Title
IMT-2013-3	Al Ryati, Nabil	Technical condition indexes doe auxiliary marine diesel engines, IMT
IMT-2013-4	Firoozkoohi, Reza	Experimental, numerical and analytical investigation of the effect of screens on sloshing, CeSOS
IMT-2013-5	Ommani, Babak	Potential-Flow Predictions of a Semi-Displacement Vessel Including Applications to Calm Water Broaching, CeSOS
IMT-2013-6	Xing, Yihan	Modelling and analysis of the gearbox in a floating spar-type wind turbine, CeSOS
IMT-7-2013	Balland, Océane	Optimization models for reducing air emissions from ships, IMT
IMT-8-2013	Yang, Dan	Transitional wake flow behind an inclined flat plate – Computation and analysis, IMT
IMT-9-2013	Abdillah, Suyuthi	Prediction of Extreme Loads and Fatigue Damage for a Ship Hull due to Ice Action, IMT
IMT-10-2013	Ramìrez, Pedro Agustìn Pèrez	Ageing management and life extension of technical systems. Concepts and methods applied to oil and gas facilities, IMT
IMT-11-2013	Chuang, Zhenju	Experimental and Numerical Investigation of Speed Loss due to Seakeeping and Maneuvering. IMT
IMT-12-2013	Etemaddar, Mahmoud	Load and Response Analysis of Wind Turbines under Atmospheric Icing and Controller System Faults with Emphasis on Spar Type Floating Wind Turbines, IMT
IMT-13-2013	Lindstad, Haakon	Strategies and measures for reducing maritime CO2 emissons, IMT
IMT-14-2013	Haris, Sabril	Damage interaction analysis of ship collisions, IMT
IMT-15-2013	Shainee, Mohamed	Conceptual Design, Numerical and Experimental Investigation of a SPM Cage Concept for Offshore Mariculture, IMT
IMT-16-2013	Gansel, Lars	Flow past porous cylinders and effects of biofouling and fish behavior on the flow in and around Atlantic salmon net cages, IMT
IMT-17-2013	Gaspar, Henrique	Handling Aspects of Complexity in Conceptual Ship Design, IMT
IMT-18-2013	Thys, Maxime	Theoretical and Experimental Investigation of a Free Running Fishing Vessel at Small Frequency of Encounter, CeSOS
IMT-19-2013	Aglen, Ida	VIV in Free Spanning Pipelines, CeSOS
IMT-1-2014	Song, An	Theoretical and experimental studies of wave diffraction and radiation loads on a horizontally submerged perforated plate, CeSOS
IMT-2-2014	Rogne, Øyvind Ygre	Numerical and Experimental Investigation of a Hinged 5-body Wave Energy Converter, CeSOS
IMT-3-2014	Dai, Lijuan	Safe and efficient operation and maintenance of offshore wind farms, IMT
IMT-4-2014	Bachynski, Erin Elizabeth	Design and Dynamic Analysis of Tension Leg Platform Wind Turbines, CeSOS
IMT-5-2014	Wang, Jingbo	Water Entry of Freefall Wedged – Wedge motions and Cavity Dynamics, CeSOS
IMT-6-2014	Kim, Ekaterina	Experimental and numerical studies related to the coupled behavior of ice mass and steel structures during accidental collisions, IMT

Report No.	Author	Title
IMT-7-2014	Tan, Xiang	Numerical investigation of ship's continuous-mode ice-breaking in leverl ice, CeSOS
IMT-8-2014	Muliawan, Made Jaya	Design and Analysis of Combined Floating Wave and Wind Power Facilities, with Emphasis on Extreme Load Effects of the Mooring System, CeSOS
IMT-9-2014	Jiang, Zhiyu	Long-term response analysis of wind turbines with an emphasis on fault and shutdown conditions, IMT
IMT-10-2014	Dukan, Fredrik	ROV Motion Control Systems, IMT
IMT-11-2014	Grimsmo, Nils I.	Dynamic simulations of hydraulic cylinder for heave compensation of deep water drilling risers, IMT
IMT-12-2014	Kvittem, Marit I.	Modelling and response analysis for fatigue design of a semisubmersible wind turbine, CeSOS
IMT-13-2014	Akhtar, Juned	The Effects of Human Fatigue on Risk at Sea, IMT
IMT-14-2014	Syahroni, Nur	Fatigue Assessment of Welded Joints Taking into Account Effects of Residual Stress, IMT
IMT-1-2015	Bøckmann, Eirik	Wave Propulsion of ships, IMT
IMT-2-2015	Wang, Kai	Modelling and dynamic analysis of a semi-submersible floating vertical axis wind turbine, CeSOS
IMT-3-2015	Fredriksen, Arnt Gunvald	A numerical and experimental study of a two-dimensional body with moonpool in waves and current
IMT-4-2015	Jose Patricio Gallardo Canabes	Numerical studies of viscous flow around bluff bodies
IMT-5-2015	Vegard Longva	Formulation and application of finite element techniques for slender marine structures subjected to contact interactions
IMT-6-2015	Jacobus De Vaal	Aerodynamic modelling of floating wind turbines
IMT-7-2015	Fachri Nasution	Fatigue Performance of Copper Power Conductors
IMT-8-2015	Oleh Karpa	Development of bivariate extreme value distributions for applications in marine technology